

Optical characterization of metallic nanoparticles: Light attenuation, laser-induced emission, data synthesis

Von der Fakultät für Ingenieurwissenschaften,
Abteilung Maschinenbau und Verfahrenstechnik
der Universität Duisburg-Essen

zur Erlangung des akademischen Grades
eines
Doktors der Ingenieurwissenschaften
– Dr.-Ing. –

genehmigte Dissertation

von

Jan Menser
aus
Duisburg

Gutachter: Prof. Dr. Christof Schulz
Prof. Dr. Kyle J. Daun

Tag der mündlichen Prüfung: 28.03.2019





This picture lets us dream of laser-induced emissions. Taken at Café Steinbruch.



Abstract

Nanotechnology is one of the key technologies, especially for energy storage for electro mobility, energy conversion, catalysis and lighting technology. Each technology requires highly specific nanomaterials, selected in size and size distribution, purity and morphology, and higher-level structures like core-shell structures, layered structures, and nanocomposites. For process control, process optimization and fundamental research various thermophysical properties need to be monitored *in situ*.

Laser-based measurements are well-suited to meeting this demand because they offer: species-selective measurement, high spatial resolution, non-destructive testing, and real-time capability.

This thesis shows the application of spectrally-resolved line-of-sight attenuation (LOSA), time-resolved laser-induced incandescence (TiRe-LII) and phase-selective laser-induced breakdown spectroscopy (ps-LIBS) for improvements in the inference of nanoparticle properties, such like nanoparticle size, thermal accommodation coefficient and saturation vapor pressure.

The modeling of laser-induced emissions requires two models, a spectroscopic model, which can be used to calculate the nanoparticle temperature from incandescence spectra, and a heat-and-mass-transfer model to calculate the particle cooling, including conduction and evaporative cooling.

The spectroscopic model applied in this work is composed of Planck's radiation law, Drude model of a free electron gas to calculate the complex refractive index, and Mie theory to describe the interaction of light with nanomaterials. To check the applicability of the chosen spectroscopic model a thorough literature review was performed and the results are compared to LOSA measurements with reasonable outcome.

The heat-and-mass-transfer model is applied by TiRe-LII and ps-LIBS measurements. It yields the heat fluxes and evaporated mass of the heated nanoparticles in the measurement volume.

Time-resolved laser-induced incandescence (TiRe-LII) is a standard measurement technique in combustion applications, for measuring primary particle sizes and the volume fraction of soot laden gas streams. In this work, the transition from soot to engineered nanoparticles made from silicon or germanium is conducted. It turns out that the chosen approach delivers very good results.

Laser-induced breakdown spectroscopy (LIBS) originates from elemental analysis of solid, liquid and gaseous samples. Recent publications showed the applicability of LIBS for particle-size determination. During cooling, the nanoparticle evaporates—to a certain extent—depending on the applied laser fluence. The atoms in the vapor are thermally excited according to the Boltzmann energy distribution and may luminesce. The luminescence intensity was modeled by a de-excitation cascade. The

primary nanoparticle size and the evaporation properties could be inferred by this technique with very good consistency to TiRe-LII, literature values and the particle-size distribution obtained through transmission electron microscopy.

Additionally, a data-synthesis approach has been developed to reduce the uncertainties of the inferred vapor pressure properties. It could be shown, that the correlation of the quantities of interest were the cause for the improvement of the uncertainty.

Zusammenfassung

Nanotechnologie ist eine der Schlüsseltechnologien, insbesondere zur Energiespeicherung für Elektromobilität, für die Energieumwandlung, Katalyse und Lichttechnik. Jede Technologie erfordert hochspezifische Nanomaterialien, die nach Größe und Größenverteilung, Reinheit und Morphologie, sowie übergeordneten Strukturen wie Core-Shell-Strukturen, Schichtstrukturen und Nanokompositen ausgewählt werden. Für die Prozesssteuerung, Prozessoptimierung und Grundlagenforschung müssen verschiedene thermophysikalische Eigenschaften in situ überwacht werden.

Laserbasierte Messungen eignen sich gut um diesen Bedarf zu decken, da sie speziessensitive Messungen, hohe räumliche Auflösung, zerstörungsfreie Prüfung und Echtzeitfähigkeit bieten.

Diese Arbeit zeigt die Anwendung von spektral aufgelöster Sichtlinienabsorption (LOSA), zeitaufgelöster laserinduzierter Inkandescenz (TiRe-LII) und phasenselektiven laserinduzierter Plasmaspektroskopie (ps-LIBS) um Fortschritte bei der Bestimmung von Nanopartikeleigenschaften wie Nanopartikelgröße, thermischer Akkommodationskoeffizient und Sättigungsdampfdruck zu erzielen.

Für die Modellierung laserinduzierter Emissionen sind zwei Modelle erforderlich: ein spektroskopisches Modell, mit dem die Nanopartikeltemperatur aus Inkandescenzspektren berechnet werden kann, und ein Wärme- und Massentransfermodell zur Berechnung der Partikelabkühlung, einschließlich Leitungs- und Verdunstungskühlung.

Das in dieser Arbeit verwendete spektroskopische Modell setzt sich aus dem Planckschen Strahlungsgesetz, dem Drude-Modell eines freien Elektronengases zur Berechnung des komplexen Brechungsindex und der Mie-Theorie zur Beschreibung der Wechselwirkung von Licht mit Nanomaterialien zusammen. Um die Anwendbarkeit des gewählten spektroskopischen Modells zu überprüfen, wurde eine gründliche Literaturrecherche durchgeführt und die Ergebnisse mit LOSA-Messungen verglichen.

Das Wärme- und Massentransfermodell wird bei TiRe-LII- und ps-LIBS-Messungen angewendet. Es liefert die Wärmeflüsse und die verdampfte Masse der heißen Nanopartikel im Messvolumen.

Die zeitaufgelöste, laserinduzierte Inkandescenz (TiRe-LII) ist eine Standardmessmethode bei Verbrennungsanwendungen, vor allem bei der Messung der Teilchengröße und des Volumenbruchs von rußbeladenen Gasströmen. In dieser Arbeit wird die Erweiterung von Ruß auf Nanopartikel aus Silizium oder Germanium durchgeführt. Es zeigt sich, dass der gewählte Ansatz sehr gute Ergebnisse liefert.

Laserinduzierte Plasmaspektroskopie (LIBS) stammt aus der Elementanalyse von festen, flüssigen und gasförmigen Proben. Kürzlich veröffentlichte Publikationen

zeigten die Anwendbarkeit von LIBS zur Bestimmung von Partikelgrößen. Während des Abkühlens verdampfen die Nanopartikel abhängig von der verwendeten Laserenergiedichte zu einem gewissen Grad. Die Atome im verdampften Nanomaterial werden entsprechend der Boltzmann-Energieverteilung thermisch angeregt und können lumineszieren. Die Lumineszenzintensität wird dabei durch eine Abregungskaskade modelliert. Die primäre Größe der Nanopartikel und die Verdampfungseigenschaften konnten durch diese Technik mit sehr guter Übereinstimmung mit TiRe-LII, Literaturwerten und der durch Transmissionselektronenmikroskopie erhaltenen Partikelgrößenverteilung gemessen werden.

Zusätzlich wurde ein Datensyntheseansatz entwickelt, um Unsicherheiten der abgeleiteten Dampfdruckeigenschaften zu reduzieren. Es konnte gezeigt werden, dass die Korrelationen zwischen den zumessenden Größen der Grund für die Verbesserung der Messunsicherheit ist.

Index

1. Introduction.....	1
2. Nanoparticle synthesis and <i>in situ</i> diagnostics.....	5
2.1. Synthesis	5
2.2. Optical <i>in situ</i> diagnostics.....	7
3. Parameter estimation.....	13
3.1. Bayesian statistics for laser-induced incandescence.....	14
3.2. Marginalizing and sampling Bayes equation.....	15
3.3. Ill-posed problems	16
3.4. Maximum entropy principle.....	17
4. Experimental setup.....	19
4.1. Microwave reactor.....	19
4.2. Reaction conditions	20
4.3. Optical measurements	21
4.4. Particle sampling	22
4.5. Location of the particles.....	26
4.5.1. 2D line-of-sight attenuation.....	26
4.5.2. 2D Rayleigh scattering.....	28
4.5.3. Laser-induced incandescence scan	30
4.5.4. Summarizing the results of the measurement techniques	31
4.6. Temperature within the measurement zone during synthesis...	32
4.6.1. Thermocouple measurements	32
4.6.2. Multiline SiO laser-induced fluorescence.....	32
4.6.3. Thermal radiation of the particles.....	34
4.6.4. Combined temperature within the observation volume.....	35
5. Optical properties of metallic nanoparticles	39
5.1. Fundamentals for understanding nanoparticle optical spectra..	39
5.1.1. Equation of radiative transfer	39
5.1.2. Absorption	40
5.1.3. Scattering	41
5.1.4. Rayleigh approximation.....	44
5.1.5. Planck spectrum.....	46
5.1.6. Semiconductor-metal transition through disorder.....	47
5.1.7. Drude model for metals.....	48
5.2. Optical properties of molten silicon and germanium	50
5.2.1. Determination of optical characteristics through the electrical properties.....	50
5.2.2. Literature review	52

5.3.	Spectrally resolved line-of-sight attenuation (LOSA) measurements	56
5.4.	Incorporating literature data through Bayesian inference	58
5.5.	Conclusions.....	64
6.	Particle sizing through laser-induced incandescence	69
6.1.	Heat and mass transfer model.....	69
6.1.1.	Laser absorption.....	72
6.1.2.	Heat conduction.....	73
6.1.3.	Evaporation	75
6.1.4.	Radiation	78
6.2.	Time-resolved particle temperature	78
6.3.	Analysis of peak temperatures	82
6.4.	Variation of the scaling factor, C_k	84
6.5.	Particle sizing through Bayesian inference	86
6.6.	Conclusions.....	91
7.	Quantification of additional plasma emissions.....	93
7.1.	Laser-plasma formation on surfaces of condensed matter	94
7.2.	Plasma expansion.....	95
7.3.	Thermal emission of plasma species.....	98
7.3.1.	Emission model	98
7.3.2.	Connection of the line-emission model to the heat-transfer model	98
7.3.3.	De-excitation cascade	99
7.4.	Results and discussion	101
7.4.1.	Effect of the laser pulse-length on the nanoparticle peak temperature and evaporation	101
7.4.2.	Prompt line emission.....	102
7.4.3.	Delayed line emissions	106
7.4.4.	Inference of particle size	107
7.5.	Conclusions.....	109
8.	Narrowing uncertainties by data synthesis.....	111
8.1.	Revised inference focused on evaporation parameters.....	111
8.1.1.	LII temperature decay	111
8.1.2.	Peak temperature LII	113
8.1.3.	LIBS atomic emission intensity	115
8.2.	Credibility regions.....	116
8.3.	Synthesizing multivariate normal distributions	117
8.4.	Results and discussion	121
8.4.1.	Silicon as a test case.....	121
8.4.2.	Refined vapor pressure properties of liquid germanium.....	123
8.5.	Conclusions.....	125

9. Outlook.....	127
10. Conclusions.....	129
Publications	133
References	135
Appendix A. Probability density distributions	147
Appendix B. Metrics.....	153
Appendix C. Application of Bayes' equation.....	157
C1. Measurement, Model, Operator.....	157
C2. Bayesian inversion	160
C3. Linear Regression	160
C4. Non-linear fitting through the example of thermal radiation...	163
C5. Bayes' statistics for laser-induced incandescence	167
Acknowledgments.....	171

Fundamental constants

Quantity	Symbol	Value and unit
Speed of light in vacuum	c	$2.997\,924\,58 \times 10^8 \text{ m s}^{-1}$
Charge of electron	e	$1.602\,176\,462 \times 10^{-19} \text{ C}$
Electron volt	eV	$1.602\,176\,6208 \times 10^{-19} \text{ kg m}^2 \text{ s}^{-2}$
Vacuum permittivity	ϵ_0	$8.854\,187\,816 \times 10^{-2} \text{ F m}^{-1}$
Planck constant	h	$6.626\,068\,76 \times 10^{-34} \text{ J s}$
Reduced Planck constant	$\hbar = h/(2\pi)$	$1.054\,571\,60 \times 10^{-34} \text{ J s}$
Avogadro constant	N_A	$6.022\,141\,99 \times 10^{23} \text{ mol}^{-1}$
Boltzmann constant	k_B	$1.380\,648\,52 \times 10^{-23} \text{ J K}^{-1}$ $8.617\,3303 \times 10^{-5} \text{ eV K}^{-1}$
Atomic mass unit	u	$1.660\,538\,73 \times 10^{-27} \text{ kg}$
Rest mass of electron	m_e	$9.109\,381\,88 \times 10^{-31} \text{ kg}$ $5.485\,799\,09 \times 10^{-4} \text{ u}$

Abbreviations

Symbol	Meaning	Unit
d_p	Particle diameter	nm
T_{index}	Temperature of the indexed property	K
λ	Wavelength	nm
α	Thermal accommodation coefficient	
ϵ	Measurement noise	
σ , STD	Standard deviation	
f_V	Volume fraction	usually in parts per million (ppm)
\mathcal{L}	Likelihood	
$\mathcal{N}(\mu, \sigma^2)$	Normal distribution with mean μ and variance σ^2	
$\Re(\mathbf{x})$	Real part of complex value \mathbf{x}	
$\Im(\mathbf{x})$	Imaginary part of complex value \mathbf{x}	
$\mathbf{m} = n_r + i n_i$	Complex refractive index, with n_r real part and n_i imaginary part	
$\epsilon = \epsilon_r + i \epsilon_{II}$	Complex dielectric function, with ϵ_r F/m real part and ϵ_{II} imaginary part	
κ_λ	Spectral opacity	1

K_{abs}	Absorption coefficient	m^{-1}
Q_{abs}	Absorption efficiency	1
K_{scat}	Scattering coefficient	m^{-1}
Q_{scat}	Scattering efficiency	1
Q_{ext}	Extinction efficiency	1
$E(\mathbf{m})$	Absorption function	
$F(\mathbf{m})$	Scattering function	
EM	Electromagnetic	
ω_p	Plasmon frequency	rad/s
τ	Mean relaxation time	s
x	Size parameter	1
Ω	Solid angle	Steradian
I	Intensity	counts
N''	Number flux	$\text{s}^{-1}\text{m}^{-2}$
v_{th}	Thermal velocity	m/s
\mathbf{J}	Jacobian matrix	
$\mathbf{\Sigma}$	Covariance matrix	
RoI	Region of interest	
QoI	Quantity/quantities of interest	
LIF	Laser-induced fluorescence	
TiRe LII	Time-resolved laser-induced incandescence	
LOSA	Line-of-sight attenuation	
LIBS	Laser-induced breakdown spectroscopy	
DSLR	Digital single lens reflex (camera)	
CCD	Charge-coupled device	
MLE	Maximum likelihood estimate	
MAP	Maximum <i>a posteriori</i> estimate	
MCMC	Markov-chain Monte Carlo	
CDF	Cumulative distribution function	
PDF	Probability density function	
FWHM	Full-width half-maximum	
RTE	Equation of radiative transport	

1. Introduction

Nanotechnology deals with particles and structures that range from 100 nm down to the atomic level, and is one of the key technologies of the twenty-first century. Especially for energy storage for electro mobility, energy conversion, catalysis and lighting technology nanostructures are of great relevance. Silicon nanoparticles, for example [2], have applications in photovoltaics, lithium-ion batteries [3], light emitters [4], and thermoelectrics [5]. All of these technologies require highly specific nanomaterials, selected in particle size and size distribution, purity and morphology, and super-structures like core-shell structures, layered structures, and nanocomposites.

There are two routes for the production of nanoparticles, the top-down and the bottom-up approach. The top-down approach starts with macroscopic base material and through etching or milling nanostructures are generated. For example, etching of photolithographic treated surfaces is the central method for the production of semiconductor chips with structure size below 10 nm [6]. In contrast, through the bottom-up approach, the nanostructure self-assembles from atoms or molecules, either in the liquid or in the gas phase. The two major bottom-up synthesis routes using gas-phase reactions starting from various molecular precursors are chemical vapor deposition (e.g., vapor phase epitaxy or atomic layer epitaxy) and homogeneous nucleation in the gas phase, especially in furnace flow reactors, flame reactors, and plasma reactors.

The widespread use of these nanoparticles motivates the development of high-throughput gas-phase synthesis techniques [7]. Developing these processes requires instrumentation that can provide spatially and temporally resolved measurements of nanoparticle sizes, precursor and intermediate species concentrations, and temperature to understand the nanoparticle nucleation and growth within the reactors, and to ensure that the resulting nanopowders have the desired properties.

Optical *in situ* measurement techniques enable spatially resolved, non-invasive measurements of temperature [8], species concentration [9], and particle volume fractions and sizes without perturbing the local physics and chemistry processes that underlie nanoparticle formation. The resulting information, on the one hand, enables a deeper understanding of the physical and chemical processes, and on the other hand gives the opportunity for optimization of synthesis processes.

In recent years, time-resolved laser-induced incandescence (TiRe-LII) has been successfully applied to aerosols formed during hydrocarbon combustion. Target properties most often were the particle size and the thermal accommodation coefficient of soot within flames and in their exhaust gases. TiRe-LII needs a laser that heats the nanoparticles within a sample volume to incandescent temperature. Subsequent to the laser pulse, the nanoparticles cool down to the gas-phase temperature in the vicinity. Interpreting TiRe-LII data requires a spectroscopic model that relates the measured instantaneous spectral intensity to the nanoparticle

temperature, and a heat-transfer model that relates the measured temperature decay to the nanoparticle size, accommodation coefficient, and vapor pressure properties.

Laser-induced breakdown spectroscopy (LIBS, sometimes also called laser-induced plasma spectroscopy, LIPS), is a measurement technique originating from elemental analysis of solids, liquids, and gases. A high-irradiance laser pulse is focused into the probe volume, which vaporizes and ionizes the sample. The resulting plasma emits radiation from electronically-excited ions, atoms, and molecules and from the interaction of these (Bremsstrahlung). Recently, it was shown, that it is possible to involve mainly the solid constituents of an aerosol [10] into the plasma process through so-called phase-selective (ps) LIBS. Consequentially, the measured emission intensity only emerges from the nanomaterial dispersed in an aerosol with a correlation of emission intensity and particle size and volume fraction.

Nanotechnology for energy storage purposes require nanoparticles made from various elements. In this study, optical *in situ* measurement techniques are used to examine the synthesis of silicon and germanium nanoparticles. To transfer the previous knowledge of laser-induced incandescence and laser-induced breakdown spectroscopy to non-carbonaceous materials these questions need to be answered:

1. How can the temperature of silicon and germanium nanoparticles be determined?
2. Does the cooling model established for soot-related LII also apply to engineered metallic particles?
3. Can the plasma emission be correlated to particle properties and fundamental characteristics such as the evaporation properties?
4. Can the large uncertainties of the evaporation properties of high-temperature nanomaterials currently reported in literature be reduced by combining LII and LIBS?

In this thesis, the applicability of laser-based measurements is shown for liquid silicon and germanium nanoparticles synthesized in a microwave-plasma reactor. The current knowledge of absorption and emission of light through nanoparticle clouds is discussed with respect to former publications and placed in a statistically rigorous context. The outcome is verified separately using extinction measurements made at the exact point of the following measurements. The verified spectroscopic model lays the foundation to be applied to TiRe-LII measurements to gain information on particle sizes and thermal accommodation coefficients. A heat transfer model that includes both evaporation and conduction heat transfer is applied. The evaporation model especially requires thermophysical properties of the nanoparticles. The inferred values are compared to transmission electron micrographs. With higher laser fluences, plasma emission occurs. The spectral position of the emissions can be assigned to constituents of the nanoparticles and not the gas-phase in the vicinity of the nanoparticles. A model, relying on phase-equilibrium between nanoparticle and vapor is deduced and applied to infer the

nanoparticle size. The thesis proceeds with a focus on vapor-pressure properties. The aforementioned measurement are repetitively analyzed, but with Antoine parameters as target properties. A data synthesis technique that benefits from combined measurement techniques that address multiple physical properties of the same sample is applied to reduce uncertainties in these parameters. The dissertation concludes with a discussion of the presented measurement techniques with a strong orientation towards the observed discrepancies of optical and vapor-pressure properties of silicon and germanium nanoparticle.

2. Nanoparticle synthesis and *in situ* diagnostics

“Nanotechnology is an idea that most people simply didn’t believe” – Ralph Merkle, 2000

In search of highly customizable materials, nanoparticles come more and more into the focus of research. Silicon nanoparticles are of interest for a wide range of applications. Examples include luminescing tracers in medicine [11] due to their adaptable luminescence spectrum, and, because of the high ion storage density, as anode material for lithium ion batteries [12]. To satisfy industrial demands, lab-scale reactors must be scaled up. This scale-up cannot easily be performed by geometrically enlarging the production facility. Due to the change of the characteristic numbers [13], e.g., the Schmidt number Sc describing the diffusive transport and the Damköhler number Da describing the convective transport scale differently with the characteristic length of an apparatus. Therefore, detailed information is required that can be provided by *in situ* diagnostics to monitor particle and gas-phase properties during nanoparticle synthesis. Furthermore, *in situ* diagnostics enable the inference of properties that are still not well known or simply not available for certain conditions.

2.1. Synthesis

Generally, two different approaches for producing nanoparticles can be identified [14]; the top-down approach where source material with a larger size is processed, e.g., milling, lithography [15, 16], thermal processing (*cf.* Figure 1 right, [17]) or electro-exploding wire [18], and the bottom-up approach, where nanoparticles are newly formed from precursors, especially the gas-phase synthesis processes used in this work. Figure 1 shows the reaction zones of three different gas-phase nanoparticle synthesis reactors.

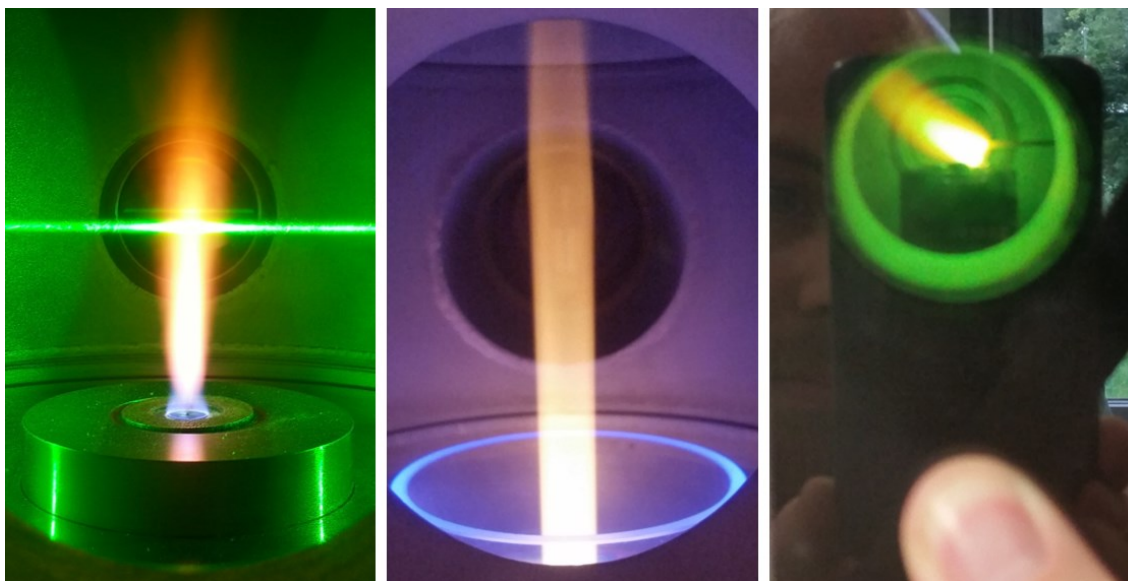


Figure 1: Images of nanoparticle synthesis processes. Left: Spray-flame synthesis of titanium dioxide nanoparticles through the combustion of titanium isopropoxide (TTIP) dissolved in ethanol. Center: Plasma synthesis of silicon nanoparticles with SiH_4 . Right: Generation of copper nanoparticles using an arc-transfer process melting and evaporating copper with subsequent inert-gas condensation into nanoparticles.

Top-down approaches most often apply different milling techniques that allow for the reduction of the particle diameter from coarse material stepwise to a fine powder. Milling usually yields a broad particle size distribution without control on the particle morphology and agglomeration. Additionally, the top-down approach is energetically less efficient than the bottom-up processes.

Bottom-up processes build up the nanoparticles from “scratch” starting at the atomic/molecular level. Therefore, a precursor material must be available as reactant that can be decomposed or evaporated through energy provided by the experimental conditions. For example, silane (SiH_4) and germane (GeH_4) are decomposed by the thermal energy [19-21] provided by an Argon plasma $\text{SiH}_4 + \Delta E \rightarrow \text{Si} + 2 \text{H}_2$, where (in this case) the silicon vapor further condenses forming silicon nanoparticles. Another example is the generation of titanium dioxide nanoparticles [22-24] through the combustion of titanium isopropoxide (TTIP) with $\text{Ti}(\text{OC}_3\text{H}_7)_4 + \text{O}_2 + \Delta E \rightarrow \text{TiO}_2 + \text{waste gas}$, where the energy is provided by the combustion process of the precursor and/or an additional fuel.

Figure 2 illustrates the synthesis of nanoparticles in the gas phase. A gaseous precursor is added to a process gas stream and thermally decomposed. The energy may be provided by a flame/combustion, a plasma or other heating mechanism, e.g., a furnace. The decomposed precursor forms a supersaturated molecule or atom vapor that condenses to the first clusters. These clusters, in turn, collide to form the initial nanoparticles. The initial particles grow further, either by the surface-condensation of additional molecules or through collisions with other particles, which is then called coalescence. Depending which time scales dominate—sintering or collision time—

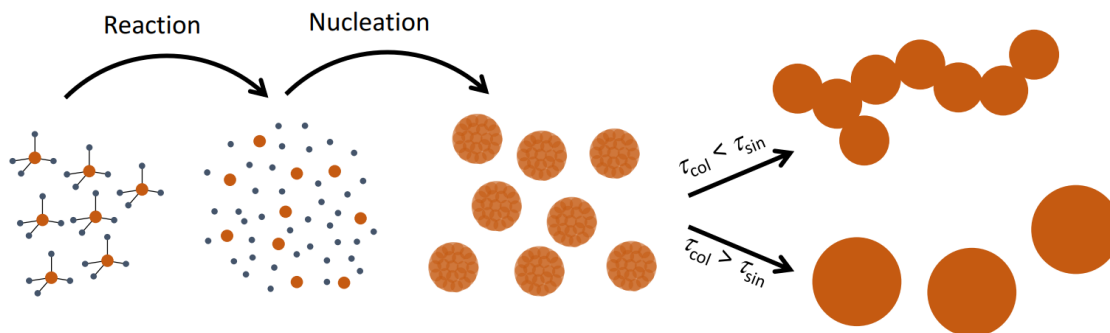


Figure 2: Principle of gas-phase nanoparticle synthesis, based on [25]

the generation of the nanoparticle powder stops either with spherical particles ($\tau_{\text{collision}} > \tau_{\text{sinter}}$) or larger agglomerates are formed ($\tau_{\text{collision}} < \tau_{\text{sinter}}$).

Obviously, combustion-based processes will mainly result in oxide nanoparticles (unless noble metal precursors are used), while plasma reactors can be operated such that an oxygen-free atmosphere is maintained, and pure metal or semiconductor nanoparticles can be produced.

2.2. Optical *in situ* diagnostics

The properties of the synthesized nanoparticles strongly depend on gas-phase temperature, cooling rate, and pressure. To gain knowledge on these properties without disturbing the process sophisticated *in situ* measurement techniques are needed, many of them are laser based.

Broadly used to measure gas-phase temperature fields is multiline laser-induced fluorescence (LIF) [8, 26-28], where the most-frequently used target species for determining temperature from the population of various rotational and vibrational levels is nitric oxide (NO) and OH. In the synthesis of SiO₂ nanoparticles the intermediate SiO has been used instead. Multiline SiO LIF is further discussed in Chapter 4.6.2.

Spectrally-resolved chemiluminescence measurements [29] enable to probe species (e.g., CH*, OH*, H*, Ar*) that are formed in an electronically-excited state as a consequence of chemical reactions. In a thermal plasma applied in this work, molecules and atoms can be electronically excited through the high gas temperature or through interaction with hot electrons. The subsequent luminescence enables to measure the decomposition products of the initial reactants. Figure 3 shows the plasma emissions during synthesis and the corresponding emission spectrum [30] with several lines corresponding to the excited supply gases (H₂ and Ar) but also contribution of Si*, which indicates an ongoing decomposition of the precursor.

Particle size and growth can be measured, for example, by extracting particles from the aerosol with molecular beam sampling into a particle mass spectrometer [9, 31] or optically with time-resolved laser-induced incandescence (TiRe-LII) [32-35].

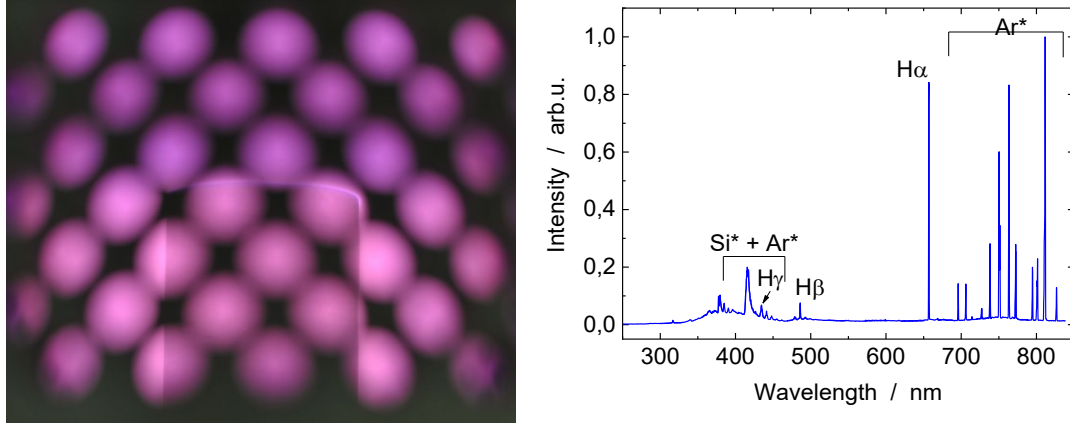


Figure 3: Emission of the Ar/H₂/SiH₄ plasma during synthesis. Left: Image of the plasma through the ventilation holes of the reactor chamber. Right: Luminescence spectrum.

Time-resolved laser-induced incandescence is an established diagnostics mainly used to recover soot/carbon-black particle sizes and volume fractions in combustion-related applications [32, 33, 36, 37]. In this technique, a laser pulse heats the nanoparticles within a sample volume of aerosol. The resulting spectral incandescence is measured as the nanoparticles return to the ambient gas temperature. In TiRe-LII the spectral incandescence of the laser-heated nanoparticles is measured as a function of time when the nanoparticles thermally equilibrate with the bath gas. The magnitude of the time-integrated incandescence signal is proportional to the particle volume fraction, while the nanoparticle size distribution is inferred from the decay of the incandescence signal after pulsed laser heating, since small nanoparticles cool faster than large ones [38].

Because the incandescence intensity decays rapidly, a reasonable temperature determination is only possible within a short time period of approximately 1 μ s subsequent to the laser heating. Mansmann et al. [39] describe the application of gated photomultiplier tubes with a subsequent temporal sampling to overcome the larger error in temperature at later points in time that would otherwise result from a measurement with a very large dynamic range. This technique offers a suitable way of enlarging the available measurement time with high signal-to-noise ratios for a more precise particle diameter determination.

Also of importance for a temperature determination is the use of spectral information. In the majority of publications the incandescence spectrum is assumed to follow the Planck spectrum weighted by the emission cross-section and the Rayleigh approximation for small particles. The intensity is often measured pyrometrically with two detectors equipped with narrowband filters. Consequentially, except from the ratio of the band-averaged signals, the spectral information is lost. Particularly at high laser fluences or uncommon materials, the underlying assumptions may not hold, and a precise incandescence spectrum is needed. Goulay et al. [40] present incandescence spectra between -11 and $+33$ ns (compared to the maximum laser pulse intensity) acquired with a spectrograph

equipped with a gated ICCD camera. The measurements, however, show, that the measured temperatures obtained from complete spectra are not necessarily consistent with the temperatures obtained from two narrow spectral bands. One possible reason for this problem is given by Mansmann et al. [41] who indicate, that non-linear effects in photomultiplier tubes can be responsible for errors in temperature determination around the peak temperature.

In the aforementioned studies, LII is mainly applied to soot/carbon black generated in flames. In this thesis metallic nanoparticles (liquid silicon and germanium) will be analyzed, such that information about the temporal variation of the signal (interpreted by a heat transfer model, *cf.* Chapter 6.1) and spectral information is needed (optical properties of metallic nanoparticles, *cf.* Chapter 5). A streak camera/spectrometer combination provides both, the temporal and spectral resolution. To the best of the author's knowledge, no other work is published, where a streak camera/spectrometer combination is used to infer temporally resolved spectra for laser-induced incandescence measurements. The basic principle is illustrated in Figure 4.

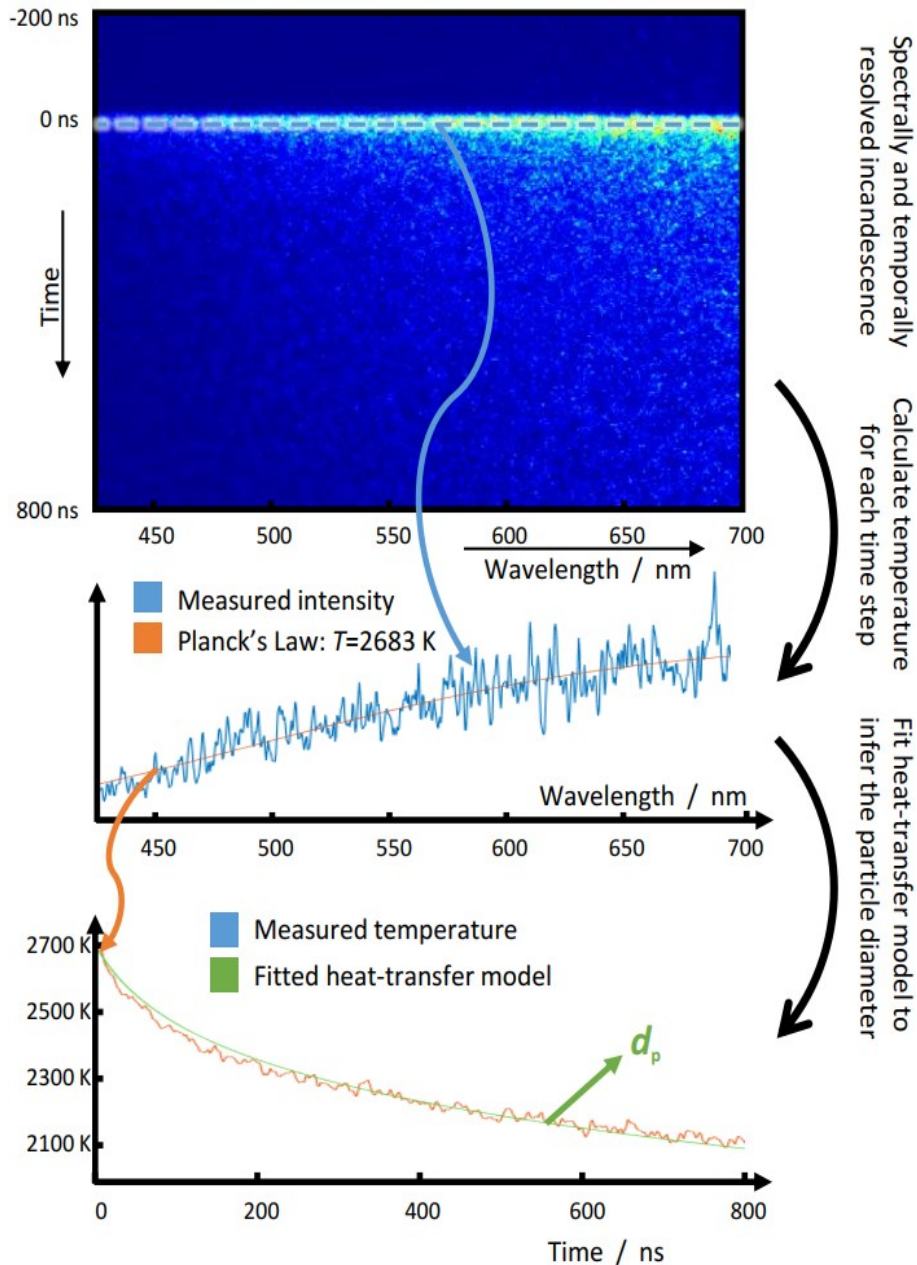


Figure 4: The principle of spectrally- and temporally-resolved laser-induced incandescence.

When the applied laser fluence is high enough to achieve impact ionization of electrons with neutral atoms and molecules, a laser-induced plasma can be formed. Subsequent to the laser pulse, these ions equilibrate to their ground state and can undergo luminescent transitions that can be spectroscopically analyzed. Laser-induced breakdown-spectroscopy (LIBS) has been applied for qualitative and quantitative bulk species detection in almost any material phase [42, 43]. LIBS can be applied to analyze the elemental composition of solids. For example the SuperCam [44] which will be send to Mars within the Mars 2020 project includes a LIBS device. The conventional application of laser-induced breakdown spectroscopy is the analysis of pure gas-phase properties. Kiefer et al. [45] use LIBS for distinguishing between hot and cold gases within a flame. Due to the temperature-dependent

breakdown probability the number of breakdown events could be used to assess the temperature range within the measurement volume. The obtained results showed very good agreement with supporting OH laser-induced fluorescence measurements. In addition to the temperature region, the mixture fraction could be measured taking the LIB spectrum into account.

To overcome pressure limitations because of uncontrollable avalanche ionization processes, Hsu et al. [46] make use of femtosecond lasers. At elevated pressures of approximately 40 bar, the mean collision time of the laser generated seed-electrons is shorter than at ambient pressures, and so uncontrollable avalanche ionization becomes dominant. According to the authors, multi-photon excitation is the main excitation process while applying femtosecond laser.

Recently, LIBS has been applied to investigate the size of inorganic nanoparticles, e.g., TiO_2 , Si, and VO_3 [10, 47]. The so-called “phase-selective” LIBS method involves ionization of the evaporated species without additional ionization of the enveloping gas phase. Tse et al. attributed atomic line emissions from neutral Ti I or V I to multi-photon excitation of the atoms evaporated from TiO_2 or VO_3 nanoparticles [10, 48]. The bandgap of nanoscale semiconductor materials is particle-size dependent, and the authors estimate a bandgap energy based on the quantum confinement effect [49] of $\Delta E_{g,10\text{nm}} = 3.22$ eV and $\Delta E_{g,3\text{nm}} = 3.43$ eV for nanoparticle of 10 and 3 nm, respectively. The change in bandgap energy alters the probability of a two-photon excitation, and therefore, the emission intensity can be used to determine nanoparticle sizes *in situ* within the aerosol. If two-photon excitation is the reason for the luminescence is not yet confirmed. In any case, two-photon excitation does not apply to metals, because they do not exhibit a bandgap and, thus, the direct absorption of photons is most likely.

Signal interpretation of aerosol LIBS, however, is challenging because there are several pathways through which the vapor of the nanoparticle can be excited to the plasma state. Moghaddam et al. [50] showed that the initial electrons that generate the plasma may come from the gas phase or from the nanoparticles through thermionic emissions or multiphoton photoelectric emissions, respectively. When the plasma is developed (within a few nanoseconds), and therefore, a mixture of free electrons, ions, and neutrals is present, laser light can additionally be absorbed by the charged matter. The highly-excited atoms and electrons can also ionize and excite the matter in the vicinity of the nanoparticle through inelastic collisions. A specific pathway strongly depends on the laser wavelength, laser energy, laser pulse length, gas-phase properties, and initial electron density [42, 43].

Figure 5 shows the basic principle of the signal analysis of acquired laser-induced plasma spectra. Firstly, the atomic line-emissions of the corresponding species is extracted. The emission follows a complex structure, which is explained in more detail in Chapter 7. A specific part of the signal is then used for further processing. In the last step, the model derived in Chapter 7.3 is fitted to the acquired data to infer nanoparticle properties, e.g., particle diameter and vapor pressure parameters.

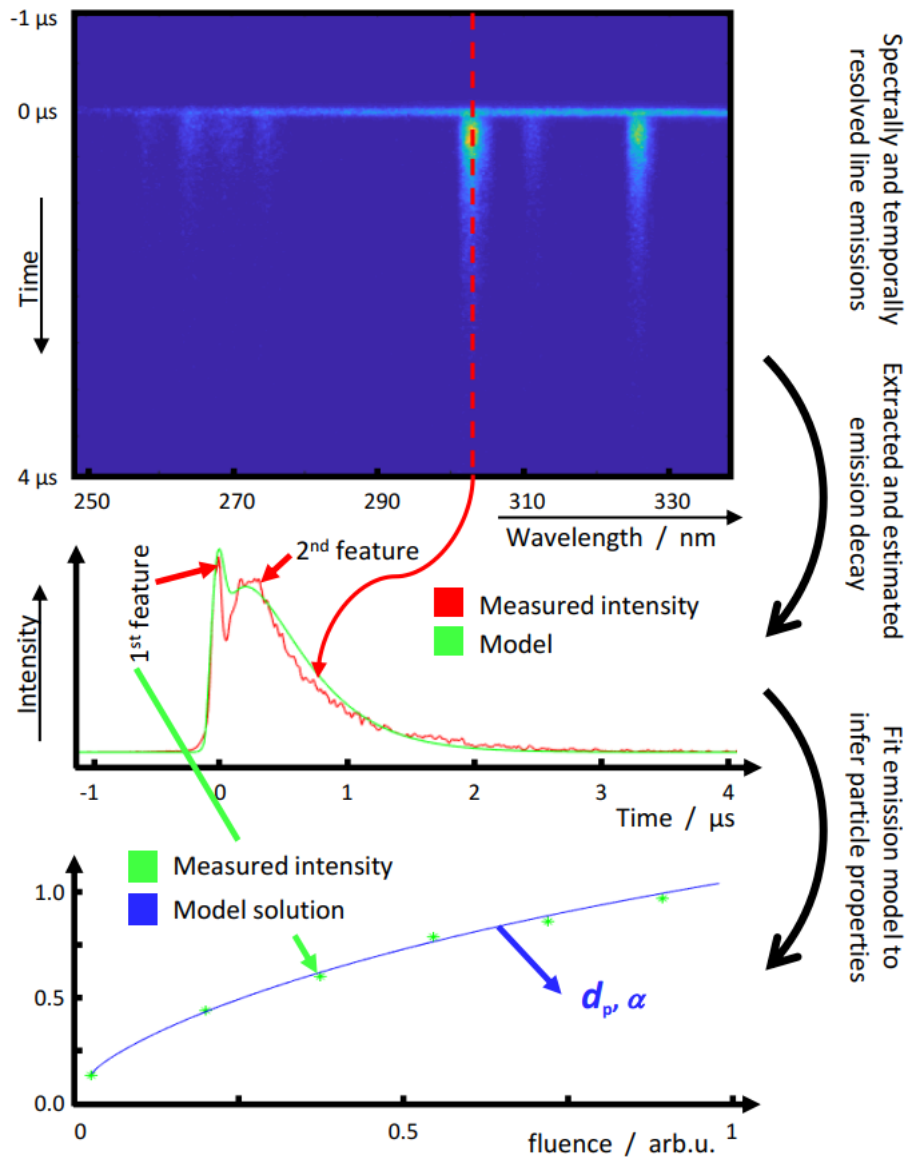


Figure 5: The principle of spectrally- and temporally-resolved laser-induced plasma spectroscopy.

3. Parameter estimation

“Today's posterior distribution is tomorrow's prior” – Dennis Lindley, 1970

This chapter summarizes common techniques and implementation strategies for a rigorous statistical evaluation of measurement and model data. Since the measurement noise of our measurements is almost perfectly normally distributed, this section gives the introduction for uncorrelated, independent noise. For a more general introduction to parameter estimation with a Bayes approach the reader is referred to Peter Hoff, “A First Course in Bayesian Statistical Methods” [51] that extensively explains the insertion of prior information with the most important probability distributions. Richard Aster et al. “Parameter estimation and inverse Problems” [1] establishes a workflow for the incorporation of uncertainties of geophysical data – but is also very informative for this work. The first chapters of Scott M. Lynch “Introduction to applied Bayesian statistics and estimation for social scientists” [52] give a very illustrative introduction to Bayesian statistics and motivate the statistical approach of interpreting measurement data.

In this work, uncertainty analysis is carried out through the Bayesian framework. Bayes’ theorem originates from probability theory and describes conditional probabilities. When several conditions are expected to occur, the conditional probability shows the probability of one condition, when another condition is known. Bayes’ theorem enables the inversion of the conclusion. Here, probabilities were used to describe both, the measurement and the model uncertainties. Generally, the assumption that measurement or parameter values are fixed is discarded, and replaced by probability density distributions of the respective values. Bayes’ theorem enables to propagate uncertainties through the complete signal analysis, presented in Appendix C.

Consider two events A and B , the probability with which both will occur is $p(A \cap B)$, with \cap the intersection between A and B . When $p(A) > 0$ and $p(B) > 0$ then the conditional probabilities $p(A|B)$ are

$$p(A|B) = \frac{p(A \cap B)}{p(B)}$$

$$p(B|A) = \frac{p(B \cap A)}{p(A)} = \frac{p(A \cap B)}{p(A)} \quad (3.1)$$

Through simple inserting and transforming the two lines of Eqs. (3.1), Bayes’ equation can be formulated

$$p(A|B) = \frac{p(B|A) \cdot p(A)}{p(B)} \quad (3.2)$$

with $p(B|A)$, pronounced “probability of B given A ”, which specifies the probability of the event B , when condition A is true, and its inverse $p(A|B)$. The probabilities of the events A and B are so-called marginal probabilities $p(A)$ and $p(B)$, that describe

the probability of an event without conditioning to the occurrence on another event, e.g., the probability $p(A)$, has just A as an event.

3.1. Bayesian statistics for laser-induced incandescence

Bayesian statistics can also be applied in the context of laser-induced incandescence measurements. The desired parameters are nanoparticle size, d_p , thermal accommodation coefficient, α , and all parameters relevant to modeling the evaporation by Antoine's equation C_1 , C_2 , and C_3 (*cf.*, Chapter 6.1.3). For this purpose, the pyrometrically-inferred temperature decay is related to the heat-transfer model defined in section 6.1.3. It is important to acknowledge that noise in the pyrometric temperature data (*cf.* preceding chapter), as well as the uncertainties in the evaporation heat transfer model, mean that many candidate solutions of $[d_p, \alpha]$ could explain the data with almost equal probabilities. Consequently, d_p and α are calculated using Bayes' methodology.

The quantities of interest, $\mathbf{x} = [d_p, \alpha]^T$ and the measured noisy pyrometric temperature data $\mathbf{T} = [T_{p,1}, T_{p,2}, \dots, T_{p,N}]^T$ with the associated noise $\boldsymbol{\sigma}_T = [\sigma_{T,1}, \sigma_{T,2}, \dots, \sigma_{T,N}]^T$ are treated as stochastic variables. The vector \mathbf{T} includes the temporally resolved pyrometric nanoparticle mean-temperature for each measured time step $T_{p,1}$, where the subscript number represents the corresponding time step. The vector $\boldsymbol{\sigma}_T$ contains the associated temperature standard deviations. To yield correct mathematic equations (Appendix C), the presented row vectors need to be transposed into column vectors through the transpose operator (superscript $T \rightarrow$ e.g., \mathbf{x}^T). Rather than treating the evaporation model parameters as deterministic, they are also modeled as stochastic variables that obey a distribution, $\boldsymbol{\theta} = [C_1, C_2, C_3]^T$. The variables in $\boldsymbol{\theta}$ are called "nuisance parameters" because they are not in the focus of the inference process but must also be inferred to properly account for uncertainty in the quantities of interest. These variables are related through Bayes' equation (3.2). Bayes' equation representing the measurement properties is given by

$$p(\mathbf{x}, \boldsymbol{\theta} | \mathbf{T}) = \frac{p(\mathbf{T} | \mathbf{x}, \boldsymbol{\theta}) p_{\text{pr}}(\mathbf{x}) p_{\text{pr}}(\boldsymbol{\theta})}{p(\mathbf{T})}, \quad (3.3)$$

where $p(\mathbf{x}, \boldsymbol{\theta} | \mathbf{T})$ is the joint posterior probability density of \mathbf{x} and $\boldsymbol{\theta}$ conditional on the observed data in \mathbf{T} , $p(\mathbf{T} | \mathbf{x}, \boldsymbol{\theta})$ is the likelihood of the measured data occurring for a hypothetical \mathbf{x} . $p_{\text{pr}}(\mathbf{x}) = p_{\text{pr}, d_p}(d_p) p_{\text{pr}, \alpha}(\alpha)$, and $p_{\text{pr}}(\boldsymbol{\theta}) = p_{\text{pr}, C_1}(C_1) p_{\text{pr}, C_2}(C_2) p_{\text{pr}, C_3}(C_3)$ are the joint prior probabilities of the parameters in \mathbf{x} and $\boldsymbol{\theta}$ based on knowledge available about these parameters before the measurement, and $p(\mathbf{T})$ is the evidence,

$$p(\mathbf{T}) = \int \int p(\mathbf{T} | \mathbf{x}, \boldsymbol{\theta}) p_{\text{pr}}(\mathbf{x}) p_{\text{pr}}(\boldsymbol{\theta}) d\mathbf{x} d\boldsymbol{\theta}, \quad (3.4)$$

used to scale Eq. (3.3) so that it satisfies the Law of Total Probability. It is called evidence because the practitioner actually witnessed the temperature measurement.

In comparison, the parts of Bayes' equation in Eqs. (3.2) and (3.3) can be connected. The likelihood is given by $p(B|A) = p(\mathbf{T}|\mathbf{x}, \boldsymbol{\theta})$ and the joint probabilities $p(A) = p_{pr}(\mathbf{x})p_{pr}(\boldsymbol{\theta})$ that combine the prior information of the parameters of interest and the nuisance parameters. The posterior probability is $p(\mathbf{x}, \boldsymbol{\theta}|\mathbf{T}) = p(A|B)$.

If the temperature measurements are independent at each measurement time and the noise is normally-distributed, the likelihood is given by

$$p(\mathbf{T}|\mathbf{x}, \boldsymbol{\theta}) \propto \exp \left\{ - \sum_{j=1}^{Nt} \frac{[T_{p,j} - T_p(\mathbf{x}, \boldsymbol{\theta}, t_j)]^2}{2\sigma_{T,j}^2} \right\}, \quad (3.5)$$

where $T_p(\mathbf{x}, \boldsymbol{\theta}, t_j)$ are found by solving Eq. (A.28) with the unknown particle size d_p and the first pyrometric temperature in \mathbf{T} as initial conditions.

Finding the values of \mathbf{x} and $\boldsymbol{\theta}$ by minimizing the summation in Eq. (3.3) equivalent to least-squares minimization, returns the maximum likelihood estimate $[\mathbf{x}, \boldsymbol{\theta}]_{MLE}$, which are the most probable set of combined values $[\mathbf{x}, \boldsymbol{\theta}]$ based on the observed data. There are two key problems with using this estimate: (i) The measurement noise contaminating the data and the large number of degrees of freedom give $p(\mathbf{T}|\mathbf{x}, \boldsymbol{\theta})$ a flat topography surrounding the maximum likelihood estimate. Reporting a single point estimate only, therefore, understates the uncertainty in these inferred parameters. (ii) This process neglects additional information about $\mathbf{x} = [d_p, \alpha]^T$ and, especially, $\boldsymbol{\theta} = [C_1, C_2, C_3]^T$ known prior to the LII measurement, which can reduce the uncertainty in the inferred values.

This additional information is incorporated into the inference through the prior probabilities in Eq. (3.3). Specifically, by definition $d_p > 0$ and $0 \leq \alpha \leq 1$, which corresponds to

$$p_{pr,d_p}(d_p) \equiv \begin{cases} 1 & d_p > 0 \\ 0 & \text{otherwise} \end{cases} \text{ and } p_{pr,\alpha}(\alpha) \equiv \begin{cases} 1 & 0 \leq \alpha \leq 1 \\ 0 & \text{otherwise} \end{cases}. \quad (3.6)$$

This means, that values of $d_p < 0$, and $\alpha < 0$ or $\alpha > 1$ have zero probability. Modeling the C_1 , C_2 , and C_3 priors as normal distributions is consistent with the Principle of Maximum Entropy, presented in Chapter 3.4.

Maximizing $p(\mathbf{x}, \boldsymbol{\theta}|\mathbf{T})$, that is proportional to $p(\mathbf{T}|\mathbf{x}, \boldsymbol{\theta}) p_{pr}(\mathbf{x}) p_{pr}(\boldsymbol{\theta})$, provides the maximum *a posteriori* estimate (MAP), $[\mathbf{x}, \boldsymbol{\theta}]_{MAP}$, which is the most probable estimate for $[d_p, \alpha, C_1, C_2, C_3]$ considering both the observed temperature data and prior knowledge about the evaporation model parameters.

3.2. Marginalizing and sampling Bayes equation

The likelihood function carries the information required to estimate the uncertainties. If the likelihood function $p(\mathbf{T}|\mathbf{x}, \boldsymbol{\theta})$ is sampled over a sufficiently large parameter space the uncertainties for a single parameter of interest can be inferred by marginalizing the likelihood function around this parameter. Especially, the

influence of the nuisance variables can be removed by integrating over their domain, leaving a 2D marginalized posterior probability density, in this case only depending on the parameters of interest $\mathbf{x} = [d_p, \alpha]^T$

$$p(\mathbf{x}|\mathbf{T}) = \int_{\boldsymbol{\theta}} p(\mathbf{x}, \boldsymbol{\theta}|\mathbf{T}) d\boldsymbol{\theta} = \int_{-\infty}^{\infty} \int_{-\infty}^{\infty} p(\mathbf{x}, \boldsymbol{\theta}|\mathbf{T}) dC_1 dC_2, \quad (3.7)$$

which can then be marginalized into 1D posterior probability densities for d_p and α ,

$$p(d_p|\mathbf{T}) = \int_0^1 p(\mathbf{x}|\mathbf{T}) d\alpha, \quad p(\alpha|\mathbf{T}) = \int_0^{\infty} p(\mathbf{x}|\mathbf{T}) dd_p. \quad (3.8)$$

Finally, these densities can be summarized by Bayesian credibility intervals (loosely interpreted as confidence regions) that contain a prescribed probability density, e.g., 90%.

Depending on the complexity and, especially, the dimension of the minimization problem, there are different pathways to calculate the likelihood function. One problem can be, that the model is not even roughly linear. Then, the shape of the probability distribution $p(d_x)$ will no longer be correlated to the shape of the data uncertainties. More precisely, a normal distributed measurement error will not be retrievable within the model parameter probability distribution.

When sampling a sufficiently large volume of the parameter space exceeds the available computational power, “smarter” sampling technique can be applied. Markov-Chain Monte-Carlo methods [53] (MCMC) utilize the Metropolis-Hastings [54] or Gibbs algorithm [55] to sample the probability density and, in the end, converge to the true probability distribution, which then can be marginalized.

3.3. Ill-posed problems

A well-posed problem has the following properties, (i) a solution exists, (ii) the solution is unique and (iii) the initial conditions change the behavior of the solution linearly. If the treated problem violates one of these properties it is ill-posed. The problems discussed in this work often violate condition (ii) and (iii).

In the context of LII measurements (*cf.* Chapters 3.1 and 6.5), several parameters need to be considered that influence the measured quantity, for example $[\mathbf{x}, \boldsymbol{\theta}] = [d_p, \alpha, C_1, C_2, C_3]$. Due to measurement noise and short observation times a variety of parameter combinations can explain the measured data. This can result in very broad and flat probability density distributions, within which no distinct parameter set is eligible. The result needs to be interpreted as a probability density.

One way of reducing the ill-posedness of a problem is by incorporating prior information. In this work, the prior information is given through literature data with associated probability density distribution. Either the mean and standard deviation was directly given in the corresponding publication or it was estimated to have a

magnitude reasonable for the applied measurement technique. When the model is not linear the violation of property (iii) will become important. In this work, the inference of the spectroscopic model in Chapter 5 is affected by non-linear features.

Priors do not necessarily need to be probability densities. It is also possible to use *structure* information like smoothness (Tikhonov regularization [56]) or sharpness (Total variation regularization [57]).

3.4. Maximum entropy principle

In the Bayesian approach—presented in this work—the likelihood, the priors and the posterior are probability densities. While the nature of the probability density of the likelihood is determined through the measurement noise, definition of the norm, and the model (Appendix A and Appendix B), the shape of the prior probability densities is often not defined properly. When uncertainties are given in scientific publications, the provided values are mean μ and standard deviation σ . However, these values do not determine the probability density distribution.

The problem is, that a suitable probability density distribution needs to be assumed, that under all plausible restrictions, guarantees an unbiased interpretation of results, which are the maximum-entropy priors. In Appendix A, the entropies for all relevant distributions are given. Here, the normal distribution yields the highest entropy, and subsequently is the outstanding candidate for the description of prior information, as long as no other restrictions are applicable.

The Principle of Maximum Entropy [58] states that the prior should only contain testable information. With the normal distribution featuring the highest entropy of probability densities, it is also mathematically convenient for the presented work, since it can easily be incorporated into the likelihood function, Eq. (3.3), which is also normally distributed.

4. Experimental setup

*“It doesn't matter how beautiful your theory is, it doesn't matter how smart you are. If it doesn't agree with experiment, it's wrong.” –
Richard P. Feynman, 1960ies*

The microwave-plasma nanoparticle synthesis reactor applied in this thesis has been used for several years for generating a variety of nanoscale semiconductor nanoparticles. The product material has been analyzed in context of composition, morphology and crystallinity, and the process has been optimized for throughput and applicability [59]. Starting from 2013, the process was getting more in the focus of optical *in situ* diagnostics [38] because many properties of the reactive flowfield were unknown. The most important property to figure out was the structure of the aerosol stream through the reactor and the particle properties (Chapter 4.5). Further required information is the gas-phase temperature, presented in Chapter 4.6.

4.1. Microwave reactor

Silicon and germanium nanoparticles were synthesized in a microwave-plasma reactor [59]. A magnetron (Fricke und Mallah, FMG 1×2.0 kW SNT) generates up to 2 kW of microwave (2.4 GHz) radiation power. The outlet is adapted to a circulator that enables a near-lossless passing of the microwave radiation towards the reactor, but dumps reflected microwave radiation into a water-cooled trap. In this trap, a microwave monitor diode measures the reflected power, which is a suitable indicator for a well-adjusted system. Behind the circulator an *E–H* tuner can be used to adjust the path-length for the *E* and *H* field separately. After that, the microwave radiation is guided into a cylindrical resonator (IPLAS, Cyrannus). A surrounding waveguide distributes the incoming radiation uniformly among five annular slits that direct the radiation towards the reaction volume in the center of the resonator. With the 2.4 GHz frequency, i.e., $\lambda = 125$ mm wavelength, the five-slot configuration gives the best possible homogeneity of the radiation power distribution in the center of the reactor. The *E–H* tuner should be adjusted to generate standing waves within the complete system from the magnetron to the resonator and maximize the power density directly in the reaction volume.

The microwave system can produce stable plasmas starting from low-pressures of a few millibar up to pressures above 1 bar. A fused-silica tube of 70 mm inner diameter shields the reacting mixture from the surrounding atmosphere. Fused silica is transparent for microwave radiation. Furthermore, the diameter of the fused-silica tube is chosen to fit to a nodal point of the standing microwave, such that the tube wall is not affected by high power densities.

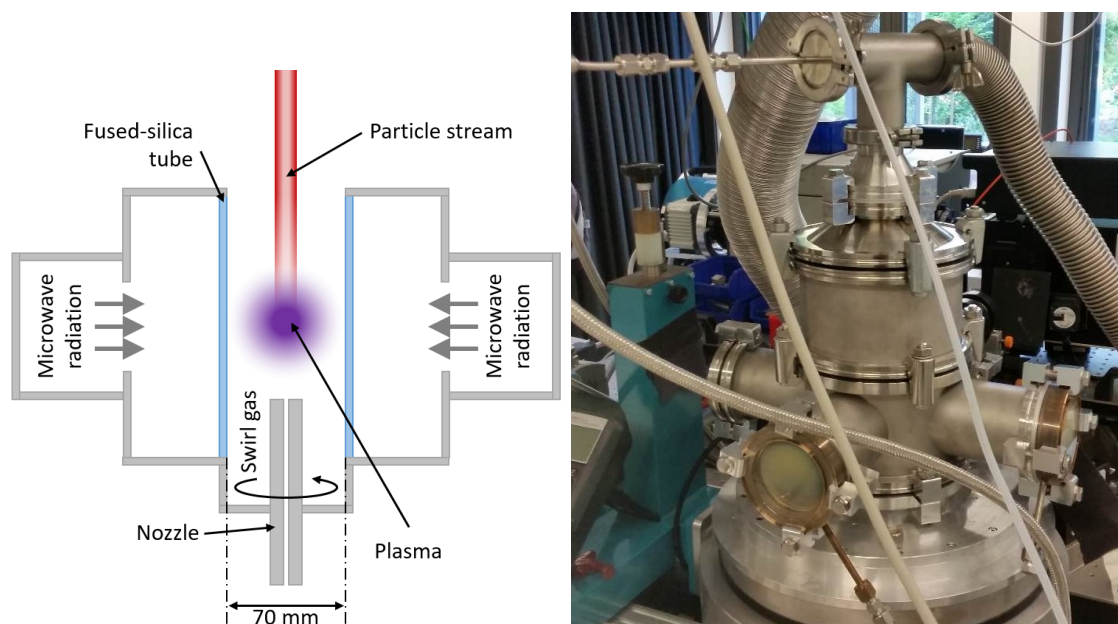
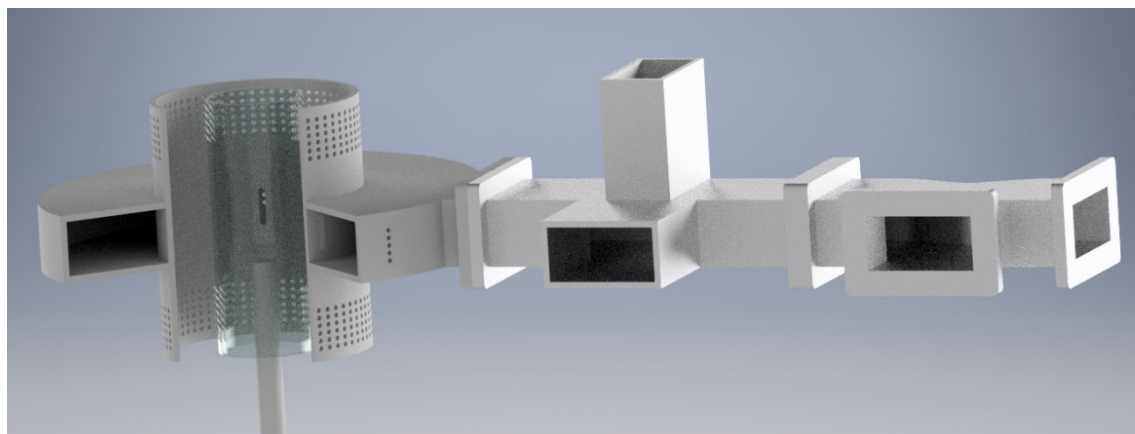


Figure 6: Top: Design of the reactor with (from right to left) the wave guide, the circulator, the $E-H$ tuner, and the resonator with the fused-silica tube and nozzle. Bottom left: Resonator and reaction chamber. Right: Photo of the vacuum chamber on top of the resonator.

A water-cooled nozzle is located directly at the lower boundary of the resonator and protrudes slightly into the plasma. Its outer diameter is 20 mm, the gas-inlet is 4 mm in diameter.

4.2. Reaction conditions

For synthesis of Si and Ge nanoparticles, silane (SiH_4) and germane (GeH_4) are used as precursor gases, respectively. These precursors together with the supporting gases (Table 1) were injected into the plasma through the nozzle. The precursors are decomposed in the plasma zone resulting in a supersaturated silicon- or germanium-atom vapor from which the nanoparticles nucleate [60]. A swirling co-flow consisting of Ar and H_2 concentrates and stabilizes the particle-laden flow into a 1 mm thick annulus with a diameter of 12 mm (chapter 4.5). This flow configuration provides

homogeneous temperature-time histories for the reacting gases and suppresses deposition of the formed particles on the reactor walls and windows.

Table 1: Reaction conditions with reaction pressure, precursor, microwave radiation power and flow rates. The bold written condition is the one mainly used for this work.

#	Pressure / mbar	Power / W	Nozzle (Prec./Ar/H ₂) / slm	Nozzle / (m/s)	Swirl gas (Ar/H ₂) / slm	Swirl gas / (m/s)	Total / (m/s)
1	55	800	0.03 / 1.5 / 0.2	163.3	6.2 / 0.5	2.07	2.99
2	70	800	0.01 / 1.76 / 0.2	146.1	5.7 / 0.5	1.51	2.55
3	80	800	0.015 / 2 / 0.2	152.5	6.6 / 0.5	1.51	2.65
4	100	800	0.03 / 2 / 0.2	115.8	6.6 / 0.5	1.21	2.03
5	120	1,000	0.015 / 2 / 0.2	95.8	7.7 / 0.5	1.16	1.73

Schreiber et al. [61] measured the viscosity of an argon plasma, with similar plasma temperatures. They found that the viscosity (ρ in Pa·s) of argon or nitrogen plasmas is in the order of water at room temperature. Consequently, the velocity of the nozzle gases is around 200 ms⁻¹ to ensure that the precursor gases in any case penetrate into the plasma region.

The flow rate had to be changed according to the reactor pressure, to achieve a steady particle flow. Otherwise a strong oscillation of the particle stream occurred.

4.3. Optical measurements

Optical measurements are made *in situ* via two optical access ports in an ISO-flange cross-piece mounted on the cylindrical resonator approximately 200 mm above the plasma region.

The incandescing particle stream is visible through the optical access-port. At this location, laser-induced incandescence measurements (LII) [34, 62] and phase-selective (low-fluence) laser-induced breakdown spectroscopy (LIBS) [10, 42] were performed within the particle-laden gas flow. The nanoparticles within the measurement volume were heated/excited using a pulsed Nd:YAG laser (Continuum PowerLite 7000). The laser fluence was adjusted with a variable reflection attenuator in the 2–100 mJ/mm² range. As shown in Figure 7b, the emission was imaged by suitable lenses onto the entrance slit of an imaging spectrometer (Acton SpectraPro SP2300) and detected in a time-resolved manner with a streak camera (Hamamatsu C10910). The transmission efficiency of the system was calibrated with a deuterium lamp in the spectral region from 240–310 nm.

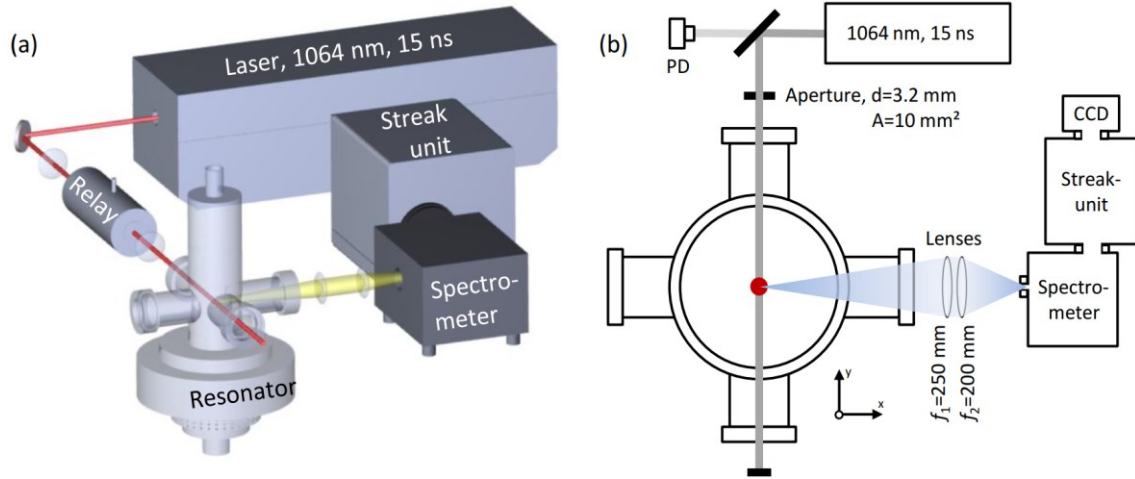


Figure 7: Experimental apparatus. a: Rendered view. b: Schematics of the optical setup.

The spectral resolution of a grating spectrometer is a superposition of the grating diffraction and the slit width band pass

$$\Delta\lambda = \underbrace{\frac{\lambda}{nbm}}_{\text{Grating}} + \underbrace{\frac{d}{nfm'}}_{\text{Slit}} \quad (4.1)$$

where m is the order of diffraction and b is the width of the illuminated grating; here assumed to be the full grating width. The equipped grating had a ruling of $n = 50$ l/mm and the focal lengths of the collimation and focusing mirror were both $f = 250$ mm. Accordingly, the spectral resolution of the grating alone is $\lambda/\Delta\lambda_{\text{grating}} = 3000$, while the resolution including the slit band-pass ($d = 500 \mu\text{m}$) is $\lambda/\Delta\lambda_{\text{spectrum}} \sim 400$ at 580 nm.

The temporal resolution was adjusted by varying the temporal dispersion of the streak unit. In Chapter 7 the behavior of atomic emissions subsequent to a strong laser pulse radiation is analyzed. The temporal intensity profile is consisting of two different excitation processes, separated by a few hundreds of nanoseconds at varying timescales. With the adjusted temporal resolution it is not possible to simultaneously observe, with sufficient accuracy, both the prompt fluorescence coinciding with the laser pulse and the secondary feature within one camera streak on the CCD chip. Instead, the detection time-scale of the streak camera was varied from $1 \mu\text{s}$ to 200 ns to capture either phenomenon individually, which yields a temporal resolution of 15 ns and 3 ns , respectively.

4.4. Particle sampling

The particle size is an important information to validate the laser optical measurements. A similar reactor, like the one used for this work, was previously characterized by Petermann et al. [59] and Knipping et al. [63], but for different synthesis conditions, which yield particle diameters smaller than 10 nm . The conditions applied during this work were entirely novel.

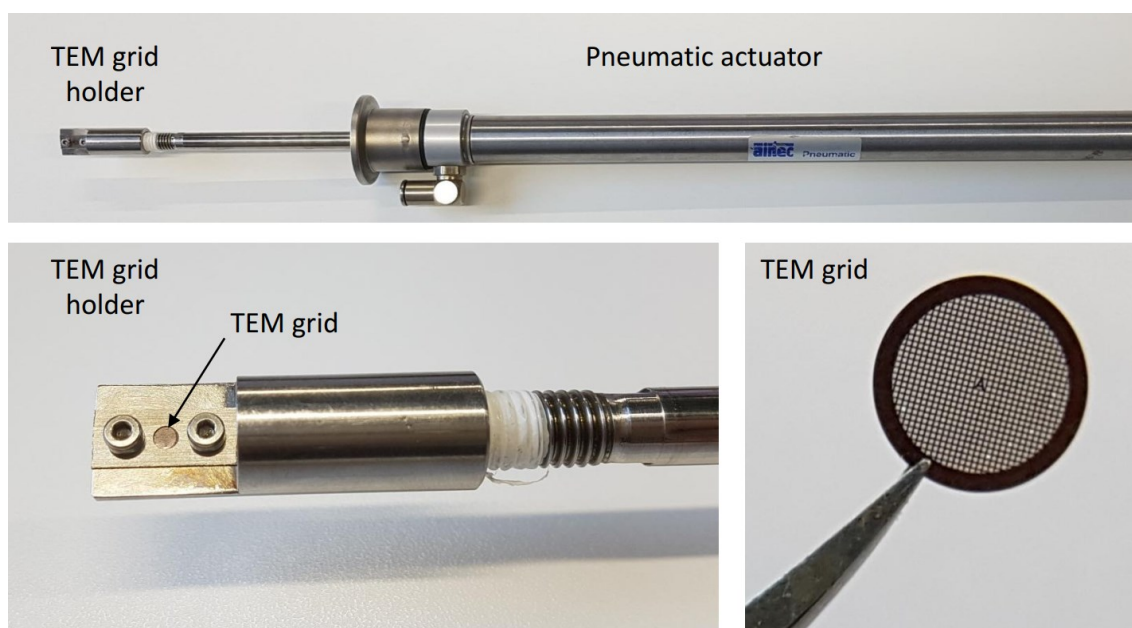


Figure 8: Device for thermophoretic nanoparticle sampling for subsequent transmission-electron microscope (TEM). Top: pneumatic sampler with attached TEM grid holder. Left: TEM Grid holder with TEM grid. Right: TEM grid S-160-3; copper grid with 300 holes per inch and carbon support film.

The particles were sampled by a pneumatically driven thermophoretic sampler (Figure 8) that carries a grid for subsequent analysis by transmission-electron microscopy (TEM). To collect enough nanomaterial for a proper determination of the particle size-distribution, the cantilever was shot into the region of interest and held there for 500 ms. Due to their high volume-to-surface ratio, nanoparticles exhibit an extrem reactivity [64], that leads to a fast oxidation of the nanoparticle surface. The particle-laden TEM grids were directly (within five minutes) attached to the goniometer of a JEOL JEM 2200FS transmission electron microscope. Figure 9 shows a selection of the captured TEM images for silicon and germanium nanoparticles synthesized with the same reaction pressure of 100 mbar.

For each reaction condition (section 4.2) several images were analyzed in terms of particle size, resulting in 500 counted particles per condition. The particle size was reasonably binned which yields a smooth cumulative distribution function (CDF). The CDF was chosen because it is smooth, easier to fit, and directly shows the median particle diameter at the 50% intersection.

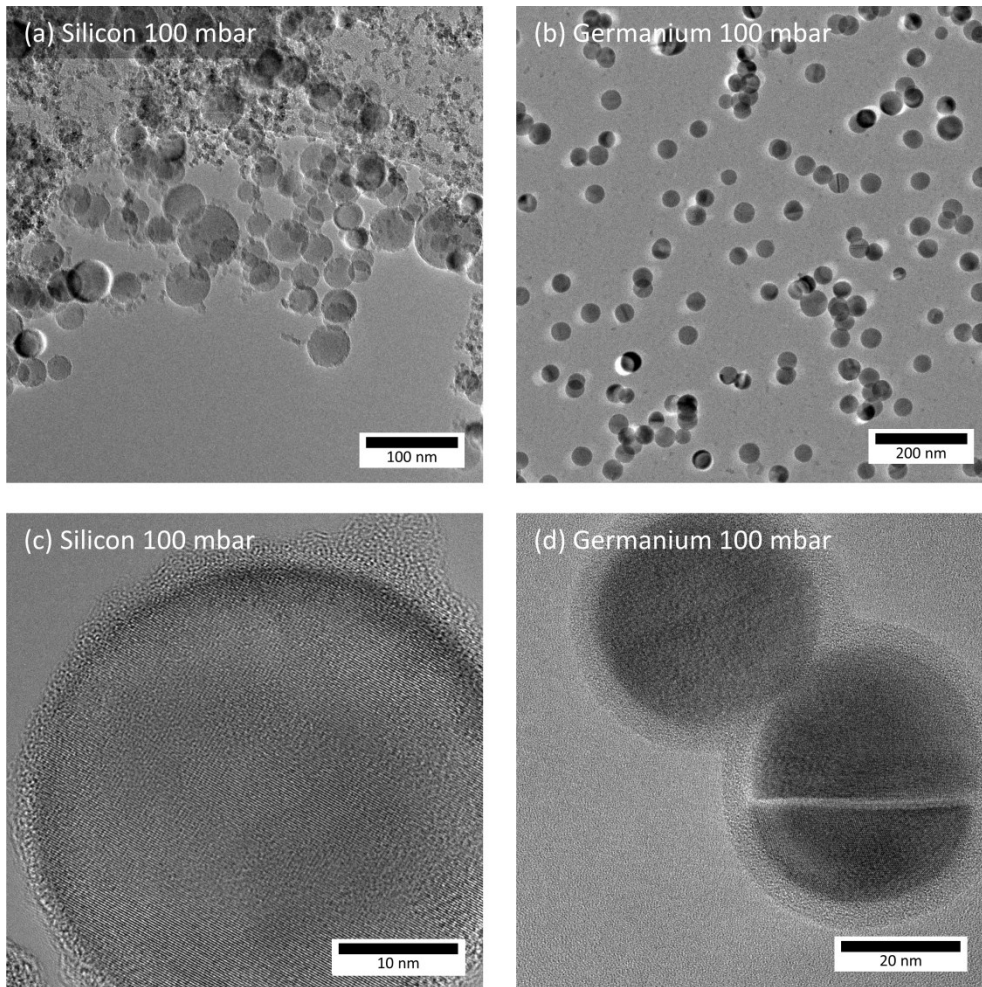


Figure 9: TEM images of thermophoretically sampled nanoparticles from the region of interest. a, c: Si nanoparticles with different magnifications. b, d: Ge nanoparticles.

Electron micrographs of sampled silicon and germanium nanoparticles show nearly perfect spheres with little agglomeration. Most of the particles are isolated or weakly linked (Figure 9 a and b). High-resolution TEM images (Figure 9 c and d) give strong evidence that the particles are single crystalline nearly without lattice defects.

Wiggers [65] revealed that, when the growth-process equilibrates the nanoparticle size distribution converges to a self-preserving log-normal distribution. Figure 10 shows that within the chosen measurement position the particle growth is not completed, due to the poor similarity of the cumulative density function (CDF) to a log-normal distribution. As consequence, normal and Weibull distributions were implemented and show a better agreement.

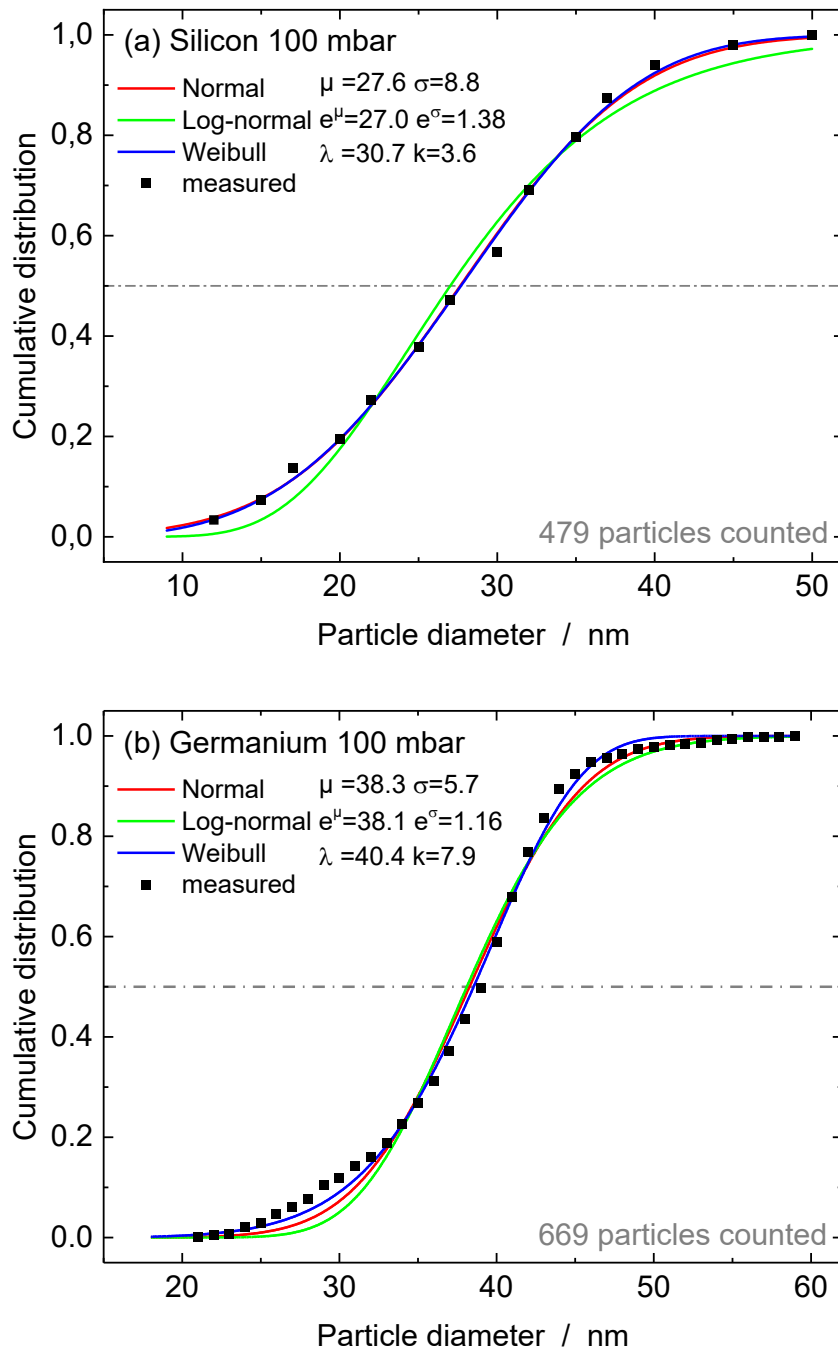


Figure 10: Cumulative distribution function for silicon (a) and germanium (b) nanoparticles. The reaction pressure was $p = 100$ mbar (Condition 4). The CDF presentation was chosen, because it enables the Kolmogorov-Smirnov test [66] to compare an empirical with a hypothetical distribution. Additionally, it yields an easy possibility to estimate the mean diameter, by selecting the particle size at probability = 0.5 (horizontal dash-dotted line).

4.5. Location of the particles

As previously described, the incoming gas stream consists of two different gas-compositions. The precursor-gas with $(\text{Si/Ge})\text{H}_4/\text{Ar}/\text{H}_2$ is injected through a nozzle surrounded by the swirling gas-stream with Ar/H_2 . The swirl was intended to reduce chemical vapor deposition of the precursor on the fused-silica tube (Figure 11). This works well for the synthesis of silicon nanoparticles but not for germanium nanoparticles. Within two hours the tube is coated with a few layers of crystalline germanium, such that the microwave radiation gets deflected.



Figure 11: Fused-silica tube coated with reaction products during synthesis.

In personal communication with H. Wiggers, one of the designers of this type of synthesis reactor, the presumption was expressed that the particle stream has an annular cross-section under our synthesis conditions. In the following sections, measurements of the particle location are shown and.

4.5.1. *2D line-of-sight attenuation*

Two-dimensional (2D) line-of sight attenuation (LOSA) is an imaging technique that directly yields a two-dimensional absorption efficiency map of the measurement volume. The principle of LOSA is elucidated in Chapter 5.1 and in Refs. [67, 68].

The light of a 100 W tungsten filament lamp was condensed on a diffusor screen. Two lenses imaged the diffuse light into the measurement volume, which is then captured by a Nikon D700 digital single-lens reflex camera (DSLR) equipped with an achromatic $f = 105$ mm macro lens (Figure 12).

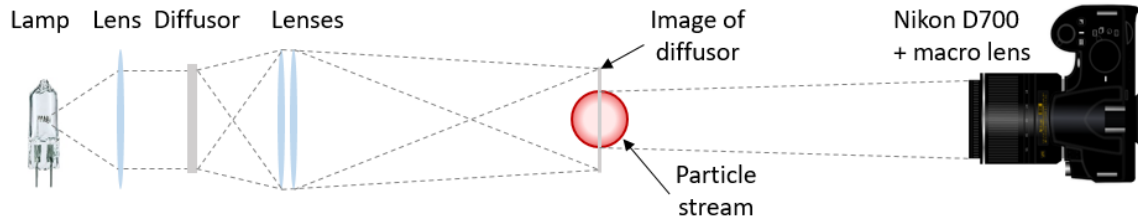


Figure 12: 2D LOSA setup: the light of a tungsten filament lamp is imaged on a diffusor and then relayed into the measurement volume. The attenuated light is recorded with a Nikon DSLR equipped with a macro lens.

The four subsequent images ($I_{t+e,\lambda}$, $I_{e,\lambda}$, $I_{lamp,\lambda}$, and $I_{dark,\lambda}$), shown in Figure 13, were pixelwise analyzed with Eq. (5.23). The resulting map showing the spatially resolved absorption coefficient was cut in half along the centerline of particle stream. One half was taken without further treatment; the other half was decomposed from a line-of-sight measurement to a radial profile by an independently developed onion-peeling algorithm [69] (Figure 14). Other reconstruction techniques including regularization techniques are presented in Refs. [56, 70, 71].

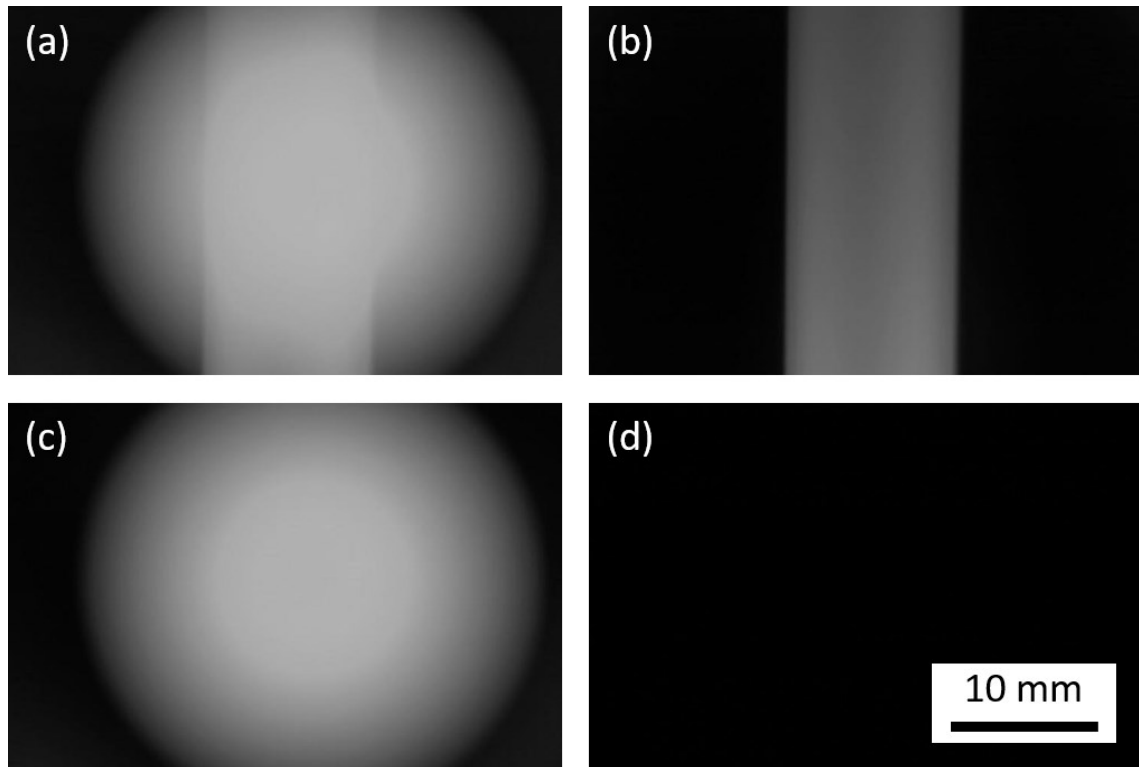


Figure 13: Red channel of the four subsequent images captured by the DSLR. a: luminescing particles in front of the background generated by the white-light source, b: without background light. c: image of the broadband light-source, d: dark image. The absorption was then determined by pixelwise calculating the opacity k with Eq. (5.23)

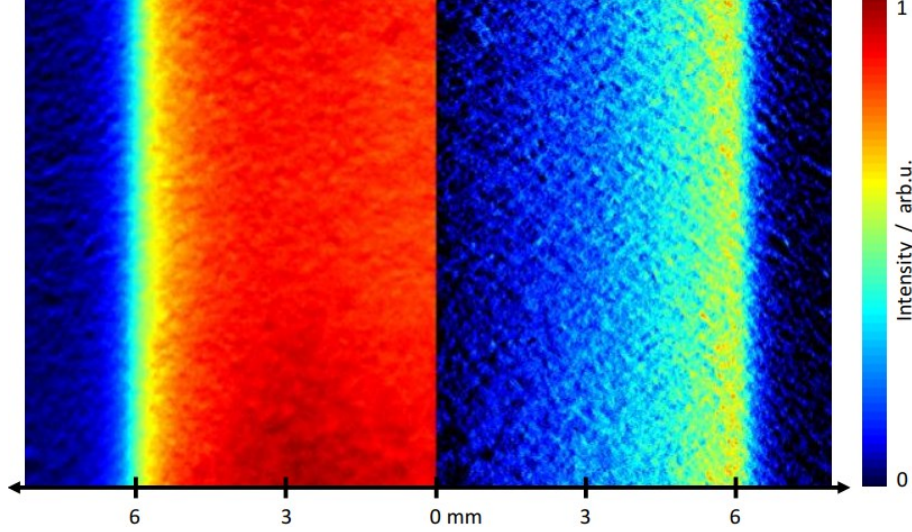


Figure 14: Line-of-sight and onion-peeled map of the absorption coefficient. The wave-like structure originates from the sandblasted diffusor plate in front of the light source.

It can be observed that the particles are mainly located in the outer region of the particle-laden stream. At the boundary at approximately $r \approx 6.5$ mm the particle concentration drops rapidly.

4.5.2. 2D Rayleigh scattering

In these experiments the frequency-doubled light from a Nd:YAG laser (Spectra physics, LAB 170) was formed into an approximately 0.5 mm thick vertical light-sheet through a sheet forming telescope (LaVision) and directed vertically through the center of the particle-laden gas stream. The scattered light was recorded by an intensified CCD camera (LaVision, ImagerIntense). The pulse length of the laser was 8 ns FWHM according to the manual. The luminescence of the incandescing particles and room light were suppressed by a short intensifier gate of 100 ns.

The scattering intensity for light collection perpendicular to the incident light beam is

$$I_{\text{scat}} \propto \frac{I_0}{R^2} \left(\frac{2\pi}{\lambda} \right)^4 \left(\frac{n_r^2 - 1}{n_r^2 + 2} \right)^2 \int_{d_p=0}^{d_p=\infty} p(d_p) d_p^6 dd_p, \quad (4.2)$$

where $\lambda = 532$ nm is the wavelength of the laser beam, R is the distance of the detector to the measurements volume, $p(d_p)$ is the particle size distribution and I_0 (laser intensity) are fixed. Thus, the scattering intensity depends on the particle diameter d_p integrated over the particle size distribution. Due to the strong dependence of I_{scat} to d_p , the highest amount of the scattered intensity is caused by the largest particles within the measurement volume.

By the assumption of spherical particles with $V_p = 4/3\pi r^3$ and a narrow mono-modal particle-size distribution, the volume fraction can be estimated with

$$f_V \propto \sqrt{I_{scat}}. \quad (4.3)$$

Figure 15a shows a photograph of the laser-illuminated section of the particle stream. The particle incandescence is clearly visible. The green laser light is scattered at locations with a sufficiently high particle volume concentration, to become observable. The intensity in this section mainly comes from the border of the visible particle stream and from outside the swirling gas-stream. The scattering in these outer sections in the image is attributed to recirculating particles. Some of the acquired images show particular vortices, which gives strong evidence for the hypothesis of recirculation.

Figure 15b shows the mean value of 1,000 Rayleigh-scattering images. On average, the particles are located within the thin layer of the particle stream forming the hollow cylinder where the laser sheet cuts through approx. 6 mm from the centerline. The Gaussian-shaped intensity profile along the laser sheet height is due the expanded Gaussian laser beam profile.

The standard deviation (STD) in the pixel counts is shown in Figure 15c. The particle volume fraction varies more strongly within an approx. 1.5 mm thick region around the cylindrical particle sheet indicating a corresponding fluctuation of the particle flow. This movement can also be seen by eye by a smooth oscillation with respect to the flow center-line. The single-shot images shown in Figure 15d–f also illustrate this oscillatory behavior of the particle stream.

The oscillation frequency can be altered by changing the microwave power. But during this work the influence of the microwave power to the conditions within the reactor is not further analyzed and kept constant.

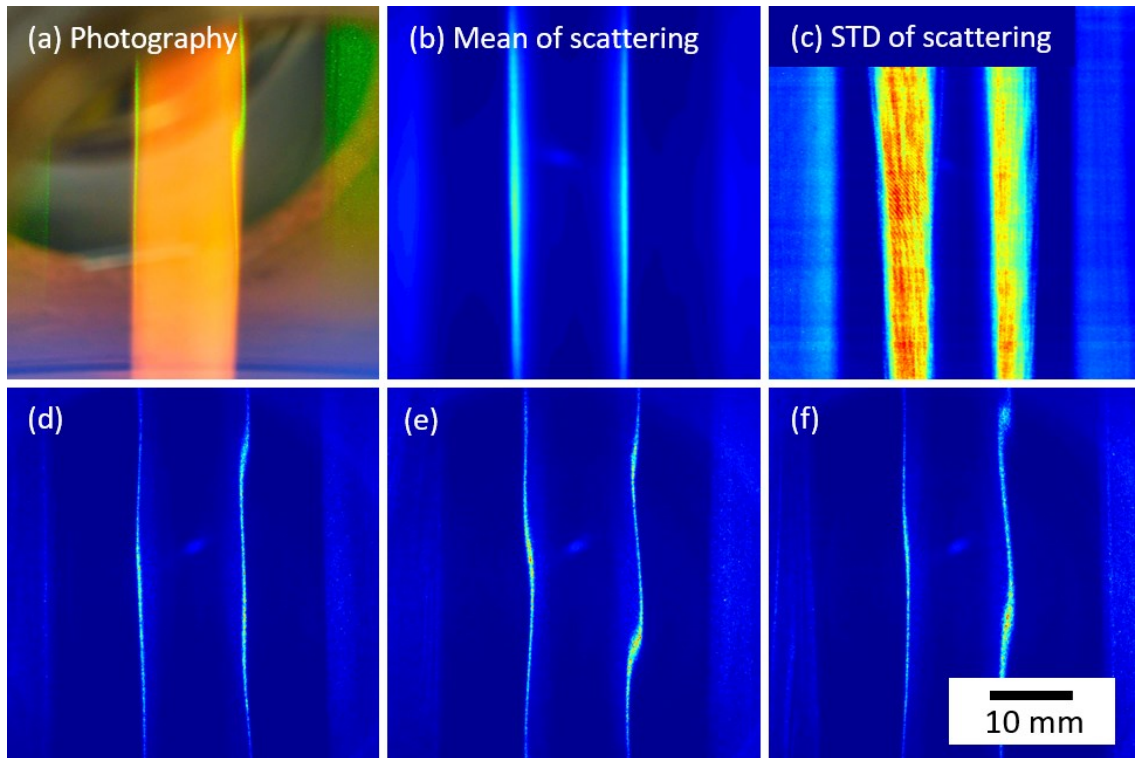


Figure 15: Scattering of the 532 nm Nd:YAG-laser light-sheet off the nanoparticle stream. a: photograph (Samsung Galaxy S7) depicts the measurement region. b: Mean Rayleigh scattering image (1000 images), c: standard deviation of the captured images. d–f: snapshot images. Images b–f are taken with an intensified CCD-camera, oriented perpendicular to the laser light-sheet plane.

4.5.3. *Laser-induced incandescence scan*

Another way of finding the location of the nanoparticles in the observable region is by measuring the particle volume fraction f_V using LII, discussed in detail in Chapter 6 with the detection scheme presented in Chapter 4.3. The magnitude of the measured incandescence signal is proportional to the volume fraction of the nanomaterial within the measurement volume [72, 73]. Because of the relative calibration of the spectrometer/streak-camera unit, only a relative volume fraction could be retrieved. To achieve spatially resolved f_V -profiles, the particle-laden gas stream was shifted through the measurement volume, in one case along the direction of the laser, and in another case along the optical axis of the spectrometer.

The spatial resolution by scanning along the laser-beam direction is the magnification of the lens-system and the slit width of the spectrometer. For these experiments, the magnification of the lens system was $M = 200 \text{ mm}/250 \text{ mm} \approx 0.8$. The slit width of the spectrometer was adjusted to $200 \mu\text{m}$, so that the imaged volume had a width of approximately $250 \mu\text{m}$. Along the optical axis of the spectrometer, the resolution is mainly determined by the diameter of the heating-laser, which was 3.6 mm .

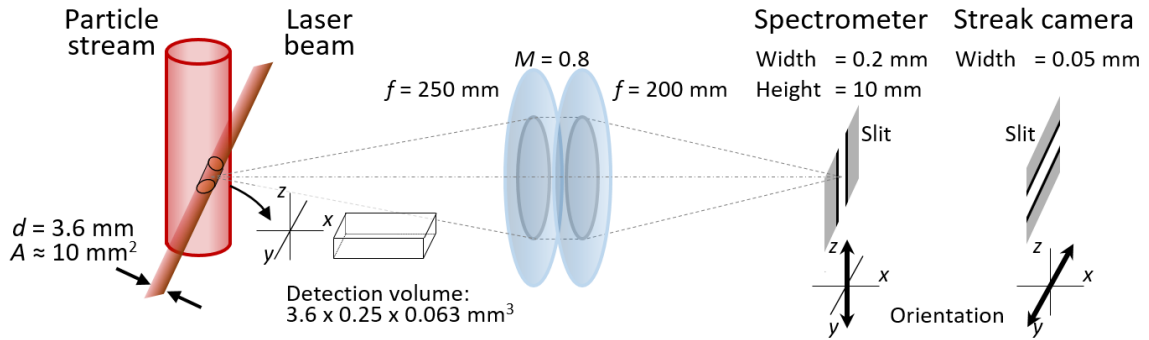


Figure 16: Simplified LII measurement setup. The laser has a cylindrical shape with a diameter of 3.6 mm. The incandescence of the heated nanoparticles are imaged onto the spectrometer slit through two lenses with a magnification of 0.8.

4.5.4. Summarizing the results of the measurement techniques

A comparison of spatial profiles taken within the particle stream using the three previously discussed measurement techniques are shown in Figure 17. The determined particle location is consistent over all of the measurement techniques. The diameter of the annular structure composed of luminescing particles during silicon nanoparticle synthesis under the condition 4 in Table 1 is $D_t = 12 \pm 1$ mm. It was also possible to derive an approximate volume fraction f_v by the 2D LOSA measurement, which yields $f_v \approx 1.6$ ppm (line-of-sight integrated). This value was used for normalizing the onion-peeled radial-profile.

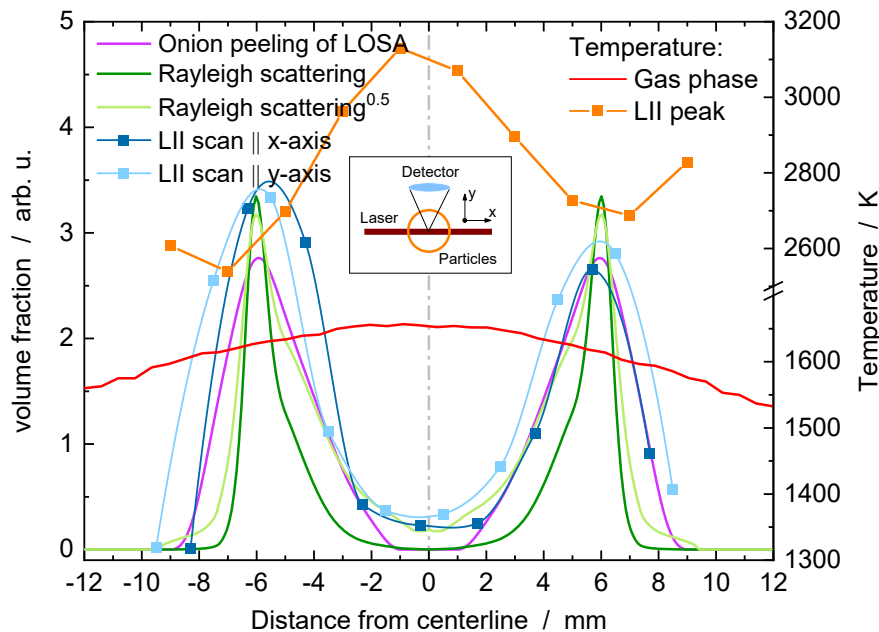


Figure 17: Location of the particles within the reactor determined by 2D LOSA, 2D Rayleigh scattering and LII scans along two directions (see inset).

To achieve the best measurement conditions for LII and LIBS the measurement position was chosen to be at the volume-fraction peak in the shell of the nanoparticle stream, directing to the spectrometer. By this choice, the laser heats particles within this region with a cross-section of approximately $4 \times 2.8 \text{ mm}^2$ (width \times height). This measurement position is used throughout the rest of this work, unless otherwise noted.

4.6. Temperature within the measurement zone during synthesis

To quantify several material properties and model parameters, e.g., conductivity and density (section 5.2.1), and energy loss by heat conduction (section 6.1.1), the gas-phase temperature is a crucial value. The gas-phase temperature is measured by three independent techniques. It is intended to calculate the mean temperature and to estimate the expected variance within the region of interest (RoI).

4.6.1. *Thermocouple measurements*

The first attempt was the application of a thermocouple. It should be considered, that the particle laden stream large uncertainties come with this technique. Four factors induce uncertainties; radiative heat losses of the thermocouple [74], coating of the thermocouple (in this case by silicon nanoparticles) which may change the emissivity, the unknown surrounding temperature, and heat conduction through the thermocouple connections.

The change of emissivity is most likely to have a large impact on the temperature measurement. A regular K-type thermocouple has an emissivity reported to be between $0.17 < \varepsilon < 0.3$ [75], while the emissivity of bulk silicon is approximately $\varepsilon \sim 0.6$ [76]. If the synthesized nanoparticles were fully covering the thermocouple surface is not known.

Farrow et al. [77] compared a corrected thermocouple to coherent anti-Stokes Raman measurements (CARS) in a laminar diffusion flame and obtained a discrepancy for a flame relevant temperature range of up to 200 K.

As a consequence, a conservative guess [78, 79] applying the thermocouple is $T_{\text{gas,thermo}} = 1600 \pm 200 \text{ K}$.

4.6.2. *Multiline SiO laser-induced fluorescence*

Multiline laser-induced fluorescence (LIF) excitation spectra are experimentally obtained and best fitted with a simulated spectrum with temperature as a free parameter. The LIF technique interrogates the thermal population of the chosen tracer's ground state energy levels. Due to their natural occurrence during the combustion of hydrocarbons with air, nitric oxide (NO), and hydroxide (OH), are well-studied tracers for multiline LIF [8, 27, 80, 81].

The temperature sensitivity is achieved based on a scan of the laser excitation wavelength over several NO transitions. Suitable electronically allowed transitions

of NO having different ground state energies are populated at higher temperatures, Therefore, the observed lines exhibit different temperature sensitivities.

A first attempt, in which the precursor gas was doped with nitric oxide, failed under synthesis conditions. As soon as silane was added to the gas stream, the nitric oxide fluorescence signal vanished. It was speculated, that affinity of the O^- ion to Si^{4+} ions within the reaction zone is much higher than the affinity to the positive nitrogen ions, so that the amount of NO was below the detection threshold. This assumption is supported by the electronegativity difference $\Delta EN(Si,O) = 1.5$ and $\Delta EN(N,O) = 0.4$, which consequently favors the formation of SiO compared to NO.

Recent developments in multiline LIF [26, 82] introduce the possibility for temperature field determination using SiO as tracer-gas. Here, the SiO A–X(2,0) transition band around 225 nm excitation wavelength was used. Seven transitions are scanned between 44282 cm^{-1} (225.825 nm) and 44292 cm^{-1} (225.77 nm), with a resolution of 0.1 cm^{-1} .

The pixelwise captured spectra are afterwards fitted using LIFSim [80]. Figure 18 shows an exemplary measurement and LIFSim fitting result of a test area within the measurement volume, representing the high-temperature region with $T_{\text{gas}} \sim 1550\text{ K}$. The derived temperature field, shown in Figure 19, utilizes the spectral fitting for each captured pixel. The resulting temperature field has a size of approx. $23 \times 35\text{ mm}^2$ with a resolution of approx. 0.5 mm/pixel .

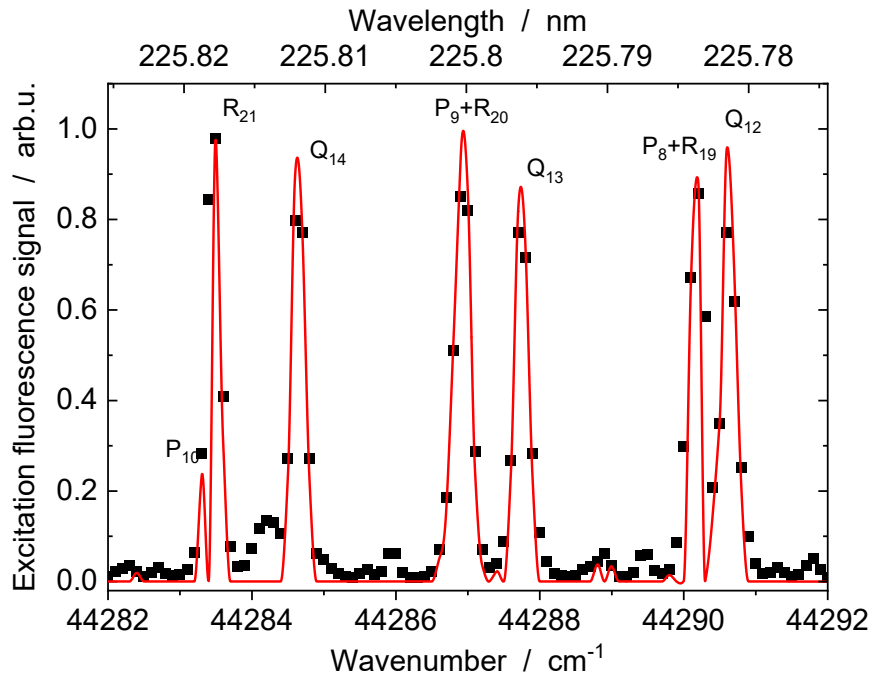


Figure 18: Example of a measured and fitted spectrum of SiO LIF of one of the high-temperature pixel of the next figure.

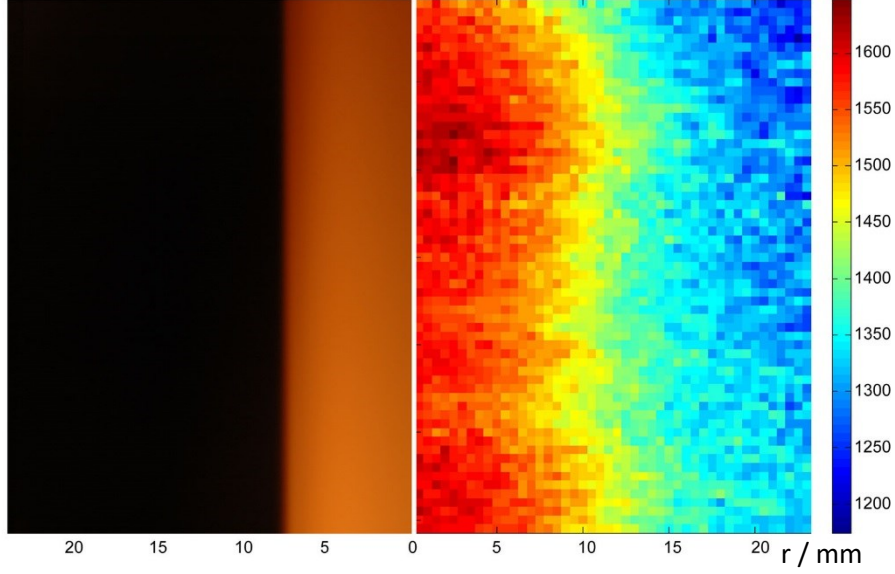


Figure 19: This figure is cut in half at the center line of the luminescing particle stream. On the left hand side, a photograph of the particle stream is imaged, on the right hand side is shown the 2D temperature field determined by multiline SiO LIF.

A temperature profile was taken along $r = 6$ mm. The resulting mean temperature was $T_{\text{LIF}} = 1550 \pm 35$ K. LIFSim does not provide an uncertainty estimate based on the measurement noise, model uncertainties and fluctuation within the probe volume. Therefore, the uncertainty is only assessed by the variation of temperature of different heights.

4.6.3. Thermal radiation of the particles

Hot particles emit thermal radiation, as described in chapter 5.1.5. The corresponding broadband radiation spectrum can be exploited to infer the particle temperature. For both the silicon and germanium material systems the published optical properties for the liquid state were used and incorporated into the fitting routine as normally distributed prior information.

The measured spectrally resolved incandescence spectrum I_j of hot silicon particles—depicted in Figure 20—shows a very low amount of noise, with $\sigma_1 < 2\%$ of the intensity mean, which is approximately five counts of the detector readout value. To infer the temperature, the Planck radiation law, $I_B(\lambda, T_p)$ (chapter 5.1.5), is utilized, weighted with the Rayleigh approximation (chapter 5.1.4) and spectroscopic properties (chapter 5.2) for metallic nanoparticles,

$$p(\mathbf{I}|T_p, \omega_p, \tau) \propto \exp \left\{ - \sum_{j=1}^N \frac{[I_j - C_k I_B(\lambda_j, T_{p,j}) E(\mathbf{m}(\omega_p, \tau)) \frac{4\pi}{\lambda}]^2}{2\sigma_I^2} \right\} p(\omega_p, \tau), \quad (4.4)$$

where C_k is a scaling factor that combines the unknown nanoparticle volume fraction f_V , the size of the measurement volume and the measurement geometry, $\mathbf{m}(\omega_p, \tau)$ is the complex refractive index of the nanoparticle material determined by the plasmon

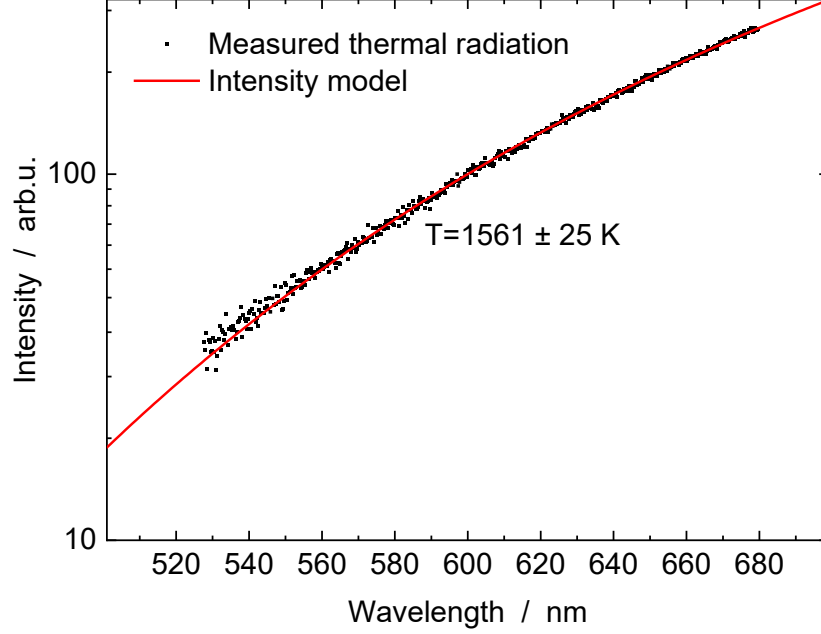


Figure 20: Thermal radiation of the hot silicon particles captured with a spectrometer and an EMCCD camera as detector. The resulting temperature is $1561 \pm 25 \text{ K}$.

frequency ω_p and mean relaxation time τ , and $p(\omega_p, \tau)$ is the normal prior of the aforementioned properties. By this, the temperature for silicon nanoparticles of $T_{\text{Pl,Si}} = 1561 \pm 25 \text{ K}$ can be inferred. A detailed example of inferring temperatures through the incandescence spectrum is shown in Appendix C.

4.6.4. Combined temperature within the observation volume

The temperature measurements shown in this chapter show a small deviation reaching from 1550 K (SiO LIF) up to 1600 K (thermocouple). The measurements are only performed for the silicon synthesis case 4, presented in Table 1. For germanium nanoparticle synthesis or other reactor pressures, no reasonable temperature measurements exist. To obtain a single value, the previously derived mean values and standard deviations are now combined to one single mean/standard deviation pair.

The inference of the temperature through the thermal radiation was achieved by the Bayesian framework (Chapter 4.6.3 and Appendix C), and the resulting probability density is a normal distribution. The uncertainty of the SiO LIF measurements and the uncertainty of the thermocouple estimate are, supported by the maximum entropy principle, also treated as normally distributed. The combination of three normal distributions can be performed by:

$$p(\theta|x) = \mathcal{N}\left(\frac{\sum \mu_i/\sigma_i^2}{\sum 1/\sigma_i^2}, \left[\sum \frac{1}{\sigma_i^2}\right]^{-1}\right) \quad (4.5)$$

The resulting temperature distributions are shown in Figure 21.

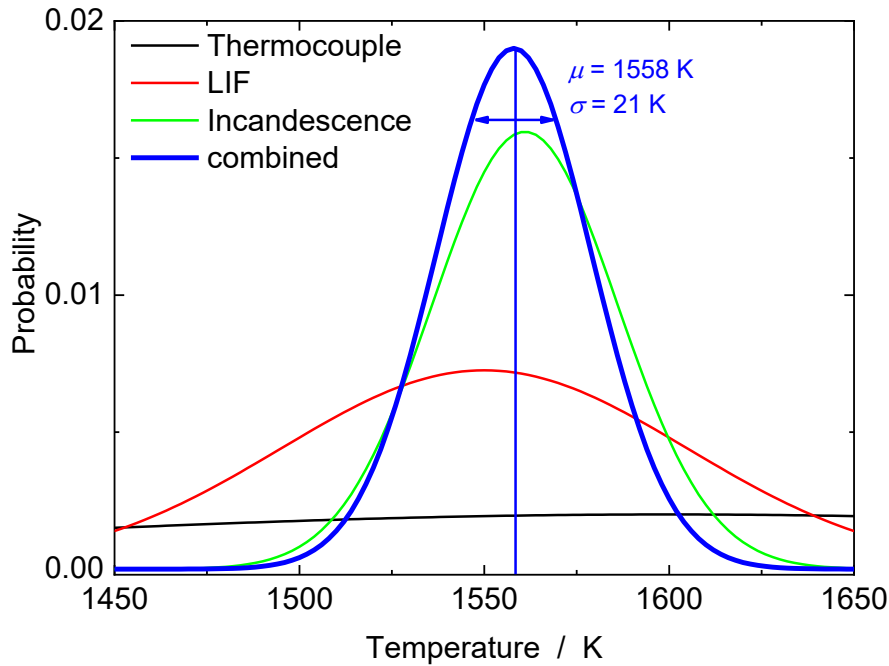


Figure 21: Temperature estimates for the three applied measurement techniques and the resulting combined temperature estimate.

It is likely, that the particles at the measurement position are in thermodynamic equilibrium with the surrounding gas phase and the measured temperatures are thus representative for both the gas-phase and the particle temperature.

It is well known that the melting point of nanoparticles decreases with decreasing diameters due to the contribution of surface energy to the overall Gibbs free energy. A calculation based on phase equilibrium results in a melting point of silicon nanoparticles of 1593 K for $d_p = 27$ nm [5, 83], while recent experiments suggest an even lower melting point [5]. Thus, it is indeed possible that the silicon nanoparticles are molten at the measurement location; if this was not the case, the spectral extinction and emission intensities observed with the spectrometer would be markedly different, since the dispersion of polycrystalline silicon (semiconductor) is completely different from that of the molten state (metal). Germanium has a melting point of 1211.4 K, and therefore, should be a liquid under these conditions.

Figure 22 visualizes the phase transition from liquid to solid. Under normal synthesis conditions, the sharp cut shifts upwards and is not visible. This situation could be repeated for silicon and germanium. In summary, it can be concluded that the nanoparticles within the measurement volume are present in the liquid phase: The incandescence spectrum is explainable with the liquid phase properties. The measured temperatures (gas phase and particle phase) are consistent and reasonable; the phase transition can be imaged and is under common conditions downstream of the measurement volume.

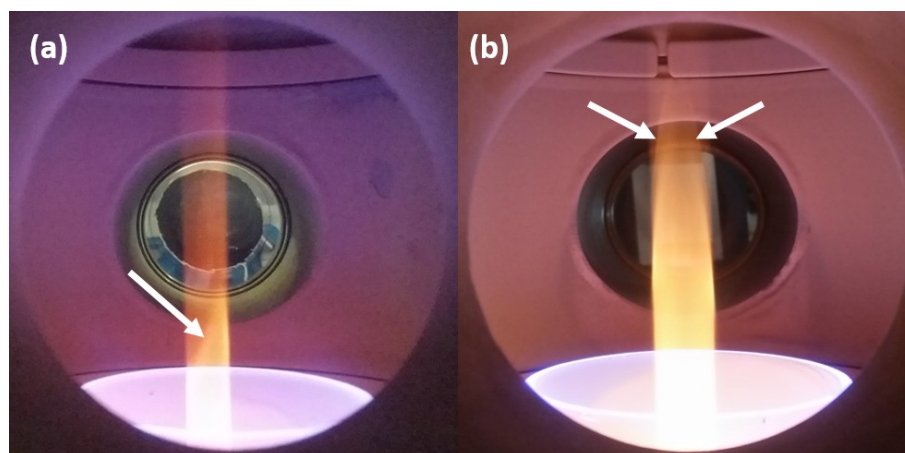


Figure 22: Images of the phase transition (liquid to solid) during nanoparticle synthesis. The shown conditions were specifically set to show the transition. The microwave power in (a) is lower compared to (b).



5. Optical properties of metallic nanoparticles

“There are two ways of spreading light: to be the candle or the mirror that reflects it.” – Edith Wharton

The basic idea of this chapter has been published in:

- K. Daun, J. Menser, R. Mansmann, S. Moghaddam, T. Dreier, C. Schulz (2017). "Spectroscopic models for laser-heated silicon and copper nanoparticles." *Journal of Quantitative Spectroscopy and Radiative Transfer* 197: 3-11.
- K. Daun, J. Menser, R. Mansmann, T. Dreier, C. Schulz (2016). "Laser-induced incandescence measurements of silicon and copper nanoparticles: spectroscopic model." 8th International Symposium on Radiative Transfer | RAD16

This chapter gives a short introduction to the properties of metals, in particular the electromagnetic properties that are used to derive the spectral absorption/emission cross-section, which, in many cases, can be summarized with an oscillator model of a nearly-free electron gas in the environment of the positively charged ion background.

5.1. Fundamentals for understanding nanoparticle optical spectra

5.1.1. Equation of radiative transfer

The equation governing the energy conservation in radiative processes is the Radiative Transfer Equation in Eq. (5.1). Consider a monochromatic beam $I_\lambda(\mathbf{r}, \mathbf{\Omega})$ with the wavelength λ propagating through the vicinity of a medium at the location s in the observation direction $\mathbf{\Omega}$ with the solid angle $d\Omega$. The radiation intensity at the point $s + ds$ then will be $I_\lambda(s, \mathbf{\Omega}) + dI_\lambda(s, \mathbf{\Omega})$. The change in radiative intensity is $\frac{dI_\lambda(s, \mathbf{\Omega})}{ds}$, and can be summed up to [84]

$$\frac{dI_\lambda(s, \mathbf{\Omega})}{ds} = -\{K_{abs}(s, \lambda) + K_{scat}(s, \lambda)\} I_\lambda(s, \mathbf{\Omega}) + K_{abs}(s, \lambda) I_{b, \lambda}(s, T), \quad (5.1)$$

where $I_{b, \lambda}(T)$ is the emission term governed by thermal radiation.

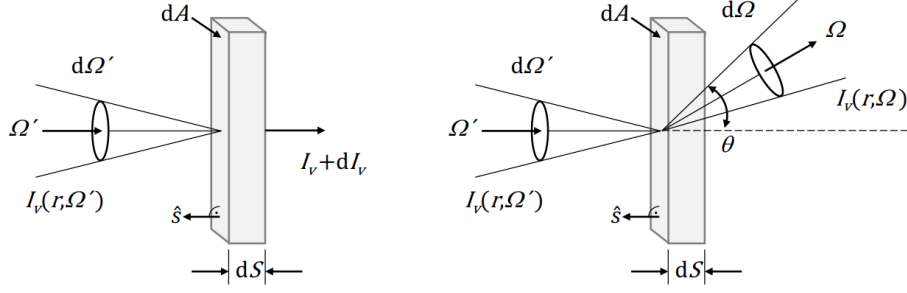


Figure 23: Nomenclature of the radiative transport equation illustrated at the examples of (left) absorption and (right) scattering.

The components of the right-hand-side of Eq. (5.1) are written out:

- $K_{\text{abs}}(\lambda, s)I_{b,\lambda}(T(s))$, where $K_{\text{abs}}(\lambda, s)$ is the spectral absorption coefficient and $I_{b,\lambda}(T(s))$ is the Planck function describing thermal radiation, both at the location s .
(Chapter 5.1.5)
- $K_{\text{abs}}(s, \lambda)I_{\lambda}(s, \mathbf{\Omega})$ describes the intensity loss due to absorption, where $I_{\lambda}(s, \mathbf{\Omega})$ is the radiation energy at location s pointing towards $\mathbf{\Omega}$.
(Chapter 5.1.2 and 5.3)
- $K_{\text{scat}}(s, \lambda)I_{\lambda}(s, \mathbf{\Omega})$ describes the intensity loss due to scattering out of the direction of detection where $K_{\text{scat}}(s, \lambda)$ the scattering coefficient.
(Chapter 5.1.3)

5.1.2. Absorption

In terms of electrodynamics, a light beam is an oscillating electro-magnetic (EM) plane wave defined by its wavelength or frequency, and its propagation vector. When this wave interacts with matter the charged constituents—mainly electrons—are forced to follow the oscillation of the electromagnetic wave due to the Coulomb force. The manner by which moving charged components interact with the rest of the material and the geometric wave-front propagation determines the optical properties, which are summarized by complex refractive index $\mathbf{m} = n_r + i n_i$. The complex refractive index is wavelength-dependent. To keep a consistent notation, the complex refractive index in this work is written as \mathbf{m} .

The real part n_r of the complex refractive index describes the refractive power, and thus, how much does the direction of the light change when passing the boundary surface between two different materials. The refractive index can be explained by a change of the light propagation velocity. $n_r = 1$ means that the light propagates with the vacuum speed of light, c_0 . $n_r > 1$ results from a retarded travelling velocity within the medium, while $n_r < 1$ indicates a faster light speed compared to vacuum.

In almost all cases, the speed of EM wave propagation through a vacuum represents the maximum value, and with $n_r \geq 1$ it follows:

$$n_r = \frac{c_0}{v}. \quad (5.2)$$

The imaginary part n_i of the refractive index describes the loss of energy within the material by absorption and is called extinction index. The wave vector \mathbf{k} of an electromagnetic wave $\mathbf{E}(\mathbf{r}, t)$ can be written using the complex refractive index as $k = 2\pi m/\lambda_0$. To simplify the formula the EM-wave is expected to propagate along the z -axis.

$$\begin{aligned} \mathbf{E}(z, t) &= \Re\{E_0 e^{i(kz - \omega t)}\} = \Re\{E_0 e^{i(2\pi(n_r + in_i)z/\lambda_0 - \omega t)}\} \\ &= e^{-2\pi n_i z/\lambda_0} \Re\{E_0 e^{i(2\pi n_r z/\lambda_0 - \omega t)}\}, \end{aligned} \quad (5.3)$$

where ω is the angular frequency, E_0 is the amplitude, z is the propagation direction and λ_0 is the wavelength of the incident light. It easily can be seen that the imaginary part of the complex refractive index acts like an exponential dampening of the EM wave, while the real part scales the propagation velocity.

Figure 23 (left) shows the principle of absorption. Light with the wavelength λ passes a medium with the thickness ds and through absorption the radiative energy changes by $dI_\lambda(s, \mathbf{\Omega})$. Analogous to Eq. (5.3), the differential change in radiative energy $dI_\lambda(s, \mathbf{\Omega})/ds = K_{\text{abs}}(s, \lambda)I_\lambda(s, \mathbf{\Omega})$ can be integrated, yielding the Lambert-Beer law

$$I_\lambda(s + ds) = I_\lambda(s) \cdot \exp\left(-\int_s^{s+ds} K_{\text{abs}}(\lambda, s') ds'\right), \quad (5.4)$$

which shows that the light intensity decays over path-length in a purely absorbing medium.

The integral within the exponential function requires a basic knowledge of the distribution of the absorbers in the optical path, which is generally not available, therefore, a homogeneous medium assumption is further applied that assumes a homogenous distribution of absorbers in the optical path and yields a mean absorption coefficient $\widetilde{K}_{\text{abs}}(\lambda)$ which, for the sake of simplicity will further be denoted as $K_{\text{abs}}(\lambda)$.

5.1.3. Scattering

Figure 23 (left) shows an example for scattering. An incident light ray with the direction $\mathbf{\Omega}$ and the radiative energy of $I_\lambda(s, \mathbf{\Omega})$ passes through a scattering medium and redirected to the direction $\mathbf{\Omega}'$ and the radiative energy of $I_\lambda(s, \mathbf{\Omega}')$. This relation was derived for spherical particles by Gustav Mie in the beginning of the 19th century [85]. His aim was to describe the spectrum of colloidal gold particles that showed a strong particle size dependence. The scattering and extinction efficiencies can be written as series in the following

$$\begin{aligned}
Q_{\text{scat}} &= \frac{2}{x^2} \sum_{n=1}^{\infty} (2n+1) (|a_n|^2 + |b_n|^2) \text{ and} \\
Q_{\text{ext}} &= \frac{2}{x^2} \sum_{n=1}^{\infty} (2n+1) \Re(a_n + b_n),
\end{aligned} \tag{5.5}$$

where $x = \frac{\pi d_p}{\lambda}$ is the size parameter and a_n and b_n represent the Mie scattering coefficient for the electric and magnetic multipoles. The Mie scattering coefficients can be expressed as functions from Riccati–Bessel functions and spherical Neumann function[86] or as functions from Riccati–Bessel functions and their derivatives[87], depending on the preference of the user. Here, the code described by Bohren and Huffman [88] is used. The Taylor expansion of the monopole efficiencies, assuming $x \ll 1$ and relative magnetic permeability $\mu_r \approx 1$, are [89]

$$\begin{aligned}
Q_{\text{scat},1} &= \frac{1}{x^2} \left| i \frac{2}{3} \frac{\mathbf{m}^2 - 1}{\mathbf{m}^2 + 2} x^3 \right|^2 \text{ and} \\
Q_{\text{ext},1} &= -\frac{6}{x^2} \Re \left(i \frac{2}{3} \frac{\mathbf{m}^2 - 1}{\mathbf{m}^2 + 2} x^3 \right),
\end{aligned} \tag{5.6}$$

The mono + quadrupole terms are

$$\begin{aligned}
Q_{\text{scat},2} &= \frac{2}{x^2} \left(\left| 2i \frac{\mathbf{m}^2 - 1}{\mathbf{m}^2 + 2} x^3 \right|^2 + \left| \frac{i}{15} (\mathbf{m}^2 - 1) x^5 \right|^2 + \left| \frac{i}{5} \frac{\mathbf{m}^2 - 1}{2\mathbf{m}^2 + 3} x^5 \right|^2 \right), \\
Q_{\text{ext},2} &= -\frac{2}{x^2} \Re \left(2i \frac{\mathbf{m}^2 - 1}{\mathbf{m}^2 + 2} x^3 + \frac{i}{15} (\mathbf{m}^2 - 1) x^5 + \frac{i}{5} \frac{\mathbf{m}^2 - 1}{2\mathbf{m}^2 + 3} x^5 \right),
\end{aligned} \tag{5.7}$$

The absorption efficiency can be calculated by $Q_{\text{abs}} = Q_{\text{ext}} - Q_{\text{scat}}$.

In general, Mie theory is the exact solution of Maxwell's equations with consistency constraints connecting the external EM field to the internal EM field. Mie derived the theory for incident plane waves with perfect spherical particles. Only with these assumptions, it is possible to solve Maxwell's equations exactly.

In Mie theory the direction and fraction of scattered light is strongly influenced by the size parameter, the size of the scattering particle d_p compared to the wavelength λ of the incident light.

Figure 24 shows the logarithm of the angular scattering efficiency for particle sizes from 30 nm to 10 μm , approximately tripled every step. The incident light ray is oriented along the horizontal axis direction from left to right and polarized parallel to the upright coordinate axis. For the smallest particles ($d_p = 30$ nm), the angular scattering efficiency is nearly symmetrical in the forward and backward scattering directions. The discrepancies between Mie theory and Rayleigh approximation are not apparent, but would already affect the measurements described in Chapter 5.3. Within the next step ($d_p = 100$ nm) the scattering efficiency shifts more towards backward-scattering. For particles with diameters around 300 nm the scattering distribution becomes obviously asymmetric. The larger the particles ($d_p > 1$ μm)

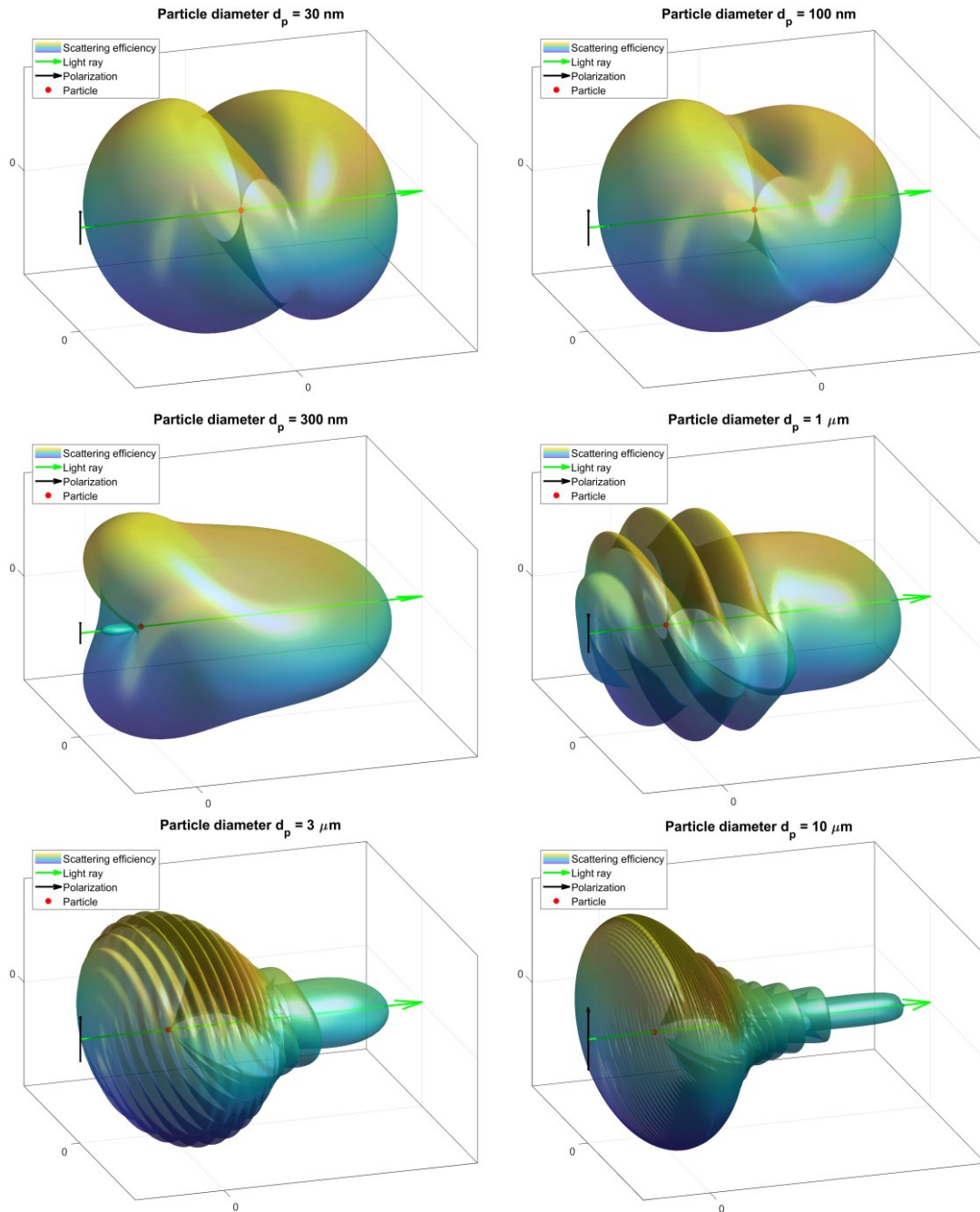


Figure 24: Development of the angular scattering efficiency for different particle diameters. The color-scale is chosen to illustrate the shape and not to have any physical relevance. The scattered light ray (green line, 532 nm wavelength) passes the particle from left to right and is upright polarized (black line). The location of the scattering particle is marked with a red dot.

become, the more the scattering structure is shifted towards the forward direction. Due to the larger contribution of high-order multipole moments in larger particles, the scattering efficiency develops several scattering peaks.

The size-dependent scattering efficiency can be roughly grouped into three categories within which the fundamental theory can be further simplified [88, 90], the Rayleigh-regime ($\pi d_p \lambda^{-1} \ll 1$ and $|\mathbf{m} \pi d_p \lambda^{-1}| \ll 1$) and the geometric optics regime

($\pi d_p \lambda^{-1} > 100$). When the conditions for the particular approximations do not hold the Mie theory should be applied.

5.1.4. Rayleigh approximation

“The expected particle diameter is much smaller than the detection wavelengths, and accordingly the governing Mie equations simplify to the Rayleigh approximation [88].”

The Rayleigh approximation is a frequently applied simplification when dealing with optical nanoparticle diagnostics. Simply spoken, the Rayleigh approximation equals the Mie theory while just using the dipole contribution, neglecting higher-order multipole terms. The resulting efficiencies can then be found simplifying Eq. (5.6)

$$Q_{\text{scat}}(d_p, \lambda) = \frac{8}{3} \left(\frac{\pi d_p}{\lambda} \right)^4 \left| \frac{\mathbf{m}^2 - 1}{\mathbf{m}^2 + 2} \right|^2 \quad (5.8)$$

$$Q_{\text{abs}}(d_p, \lambda) = \frac{4\pi d_p}{\lambda} \Im \left(\frac{\mathbf{m}^2 - 1}{\mathbf{m}^2 + 2} \right) = \frac{4\pi d_p}{\lambda} E(\mathbf{m}), \quad (5.9)$$

where $\mathbf{m} = n_r + in_i$ is the complex refractive index and $\boldsymbol{\varepsilon} = \varepsilon_r + i\varepsilon_{\text{I}} = \mathbf{m}^2$ is the (wavelength-dependent) dielectric function; the two parameters are related by $\varepsilon_r = n_r^2 - n_i^2$ and $\varepsilon_{\text{I}} = 2n_r n_i$. The absorption function is $E(\mathbf{m}) = \Im[(\mathbf{m}^2 - 1)/(\mathbf{m}^2 + 2)]$. Now, Q_{abs} denotes an efficiency, but the absorption coefficient is also of interest that can be calculated by $K_{\text{abs}}(\lambda) = 1/4 N_p \pi d_p^2 Q_{\text{abs},\lambda}(d_p, \lambda)$, where N_p is the particle number density.

The angular scattering intensity can be calculated by

$$I_{\text{scat}}(\theta) = \frac{I_0}{R^2} \frac{1 + \cos^2 \theta}{2} \left(\frac{2\pi}{\lambda} \right)^4 \left(\frac{n_r^2 - 1}{n_r^2 + 2} \right)^2 \left(\frac{d_p}{2} \right)^6 \quad (5.10)$$

where θ is the angle separating the light beam and the detector and R the distance from scattering particle to the detector.

The Rayleigh solution assumes that scattering does not bias the extinction, with $Q_{\text{ext},\lambda} \approx Q_{\text{abs},\lambda}$, but the Mie solution accounts for the full extinction $Q_{\text{ext},\lambda} = Q_{\text{abs},\lambda} + Q_{\text{scat},\lambda}$. Using $d_p = 27$ nm (silicon) and $d_p = 38$ nm (germanium) the scattering efficiency Q_{scat} for the visible spectrum (400–700 nm) is approximately 12 times smaller than the absorption efficiency.

For optical measurements of soot in flames, usually the Rayleigh approximation is used. It is approximately true for carbon based materials, but may not be transferrable to other materials, like silicon or germanium. The reason is the typical particle diameter of soot in standard flames around $d_{p,\text{soot}} \sim 30$ nm [73, 91].

To check the applicability of the Rayleigh approximation the size parameter $\pi d_p \lambda^{-1}$ and the phase-shift parameter $|\mathbf{m} \pi d_p \lambda^{-1}|$ need to be smaller than one. The refractive index is only suitable for homogeneous matter, which soot from hydrocarbon

combustion generally is not. This can be seen through the large variation of reported $E(\mathbf{m})$ values ranging from 0.2–0.6. To achieve a first assessment of the applicability the value of the complex refractive index of homogeneous pure soot is used, with $\mathbf{m}_{\text{soot,vis}} \approx 1.567 + i \cdot 0.52$ [92]. Consequentially, $\pi d_p \lambda^{-1} = 0.178 \ll 1$ and $|\mathbf{m} \pi d_p \lambda^{-1}| = 0.29 \ll 1$. Molten silicon and germanium (*cf.* Chapter 5.2.2), have refractive indexes of $\mathbf{m}_{\text{Si},532\text{nm}} = 2.51 + i \cdot 4.82$ and $\mathbf{m}_{\text{Ge},532\text{nm}} = 2.02 + i \cdot 4.69$, respectively, where the second condition is $|\mathbf{m} \pi d_p \lambda^{-1}| \approx 1$ is violated.

As reported in the literature [38, 67, 68, 73, 92-94], the absorption function of soot, $E(\mathbf{m})$, varies in magnitude from 0.2 up to 0.6, it is approximately independent of wavelength, over the LII detection range. Thus, the varying absolute value may bias the determination of volume fraction, but not the inferred temperature.

The extent to which the Rayleigh approximation deviates from Mie theory is shown in Figure 25. It shows the angular scattering efficiencies of Mie theory and Rayleigh approximation for silicon (first row), germanium (second row) and soot (last row). The particles are illuminated by an unpolarized light ray $(E_{\parallel}^i + E_{\perp}^i)/2$ with $\lambda = 500$ nm. For all three materials the Rayleigh approximation yields a symmetric scattering behavior (forward \leftrightarrow backward scattering). Just the magnitude changes, which is highest for silicon and lowest for soot due to the magnitude of the real part of the refractive index. In contrast, Mie theory predicts a change in scattering direction, where silicon and germanium have a more pronounced backwards scattering efficiency, but soot scatters more towards the forward direction.

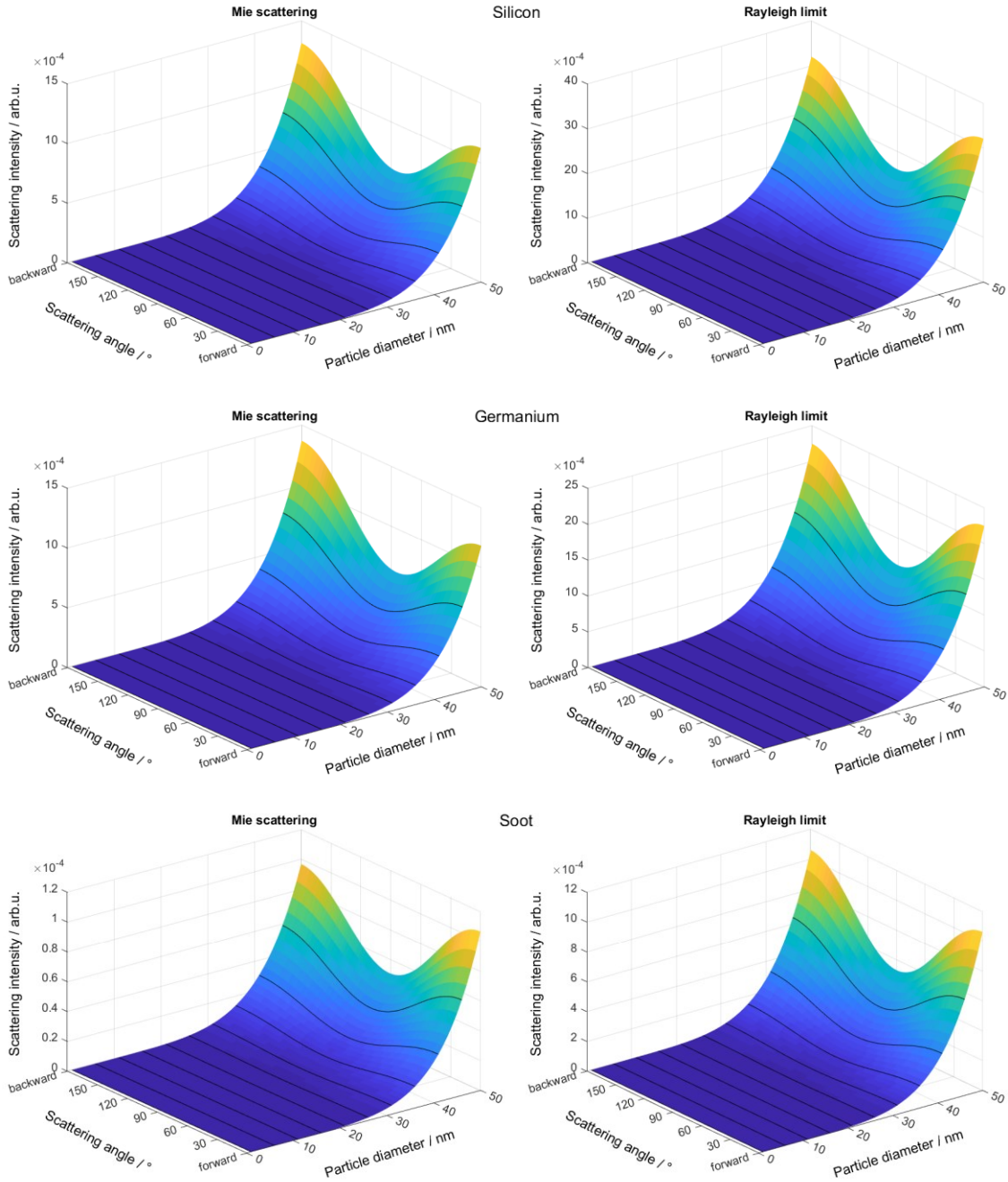


Figure 25: Angle-dependent scattering efficiency for silicon (first row), germanium (second row) and soot (third row). For each material, the complex refractive index for $\lambda = 500$ nm from the majority phase is used. The left column shows the scattering efficiency when using the Mie theory for spherical particles, the right column shows the result for the Rayleigh approximation.

5.1.5. Planck spectrum

Hot objects emit electromagnetic radiation, with which intensity and spectral distribution depends on the absolute temperature. The radiation originates from thermal motion of charged particles (protons and electrons) in matter. Due to the coupling of internal electro-magnetic fields it is possible to convert kinetic energy to

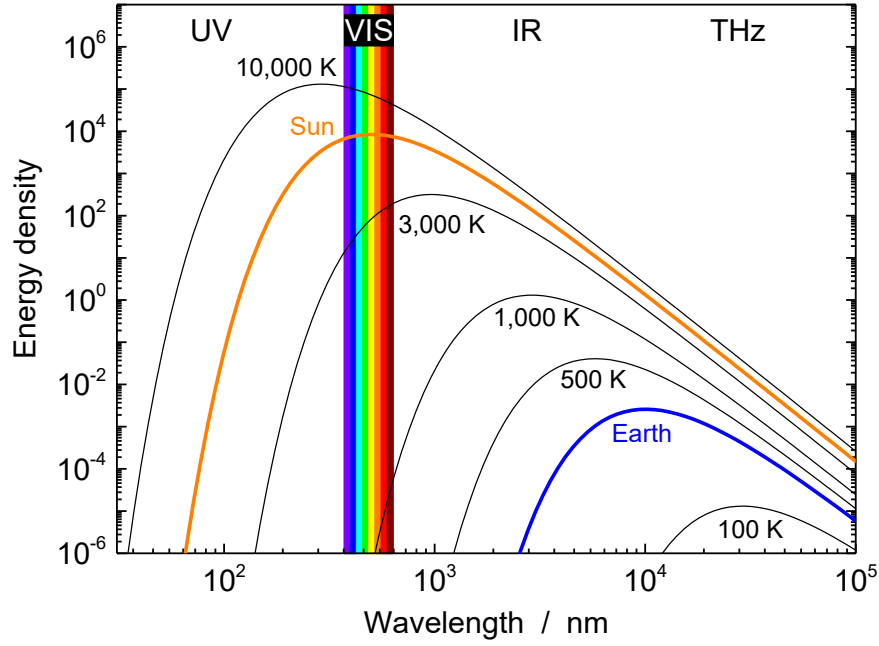


Figure 26: Blackbody radiation for different temperatures (100–10,000 K). The wavelength is subdivided into spectral regions to guide the eye.

electromagnetic energy. Planck's law describes the contour and the intensity of blackbody radiation

$$I_B(\lambda, T)d\lambda dA = \frac{2\pi hc^2}{\lambda^5} \frac{1}{\exp\left\{\frac{hc}{\lambda k_B T}\right\} - 1} d\lambda dA. \quad (5.11)$$

where $d\lambda$ is the wavelength range and dA the emitting normal surface.

The spectroscopic model is used to infer the particle temperature independent of the particle size, since d_p (along with solid detection angle Ω , volume fraction f_v , probe volume thickness, N_p , $d\lambda$, and other constants) can be included into the calibration coefficient C_k in Eq. (5.11) to yield

$$J_\lambda(t) = C_k I_b[\lambda, T_p(t, d_p)] K_{\text{abs}}(d_p, \lambda), \quad (5.12)$$

where $K_{\text{abs}}(d_p, \lambda) = K_{\text{abs}}(\lambda) = \frac{4\pi d_p}{\lambda} \Im\left(\frac{\varepsilon-1}{\varepsilon+2}\right) = \frac{4\pi d_p}{\lambda} E(\mathbf{m})$ for the Rayleigh approximation and $K_{\text{abs}}(d_p, \lambda) = K_{\text{abs, Mie}}(d_p, \lambda)$ for the Mie-theory solution.

While the optical properties of soot are notoriously ill-defined and not amenable to a simple theoretical model [95, 96], those of liquid silicon and germanium can be described using the Drude model (e.g., [97-99], and next chapter 5.1.7).

5.1.6. Semiconductor-metal transition through disorder

Silicon and germanium are both known to be semiconductors under normal conditions. The bandgap that separates valence and conduction band can be explained by the nearly free electron gas in an ordered system, like a crystalline lattice, described by Kittel, Chapter 7 [100]. At the first Brillouin zone, where the

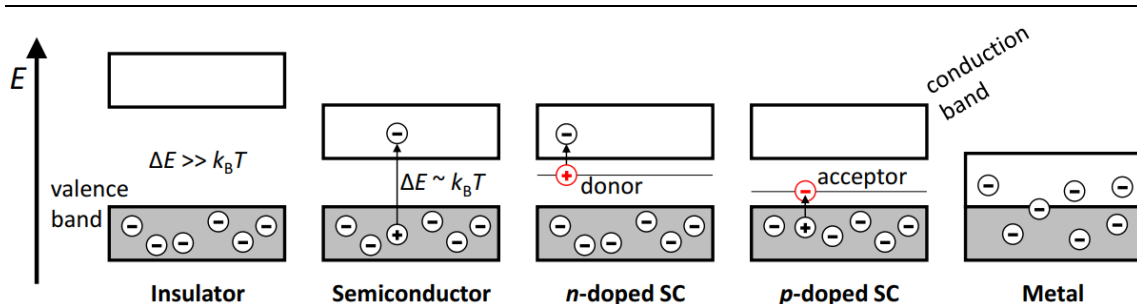


Figure 27: Band structure of insulators, doped and undoped semiconductors, and metals.

Bragg condition is fulfilled. The wave function results in a standing wave through the Umklapp process, and as consequence, at the reciprocal lattice vector $k = \pm n \cdot \pi/a$, with the lattice constant a and a natural number n , a forbidden zone develops. In Figure 27 a simplified energy-band model is shown.

The formation of a bandgap is strongly linked to the periodicity of the underlying order of the material. When adding disorder to a semiconductor, like in n - or p -doped semiconductors (depending of the number of valence electrons of the dopant) further acceptor and donor levels in the forbidden zone develop.

The liquefaction also is a process, which adds disorder to the lattice, and so blurs the strong separation between valence and conduction band [101]. According to [97, 98, 102] the tetrahedral structure of silicon is disrupted upon liquefaction. As a consequence, all of the valence electrons contribute to the formation of a conduction layer. Hodgson [103] explains, that this assumption is not entirely true, because the effective electron mass is measured to be smaller than the real electron mass. It follows, that the effective number of electrons provided by each atom is larger than the number of valence electrons for liquid metals.

Table 2: Properties of Si and Ge:

	Silicon	Germanium
Mass:	28.085 u = 4.663×10^{-26} kg	72.63 u = 12.059×10^{-26} kg
Bandgap energy:	1.17 eV	0.75 eV
Transition type:	indirect	indirect

5.1.7. Drude model for metals

In the classical interpretation of Drude theory, conduction-band electrons accelerate due to Columbic forces imposed by the oscillating electromagnetic field of light. But, their motion is damped by collisions between electrons and the background of ions and atoms. These collisions are the mechanism that couples the electromagnetic radiation to the internal energy of the liquid metal.

More fundamentally, the response of electrons to an electro-magnetic wave is described by the polarization, here just the electric part is shown

$$\mathbf{P}(\mathbf{r}, \omega) = \varepsilon_0 \chi_e(\omega) \mathbf{E}(\mathbf{r}, \omega), \quad (5.13)$$

with the polarization \mathbf{P} , the vacuum permittivity $\varepsilon_0 = 8.8541 \times 10^{-12} \text{ Fm}^{-1}$, which defines the capability of vacuum to permit electric fields, the electric susceptibility $\chi_e = \varepsilon - 1$, which indicates the degree of polarizability of the dielectric material, $\omega = 2\pi\nu = 2\pi c_0/\lambda$ the angular frequency of the incident EM wave, and \mathbf{E} the electrical field strength.

To gain inside into the basic frequencies and resonances the Lorentz oscillator-model can be applied. It describes the coupling of the electrons to the positively charged background induced by atoms and ions of the material,

$$m \frac{d^2 x}{dt^2} + m\gamma \frac{dx}{dt} + m\omega_0^2 x = -qE(t), \quad (5.14)$$

which is, basically, the differential equation of a externally driven and damped harmonic oscillator with the mass of the moved object m (here electrons), γ the damping constant, ω_0 the resonance frequency of the undamped oscillator, and q the charge of the accelerated particle. The damping is induced by collisions or deflections of the moving electrons with atoms, ions and impurities of the quasi-steady lattice background.

The solution to Eq. (5.9) is

$$x_0 = \frac{qE}{m} \frac{1}{\omega_0^2 - \omega^2 - i\gamma\omega}. \quad (5.15)$$

The dipole moment of a single oscillator is $p = qx_0$, and for an ensemble of oscillators with a given density n is $P = np$. The electrical susceptibility can then be rewritten to

$$\varepsilon(\omega) = 1 + \frac{f}{\omega_e^2 - \omega^2 - i\gamma\omega}, \text{ with } f = \frac{nq^2}{m\varepsilon_0}. \quad (5.16)$$

The Lorentz-oscillator model is more comprehensive than needed to explain a simple metal and can be simplified to the Drude model by setting the fundamental frequency to zero, $\omega_e = 0$, applying the charge of an electron $q = -e$, invert the scattering frequency yielding a mean scattering time $\tau = 1/\gamma$, and relate the enumerator to the plasma frequency $\omega_p = \sqrt{f}$. Through this simplification, the complex dielectric function, separated in real and complex part, is [97, 104]

$$\varepsilon_I = 1 - \frac{\omega_p^2 \tau^2}{\omega^2 \tau^2 + 1}, \varepsilon_{II} = \frac{\omega_p^2 \tau}{\omega(\omega^2 \tau^2 + 1)}, \quad (5.17)$$

where ω_p is the plasma frequency of the electrons and τ is the mean relaxation time, which is related to the collision frequency between electrons and atoms/ions.

The plasma frequency is given by [105]

$$\omega_p = \sqrt{\frac{n_{e,\text{liq}} e^2}{\epsilon_0 m_e}}, \quad (5.18)$$

with m_e the rest mass of an electron, and $n_{e,\text{liq}}$ is the electron number-density within the liquid metal.

The relaxation time can be inferred from the current density $\mathbf{j} = -n_{e,\text{liq}} e \mathbf{v}$ and the mean electron drift velocity $\mathbf{v} = e \mathbf{E} \tau / m_e$. With Ohms law $\mathbf{j} = \sigma_{\text{DC}} \mathbf{E}$, the mean relaxation time is

$$\tau = \frac{m_e \sigma_{\text{DC}}}{n_{e,\text{liq}} e^2}, \quad (5.19)$$

which physically corresponds to the average time scale between electron scattering events.

5.2. Optical properties of molten silicon and germanium

To determine the optical properties two different pathways coexist; a direct measurement (Eq. (5.23)) or an indirect measurement of the electrical properties (see Eq. (5.18) and Eq. (5.19)), as they are used to calculate the Drude parameters.

5.2.1. *Determination of optical characteristics through the electrical properties*

Equations (5.18) and (5.19) highlight the connection between the electrical and optical properties of Drude metals. Therefore, the constant specific current conductivity, the density of conduction band electrons, and the mass of an electron must be known.

The electron density is found from the atomic number density assuming that each silicon or germanium atom contributes its four valence electrons to the conduction band. The available literature data is shown in Table 3 and Table 4.

Table 3: Temperature dependence of the densities of liquid silicon (a) and germanium (b). When possible the validity range of the measurements is noted.

(a) Density of silicon $\rho / \text{kg m}^{-3}$	Valid T range / K	Ref.
$2570 - 0.936 (T/K - 1686)$	< 1770	CRC Handbook 84th Ed. [106]
$2580 - 0.16 (T/K - 1687) - 1.15 \times 10^{-7} (T/K - 1687)^2$	1350–1850	Rhim, 1997 [107]
$2583 - 0.19 (T/K - 1687) - 1.98 \times 10^{-7} (T/K - 1687)^2$	1370–1830	Zhou, 2003 [108]
$2575 - 1 (T/K - 1686)$	1668–1930	Kimura, 1997 [109]
(b) Density of germanium $\rho / \text{kg m}^{-3}$	Valid T range / K	Ref.
$5600 - 0.55 (T/K - 1210.25)$	< 1870	CRC Handbook 84th Ed. [106]
$5670 - 0.542 (T/K - 1210.25)$	1150–1400	Rhim, 2000 [110]
$6170 - 0.442 T/K$	1200–1600	Nakanishi, 1999, [111]
$5088 - 0.717 (T/K - 1118.2)$	1200–1750	Sato, 2000 [112]
$4982 - 1.733 (T/K - 1117.4)$	1200–1700	Tokizaki, 1993, from [112]
$5570 - 0.371 (T/K - 1207)$	1180–1500	Martin-Garin, 1975 [113]

Table 4: Temperature dependence of the DC conductivities of liquid silicon and germanium. When possible the validity range of the measurements is noted.

(a) conductivity of silicon $\sigma / \text{S m}^{-1}$	Valid T range / K	Ref.
$8.8496 \times 10^5 (T/K - 1000)^{-1}$	1713–1820	Cusack, 1963 [114]
1396.65	1400–1650	Sasaki, 1995 [115]
$5.288 \times 10^6 (T/K + 4424)^{-1}$	1420–1520	Schnyders, 1996 [116]
(b) conductivity of germanium $\sigma / \text{S m}^{-1}$	Valid T range / K	Ref.
1587.5	1232	Cusack, 1963 [114]
$3.703 \times 10^6 (T/K + 2474)^{-1}$	940–1100	Schnyders, 1996 [116]

The temperature of the particles at the measurement location is well known. As discussed in chapter 4.6, at this location a gas phase temperature of $T_p = 1558 \pm 21$ K is assumed. The density and the DC conductivity are also temperature-dependent, therefore, the standard deviation of the assumed temperature affects the standard deviation of the properties. To quantitatively derive the mean value and the standard deviation a Monte-Carlo approach was used, where the temperature is

modeled as independent and normally-distributed variable simulating 100,000 samples. The resulting sample sequence is fitted by a normal distribution to attain the mean and the standard deviation.

The density of silicon and germanium at the observed temperature is $\bar{\rho}_{\text{Si},1600\text{ K}} = 2626.4 \pm 101.6 \frac{\text{kg}}{\text{m}^3}$ and $\bar{\rho}_{\text{Ge},1600\text{ K}} = 5101.7 \pm 510.9 \frac{\text{kg}}{\text{m}^3}$

With Eq. (5.18) $\omega_p = \sqrt{\frac{n_{e,\text{liq}}e^2}{\epsilon_0 m_e}} = \sqrt{\frac{4\rho_{\text{Ge/Si,liq}}e^2}{\epsilon_0 m_e m_{\text{Ge/Si}}}}$ the plasmon frequency and standard deviation can be inferred:

$$\bar{\omega}_{\text{Si},1600\text{ K}} = 2.676 \times 10^{16} \pm 5.229 \times 10^{14} \text{s}^{-1}$$

$$\bar{\omega}_{\text{Ge},1600\text{ K}} = 2.320 \times 10^{16} \pm 1.170 \times 10^{15} \text{s}^{-1}$$

Similarly, the relaxation time can be inferred accounting for the uncertainties in temperature and literature values. The DC conductivity for silicon and germanium are, $\bar{\sigma}_{\text{Si},1600\text{ K}} = 1251.8 \pm 335.2 \text{ Sm}^{-1}$ and $\bar{\sigma}_{\text{Ge},1600\text{ K}} = 1248.1 \pm 340.2 \text{ Sm}^{-1}$. Using Eq. (5.19) the mean relaxation time can be calculated by $\tau = \frac{m_e \sigma_{\text{DC}}}{n_{e,\text{liq}} e^2} = \frac{m_e m_{\text{Si/Ge}} \sigma_{\text{DC}}}{4\rho_{e,\text{liq}} e^2}$:

$$\bar{\tau}_{\text{Si},1600\text{ K}} = 1.974 \times 10^{-16} \pm 5.348 \times 10^{-17} \text{s}$$

$$\bar{\tau}_{\text{Ge},1600\text{ K}} = 2.645 \times 10^{-16} \pm 7.750 \times 10^{-17} \text{s}$$

Obviously, the uncertainty of the relaxation time is much higher because the equation includes two sources of uncertainty: the density and the DC conductivity. Finally, the uncertainty in τ is $\pm 25\%$, while the uncertainty in ω is 2–5 %, but in general, the derived values are sufficiently accurate to be applied as priors and results in a much better *a posteriori* probability. Outside the documented temperature regimes an extrapolation (not shown here) to higher temperatures was done, assuming the described linear model for σ_{DC} and ρ .

5.2.2. Literature review

The thermophysical and electrical properties of molten silicon and molten germanium are well-studied, due to the importance of these materials for semiconductor electronics and thermoelectric materials. In contrast, the optical properties of molten silicon and germanium have been disseminated through only five and three independent studies, respectively. Basically, four different experimental approaches are utilized in the literature to measure the optical properties and one theoretical derivation:

1. Ellipsometry measurements incorporate the knowledge of polarization and angle of the incident and scattered light to derive a full set of optical properties, especially the complex dielectric permittivity, as well as the complex refractive index.

2. Reflectance measurements of the material surface yield the emissivity ϵ for the respective wavelength by dividing the incident with the reflected light intensity. The definition of emissivity is given by $\epsilon_\lambda = \frac{4n}{(n+1)^2+k^2}$ with which the complex refractive index can be calculated.
3. Comparing the emission of a hot material surface to blackbody radiation of the same temperature which then yields the emissivity $\epsilon_\lambda = \frac{I_s(\lambda,T)}{I_b(\lambda,T)}$.
4. Applying a theoretical integration equation approach. For details *cf.* Ref. [117]

Table 5: documented Drude parameter for silicon and germanium.

	Measured property	Validity	Ref.	Year - Technique
Si	$\epsilon_\lambda = 0.267 \rightarrow$ $\omega_p = 2.68 \times 10^{16} \text{ rad/s}$ $\tau = 2.18 \times 10^{-16} \text{ s}$	T = 1668.15 K 500–800 nm	Takasuka [118]	1997 - Emissivity by reflectance
Si	$\omega_p = 34.1 \text{ eV}$ $= 5.18 \times 10^{16} \text{ rad/s}$ $\beta = 1.25 \times 10^{16} \text{ 1/s} \rightarrow$ $\tau = 0.8 \times 10^{-16} \text{ s}$	T = 1668.15 K 334–633 nm	Jellison [119]	1992 - Ellipsometry
Si	$\epsilon^2 = -27.3 + 48.7i$ $\omega_p = 2.50 \times 10^{16} \text{ rad/s}$ $\tau = 2.12 \times 10^{-16} \text{ s}$	~1900 K 355–1064 nm	Li [120]	1987 - Complex dielectric function with reflectance
Si	$\omega_p = 2.64 \times 10^{16} \text{ rad/s} \pm 5\%$ $\tau = 2.10 \times 10^{-16} \text{ s} \pm 5\%$	1668–1800 K 650–1550 nm	Kawamura [97]	2005 - Emissivity by blackbody radiation
Si	$\omega_p = 2.87 \times 10^6 \text{ rad/s}$ $\tau = 1.59 \times 10^{-16} \text{ s}$	Liquid	Fuchs [117]	2000 - theoretical
Ge	$\omega_p = 26.5 \text{ eV}$ $= 4.02 \times 10^{16} \text{ rad/s}$ $\beta = 0.86 \times 10^{16} \text{ 1/s} \rightarrow$ $\tau = 1.19 \times 10^{-16} \text{ s}$	T = 1203.15 K 334–633 nm	Jellison [119]	1987 - Ellipsometry
Ge	$\epsilon_\lambda = 0.202 \rightarrow$ $\omega_p = 2.5 \times 10^{16} \text{ rad/s}$ $\tau = 2.51 \times 10^{-16} \text{ s}$	T > 1210.15 K 600–800 nm	Takasuka [102]	1997 - Emissivity by reflectance
Ge	$R(\lambda) \sim 66\%$ $\omega_p = 2.47 \times 10^{16} \text{ rad/s}$ $\tau = 2.47 \times 10^{-16} \text{ s}$	T = 1203.15 K 240–440 nm	Abraham [121]	1963 - Reflectivity by reflectance

The highest-reported temperature is approximately 1900 K, which is far below the temperatures reached during laser-induced incandescence measurements. For silicon, the parameters found from the electrical conductivity and density are $\omega_p =$

2.676×10^{16} rad/s and $\tau = 1.974 \times 10^{-16}$ s, which closely match the parameters reported by Takasuka et al. [118], Li and Fauchet [99], and Kawamura et al. [97]. The value of the plasmon frequency provided by Fuchs et al. ([117] and Table 5) of $\omega_p = 2.87 \times 10^6$ rad/s differ significantly from all other values. This suggests that a typesetting error corresponding to a misplaced decimal is probable. In Figure 28 this value was fixed by changing the value to $\omega_p = 2.87 \times 10^{16}$ rad/s. Far less experimental data are available for liquid germanium; only the results of Abraham et al. [121] and Takasuka et al. [102] are consistent with the derived values by σ_{DC} and ρ in Chapter 5.2.1. The values provided by [122] seem unreasonable and inconsistent to the all other sources.

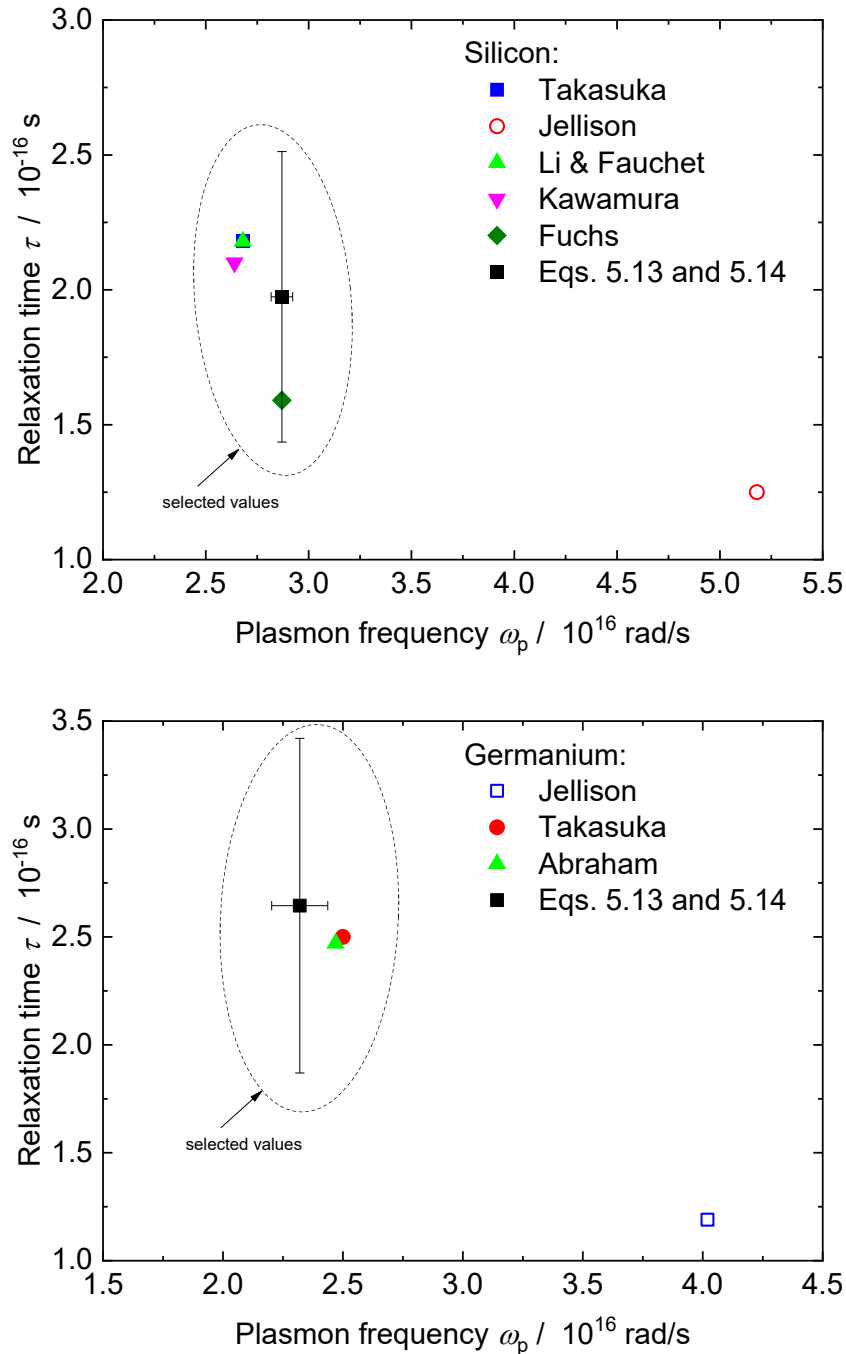


Figure 28: Collection of all reported Drude parameters from silicon and germanium.

It should be noted, that the provided values are for bulk material, and not for nanoparticles. An important parameter of the applicability of Drude theory is the electron mean free path. When the mean free path of the electron is longer than the enclosing nanoparticle, its wave function cannot solely be described by material parameters, and in addition will be affected by the size of the nanoparticle. Werner et al. [123] and Seah et al. [124] both estimate the electron mean free path to be in the order of the nanoparticle diameter. With this finding, the electron confinement effect should be incorporated.

In contrast to the aforementioned publications, the electron mean free path can be estimated [125] by

$$\lambda_e = \frac{\sigma_{\text{DC}} h}{(n_e)^{2/3} e^2} \left(\frac{3}{8\pi} \right)^{1/3}, \quad (5.20)$$

where σ_{DC} is the DC conductivity, also shown in Table 4, n_e is the electron density (Eqs. (5.18) and (5.19)) and e is the charge of an electron. With the values of liquid silicon at 1600 K the electron mean free path is $\lambda_e \sim 0.373 \times 10^{-12} \text{ m} \ll d_p$, therefore, electron confinement effects should be negligible.

A potential electron confinement effect is not part of the analysis of this work, but deviations from Drude theory might occur. Generally, confinement effects broaden sharp features (*cf.* [126, 127], which describe similar effects, but for Raman spectroscopy).

5.3. Spectrally resolved line-of-sight attenuation (LOSA) measurements

While observing the transmission of light through a semitransparent material system the fraction of light that is collected by the detector is influenced by absorption and scattering out of the optical path, which, combined, is called extinction. The transmission τ_λ or the extinction coefficient K_{ext} , respectively, are determined by the Lambert-Beer law [128] (*cf.* Eq. (5.4) and Chapter 5.1.2)

$$\begin{aligned} \tau_\lambda = \frac{I_\lambda}{I_{0,\lambda}} &= \exp\left(-\int_{-\infty}^{\infty} K_{\text{ext}}(\lambda, s) ds\right) = \exp(-L \widetilde{K}_{\text{ext}}(\lambda)) \\ &\rightarrow K_{\text{ext}}(\lambda) = \frac{1}{L} \ln\left(\frac{I_{0,\lambda}}{I_\lambda}\right), \end{aligned} \quad (5.21)$$

with the path-length along the optical axis L , and $I_{0,\lambda}$ and I_λ are the incident and transmitted light intensity, respectively. The Rayleigh-approximation for the absorption function yields

$$E(\mathbf{m}) = \frac{\lambda K_{\text{ext}}(\lambda)}{6 \pi f_V}, \quad (5.22)$$

with the volumetric concentration of the nanoparticles f_V .

The optical setup is shown in Figure 29. The upper part shows an image of the measurement setup. On the left hand side, the light of a halogen lamp with internal condenser optic is shone onto a diffusor plate and then imaged via two lenses into the measurement volume. From there, two additional lenses image the attenuated light onto the spectrometer slit.

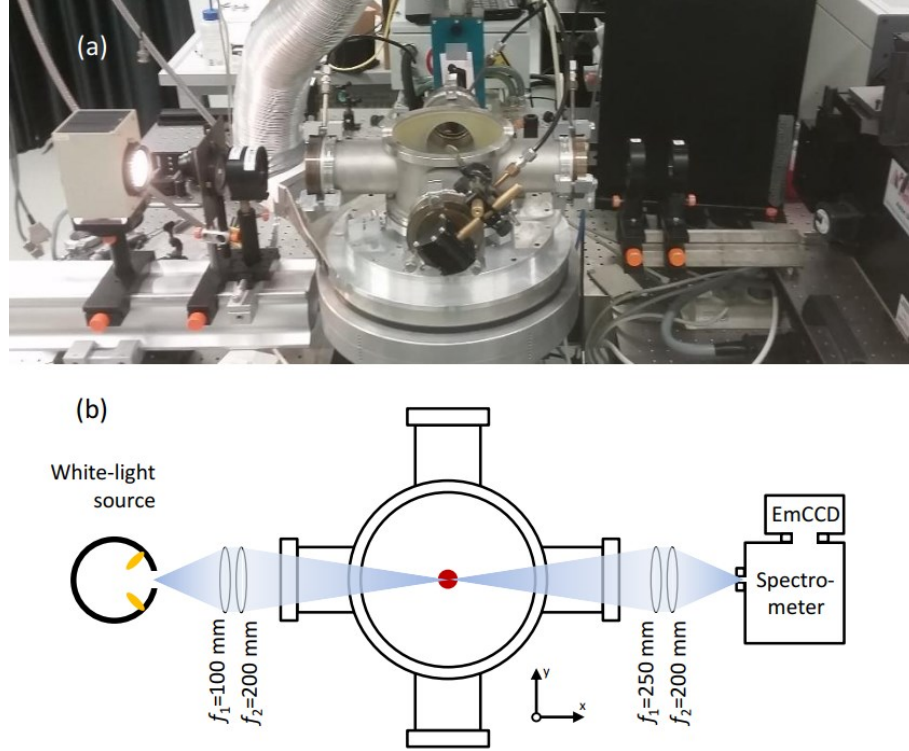


Figure 29: a: Photo of the disassembled reactor with white-light source. The spectrometer is the one used for LII measurements, for LOSA another spectrometer was attached. b: Schematics of the optical setup for LOSA measurements.

Similar to the imaging experiments described in Chapter 4.5.1, the spectrally-resolved LOSA data is obtained by sequentially acquiring four spectra, schematically shown in Figure 30. With the lamp on and the particles present, the intensity incident on the spectrometer $I_{t+e,\lambda}$ consists of transmitted incident intensity, incandescence emitted by the silicon nanoparticles (heated within the plasma region of the reactor), and scattered light from the plasma. The intensity due to thermal emission from the nanoparticles, $I_{e,\lambda}$, is isolated by making a measurement with the lamp off (subtracting these measurements also removes the dark current.) This measurement is normalized by the transmitted intensity through a transparent medium, which is made by subtracting the intensity measured with the lamp on and no particles, $I_{lamp,\lambda}$, and a dark signal measurement, $I_{dark,\lambda}$, made by covering the optical port of the spectrometer. The spectral opacity, $\kappa_\lambda = K_{ext,\lambda}L$, is found by

$$\kappa_\lambda = -\ln\left(\frac{I_\lambda}{I_{\lambda,0}}\right) = -\ln\left(\frac{I_{t+e,\lambda} - I_{e,\lambda}}{I_{lamp,\lambda} - I_{dark,\lambda}}\right). \quad (5.23)$$

Assuming that the nanoparticle sizes are uniform, the local absorption coefficient is related to the nanoparticle absorption coefficient by $K_{ext,\lambda} = N_p \pi d_p^2 / 4 Q_{ext,\lambda}$, where N_p is the local nanoparticle number density.

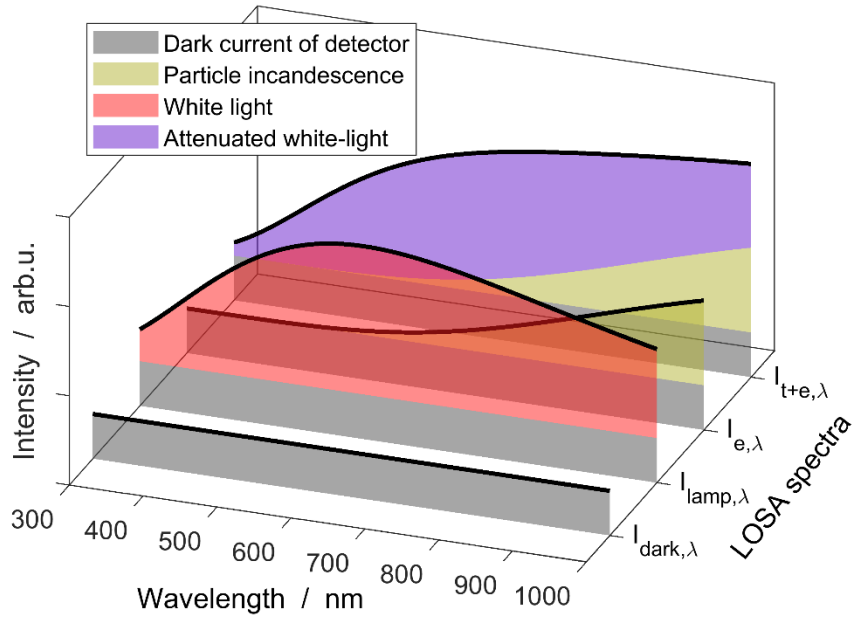


Figure 30: Four exemplary spectra required for a single LOSA measurement: the dark spectrum $I_{\text{dark},\lambda}$, the illumination spectrum $I_{\text{lamp},\lambda}$, the incandescence spectrum $I_{e,\lambda}$, and the attenuated spectrum $I_{t+e,\lambda}$, arranged along the y -axis. Each spectrum consists of different components illustrated by different colors: light grey is the dark current of the detector, olive green is the incandescence spectrum of the hot particle, red is the spectrum of the white-light source and purple is the attenuated spectrum.

The silicon and germanium nanoparticles are synthesized under the same conditions described in chapter 4.2. The particle size distributions were measured by transmission-electron microscopy (chapter 4.4) and satisfy the condition that the size parameter (introduced in section 5.1.3, $x = \pi d_p / \lambda$) is much smaller than 1 over the wavelengths of interests for LII measurements ($400 \text{ nm} < \lambda < 700 \text{ nm}$).

5.4. Incorporating literature data through Bayesian inference

The aforementioned measurements yield the extinction efficiency $Q_{\text{ext,meas}}$ as result. Since the nanoparticle volume fraction f_v and the exact dimensions of the measurement volume are not known, these parameters are condensed into the scaling factor C_k from Eq. (5.12), which can be used to scale the model solution $Q_{\text{ext,model}}$.

The quantities of interest are the plasmon frequency and mean relaxation time, $\mathbf{x} = [\omega_p, \tau]$, the scaling factor C_k is treated as nuisance parameter with a non-informative prior. The probability density is then maximized by a least squares approach (*cf.* Appendix C3) to find the maximum *a posteriori* estimate \mathbf{x}_{MAP} for the Drude parameters.

In the following $p(\mathbf{x}, C_k | \mathbf{Q}_{\text{ext}})$ is the posterior probability density, related to the given information through Bayes equation,

$$p(\mathbf{x}, C_k | \mathbf{Q}_{\text{ext}}) \propto \exp \left\{ - \sum_{j=1}^{Nt} \frac{[Q_{\text{ext, meas}, j} - C_k \cdot Q_{\text{ext, model}}(\mathbf{x}, \lambda_j)]^2}{2\sigma_{Q, j}^2} \right\} p_{\text{prior}}(\mathbf{x}). \quad (5.24)$$

$Q_{\text{meas}, j}$ is the measured extinction efficiency, $Q_{\text{ext, model}}(\mathbf{x}, \lambda_j)$ the model solution for the given Drude parameters, $\mathbf{x} = [\omega_p, \tau]$ is a vector containing the fitting variables, C_k the nuisance parameter that is integrated out for parameter inference, which includes collection efficiency and a scaling to the efficiency of the optical system, particle volume fraction in the measurement volume and other values, $\sigma_{Q, j}^2$ is the variance of the measured extinction for the data point of interest and $p_{\text{prior}}(\mathbf{x})$ is the prior information incorporated into the model, described below.

The complex refractive indexes of germanium and silicon were calculated by the Drude model, discussed in section 5.1.7 and significantly differ from those of soot; especially the imaginary part of \mathbf{m} is ten times larger compared to soot.

Figure 31 and Figure 32 show that the measured spectral opacity is consistent with Drude theory combined with Rayleigh approximation and Mie theory. To illustrate the parameter range of ω_p and τ which match the LOSA measurements, the Drude dispersion model was solved with three different assumptions:

1. Fixed Drude parameters at the mean of all reported literature values
2. No assumption on ω_p and $\tau \rightarrow$ maximum likelihood estimate.
3. ω_p and τ vary with the standard deviation of the literature values around the mean value \rightarrow maximum *a posterior* estimate.

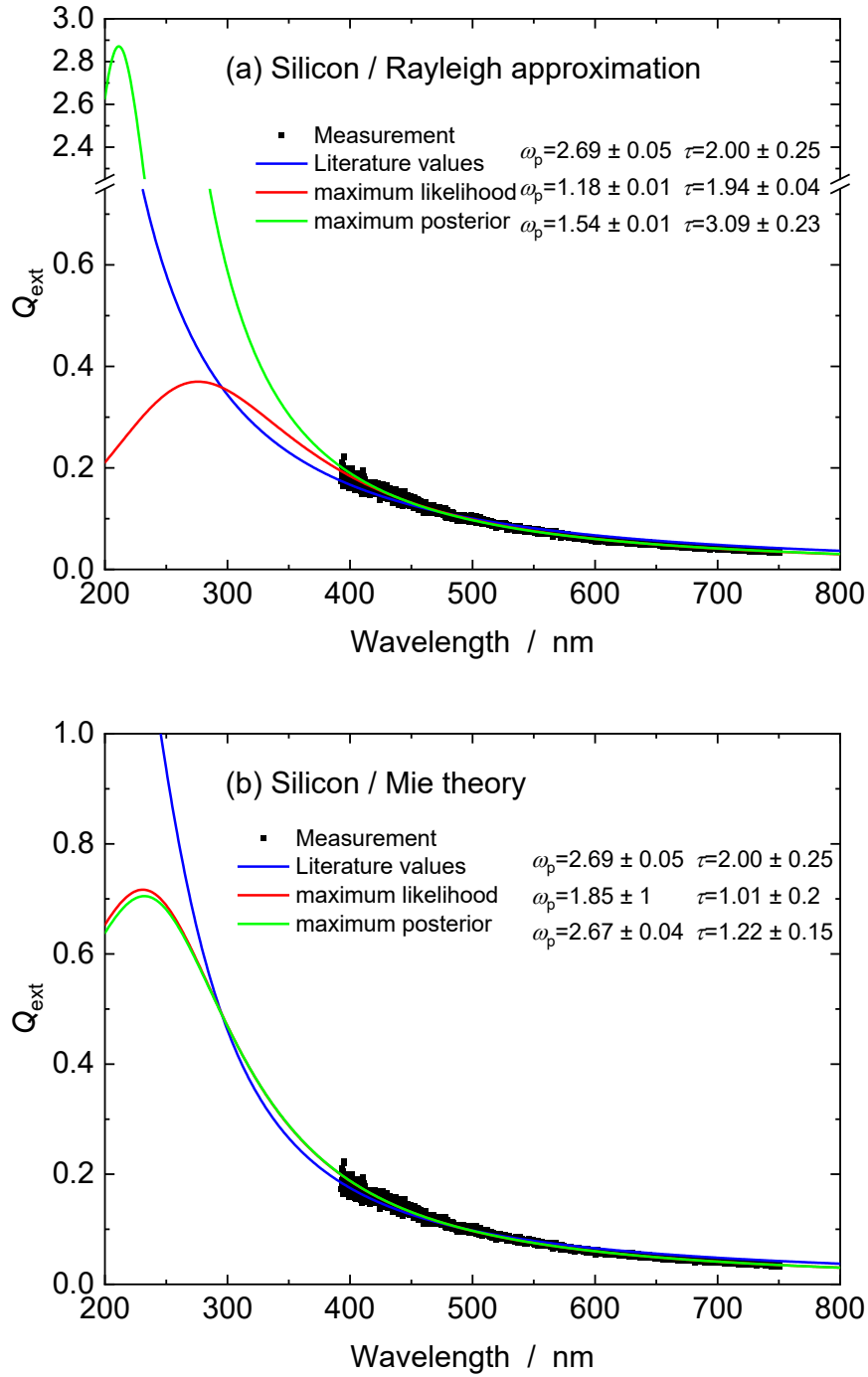


Figure 31: *In situ* line-of-sight attenuation (LOSA) measurements of silicon nanoparticles and three different models of including prior information about Drude parameter: Blue lines: ω_p and τ fixed to the mean of the literature values, green lines: ω_p and τ may vary by the mean and the standard deviation of the literature values, and red lines: no assumption on ω_p and τ , which basically is the maximum likelihood estimate. a: Results applying Rayleigh approximation and b: Solution of Mie-theory. The maximum likelihood estimate is the solution without prior information on ω_p and τ , while the maximum posterior estimate uses a normal prior with mean and sigma estimated in Chapter 5.3.

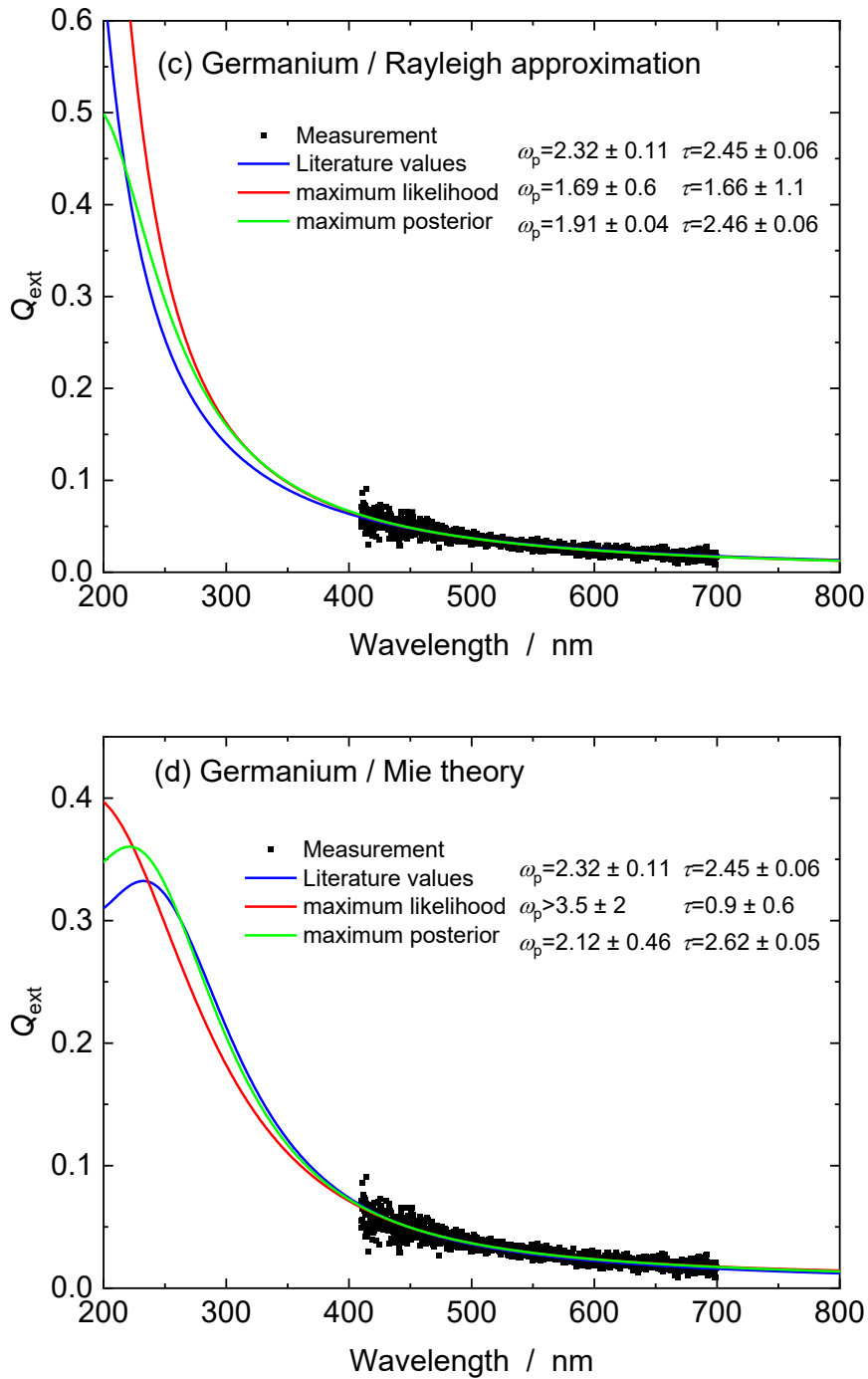


Figure 32: *In situ* line-of-sight attenuation (LOSA) measurements of germanium nanoparticles and three different modes of including prior information about Drude parameter: Blue lines: ω_p and τ fixed to the mean of the literature values, green lines: ω_p and τ may vary by the mean and the standard deviation of the literature values, and red lines: no assumption on ω_p and τ . a: Results applying the Rayleigh approximation, b: solution of Mie theory. The maximum likelihood estimate is the solution without prior information on ω_p and τ , while the maximum posterior estimate uses a normal prior with mean and sigma estimated in Chapter 5.3.

The inferred optical properties are plotted in Figure 33. Depending on the selected prior they differ significantly from the literature values: while the inferred values underestimate the literature-values using the Rayleigh approximation for both materials, Mie theory's solution gives a more reasonable result.

Figure 33 and Figure 34 show the inferred values ω_p and τ for silicon and germanium. The marginalized likelihood or posterior function, respectively (isolines in black), is plotted together with the linearized estimate \mathbf{x}_{MLE} (maximum likelihood estimate, assuming no prior information) or \mathbf{x}_{MAP} (maximum *a posteriori* estimate, assuming normal prior) and the corresponding literature values (blue lines and symbols). The range of ω_p and τ were limited to reasonable values in order to save computational time.

The shape of the likelihood or posterior probability distributions differ from a normal distribution due to the nonlinearity of the measurement model. Each of the probability distribution in the next four plots seem to be combined out of two branches which merge for large values of $\omega_p > 3.5 \times 10^{16} \text{ s}^{-1}$, but are separated in the observed parameter range.

The likelihood probability distributions yield very wide uncertainties, and indicate that this is an ill-posed problem (*cf.* discussion in chapter 5.5). One way of reducing the ambiguity is adding prior information, here in the form of the literature values with the corresponding Gaussian distributed uncertainties. It shows, that the combined solution (measurement + literature prior) yields much lower uncertainties.

In the case of silicon, the resulting uncertainties are apparently smaller than the literature uncertainties. The maximum posterior estimate of the plasmon frequency matches the literature very well, but the mean relaxation time is nearly 40% apart from the provided values.

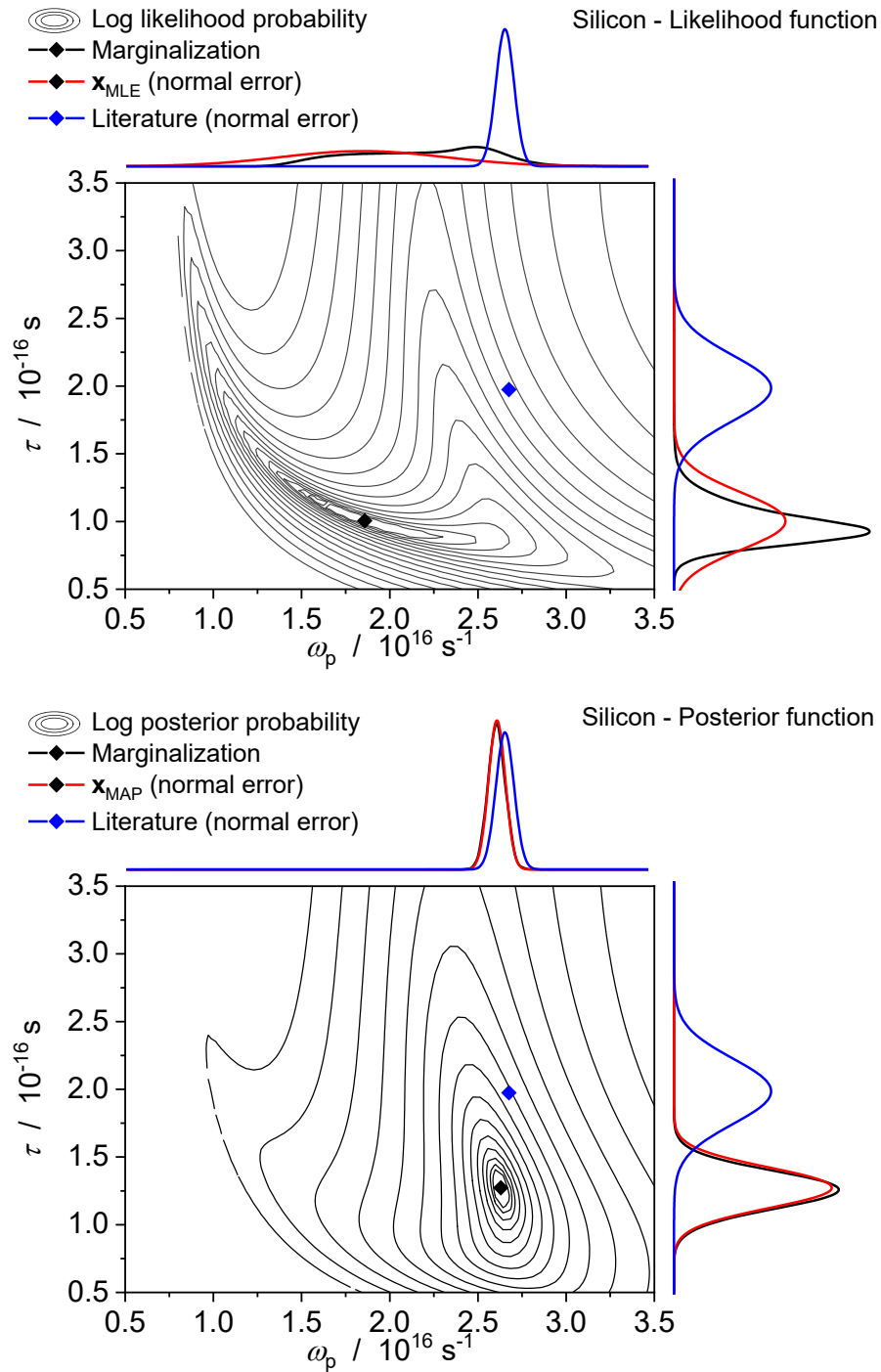


Figure 33: Inferred Drude parameters through Mie-theory for silicon.

For germanium (Figure 34), the plasmon frequency ω_p and the mean relaxation time τ do not match the literature values well but yield reasonable results when using normal priors of the literature values, with approximately $\pm 20\%$ in both parameters.

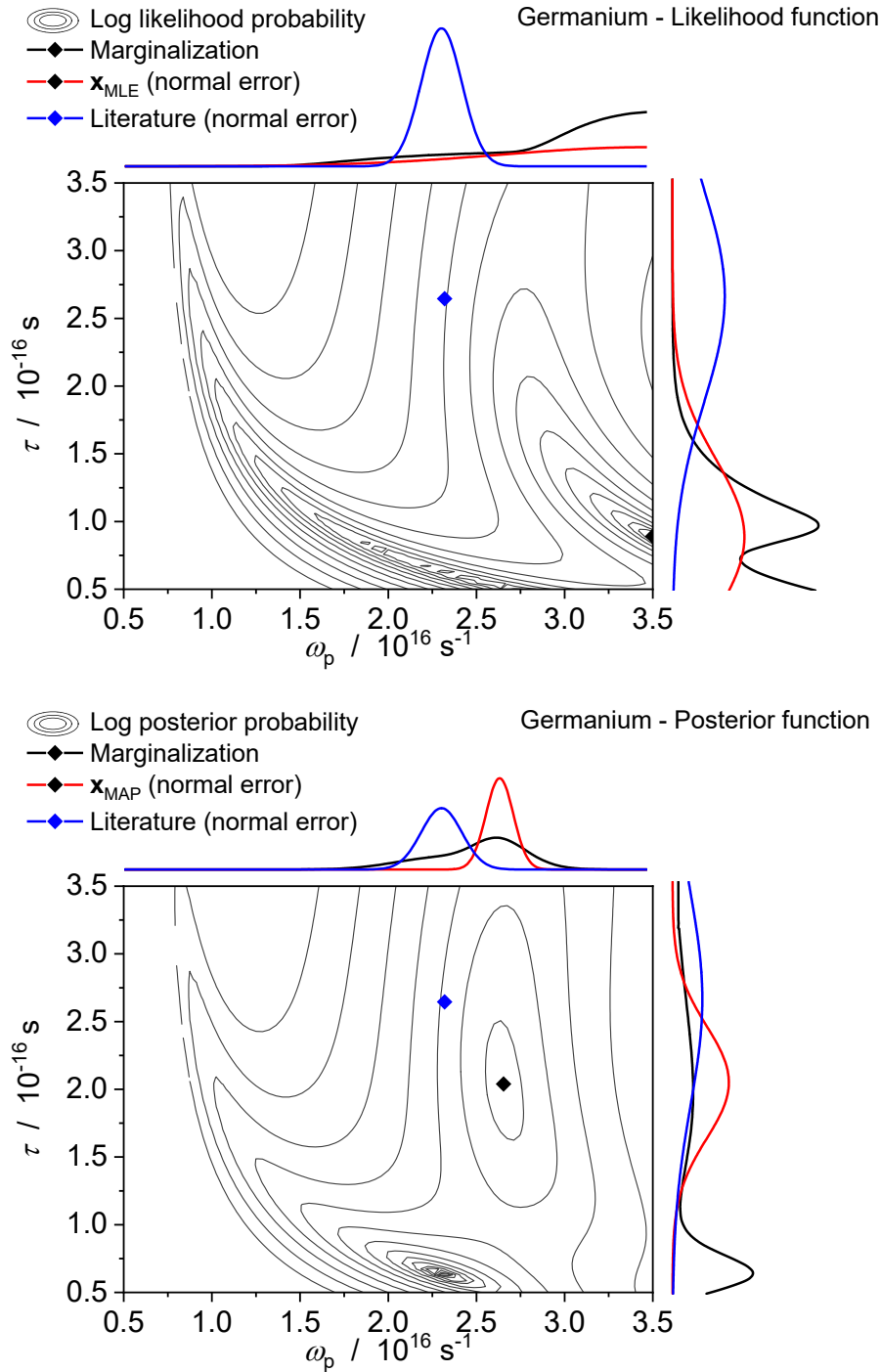


Figure 34: Inferred Drude parameters through Mie-theory for germanium.

5.5. Conclusions

As expected, the maximum *a posteriori* estimate shows smaller uncertainties than the corresponding literature values, but generally the literature values lie outside of the 90% credibility contours. To explain the discrepancy between parameters inferred in this study and those reported in the literature, the impact of the Drude parameters to the theoretical absorption or extinction efficiency is analyzed in Figure 35.

The plasmon frequency ω_p and the mean relaxation time τ are inferred by a least-squares fitting, which assumes a linearized model at the point estimate \mathbf{x}_{MLE} . When the applied model is highly non-linear \mathbf{x}_{MLE} will still be correct but the uncertainties can be biased. To check this, the likelihood function is sampled over a (sufficiently) large parameter range. Following Eq. (5.24), the necessary parameters are ω_p , τ , and C , while C is a nuisance parameter which incorporates the particle volume fraction, optics collection efficiency and other constants. During marginalization, the scaling factor C is integrated out, thus the correlation of the mean relaxation time τ with C is obfuscated.

These three parameters (ω_p , τ , C) are sampled from zero to three times of their maximum likelihood estimate in more than 500 steps each to gain a sufficiently smooth surface. The three-dimensional likelihood or posterior density is marginalized along the C -axis because it contains no necessary information for this work. Fortunately, the resulting marginalized probability density is two-dimensional, and so can easily be visualized.

The likelihood functions, shown in Figure 33 and Figure 34 (top; black lines), imply that the solution without prior information is considerably ill-posed. The maximum likelihood estimate (black symbol) for silicon and germanium lie in the center of the “valley” of the likelihood function, but along the valley no distinct point for the solution is clearly assignable.

To overcome the ill-posedness, reported literature values (blue lines and symbols) are incorporated as normal priors. The inferred maximum *a posteriori* estimates (MAP; red lines) and corresponding uncertainties are much closer to the literature values.

In Figure 31 and Figure 32 the spectra were superimposed with the Rayleigh or Mie solution, but with a wider spectral range from 200–800 nm, while the absorption spectra were measured at 380–750 nm and 410–700 nm for silicon and germanium, respectively. Obviously, the most sensitive spectral range for inferring ω_p and τ is in the near UV (from 200–400 nm). To assess the effect of varying optical parameters, the sensitivity of the Mie- and Rayleigh model in the applied spectral range is further analyzed. Figure 35 shows the differences of the extinction and absorption for a variety of plasmon frequencies and relaxation times (through the example of silicon). The spectra resulting from the literature values are located on the left, center part of the graphs. From there, moving to the right hand side, the plasmon frequency is iteratively doubled and tripled. The mean relaxation time is divided by two when moving upwards in the graphs and doubled when moving downwards. All these graphs show a distinct absorption peak which shifts upon changing the plasmon frequency. Lower values of ω_p shift the peak to longer wavelengths. With values of $\omega_{p,lit}/3 \approx 9 \times 10^{15}$ rad/s the peak shifts into the observation wavelength applied in this work above approximately 400 nm. Generally, for the selected spectral range, plasmon frequency and mean relaxation time need to be limited by prior information.

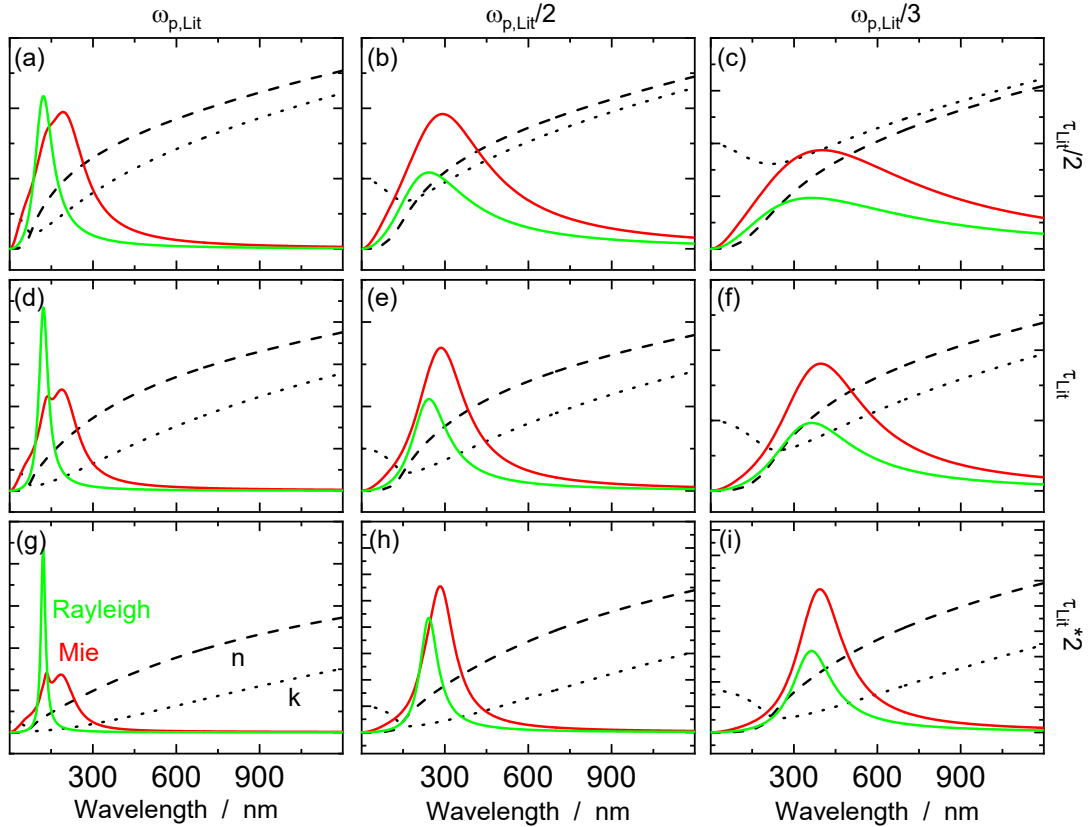


Figure 35: Expected absorption efficiencies for the Rayleigh and Mie solution when changing the plasmon frequency and the mean relaxation time. Additionally plotted is the real and imaginary part of the complex refractive index. The plasmon frequency is varied from left to right, first column literature values, second column divided by 2, and third column divided by 3. The mean relaxation time is also varied, first row literature value divided by 2, second row no division, third row doubled.

The applied spectroscopic model also has an impact on the appearance of the spectra: while the Rayleigh approximation only generates one distinct peak, Mie theory produces a more complex structure with—probably—more peaks, from which the additional ones are spectrally broader and displaced. For the Rayleigh approximation only the electric dipole contribution is used, while the Mie solution applies the multipole development. The dipole and quadrupole contributions of the scattering and extinction efficiency are given in Eq. (5.6) and (5.7). For these conditions (optical properties of molten silicon, nanoparticle size of 27 nm), the quadrupole contribution of the extinction efficiency is ten times smaller than the dipole contribution and the spectral positions of the dipole and quadrupole peak efficiency is similar. Consequentially, the quadrupole contribution is not the origin of the complex peak structure of the Mie solution under the given conditions. Because of the minor effect of the quadrupole contribution, it is not shown here.

In the wavelength range commonly encountered in laser-induced incandescence, the resulting spectra are nearly undistinguishable, which complicates the inference of Drude parameters and shows the ill-posedness of the problem, as already referenced in Chapter 3.3.

Due to the multipole development in Mie theory, more features are modeled, therefore this approach should, in general, lead to a more robust solution, when the particle diameter is known. However, the particle diameter is also a parameter of interest which may then also induce further uncertainties. For particles smaller than 40 nm, the influence of higher order multipoles is negligible and it can be reasonable to assume the expected diameter for the inference of ω_p and τ .

6. Particle sizing through laser-induced incandescence

“Measure what is measurable, and make measurable what is not so.”

– Galileo Galilei

This basic idea of this Chapter has been published in:

- J. Menser, K. Daun, T. Dreier, C. Schulz (2016).
“Laser-induced incandescence from laser-heated silicon nanoparticles.”
Applied Physics B 122(11): 277.
- J. Menser, K. Daun, T. Dreier, C. Schulz (2016).
“Validation of the evaporation model for LII/LIBS characterization of silicon nanoparticles.”
7th International Workshop and Meeting on Laser-Induced Incandescence
- J. Menser, K. Daun, T. Dreier, C. Schulz (2018).
“Transition from laser-induced incandescence (LII) to laser-induced breakdown (LIBS).”
8th International Workshop and Meeting on Laser-Induced Incandescence

This chapter lays a theoretical foundation for understanding laser-induced incandescence particle-temperature decays. Generally, LII needs two models for data evaluation: a spectroscopic model to infer the time-resolved particle temperature from the measured incandescence signal (chapter 5), and a heat-transfer model to calculate particle sizes and additional parameters from the particle-temperature decay (discussed in this chapter). The fundamentals for fitting models to the acquired measurement data have been already discussed in chapter 3, which focuses on Bayesian inference and the estimation of suitable credible intervals.

In this chapter the models itself and the *in situ* measurement of silicon and germanium nanoparticles within the gas are reviewed and discussed.

6.1. Heat and mass transfer model

The heat- and mass-transfer (HMT) model describes the heating of nanoparticles by laser pulses, and the subsequent cooling of nanoparticles through evaporation and conduction. These processes are governed by differential equations that can be solved for time-resolved particle temperatures, Eq. (6.1), and nanoparticle masses, Eq. (6.2). Figure 36 illustrates the energy- and heat-transfer processes involved in the principle of LII.

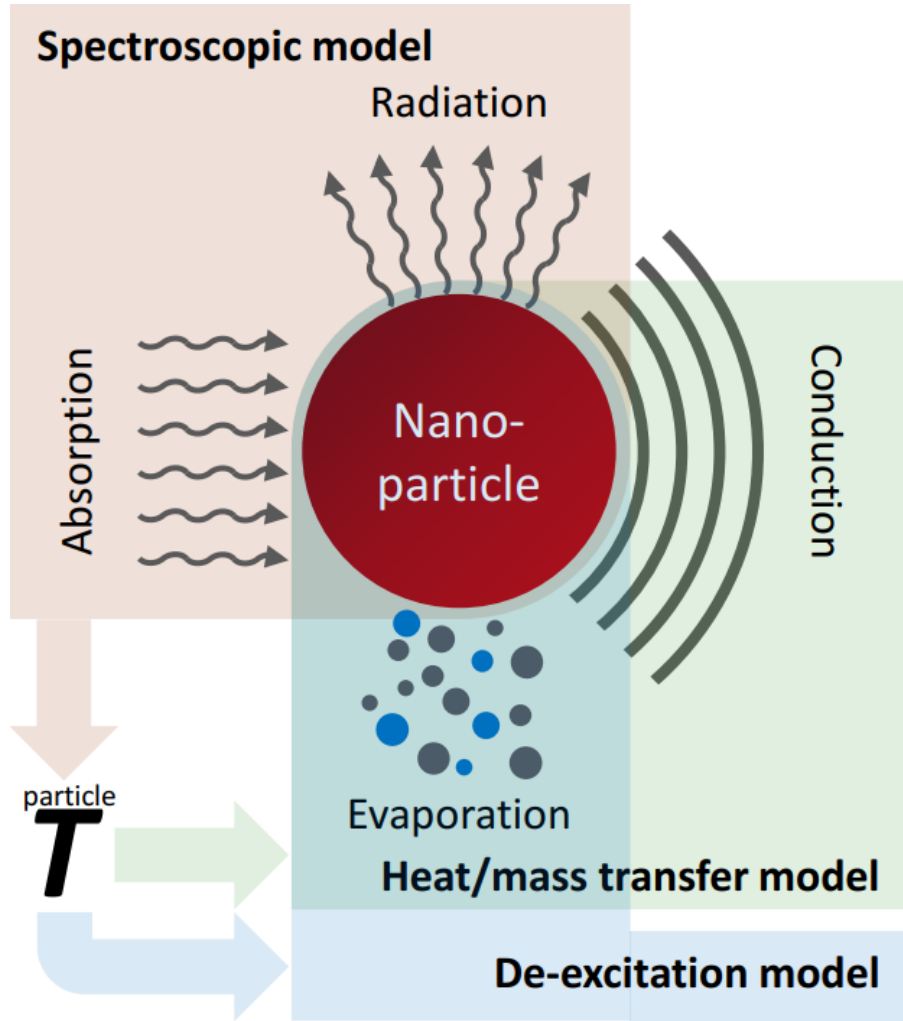


Figure 36: Principle of the LII heat- and mass-transfer model, illustrated by a single spherical nano-particle. In this work, three models are presented, the spectroscopic model, the heat-/mass-transfer model and an excited-atom deexcitation model. The graph illustrates the connection of these models.

The change in internal energy of a nanoparticle during an LII event is

$$\frac{dU}{dt} = mc_p \frac{dT}{dt} = \dot{Q}_{\text{int}} = \dot{Q}_{\text{abs}} + \dot{Q}_{\text{cond}} + \dot{Q}_{\text{evap}} + \dot{Q}_{\text{rad}} \quad (6.1)$$

with \dot{Q}_{abs} (in J/s) the absorbed laser energy by a nanoparticle, \dot{Q}_{cond} the energy dissipation by heat conduction, \dot{Q}_{evap} the energy dissipation by evaporative cooling, and \dot{Q}_{rad} energy loss by radiation.

Within the LII-community [32, 129], there is an ongoing debate, if the conversion from $dU/dt = mc_p dT/dt$ is correct, or if the complete partial differential should be taken into account. Here, the model by Daun et al. [130, 131] is taken because it shows a sufficient consistency over all observed fluences.

The mass balance is

$$\frac{dm}{dt} = -m_v \frac{\dot{Q}_{\text{evap}}}{\Delta H_v} \quad (6.2)$$

with m_v the molecular mass of the evaporated species, and ΔH_v the evaporation enthalpy.

The nanoparticle synthesis reactor utilized in this work was previously known to produce isolated spherical nanoparticles [59], and with this simplifies the models describing the optical properties as well as the heat transfer properties.

When the particle diameter is considerably smaller than the mean free path in the gas phase, the interacting gas molecules can effectively transport energy from the particle surface to the continuum without excessively heating the immediate particle environment.

The mean free path λ_g can be approximated by

$$\lambda_{g,S} = \frac{\mu}{p_g} \sqrt{\frac{\pi k_B T_g}{2 m_g}} \quad (6.3)$$

where the dynamic viscosity μ can, again, be approximated by the kinetic theory of ideal gases [132] and is valid up to 1600 K, and p_g the gas pressure. The temperature-dependent mean free path is

$$\lambda_{g,S} = \frac{\mu_0 T_{0,S} + \xi}{p_g T_g + \xi} \left(\frac{T_g}{T_{0,S}} \right)^{\frac{3}{2}} \sqrt{\frac{\pi k_B T_g}{2 m_g}} \quad (6.4)$$

with $T_{0,S} = 273.15$ K as reference temperature, $\xi = 165.0$ K the Sutherland constant for argon and $\mu_0 = 23.4 \times 10^{-6}$ Pa s as reference viscosity of argon [133].

Another definition of the mean free path is given by Loyalka [134], with

$$\lambda_{g,L} = \frac{4}{5} \frac{T_g}{p_g} \underbrace{\kappa(T_{0,L}) \left(\frac{T_g}{T_{0,L}} \right)^\omega}_{\kappa(T_g)} \sqrt{\frac{m_g}{2 k_B T_g}}. \quad (6.5)$$

This definition is based on the thermal conductivity which is expressed as an approximation with $\kappa(T_g) \approx \kappa(T_{0,L}) (T_g/T_{0,L})^\omega$, with the reference temperature $T_{0,L} = 298$ K, the reference thermal conductivity $\kappa(T_{0,L}) = 0.017$ W/(m K), and the viscosity coefficient $\omega = 0.81$ for argon as bath gas.

For the conditions of this work, the mean free path determined by Sutherland's formula is $\lambda_{g,S} > 5 \mu\text{m}$ and the mean free path by Loyalka's formula is $\lambda_{g,L} = 1.04 \mu\text{m}$; consequentially, heat transfer takes place in the free molecular regime.

In the free molecular regime the energy transfer from a nanoparticle surface is calculated

$$\dot{Q} = \pi d_p^2 N'' \Delta E = \pi d_p^2 \frac{n v_{th}}{4} \Delta E \quad (6.6)$$

where πd_p^2 is the effective cross-section of energy transfer, ΔE the energy transferred by each encounter, and N'' is the number flux of events in $\text{m}^{-2}\text{s}^{-1}$, which can further be separated into $nv_{th}/4$, where n is the number density and v_{th} is the mean thermal velocity of the main involved species. The mean thermal speed is calculated by $v_{th} = [8k_B T / (\pi m)]^{1/2}$, with T and m of the selected species.

Figure 37 shows the three main contributions of the heat transfer: heat conduction, evaporation, and radiation. The impact of each mode varies depending on the particle temperature, particle diameter, and gas environment. For temperatures slightly above the gas-phase temperature, heat conduction is the most prominent heat-transfer mode. For silicon the evaporation starts to dominate the heat transfer balance around 2500 K due to the exponential growth of vapor pressure with temperature. Radiative cooling is the least significant mode of cooling. In Figure 37 the net radiative cooling rate $\dot{Q}_{\text{rad,net}} = \dot{Q}_{\text{rad,cooling}} - \dot{Q}_{\text{rad,heating}}$ is shown.

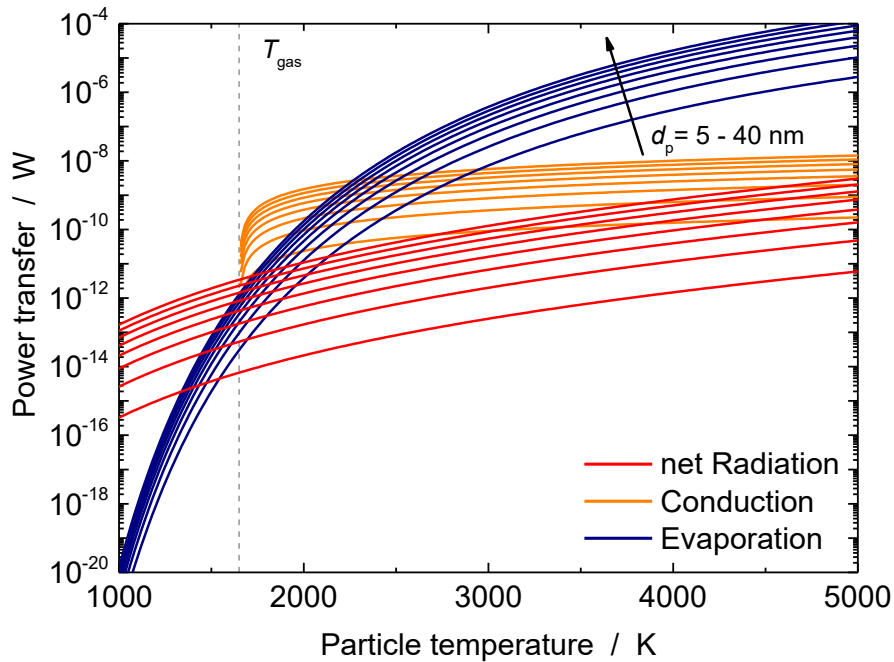


Figure 37: Illustration of heat transfer for conduction, evaporation, and radiation against the surface temperature for silicon particles of diameters between 5 and 40 nm in 5 nm intervals.

6.1.1. Laser absorption

Before the heating laser pulse, it is assumed that the particle temperature is in thermodynamic equilibrium with the surrounding gas phase. At the start of the laser pulse, the particles are heated from the gas phase temperature to the peak

temperature within a very short time span, usually 5–20 ns. The absorption term includes the absorption cross section C_{abs} and the temporally resolved laser fluence profile, $F_{\text{laser}}(t)$

$$\dot{Q}_{\text{abs}} = C_{\text{abs}} F_{\text{laser}}(t) \quad (6.7)$$

The temporal profile of the laser pulse is assumed to be Gaussian, which simplifies the modeling. The integral $\int_{-\infty}^{\infty} F_{\text{laser}}(t)dt$ is the absolute applied laser fluence. The absorption cross-section is calculated by the spectroscopic model presented in chapter 5.

In many publications concentrating on soot analysis, particle heating is not included in the model, due to uncertain optical properties of the measured species at the boiling temperature [37, 135]. Another problem is the large diversity of chemical composition and morphology, reaching from very small poly-aromatic hydrocarbons, over graphene(-oxides) flakes, different degrees of crystallization (graphite / amorphous, maturity), long-chained or compact particulate structures, and mixture of all.

6.1.2. Heat conduction

Heat conduction is important in the entire temperature range. It represents the energy transfer of the heated particles into the gas phase by collisions of gas molecules with the nanoparticle surface, according to

$$\dot{Q}_{\text{cond}} = \pi d_p^2 \frac{n_g v_{\text{th}}}{4} \alpha \langle E_0 - E_i \rangle_{\text{max}}, \quad (6.8)$$

where the number density $n_g = P_g/(k_B T)$ is defined by the ideal gas law, the thermal velocity of the surrounding gas is $v_{\text{th}} = [8k_B T_g/(\pi m_g)]^{1/2}$, m_g the molar weight of the colliding species, and $\langle E_0 - E_i \rangle$ is the mean energy transferred per collision, when a gas molecule scatters off the nanoparticle surface. The term can be rewritten by $\alpha \langle E_0 - E_i \rangle_{\text{max}}$ where $\langle E_0 - E_i \rangle_{\text{max}} = 2k_B(T_p - T_g)$ is the maximum energy transfer allowed by thermodynamics corrected with the thermal accommodation coefficient (TAC) α .

Of all the parameters in the spectroscopic- and heat-transfer models, α is subject to the greatest level of uncertainty. Its value is not accessible by other techniques than LII and molecular dynamics (MD) modeling. The best attempt to quantify α for LII measurements on silicon nanoparticles is by Sipkens et al. [38, 136], who found $\alpha = 0.35$ for Si in argon and $\alpha = 0.11$ for Si in helium through molecular dynamic calculations. Due to the absence of values for Si in hydrogen, helium was chosen as an alternative. Using this value, Sipkens et al. recovered nanoparticle size parameters from TiRe-LII data that were consistent with the Sauter mean diameter inferred from BET analysis [137].

The nanoparticle synthesis works with a gas mixture of argon and hydrogen, where consequently, the term $N''\alpha$ separates into $N''_{\text{Ar}}\alpha_{\text{Ar}} + N''_{\text{He}}\alpha_{\text{He}}$. N''_{Ar} and N''_{He} are given from the synthesis conditions. In the case of free-molecular heat conduction within a gas mixture, Eq. (6.8) can be written for each species, using the corresponding partial pressure and molecular mass to calculate the incident number flux of each gas phase species, and also a separate thermal accommodation coefficient for each species

$$\dot{Q}_{\text{cond}} = \pi d_p^2 \left(\frac{n_{\text{g,Ar}} v_{\text{th,Ar}}}{4} \alpha_{\text{Ar}} + \frac{n_{\text{g,H}_2} v_{\text{th,H}_2}}{4} \alpha_{\text{H}_2} \right) 2k_B(T_p - T_g), \quad (6.9)$$

with $n_{\text{g,sp.}}$, $v_{\text{th,sp.}}$ and $\alpha_{\text{sp.}}$ the respective densities, thermal velocities, and accommodation coefficients for each species. The atmosphere within the reactor used in this work consists of approximately 93% Ar and 7% H₂, depending on the operating conditions (chapter 4). The precursor (~ 0.3 Vol % SiH₄ or GeH₄) can be neglected in the heat-transfer analysis. Assuming that the bath-gas temperature is 1600 K, the corresponding incident number fluxes for Ar and H₂ are 9.54×10^{25} and 3.21×10^{25} molecules/(m²s), respectively. While the gas consists of 7% H₂, this species accounts for 25% of the gas–surface collisions, due to the higher molecular speed of H₂ molecules compared to the more massive Ar atoms. Since the reaction conditions are known, the accommodation coefficient can be summed to $\alpha_{\text{eff}} = 0.3$.

While helium and hydrogen (H₂) having the same proton and electron number, the chemical bonding (atom \leftrightarrow diatomic molecule), the mass ($m_{\text{H}_2} \approx 2$ u \leftrightarrow $m_{\text{He}} \approx 4$ u) and the heat capacity ($c_{v,\text{H}_2} \approx 12.5$ J/(mol K) \leftrightarrow $c_{v,\text{He}} \approx 20.4$ J/(mol K)) are considerably different, and accordingly one may anticipate that the TAC for Si/He may be different than that for Si/H₂. However, the low number density of H₂ will not strongly affect the resulting accommodation coefficient. For the sake of completeness $\alpha_{\text{eff}} = 0.26$ for $\alpha_{\text{H}_2} = 0$ and $\alpha_{\text{eff}} = 0.51$ for $\alpha_{\text{H}_2} = 1$.

The results presented by Sipkens et al. [38, 136] can be used to predict possible trends for the TAC of germanium in monoatomic gases. In Figure 38, the bath-gas dependent curves of the TACs of silicon, molybdenum, and graphite in monoatomic bath gases follow $\alpha \sim (m_{\text{gas}}/m_{\text{solid}})^{1/2}$, which can be utilized to estimate $\alpha_{\text{Ge/Ar}} \approx 0.2$ and $\alpha_{\text{Ge/He}} \approx 0.06$. Sipkens et al. applied molecular dynamics simulations to infer the energy transfer from the nanoparticle surface to the interacting gas-phase species. The values are evaluated for monoatomic gases such like argon, neon and helium.

The derived thermal accommodation coefficient, α , is influenced by the reduced mass $\mu = m_g/m_s$, where m_s is the atomic mass of the particle surface material and m_g is the atomic mass of the interacting gas. No characteristic function has been published, so far. The estimated accommodation coefficients for germanium are only used as an initial guess during least squares fitting, and will not affect the result at all.

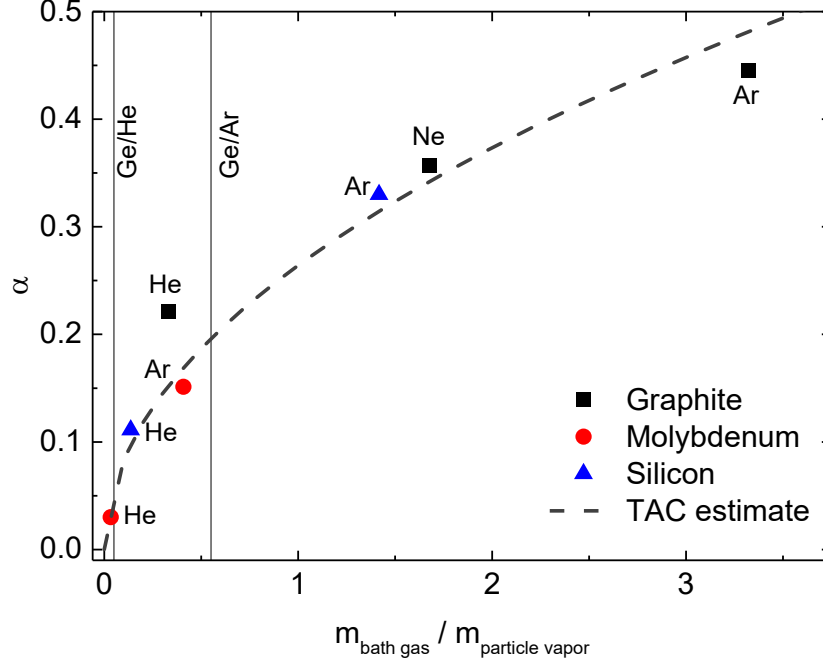


Figure 38: TACs for graphite, molybdenum, and silicon. The overall trend is shown with a square-root dependence, which allows for a rough estimate of the TACs for germanium [38, 136].

6.1.3. Evaporation

The evaporative heat transfer rate is given by [35, 38, 136, 137]

$$\dot{Q}_{\text{evap}} = \pi d_p^2 N_v'' \Delta H_v = \pi d_p^2 \frac{n_v v_{\text{th}}}{4} \Delta H_v, \quad (6.10)$$

where N_v'' is the number flux of evaporated molecules above the nanoparticle surface, the number density n_v and the mean thermal speed v_{th} , ΔH_v is the latent heat of vaporization, and m_v is the molecular mass of the evaporating species. Equation (6.10) neglects recondensation of evaporated species, which is reasonable given the large surface energy of the laser-heated nanoparticles relative to the potential well depth between the atoms and the nanoparticle surface.

For a bulk material, the vapor pressure is related to the latent heat of vaporization or evaporation enthalpy through the Clausius–Clapeyron equation,

$$\frac{dp_v}{dT} = \frac{\Delta H_v}{\Delta V_v T_v} \quad (6.11)$$

where p_v is the saturation vapor pressure and $\Delta V_v = V_{\text{vapor}} - V_{\text{liquid}}$ is the difference of the molar volume of the vapor and liquid. With $V_{\text{liquid}} \ll V_{\text{vapor}}$ one can approximate $\Delta V_v \approx V_{\text{vapor}}$, which results in the following approximation of the Clausius–Clapeyron equation

$$p_v^0 = A \exp\left(-\frac{\Delta H_v}{k_B T_p}\right). \quad (6.12)$$

This equation assumes phase equilibrium between the liquid and the vapor on either side of the phase interface. The constant $A = p_{\text{ref}} \exp[\Delta H_v / (k_B T_{\text{ref}})]$ consists of two integration constants p_{ref} and T_{ref} .

In this work, the Antoine equation was applied. On the one hand, the Antoine equation has the advantage that many publications directly provide the required parameters, and on the other hand it enables a better fit to measured vapor pressures due to an additional fitting parameter. In literature, an even more precise equation, the DIPPR101 [138], is reported that uses four free parameters and generates a ten times better quality of fit for the saturation vapor pressure of water compared to the Clausius–Clapeyron equation. Here, the vapor pressure is reported in base-10 logarithm according to Antoine’s equation

$$\log_{10}(p_v^0) = \frac{C_1}{T + C_3} + C_2 \quad (6.13)$$

with p_v^0 in units of Pascal, $\Delta H_v = C_1 \ln(10)$ and $A = \exp[C_2 \ln(10)]$. In most cases, C_3 is close to zero and will be kept out of the inference process.

Priors for C_1 and C_2 are derived from values for these parameters reported in the literature, e.g., Refs. [139-142]. Specifically, Gaussian prior densities for C_1 and C_2 are prescribed, centered on the parameters recommended by Sevast’yanov et al. [143] with standard deviations equating to 2.5% of the mean values (corresponding to a standard error of $\pm 5\%$), based on experimental uncertainties reported by Tomooka et al. [139].

For liquid silicon Sevast’yanov et al. recommend $C_1 = -20,567$ K and $C_2 = 10.94$ and observe that the vapor almost entirely consists of atomic silicon over the temperatures important to LII. This value of C_1 corresponds to a latent heat of vaporization of 6.53×10^{-19} J/molecule, or 389 kJ/mol. Table 6 shows that these values are consistent with tabulated vapor pressure data presented by Desai [142], and coefficients reported by Tomooka et al. [139], inferred from Knudsen effusion-cell experiments. While Sevast’yanov’s paper does not directly provide uncertainties for their recommended C_1 and C_2 values, Tomooka et al. report approximately 5% uncertainties on their experimentally-derived C_1 and C_2 values [139], which will be adopted for an uncertainty analysis.

The Antoine coefficients for germanium were published by Stevanovic[144], Severin[145] and Honig [146]. The provide values are consistent with around $C_1 \approx -17,000$ K and $C_2 \approx 10.6$. Within this list only Severin et al. provided the uncertainty with their measurements with $\pm 1.4\%$ for C_1 and C_2 . For this work the values of $C_1 = -17,300$ K $\pm 5\%$ and $C_2 = 10.6 \pm 5\%$ are utilized, which corresponds fairly well with the variation of literature values. The uncertainty of $\pm 5\%$ was chosen to reflect the variation within the set of parameters.

Table 6: Antoine parameters reported in literature of silicon and germanium.

	C_1 / K	C_2	Validity T range / K	Ref.	Year - Technique
Si	-26,580 ± 602	14.25 ± 0.31	1770–2035	Lopatin [140]	2012 - Knudsen cell
Si	-20,567	10.94	1700–3400	Sevast'yanov [141]	2010 - literature review
Si	-20,800 ± 1,000	10.84 ± 0.53	2150–2320	Tomooka [139]	1998 - Knudsen cell
Si	-20,370	10.8	1948	Desai [142]	1985 - Knudsen cell
Si	-20,635	11.14	1700–2500	Stevanovic [144]	1984 - Thermodynamics
Ge	-17,547	10.72	1700–2500	Stevanovic [144]	1984 - Thermodynamics
Ge	-18,570	6.116	1608–1885	Searcy [147]	1955 - Torsion methode
Ge	-17,410 ± 230	10.83 ± 0.16	1134–1647	Severin [145]	1991 - Knudsen cell
Ge	-13,294	9.64	1370–2830	Stull [148]	1972
Ge	-12,590	7.98	1300–2200	Lamoreaux [146]	1983 - Thermodynamics
Ge	-15,996	10.12	1100–3100	Honig [149]	1969 - Crucible

The equations used to model evaporation, e.g., Eq. (6.13) assume a flat surface topography. For nanoparticles, the local surface curvature is important, and modifies the surface energy. The Kelvin equation [150, 151] accounts for the increased surface energy

$$p_v = p_v^0 \exp \left[\frac{4\gamma(T_p)}{d_p \rho(T_p) RT_p} \right] = B \exp \left[-\frac{1}{k_B T_p} \left(\Delta H_v - \frac{4\gamma}{nd_p} \right) \right], \quad (6.14)$$

where B is a parameter with all constants, the surface tension γ is taken from Ref. [140, 152, 153] and n is the number density of the liquid silicon or germanium. The temperature-dependent surface tension of silicon and germanium reported by Aqra et al. [153] are $\gamma_{Si}(T_p) = 876 - 0.32(T_p - 1687 \text{ K})$ (mJ m⁻²) and $\gamma_{Ge}(T_p) = 571 - 0.074(T_p - 1210.25 \text{ K})$ (mJ m⁻²).

At the particle sizes investigated here, the change of vapor pressure for temperatures up to 5000 K the Kelvin equation only elevates the vapor pressure by approx. 1%,

and is consequentially much smaller than the uncertainty of the vapor pressure. For further evaluation, the vapor pressure elevation by the Kelvin effect will be neglected.

6.1.4. Radiation

Finally, radiative cooling is given by

$$\dot{Q}_{\text{rad}} = \int_0^{\infty} \pi^2 d_p Q_{\text{abs}}(d_p, \lambda) I_b(\lambda, T_p) d\lambda. \quad (6.15)$$

The emission efficiency equals the absorption efficiency according to Kirchhoff's law, as described in Chapter 5. Michelsen et al.[129] summarize the common approximations to the integral form in Eq. (6.15).

One approach using the Rayleigh approximation and solving the integral yields [154]

$$\dot{Q}_{\text{rad}} = 199\pi^3 d_p^3 (k_B T_p)^5 h^{-4} c^{-3} E(\mathbf{m}). \quad (6.16)$$

The emitted power follows the fifth power of the particle temperature without further subtracting the gas-phase temperature.

Another discussed radiation term under the assumption of a perfect black body absorption is given by Melton et al. [155]

$$\dot{Q}_{\text{rad}} = \pi d_p^2 \sigma_{\text{SB}} (T_p^4 - T_g^4), \quad (6.17)$$

where the Stefan-Boltzmann constant is $\sigma_{\text{SB}} = 5.679 \times 10^{-8} \text{ Wm}^{-2}\text{K}^{-4}$. At $T_p = T_g$ the nanoparticles in the measurement volume absorb the same intensity, which they emit, and therefore no cooling occurs.

Figure 37 reveals, that the radiative heat transfer, incorporated by Eq. (6.15), is at least three orders of magnitude lower than the other described heat transfer mechanisms. Due to the minor effect of radiation, it will not further be considered in the applied heat transfer model.

6.2. Time-resolved particle temperature

Because nanoparticles absorb and emit thermal radiation, the spectroscopic model can be used to infer nanoparticle temperatures as well as the unknown constant C_k in Eq. (5.12). Time-resolved spectral measurements carried out with the streak camera can therefore be used to determine the temporal variation in particle temperature even during evaporative conditions. For this purpose, the streak camera spectral range is set to 425–700 nm, with an equivalent pixel width of 0.4 nm; this range should include the peak incandescence for particle temperatures greater than 2900 K and is therefore well-suited for pyrometry.

The time-resolved particle temperature was inferred by the same technique described in Appendix C. In contrast to a numerical experiment, the

Poisson/Gaussian noise distribution is not known in advance. Here, the standard deviation was inferred by a two-fold cross-validation approach. Due to the assumption of uncorrelated noise, two alternating image lines with almost same intensity can be used to assess the standard deviation of the opposite line. If the cross-validation was not applicable the zero-centered probability distribution is calculated by subtracting the smoothed spectrum from the raw spectrum.

The laser fluence directly influences the maximum temperature reached during the LII experiment (Chapter 6.3). For example, in Figure 39 a temperature trace of heated silicon nanoparticles with a laser fluence of $F_{0,\text{Si}} = 8 \text{ mJ/mm}^2$ is shown. This fluence was chosen because at this value the peak temperature crosses the evaporation temperature. This leads to a maximum LII intensity without significantly reducing the initial particle size due to evaporation during laser heating. Germanium already reaches the “plateau” regime at 2 mJ/mm^2 . Additionally, Figure 39 shows the constant C_k as a function of time, discussed later.

Since the streak-camera images contain approximately 350,000 pixels, a direct “all at once” regression between simulated and measured images is prohibitively time-consuming. Instead, $[C_k, T_p(t_k)]$ are estimated at each measurement time by regressing Eq. (5.12) to the k^{th} row of pixels. While one would expect C_k to be constant over the entire image, Figure 39 shows that this parameter initially drops abruptly just after reaching the peak temperature and then approaches a constant value. This problem is discussed in Section 6.4.

The right graph in Figure 40 shows the fit between the extracted experimental spectral profiles from the streak-camera image (left panel) and simulated incandescence spectra at 0 (peak incandescence), 50, and 100 ns. Even though the experimental spectra show considerable noise, the simulated profiles closely match the experimental ones in all cases, even at the peak incandescence.

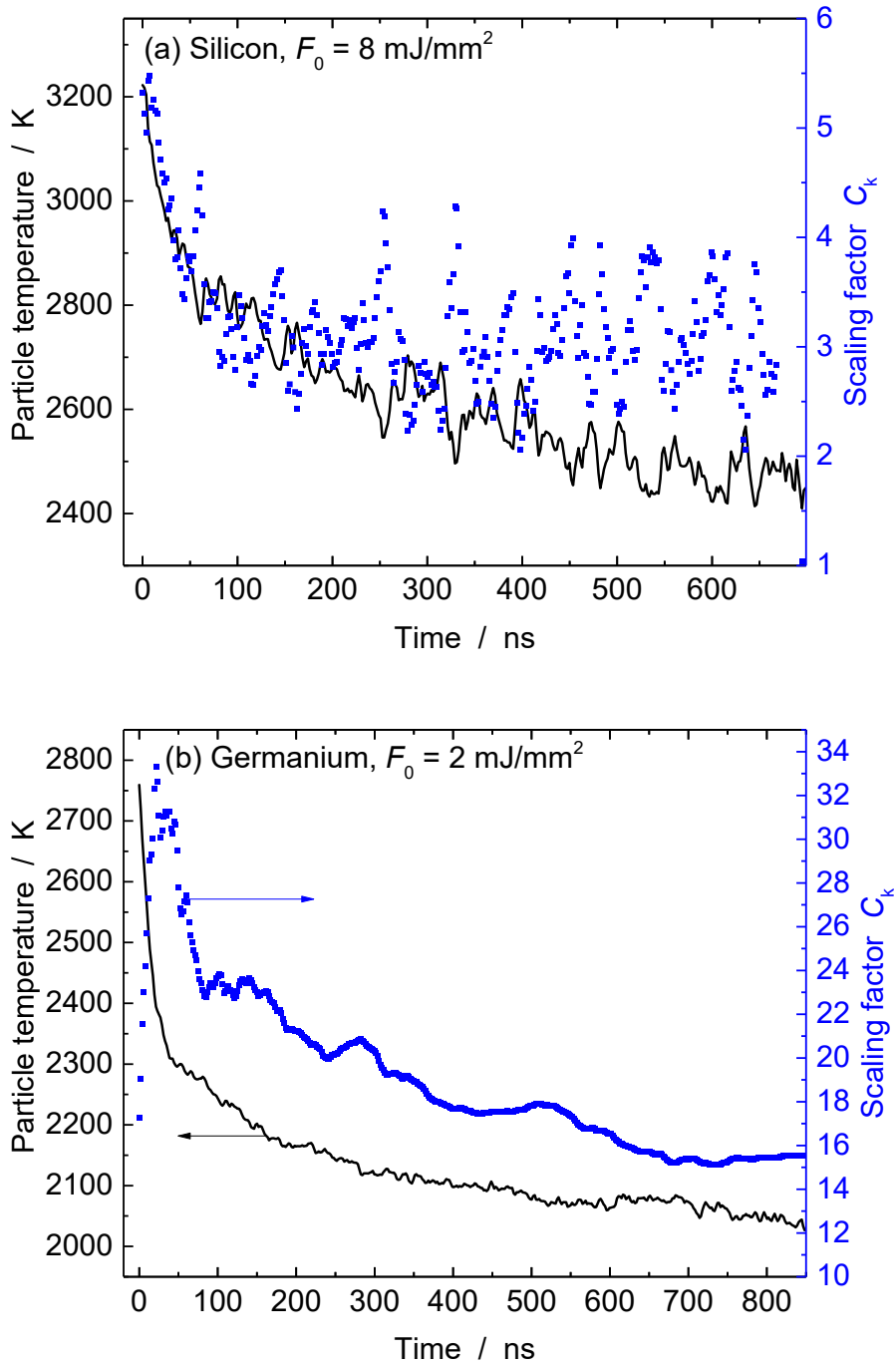


Figure 39: Streak camera pyrometry. The time axis is adjusted to the peak incandescence at 500 nm. Estimates for $T_{p,k}$ and C_k are found by fitting Eq. (5.12) to each row of pixels (spectrum k) corresponding to time step t_k . Variation in C_k with time (right y-axis) and the particle temperature (left y-axis). a: Temperature trace for silicon and b: for germanium

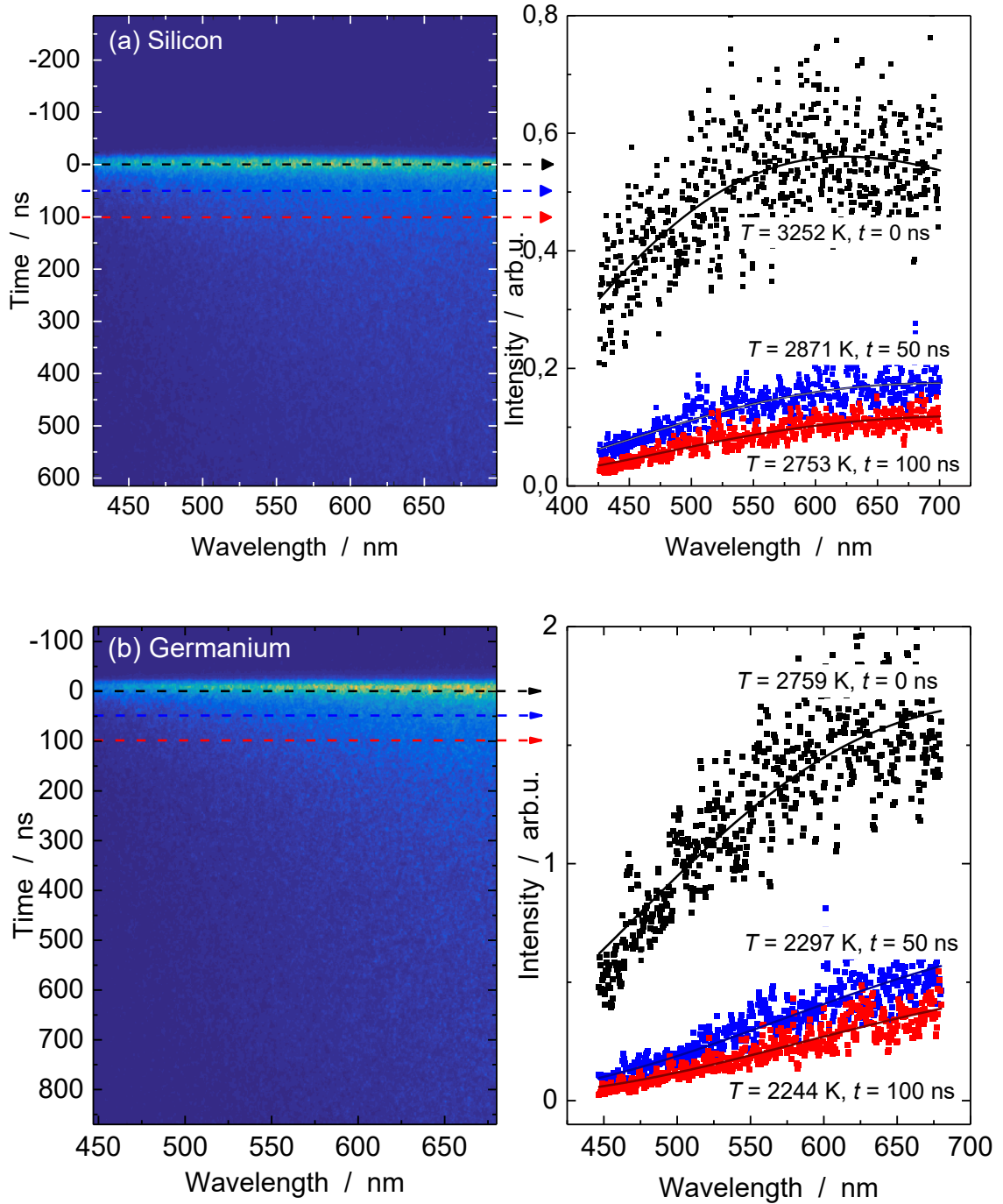


Figure 40: Results of the time-resolved pyrometry measurements with the streak-camera. The plot on the right shows the fits (solid lines) of the measured incandescence spectra (symbols; rows on the streak image (left panel) marked with dashed lines) using Eq. (5.12). Measurement times (0, 50 and 100 ns after the laser pulse) correspond to those shown on Figure 41. a: Measurements of silicon for $F_0 = 8 \text{ mJ/mm}^2$ and b: Measurements of germanium for $F_0 = 2 \text{ mJ/mm}^2$

6.3. Analysis of peak temperatures

The heat-transfer model, Eq. (6.1) is able to describe the temporal variation of the particle temperature including laser-induced heating. As noted above, the influence of the streak-camera instrument function on the signal is most pronounced near the peak temperature, where the temporal variation of J_λ is highest. Accordingly, the measured and simulated temperatures at $t = 0$ ns (peak streak image incandescence/simulated temperature), as well as 50 and 100 ns after the peak (*cf.*, Figure 40) are compared to the model predictions at these particular times. Figure 41 shows that the pyrometric temperature tracks the peak temperature well. All of these temperatures increase linearly with the laser fluence until the boiling point of the examined species is approximately reached—silicon: 8 mJ/mm² and germanium: 2 mJ/mm². At higher temperatures, T_p increases more slowly with increasing F_0 . Beyond this point, a larger fraction of the laser pulse energy is lost through evaporation.

The transition from a linear to non-linear increase of $T_{p,\max}$ with F_0 occurs close to the boiling temperature of the observed materials. At temperatures below the boiling temperature, the peak nanoparticle temperature is determined largely by equating the change in sensible energy, left-hand-side of Eq. (6.1), to q_{laser} , thus $T_{p,\max}$ increases linearly with F_0 . At higher temperatures, an increasing fraction of the laser heating is lost to q_{evap} , *cf.* Chapter 6.1.3, which reduces $dT_{p,\max}/dF_0$. The nanoparticle temperatures exceed the boiling point of the material because the laser heating rate exceeds the evaporation rate, which is limited by the fraction of silicon atoms having energies that exceed the cohesive energy of the liquid state, $\propto \exp[-\Delta H_v/(k_B T_p)]$. Consequently, the excess laser heating increases the sensible energy of the nanoparticle that causes superheating.

This behavior is discussed in more detail in [156]. A non-dimensional fluence and temperature was introduced to reveal the effect of evaporation in a more comprehensive way to derive a general formula for estimating peak temperatures reached during laser-induced heating.

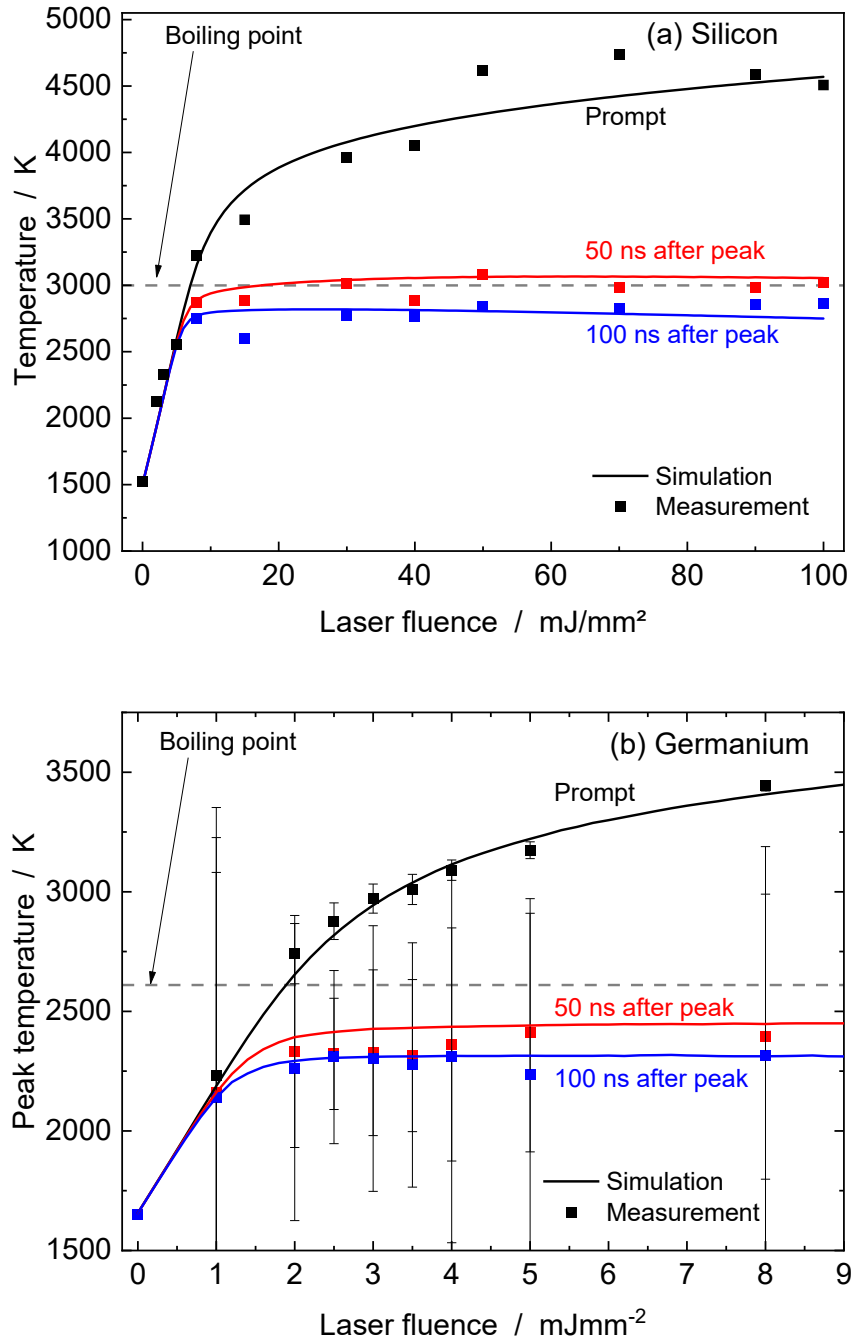


Figure 41: Simulated particle temperatures (lines) and pyrometrically-measured values (symbols) as a function of laser fluence F_0 . The dashed lines shows the boiling point of silicon and germanium at 100 mbar [143]. The maximum temperature increases linearly with fluence below 8 mJ/mm²/3000 K for silicon (a) and 2 mJ/mm²/2600 K for germanium (b).

6.4. Variation of the scaling factor, C_k

The scaling factor, C_k , in Eq. (5.12) relates the measured signal intensity to the incandescence from the nanoparticles in a specific measurement situation, and accounts for factors that include the nanoparticle volume fraction, the signal collection efficiency, and the photoelectric efficiency of the detectors. The laser fluence is not included in the scaling factor, because it should only have an impact on the nanoparticle temperature that is scaled properly by Planck's law. Intriguingly, however, Figure 39 shows that the scaling factor C_k is largest close to the laser pulse/peak temperature and then decays to a near constant value over approximately 50 to 200 ns.

When the fluence, F_0 , is increased to the point at which the peak temperature reaches the boiling point of the nanomaterial, the scaling factor C_k at the laser pulse is approximately two times larger compared to the scaling factor of the unheated particles and subsequently, it decays to lower values.

The increase of the scaling factor can be analyzed through the utilization of dimensionless fluence and dimensionless scaling factor, defined through

$$\underline{F} = \frac{F_0}{F_{\text{boil}}} \quad (6.18)$$

$$\underline{C} = \frac{C_k}{C_{k,\text{boil}}} \quad (6.19)$$

where F_0 is the laser fluence, F_{boil} is the laser fluence, which was applied when the nanoparticles exactly reach the boiling temperature, C_k is the inferred scaling factor and $C_{k,\text{boil}}$ is the inferred scaling factor, when reaching the boiling temperature.

When looking at moderate fluence regimes at approximately $\underline{F} = 1$, both materials show a linear behavior in $\underline{C}(\underline{F})$. For fluences from 0 to 4 \underline{F} , the scaling factor enhancement scales linearly with the fluence, *cf.* Figure 42.

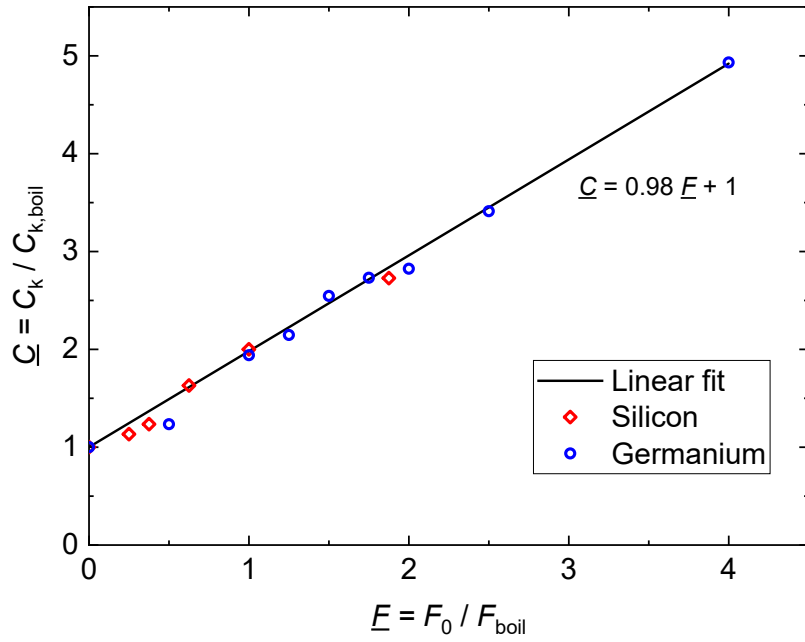


Figure 42: Development of the dimensionless scaling factor \bar{C} with different fluences, for silicon (red symbols) and germanium (blue symbols). A straight line was added to guide the eye.

Through the introduction of a dimensionless fluence and a scaling factor, a common trend could be observed. For silicon and germanium, \bar{C} scales linearly with the same slope and intercept with

$$\bar{C} = 1 + 0.98 \bar{E} \quad (6.20)$$

The traces of the dimensionless scaling factors for silicon and germanium collapse onto a single line, which can be described through a linear connection. The temporal development of the scaling factor is further analyzed by Sipkens et al. [156, 157]

Further measurements of silicon at fluences ranging from 15 to 100 mJ/mm² → 2 to 12.5 \bar{E} reveal a rather complex fluence dependence: Between 5 and 30 mJ/mm², a fast descending C_k after the laser pulse was measured, and above 30 mJ/mm², an ascending C_k after the laser pulse was measured.

The most obvious explanation for a descending C_k after the laser pulse at high fluences is due to an evaporation-induced decrease of the particle volume fraction. According to the evaporation model, at 8 mJ/mm² for silicon and 2 mJ/mm² for germanium, both shown in Figure 39, the evaporation of the nanomaterial is approximately 5% of the particle mass, which should correspond to a 5% decrease of the scaling factor during the evaporation phase, while we observe a reduction in C_k of almost 50%. Therefore, this phenomenon cannot be explained by evaporation alone.

Additional signal contributions from non-thermal origin (anomalous cooling, enhanced absorption, Bremsstrahlung [94, 158]) can potentially impact the signal

level during and shortly after the laser pulse. Variations in C_k with fluence could be the evidence for the formation of microplasmas surrounding the nanoparticles, and additional heating through inverse Bremsstrahlung due to the strong coupling of the laser and the plasma. One would expect that Bremsstrahlung from the plasma would contribute to the observed signal (incandescence plus Bremsstrahlung), and thus equate to a hypothetical aerosol having a larger nanoparticle volume fraction (and larger C_k) [94, 136]. In contrast to the integrated thermal particle radiation ($I_{\text{thermal,total}} \sim \sigma T_p^4$ for a flat surface), Bremsstrahlung scales with $I_{\text{Bremsstrahlung}} \sim T_e^{1/2}$ [159] to the electron temperature.

The increasing scaling factor after the laser pulse can perhaps be attributed to the instrument response function of the detection system, which results in a temporal blurring of the measured intensities. The finite instrument response function has the largest effect in cases of rapid temporal signal intensity variations at high laser fluences around the laser pulse/peak temperature. Quantifying the influence of the temporal response of the streak camera/spectrometer unit was done by Sipkens et al. [160] with the outcome that the non-linear signal increase with temperature is biasing the derived mean temperature to higher values. At lower temperatures the overall intensity decreases, which results in an underestimation of the scaling factor for the mean intensity. For this work, a reduction of the scaling factor C_k at the laser pulse was due to blurring of the intensity profiles by an instrument function at the peak temperature for the high-fluence regime. This indicates that the temporal resolution of the detector is too low at these fluences. A higher temporal resolution yields an almost constant C_k after the laser pulse but is not suitable for LII analysis.

So far, it is not fully clarified which of the potential non-thermal effects cause this behavior. The possible formation of a microplasma enveloping the nanoparticle during laser heating, and its influence on the detected LII signal, is the focus of ongoing research.

6.5. Particle sizing through Bayesian inference

An estimate of the measurement noise contaminating the pyrometric temperatures is needed to quantify the likelihood, presented in chapter 3.1

$$p(\mathbf{T}|\mathbf{x},\boldsymbol{\theta}) \propto \exp\left\{-\sum_{j=1}^{Nt} \frac{[T_{p,j} - T_p(\mathbf{x},\boldsymbol{\theta},t_j)]^2}{2\sigma_{T,j}^2}\right\}, \quad (3.5)$$

While the measurement noise can, in principle, be found from the variance of temperatures inferred from n independent streak images, instead $\sigma_{T,j}$ is estimated from the residuals between the pyrometrically-inferred temperatures and a smooth interpolating curve. The residuals are approximately equal in magnitude at all measurement times, and obey a normal distribution with a standard deviation of ~ 100 K.

The nanoparticle diameter and thermal accommodation coefficient are inferred from an LII measurement made using a laser fluence of 8 mJ/mm² with silicon (Figure 43a) and 2 mJ/mm² with germanium (Figure 43b). Figure 43 shows the pyrometric data, the modeled data corresponding to the *a posteriori* estimate, as well as the probability density contours, $p(\mathbf{x} | \mathbf{T})$, and marginalized probabilities for d_p and α . The results show the MLE estimate:

- Silicon: $\mathbf{x}_{\text{MAP}} = [25.6 \text{ nm}, 0.195]$,
with 90% credibility intervals $d_{p,90\%} = [0 \text{ nm}, 43 \text{ nm}]$ and $\alpha_{90\%} = [0, 0.35]$.
- Germanium: $\mathbf{x}_{\text{MAP}} = [49.4 \text{ nm}, 0.42]$,
with 90% credibility intervals $d_{p,90\%} = [0 \text{ nm}, 100 \text{ nm}]$ and $\alpha_{90\%} = [0, 0.9]$.

These credibility intervals can be interpreted to mean that the “true” values lie within the corresponding interval with 90% probability, in view of the noisy temperature and uncertainties in the evaporation model. These ambiguous results are not surprising, given that nanoparticle cooling is dominated by evaporation heat transfer (*cf.* Figure 37) over the recorded temperature range. The wide credibility intervals for d_p are due to uncertainty in the evaporation model, although this interval contains the primary particle sizes inferred from the TEM analysis, shown in Figure 10.

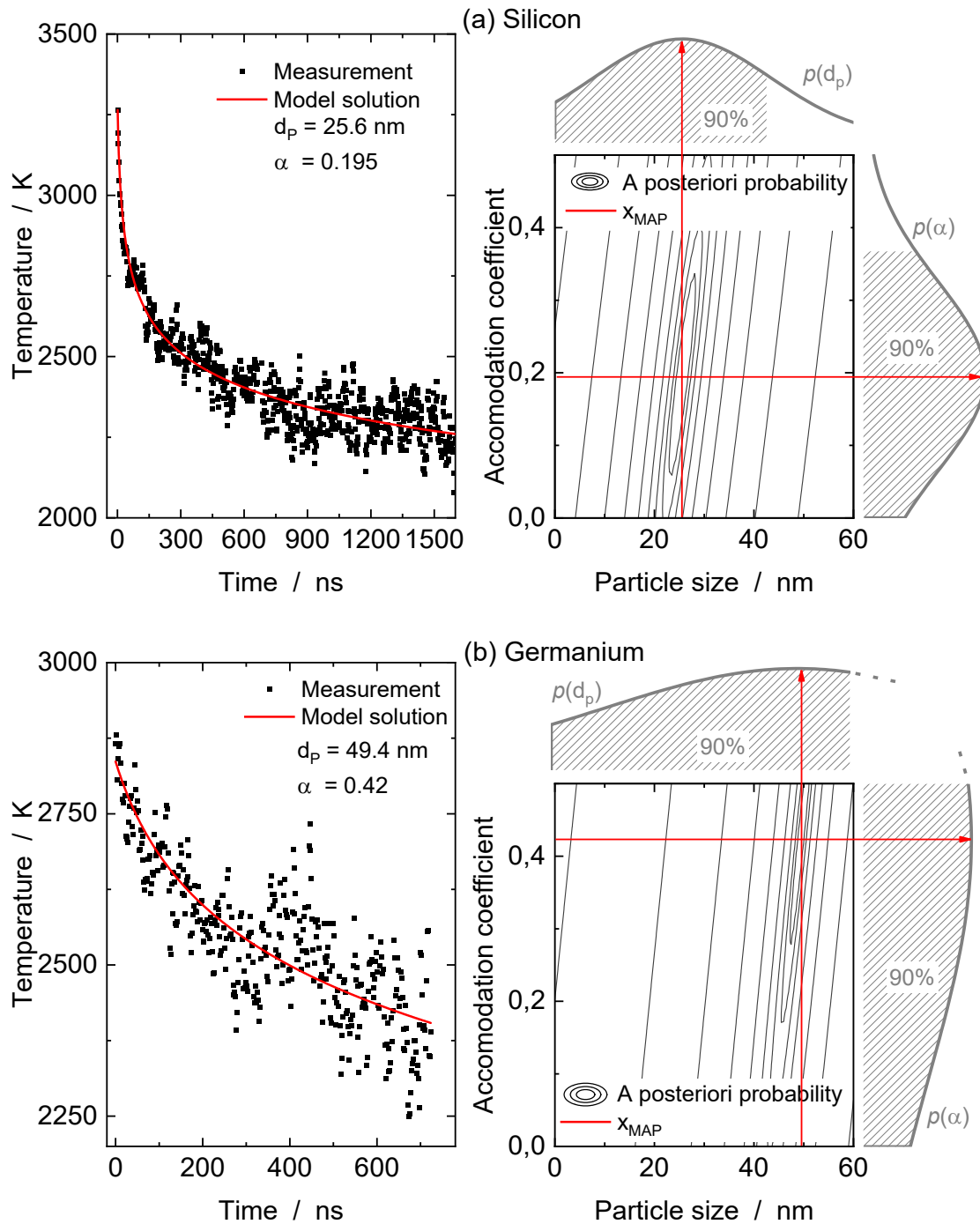


Figure 43: Results of the Bayesian inference of d_p and α , for a: Silicon with a fluence of 8 mJ/mm² and for b: Germanium with a fluence of 2 mJ/mm² using pyrometric temperatures starting from 15 ns after the peak incandescence. Contours denote marginalized posterior probabilities, plotted on a log scale. An analysis of a streak image gives a robust estimate of d_p and α .

Figure 44 shows the likelihood and credibility intervals obtained assuming fixed values for C_1 and C_2 . This results in much narrower *a posteriori* densities for d_p and α , but this treatment does not reflect the true state of knowledge in the evaporation model, as indicated by Table 6. Consequently, neglecting this uncertainty would lead

one to have more confidence in the recovered parameters than can be justified based on uncertainty in the evaporation model. The inferred values are:

- Silicon: $\mathbf{x}_{\text{MLE}} = [25.5 \text{ nm}, 0.15]$,
with 90% credibility intervals $d_{p,90\%} = [21 \text{ nm}, 28 \text{ nm}]$ and $\alpha_{90\%} = [0, 0.26]$.
- Germanium: $\mathbf{x}_{\text{MLE}} = [54.1 \text{ nm}, 0.43]$,
with 90% credibility intervals $d_{p,90\%} = [50 \text{ nm}, 57 \text{ nm}]$ and $\alpha_{90\%} = [0.24, 0.62]$.

It needs to be noted, that the \mathbf{x}_{MAP} , which accounts for the uncertainty in the evaporation parameters and the \mathbf{x}_{MLE} , which considers the evaporation parameters as perfectly-known, fit very well, which point out a good agreement of measurement and literature values of C_1 and C_2 .

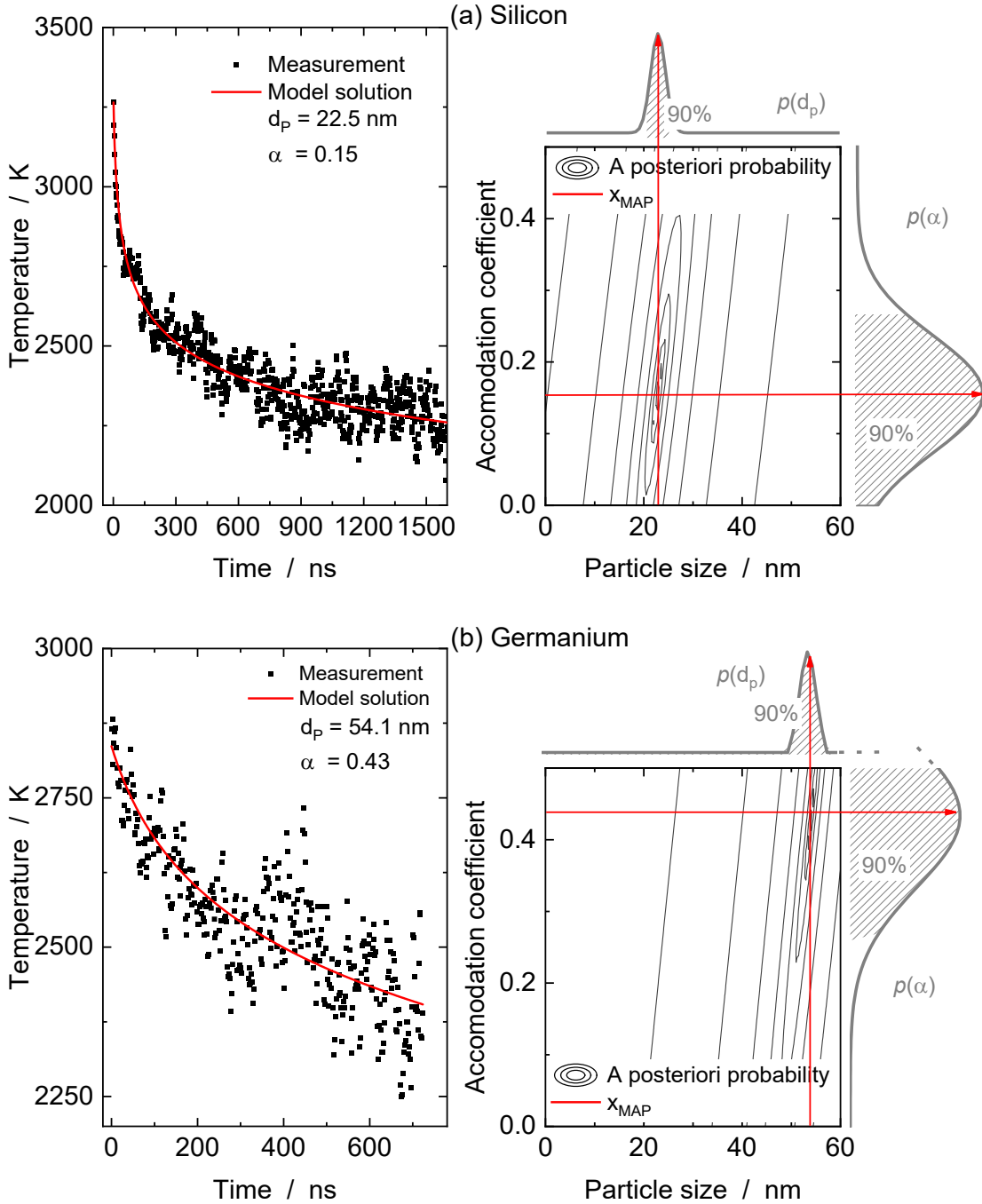


Figure 44: Results of the Bayesian inference of d_p and a , compared to Figure 43 with fixed evaporation parameters C_1 and C_2 .

Significant uncertainty in the thermal accommodation coefficient is expected because the temperature decay around the peak temperature is nearly independent of α . Although this technique does not account for uncertainty in gas temperature and pressure, a parametric analysis showed that the inferred parameters were insensitive to variations in p_g and T_g , due to the dominance of evaporation during the relevant phase of particle cooling. The credibility interval for the thermal accommodation coefficient of silicon almost contains the MD-inferred value of ~ 0.3

from Sipkens et al. [38] or the values estimated in Chapter 6.1.2 for germanium ~ 0.2 .

6.6. Conclusions

Time-resolved laser-induced incandescence (TiRe-LII) was used to measure the diameters of gas-borne silicon and germanium nanoparticles in microwave-plasma-heated reactive flows. The quantitative interpretation of TiRe-LII signals requires the knowledge of spectroscopic properties of the laser-heated material as well as heat-transfer models. Model parameters and the underlying measurements are subject to uncertainties and experimental error. These uncertainties can be accounted for through Bayesian inference; the outcome of which provides not only most likely values of the parameters of interest but also their uncertainties in terms of credible intervals.

Subsequently, a detailed heat transfer model that considered parametric uncertainty in the evaporation submodel, and a free molecular heat conduction model that considers gas mixtures were presented. The underlying thermo-physical properties of liquid silicon and germanium show large uncertainties for the observed temperatures. Consequently, the nanoparticle sizes were calculated by a heat-conduction model that was extended by Bayesian inference to include the 1 evaporation properties as nuisance parameter with the published standard deviation. While previous work neglected the uncertainty of these values, which led to a strong underestimation of uncertainty, accounting for these uncertainties widens the credible intervals for d_p and α , but more accurately reflects the state of knowledge about these quantities.

More broadly, this chapter highlights the application of TiRe-LII to aerosols of synthetic nanoparticles, where thermo-physical properties and their uncertainties are well documented. This enables a rigorous uncertainty analysis on the parameters of interest d_p , α , C_1 and C_2 by Bayesian inference. The strategy demonstrated here in case of silicon and germanium can be transferred to other inorganic nanoparticles as well as soot.

At higher fluences (silicon: $> 8 \text{ mJ/mm}^2$ and germanium: $> 2 \text{ mJ/mm}^2$), atomic line emission which can be attributed to thermally-excited monoatomic silicon atoms at 288 nm or germanium at 303 and 326 nm, respectively, were observed and are discussed in more detail in chapter 7. These lines do not interfere with the temperature determination from 450 to 700 nm.

7. Quantification of additional plasma emissions

“Plasma, in physics, an electrically conducting medium in which there are roughly equal numbers of positively and negatively charged particles, produced when the atoms in a gas become ionized. It is sometimes referred to as the fourth state of matter, distinct from the solid, liquid, and gaseous states.” - Encyclopædia Britannica

The basic idea of this Chapter has been published in:

- J. Menser, K. Daun, T. Dreier, C. Schulz (2017).
Laser-induced atomic emission of silicon nanoparticles during laser-induced heating."
Applied Optics 56(11): E50-E57.
- J. Menser, K. Daun, T. Dreier, C. Schulz (2016).
“Validation of the evaporation model for LII/LIBS characterization of silicon nanoparticles.”
7th International Workshop and Meeting on Laser-Induced Incandescence
- J. Menser, K. Daun, T. Dreier, C. Schulz (2016).
“Laser-induced atomic emission of silicon nanoparticles during the synthesis in a microwave-plasma reactor”
Laser Applications to Chemical, Security and Environmental Analysis (LACSEA)

The basic principles to describe laser-induced atomic line-emissions will be presented in this chapter and shown in Figure 45. Generally, the heat-transfer model presented in chapter 6.1 is needed to estimate the amount and temperature of the evaporated species through the nanoparticle upon laser heating. The luminescent transitions of hot, evaporated atoms in the vicinity of the nanoparticle are simulated through a de-excitation cascade.

Plasma is the—so called—fourth state of matter, within which neutrals, ions and electrons are present individually; not bound in molecules and atoms. In this particular case, the population of neutrals consists of neutral gas-phase species and neutral evaporated material. Ions are already present in the gas-phase, since the synthesis is based on a microwave plasma process and thermally excited evaporated species. Due to electronic neutrality, the total charge should be zero, with $Q_{\text{particle}} + Q_{\text{ions}} + Q_{\text{electrons}} = 0$. References [42, 43], provide a foundation for the principles of laser-induced plasma spectroscopy.

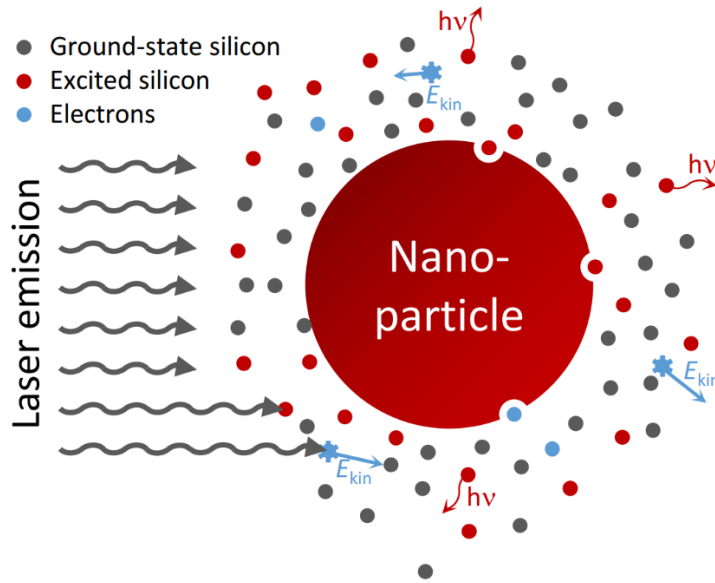


Figure 45: Principle of laser-induced emissions through the evaporated species. Additionally, the incident laser light can be absorbed by the vapor and yield highly energized electrons and atoms.

In this work, a laser with a higher fluence compared to common laser-induced incandescence measurements (with approximately 8 mJ/mm^2 for silicon and 2 mJ/mm^2 for germanium) is applied to heat the nanoparticle beyond the boiling temperature and significant amounts of nanoparticle mass can be evaporated. The atoms, ions, and molecules ejected from the nanoparticle surface are assumed to have the same temperature as the nanoparticle and so the energy levels of each species obey a Maxwell–Boltzmann distribution [161, 162]. The evaporated species could (i) interact with the laser pulse; and (ii) due to their thermal energy distribution, they may emit photons to relax to the ground state. Case (i) is relevant at high laser fluences near the gas-phase breakdown threshold (*cf.* Chapter 7.1), while case (ii) applies to low fluence applications, mainly for phase-selective laser-induced breakdown spectroscopy and laser-induced incandescence, summarized in Chapter 7.3.1.

7.1. Laser-plasma formation on surfaces of condensed matter

The basic principle of plasma formation can be subdivided into two classes, collisional excitation/ionization through highly energized electrons or ions or photonic excitation/ionization, e.g., through direct or multiphoton absorption. The specific pathway is determined by the laser power-density and the wavelength.

While these two classes are relevant for LIBS on solids or the gas-phase, the generation of the initial electrons is, in the following discussed for solids [42, 159], where three regimes, depending on the laser pulse-length can be identified:

1) Femtosecond laser pulse

The electrons in conductive samples can directly absorb the laser radiation and form electron-hole plasmas from which the plasma plume expands. Within semiconductors this electron-hole plasma is created predominantly through multi-photon excitation.

2) Picosecond laser pulse

Through non-thermal melting, electrons are ejected from the surface. In this context, non-thermal means an excess of excited electrons with subsequent thermalization into thermal motion [163]. These free electrons are absorbing laser radiation and form a plasma with the surrounding gas atmosphere.

3) Nanosecond laser pulse

The surface is thermally-melted and vaporized. Evaporated atoms, ions and electrons further absorb radiation during the laser pulse by inverse Bremsstrahlung. The probability for multiphoton ionization is low.

7.2. Plasma expansion

To estimate the dynamics of an evolving plasma, the laser has been focused into the measurement volume generating a gas-phase breakdown of the particle-laden gas-stream. The formed plasma starts to expand from the focal spot of the laser and gradually equilibrates with the surrounding gas-phase. One should consider, that the gas-phase breakdown requires a much higher laser power-density compared to the formation of a plasma from solids. But, due to the fast expansion, the initial plasma enveloping the nanoparticle grows to a macroscopic object within 200 ns, and therefore fluid dynamic effects are likely to superimpose with the effects described in this chapter.

The Nd:YAG laser used in these experiments emits a laser beam with a pulse-length of 8 ns yielding a fluence of 100 mJ/mm², which results in an irradiance of $W_0 \approx 10^7$ W/mm². Below 10⁸ W/mm² thermal processes are dominant. The typical timespan for the present conditions is determined by the duration of the laser-pulse with approx. 14 ns. Subsequently, the plasma expands.

In most textbooks on laser-induced plasmas [42, 43, 164] the major focus is on ablation processes at surfaces. The expansion at surfaces are constricted by the probed material itself. In the present case, the nanoparticle is small compared to the surrounding gas phase volume and has a curved surface. Consequentially, it does not constrict the plasma expansion to a nearly two-dimensional case; instead, it grows volumetrically. Measurements of plasma expansion of a gas-phase plasma breakdown reveal an expansion in three phases. Figure 47 shows the integrated intensity of the plasma and the estimated plasma volume.



Figure 46: Questar QM100 far field microscope. With a focus distance of 30 cm used in this experiment, the microscope has an f-number of 20, a depth of field of 56 μm and a magnification around 4 resulting in a resolution of 10 $\mu\text{m}/\text{pixel}$.

The images were captured with an intensified charge coupled device (CDD) (LaVision, Imager ProX2) coupled to a Questar far-field microscope (Figure 46), with a shortest gate length of 50 ns.

The plasma was generated with focused laser radiation of 100 mJ/pulse at 1064 nm (Quanta Ray, LAB 170). To achieve the temporal synchronization of the camera images to the laser-plasma development, the gate of the intensifier was adjusted, using the first initial occurrence of plasma emissions in the images as temporal point of origin, $t = 0$ ns. The development of the expansion velocity implies three temporal regimes, which are also discussed by Singh et al. [42]. (It has to be noted, that these authors analyze a gas-phase breakdown, which can differ from the conditions described in this chapter where the plasma state only persists in the vicinity of the nanoparticles.)

- From ignition to 300 ns: $v_{\text{exp}} \approx 2000 \text{ m/s} > v_{\text{sound}}$. In this phase, most probably hot electrons and ions excite the surrounding gas phase through collisions. The thermal velocity can be estimated with $v_i = \sqrt{kT_i/m_i}$, and yields an ion temperature of approximately $T_i \approx 1 \text{ eV} \approx 10,000 \text{ K}$.
- From 300 ns to 1 μs : shock-wave expansion with $v_{\text{exp}} \approx v_{\text{sound}} = 300 \text{ m/s}$. During this period, the plasma expands and loses energy by radiation. Figure 47 reveals a loss of the radiation intensity by a factor of 10 during this time span. Shock-wave propagation after laser-induced plasma is a widely-discussed effect and can induce further excitation of gas-phase species at the shock-front.

- From 1 μs to extinction: decreasing velocity of the plasma expansion. The shock-front loses energy with time and decelerates. The hot electrons and ions thermalize and recombine through gas-phase collisions.

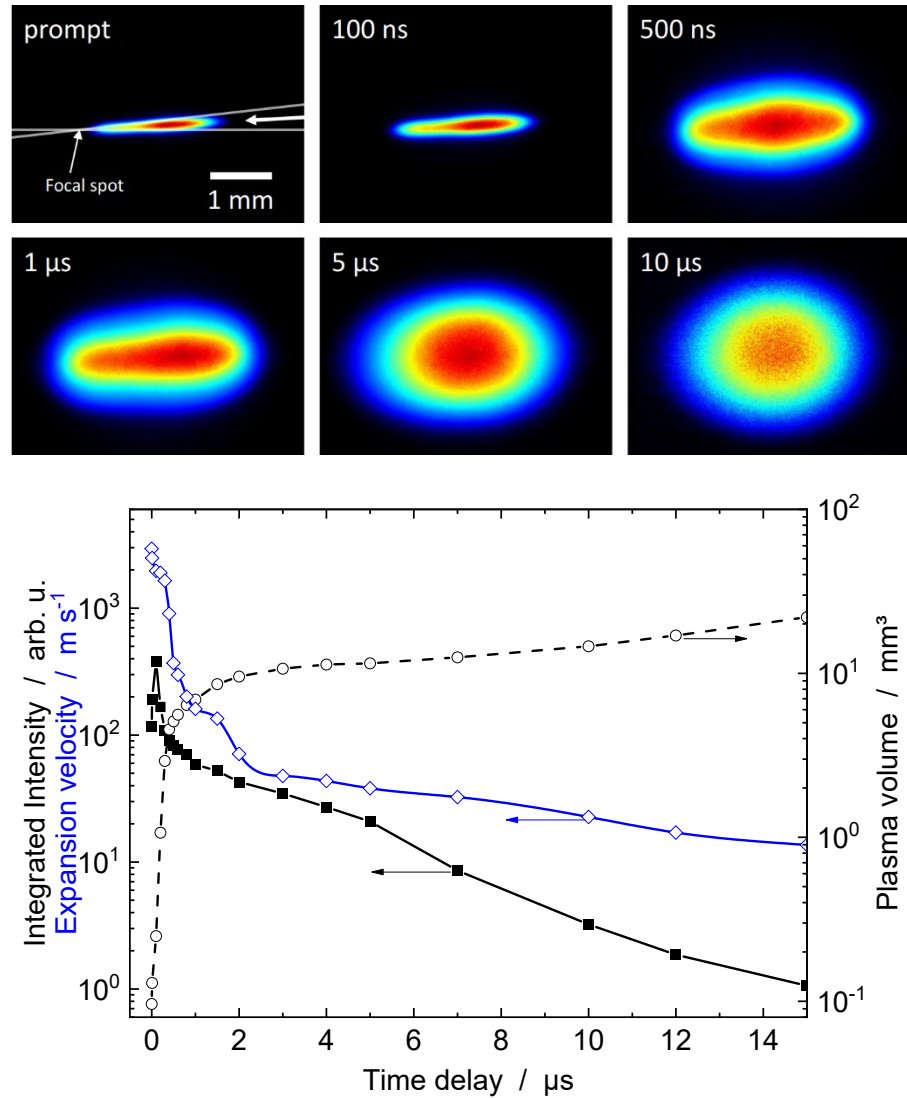


Figure 47: Top: Images of plasma emissions during a gas-phase breakdown. The color scale is normalized by the maximum readout value per image. Bottom: Intensity (black filled symbols) and estimated volume of the plasma emissions (black blank symbols). The intensity calculated by summing up the measured intensity counts after background subtraction. The volume is estimated by assuming axial symmetry along the laser axis. The asymmetric shape in the first two images comes from the, at this time, conical shape of the focused laser beam. The expansion velocity is displayed as blue blank symbols.

The temporal resolution of the intensified CCD camera measurements is restricted to the gate length of 50 ns of the intensifier, and will not capture the full dynamics of the plasma evolution.

7.3. Thermal emission of plasma species

7.3.1. Emission model

It is important to distinguish between broadband and line emissions. Generally, both types occur in plasmas; electronically excited atoms, ions, and molecules can lead to line emissions [10, 165, 166] while the collisions of electrons, neutrals, and ions can produce broadband radiation [50, 167-169]. In this chapter only line emissions of hot atoms are considered.

Figure 48 shows an artificial signal trace during LIBS/LII measurements in the UV at 288 nm. The prompt peak, discussed in Section 7.3.3 and 7.4.2 arises from thermally excited silicon atoms during evaporation of the nanoparticles. The delayed feature is hypothesized to originate from additional excitation of the neutral gas-phase in the vicinity of the evolving plasma, as discussed in Section 7.4.3.

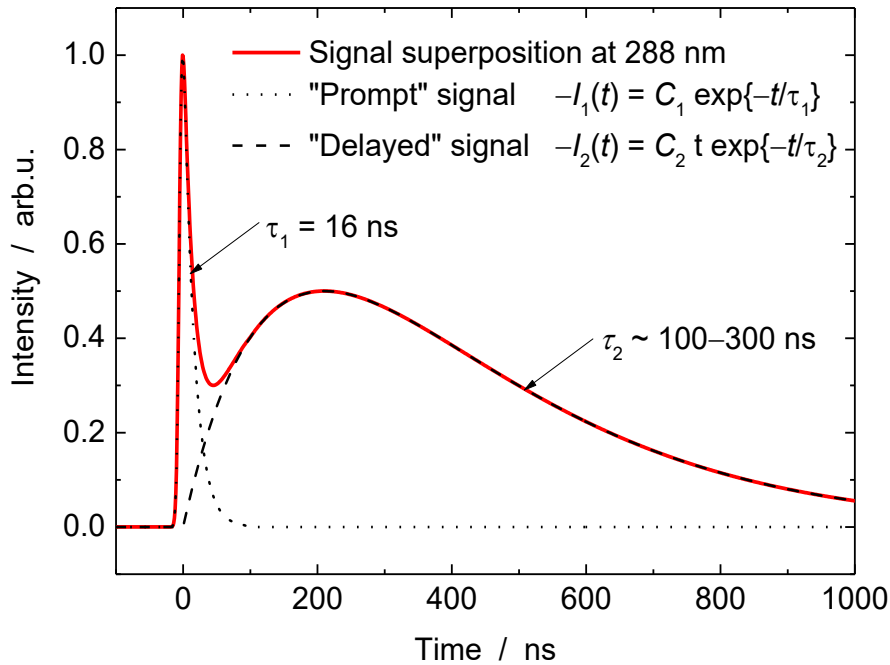


Figure 48: Simulated signal traces of experimentally observed atomic line emissions of silicon composed of a prompt feature, mainly determined by the fluorescence lifetime of Si at 288 nm, and the “delayed” component revealing a much longer intensity decay.

7.3.2. Connection of the line-emission model to the heat-transfer model

During and after laser heating, the atomic emission intensity depends on the number density of gas-phase silicon atoms within the probe volume. The number density can be calculated by a heat transfer model [38, 130], which, based on LII measurements, relates the time-dependent particle temperature T_p to the particle diameter d_p and

the amount of evaporated silicon atoms in Eq.(6.1).

$$\frac{\pi d_p^3(t)}{6} \rho c_p \frac{dT_p}{dt} = q_{\text{abs}}(t) - q_{\text{evap}}(T_p) - q_{\text{cond}}(T_p) - q_{\text{rad}}(T_p), \quad (7.1)$$

where $q_{\text{abs}}(t)$ describes the absorption of laser energy by the nanoparticles, ρ and c_p are the density and the heat-capacity of molten silicon, and q_{evap} , q_{cond} , q_{rad} , are heat transfer by evaporation, conduction, and radiation, respectively. The laser pulse absorption $q_{\text{abs}}(t)$ is mainly determined by the spectroscopic properties of the particles. Within the measurement volume, the nanoparticles are liquid and their absorption and emission behavior can be explained by Drude theory [98, 170] for quasi-free electrons. Nanoparticle sizes inferred from this heat transfer model match those found through *ex situ* analysis in Refs. [34, 171] and Chapter 4.4.

This chapter focuses on evaluating the evaporative heat transfer, since it plays a crucial role in the observed emissions. For the current experimental conditions, the nanoparticle diameter is smaller than the molecular mean free path in the bath gas ($>1 \mu\text{m}$) and the equations presented in Chapter 6.1 can be simplified to

$$\frac{\pi d_p^3(t)}{6} \rho c_p \frac{dT_p}{dt} = q_{\text{abs}}(t) - q_{\text{evap}}(T_p). \quad (7.2)$$

7.3.3. De-excitation cascade

The observed atomic line emissions depend on the number fluxes of evaporated electrons, ions, and neutrals. The number flux of atomic silicon is given by Eq. (7.3), which is obtained assuming equilibrium across the phase interface. Likewise, under equilibrium conditions, the energies of electrons far above the Fermi level also obey a Boltzmann distribution at T_p , and a fraction of these electrons have sufficient energy to overcome the thermionic work function, W , and ionization potential, Φ_e , and will be emitted from the surface. Under conditions of restricted equilibrium between the electrons and the surface (i.e., negligible ion emission), the rate of thermionic emission is given by the modified Richardson-Dushman equation [172, 173]

$$\begin{aligned} N_e'' &= \frac{n_e v_{e,\text{th}}}{4} = \frac{1}{4} \underbrace{2 \left(\frac{2\pi m_e T_p}{h^2} \right)^{\frac{3}{2}}}_{n_e} \exp \left[-\frac{W - \Phi_e}{k_B T_p} \right] \underbrace{\left[\frac{8k_B T_p}{\pi m_e} \right]^{\frac{1}{2}}}_{v_{e,\text{th}}} \\ &= A T_p^2 \exp \left[-\frac{W - \Phi_e}{k_B T_p} \right], \end{aligned} \quad (7.3)$$

where n_e and $v_{e,\text{th}}$ are number density of electrons and their thermal velocity, h is Planck's constant and $A = 7.503 \times 10^6$ electrons/(nm²sK²) is Richardson's constant. Hauge et al. report $W = 6.89 \times 10^{-19}$ J/electron (4.3 eV) for molten silicon [174].

Following Refs. [175, 176] the ionization potential Φ_e is modeled as

$$\Phi_e(t) = \frac{N_e^2(t)e^2}{4\pi\epsilon_0 d_p(t)}, \quad (7.4)$$

where $N_e(t)$ is the number of electrons emitted between start of heating and time t , and ϵ_0 is the vacuum permittivity. While electronic emission can also be stimulated by multiphoton ionization with short-pulse lasers, other laser excitation experiments show that photoelectric emission can be neglected given the low energy of incident photons at 1,064 nm ($e_p = h\nu = 1.87 \times 10^{-19}$ J/photon) compared to the work function [177].

The similarity of Eqs. (6.12) and (7.3) highlights that the same assumptions underlie emissions of atoms and electrons: (i) a local quasi-equilibrium applies at the phase interface; and (ii) atoms and electrons travel ballistically without undergoing collisions in the vicinity of the nanoparticle surface. Moreover, while separate electron and atom temperatures must be used in cases of femtosecond and picosecond laser pulses [178], the nanosecond timescale of laser heating is several orders of magnitude longer than the electronic relaxation time, which permits electrons and atoms to equilibrate within the nanoparticle [177].

A fraction of the evaporated silicon atoms is electronically excited, which leads to measurable atomic line emissions. Since local thermal equilibrium prevails across the nanoparticle surface, the electronic states of evaporating atoms are occupied according to the Boltzmann energy distribution

$$\frac{n_i}{n_0} = \frac{g_i}{Z_0} \exp\left(-\frac{E_i - E_0}{k_B T_p}\right), \quad (7.5)$$

where n_i is the number density of atoms in the excited state, n_0 the number density of atoms in the ground state, E_i and E_0 are the energies of the respective states, g_i is the degeneracy of the excited state and Z_0 the partition function of the ground state [179]. Consequently, the line strength $I_{i \rightarrow j} \propto \Delta E_{i \rightarrow j} / 4\pi N_i A_{ij}$ is proportional to the energy difference of the interacting states $\Delta E = E_i - E_0$, the number of atoms N_i in this state and the Einstein coefficient for spontaneous emission A_{ij} , as the energy levels of the evaporated species cascade towards the ground state. The population of the individual states can be calculated by solving

$$\frac{dN_i}{dt} = \sum_{k=i+1}^N N_k A_{ki} - N_i \sum_{j=1}^{i-1} A_{ij} + \dot{N}_i, \quad (7.6)$$

where A_{xy} are the corresponding Einstein coefficients. The first and second sums on the right hand side describes the population of the observed state from higher states and the depopulation into lower energy states, respectively, while the last term is the production of atoms in the i^{th} state due to evaporation of the nanoparticle, which is calculated using Eqs. (7.5) and (7.6).

To account for possible thermal ionization, the ratio of silicon ions to neutrals is calculated using the Saha equation

$$\frac{n_e n_{\text{Si},i}}{n_{\text{Si},0}} = \frac{Z_e Z_{\text{Si},i}}{Z_{\text{Si},0}} Z_{\text{th}} \exp\left(-\frac{W_i}{k_B T_p}\right), \quad (7.7)$$

which comes from applying the law of mass action to evaporating atoms, ions, and electrons [172, 173], assuming the vapor outside of the nanoparticle surface is in local thermal equilibrium. In Eq. (7.7), $n_{\text{Si},0}$ and $n_{\text{Si},i}$ are the number densities of neutrals (Si I) and ions (Si II), $Z_{\text{Si},e}$ and $Z_{\text{Si},0}$ are the associated partition functions, equal to approximately 5.6 and 9.1 for the temperatures encountered in this study ($\sim 4,000$ K), and Φ is the ionization energy of Si I, 13.1×10^{-19} J/atom (8.19 eV)[180]. Substituting the electron number density found from the Richardson-Dushman equation into Eq. (7.3) results in the Saha-Langmuir equation,

$$\frac{n_{\text{Si},1}}{n_{\text{Si},0}} = \frac{Z_{\text{Si},1}}{Z_{\text{Si},0}} \exp\left(-\frac{W - W_i - \Phi_e}{k_B T_p}\right). \quad (7.8)$$

Multiplying Eq. (7.6) by this ratio gives the number fluxes of silicon ions and atoms.

7.4. Results and discussion

7.4.1. *Effect of the laser pulse-length on the nanoparticle peak temperature and evaporation*

The laser pulse-length of 14 ± 2 ns (Continuum Powerlite 7000, Chapter 4.3) was measured with a fast photodiode (Thorlabs DET10A, 1 ns rise time) connected to a fast oscilloscope (Tektronix DPO70404C, 4 GHz bandwidth). Due to the ratio of laser-heating and evaporative cooling, the measured peak temperature is sensitive to the laser pulse-length. Therefore, for modeling and fitting the peak temperature the temporal laser pulse profile has been explicitly incorporated into the model.

Figure 49 illustrates the amount of evaporated silicon mass for the same nanoparticle sizes and laser fluences, as a fraction of the initial nanoparticle mass. Obviously, the fraction of evaporated material rises with increasing fluence, from approximately 15% for 10 mJ/mm^2 up to 70% for 50 mJ/mm^2 . At a fluence of 100 mJ/mm^2 (not plotted), the nanoparticles completely evaporate. The peak nanoparticle temperature exceeds the boiling point of the bulk material because the duration of laser heating is much shorter than the characteristic timescale of evaporation set by the Clausius–Clapeyron equation, Eq. (6.13). Since the evaporation cooling rate is set, a shorter laser pulse causes the laser pulse energy to “accumulate” in the nanoparticle, resulting in superheating. Conversely, a longer-duration laser pulse results in a lower nanoparticle peak temperature, even though more energy is imparted into the nanoparticle. Reference [34] describes this phenomenon in more detail.

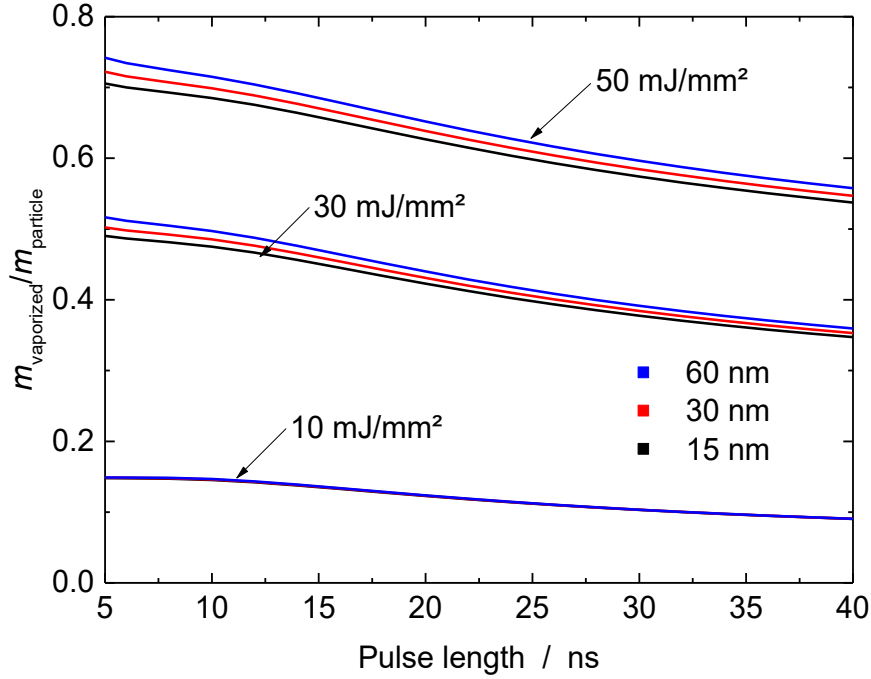


Figure 49: Simulated dependence of the fraction of evaporated silicon to the starting mass of the particle for particle sizes of 15, 30, 60 nm and fluences of 10, 30, and 50 mJ/mm².

7.4.2. Prompt line emission

A close examination of the streak camera data (*cf.* Chapter 4) reveals spectral lines corresponding to silicon and germanium, but not argon. In the phase-selective LIBS regime, nanoparticles are partially or fully evaporated, but, in contrast to high fluence LIBS (e.g., [42]), no gas breakdown takes place [48]. Here, the focus is specifically on the temporal variation of the strong atomic transitions of silicon from the 3s²3p² energy level to the 3s²3p4s level at 251.61 nm (³P⁰ → ³P) and 288.15 nm (¹P⁰ → ¹D), and of germanium from the 4s²4p5s energy level to the 4s²4p² level at 303.90 nm (¹P⁰ → ¹D), 306.70 nm (³D⁰ → ¹S), 312.48 nm (³P⁰ → ¹D) and 326.95 nm (³P⁰ → ¹D).

For silicon, the line emissions were observed starting at fluences of 8 mJ/mm², up to 100 mJ/mm². In a typical temporal signal curve for the two observed silicon lines, shown in Figure 50, two temporal regimes are observable: a prompt peak that temporally coincides with the laser pulse, and a delayed feature that reaches its maximum several hundred nanoseconds after the laser-pulse and decays at a much slower rate. The emission model outlined in Section 7.3.1 only describes the primary feature. After integrating the signal for 50 ns in the neighborhood of the prompt peak it is compared to the accumulated value resulting from the emission model defined in Eqs. (7.3)–(7.7), incorporated into the heat transfer model from Section 7.3.2. A key parameter for this model is the peak particle temperature that determines the fraction of evaporation and the thermal populations of the interrogated lower energy levels of each transition.

With germanium, the first observable emissions start earlier at approximately 2 mJ/mm^2 , but due to the low signal-to-noise ratio are not plotted in Figure 52. The measurements were performed up to 14 mJ/mm^2 . Germanium low-fluence LIBS also exhibits the second, delayed feature with nearly the same temporal behavior as seen in the measurements on the silicon aerosol.

The difference in onset fluences for observable atomic line emission between silicon and germanium corresponds with the LII measurements in Chapter 6.3. In Figure 41 the peak temperature against laser-fluence is depicted. For silicon, the maximum heat-up temperature exceeds the boiling temperature at 8 mJ/mm^2 and for germanium at 2 mJ/mm^2 . These values perfectly correspond to the onset fluences of low-fluence LIBS. This fact leads to the assumption that the evaporation of nanoparticle mass is the originating effect of the atomic line emissions, and so the observed emissions are directly coupled to the evaporation model discussed in Chapter 6.1.3.

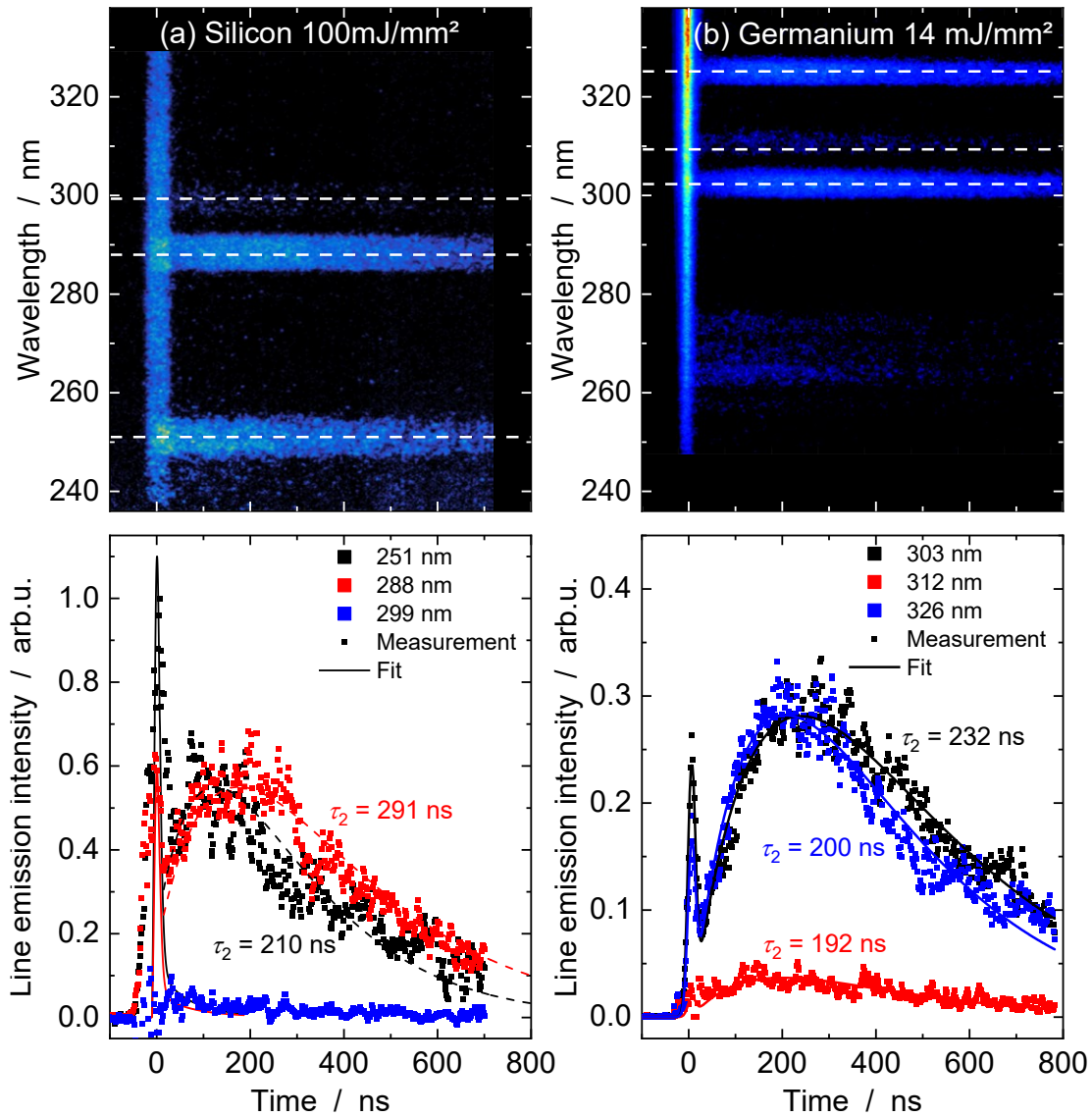


Figure 50: (a, top) Typical temporal vs. spectral emission chart of atomic line emissions from Si for a fluence of 100 mJ/mm². The three observable lines are at 251, 288, and 299 nm. (b, top) Same for Ge for a fluence of 14 mJ/mm². The three observable lines are at 303, 312, and 326 nm. (a&b, bottom) Temporal profiles (symbols) of the signal intensities of these three lines after background subtraction to avoid a crosstalk from the prompt broadband emission. The lines show the result of the presented model. The lines represent the lifetime determination of the delayed emission feature.

By comparing the measured intensities of the two observable silicon lines it is possible to derive an approximate temperature for the Si atoms via a Boltzmann plot [166] as shown in Figure 51 along with an effective nanoparticle temperature inferred from pyrometry as well as a simulated nanoparticle temperature obtained from Eq. (7.1). The Si atom temperature is subject to large uncertainties since the experiment only produces two lines with sufficient intensity for this calculation: a realistic confidence interval for the atom temperature of the prompt peak (at $t < 50$ ns) is $T \pm 1,000$ K, and $T \pm 3,000$ K for the delayed peak (at $t > 50$ ns). For

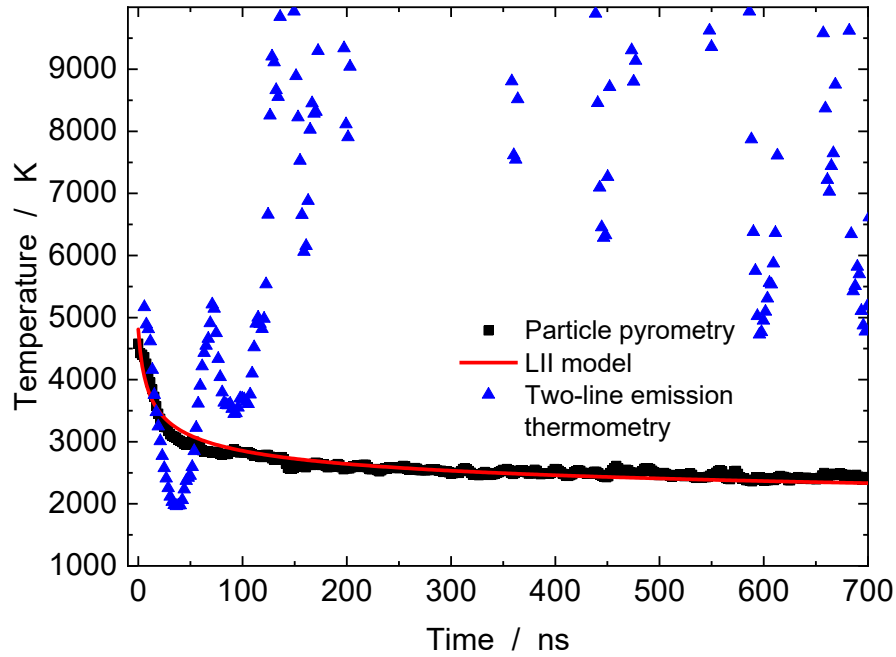


Figure 51: Comparison of the nanoparticle temperature (black symbols) with the atom temperature of the evaporated silicon atoms (blue symbols) using a laser fluence of 100 mJ/mm^2 . The simulated signal traces based on the LII model is shown as red curve and yields a particle diameter of $d_p = 32 \pm 17 \text{ nm}$.

temperatures above 8,000 K the intensity ratio of the two lines flattens out, resulting in unphysical results (Figure 51, 200–350 ns). Initially, the atom temperature drops from above 5,000–2,000 K with nearly the same slope as for the nanoparticle temperature, suggesting that the energy states of the evaporated silicon atoms are consistent with those within the nanoparticle; this observation is consistent with the assumption of local thermal equilibrium across the nanoparticle surface, as described above. From 50 ns to approximately 200 ns after the peak temperature the silicon atom temperature abruptly rises to a peak of 10,000 K, which corresponds to the onset of the delayed signal contribution (Figure 50 bottom) indicating additional excitation pathways that are no longer connected to the temperature of the nanoparticle. At longer times, the atom temperature measurement strongly fluctuates due to the poor signal-to-noise ratio.

Figure 52 shows the variation of atomic line emission intensities at 288 and 251 nm with laser fluence. Line emission is observed starting at fluences of 10 mJ/mm^2 with a steep gradient that flattens out at higher laser fluences. The solid lines show the corresponding simulations. Neither the measurements nor the model reveal a sensitivity of the peak line intensity of the prompt peak to the pressure of the ambient gas. This observation is consistent with the fact that the short time scale of luminescence (16 ns) relative to the average duration between collisions within the gas ($\sim 15 \text{ ns}$), with which collisional quenching of the excited silicon atoms within the fluorescence lifetime is not likely.

7.4.3. *Delayed line emissions*

The presented model does, however, not explain the delayed signal increase, which indicates the presence of a different pathway for populating high energy states of the silicon atoms in the gas phase. While the prompt signal originates from the initial energy carried by the atoms and ions after evaporation (without significant interaction with the gas phase and plasma during their excited-state lifetime), the delayed signal contribution arises from excitation through collisional energy transfer in the gas/plasma surrounding of the nanoparticle. Consequently, a physical interpretation of the delayed signal must consider the local density of silicon atoms, ions, and electrons in the gas phase as well as the Saha equation, which describes the state of local thermal equilibrium between these species that arises through gas-phase collisions. Based on these considerations, it was evaluated which of the possible mechanisms is able to generate the observed amount of excited silicon atoms. Potential mechanisms include: (i) the recombination of thermally-ionized silicon with electrons emitted from the laser-heated particle according to $\text{Si}^+ + \text{e}^- \rightarrow \text{Si}^*$; and (ii) effects in the plasma that has absorbed additional energy through inverse bremsstrahlung, leading to the generation of additional silicon ions or enables electron-impact excitation.

The first hypothesis concerns recombination of free electrons with thermally-excited silicon ions “ejected” and excited by the laser-heated nanoparticle without further energy gain through the plasma. This requires a significant concentration of Si^+ , which will decay into highly-excited neutral silicon. Solving the Saha-Langmuir equation (7.8) yields the thermal ionization fraction for the surface/gas interface. In the presented experiments, a peak temperature of approximately 5,000 K at a fluence of 100 mJ/mm² was observed. At this point the ionization is below 0.5%. This degree of ionization is insufficient to explain the intensity of the delayed emission feature. This mechanism would also not explain the observed time characteristics. In case of silicon ions being generated as a consequence of the interaction with the laser pulse, the resulting signal would be prompt as well, but with a different decay constant.

The abrupt increase in temperature of the evaporated Si atoms at the onset of the delayed signal (Figure 51) indicates an additional mechanism for exciting these atoms, which has not yet been described for low-fluence LIBS before [10, 181]. Electron-ion recombination with preceding generation of silicon ions by electron-impact ionization or electron-impact excitation can explain this behavior. These effects solely occur in the plasma or gas-phase, and therefore, the Saha equation is necessary in order to calculate the degree of ionization. At temperatures of 5,500 K the ionization exceeds 1%, and dominates above 9,500 K. But even for temperatures of 9,500 K, the expected silicon-ion line-emission intensity is below 0.1% of the silicon atom emission intensity due to the higher upper energy levels of ions compared to neutral atoms. This suggests that ionized silicon will not be observable in these measurement conditions. Unfortunately, it is not possible to discern whether

electron-impact ionization followed by recombination or electron-impact excitation, or a combination of both, is responsible for the second peak of delayed emission.

The strong electromagnetic field of the laser pulse can be absorbed by electrons more efficiently than by neutrals and ions. While the Saha equation assumes local thermal equilibrium (LTE; $T_{\text{electron}} = T_{\text{gas}}$), the enhanced energy absorption of the electrons can violate the LTE condition and provides an additional energy storage with $T_{\text{electron}} > T_{\text{gas}}$. A subsequent equilibration enables the hot electrons to ionize and excite additional silicon atoms, and thus may explain the delayed onset of the second signal component. In case of laser-induced plasmas forming a gas-phase breakdown it has been shown that the choice of time delay between laser excitation and measurement is crucial to obtain an equilibrium for quantitative measurements [42]. Recent publications have not shown delayed emissions for low-fluence LIBS without excitation of the gas phase[48]. Understanding this phenomenon is the subject of ongoing research.

7.4.4. Inference of particle size

It is also possible to infer particle size from atomic line emissions in the low-fluence LIBS regime. The noise of the atomic line emission intensity measurements is assumed to be independent at each measurement time and normally-distributed. Then, the likelihood is given by

$$p(\mathbf{I}_{\text{LIBS}}|\mathbf{x}, \boldsymbol{\theta}) \propto \exp \left\{ - \sum_j \frac{[I_{\text{LIBS},F_0} - C_{\text{LIBS}} I_{\text{LIBS}}(\mathbf{x}, \boldsymbol{\theta}, F_0)]^2}{2\sigma_{I,j}^2} \right\}, \quad (7.9)$$

where I_{LIBS,F_0} is the integrated intensity of the prompt feature imaged in Figure 52, and $I_{\text{LIBS}}(\mathbf{x}, \boldsymbol{\theta}, F_0)$ is the solution of the de-excitation cascade in Chapter 7.3.3. Because the absolute intensity of the atomic line emissions is affected by many external influences, for example the volume fraction of nanoparticle f_v and the efficiency of the optical system, these values are merged into a single scaling factor C_{LIBS} . In this case, d_p is the parameter of interest \mathbf{x} , and vapor pressure related properties C_1 and C_2 , and the scaling factor C_{LIBS} are nuisance parameters, that must be considered during least-squares minimization.

Analogously to chapter 6, the values of \mathbf{x} and $\boldsymbol{\theta}$ were found by minimizing the summation in Eq. (7.9). The resulting maximum likelihood estimate $[\mathbf{x}, \boldsymbol{\theta}]_{\text{MLE}}$ is the most probable value of the quantities-of-interest \mathbf{x} and the nuisance parameters $\boldsymbol{\theta}$. Especially, the nuisance parameters $\boldsymbol{\theta} = [C_1, C_2]^T$ are known prior to the measurement, and are used to reduce the uncertainty in the inferred values. The resulting posterior probability density is then defined by

$$p(\mathbf{x}, \boldsymbol{\theta}|\mathbf{I}_{\text{LIBS}}) = \frac{p(\mathbf{I}_{\text{LIBS}}|\mathbf{x}, \boldsymbol{\theta})p_{\text{pr}}(\mathbf{x})p_{\text{pr}}(\boldsymbol{\theta})}{p(\mathbf{I}_{\text{LIBS}})} \quad (7.10)$$

In Figure 52 the maximum a-posterior probability obtained through Eq. (7.10) are shown for silicon and germanium. In the case of silicon two lines have been utilized, in the case of germanium three lines were used.

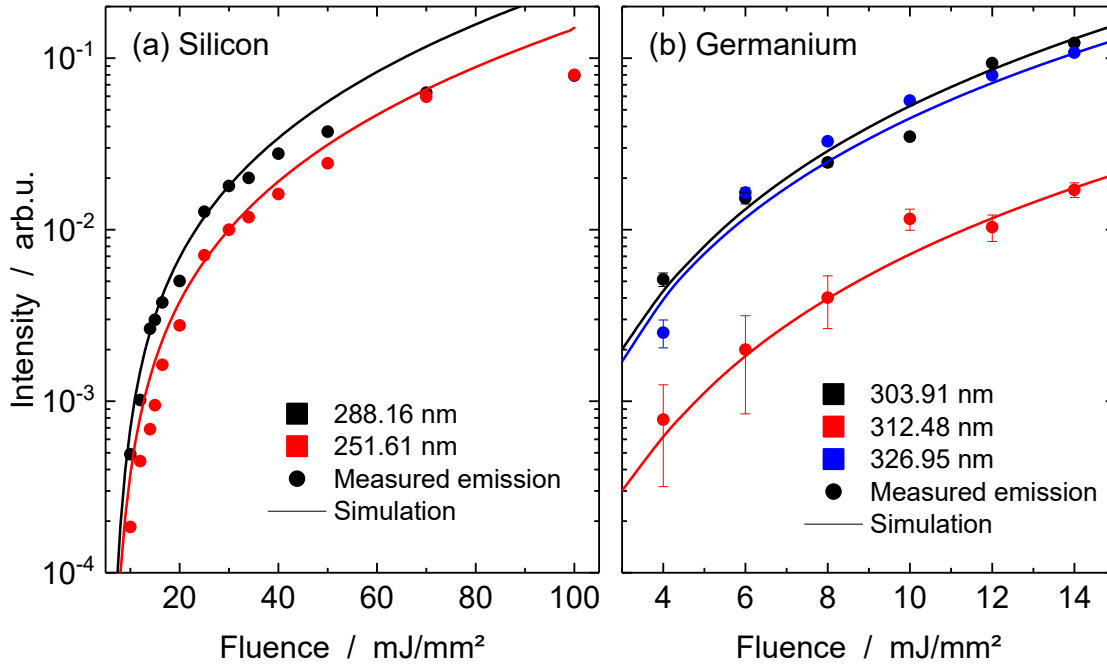


Figure 52: (a) Measured (symbols) and simulated (lines) atomic line emissions. (a) Silicon: the red parts show the results of the 251 nm line, while the black parts show the ones of the 288 nm line. (b) For germanium three lines were detectable within a suitable detection wavelength range, 303.91 nm (black), 312.48 nm (red) and 326.95 nm (blue).

The agreement between the simulated and measured fluence dependence of Si and Ge fluorescence emissions and the silicon atom temperature within the first 50 ns (Figure 50 and Figure 52) strongly suggests that the prompt emission is due to thermally-excited silicon atoms. These results also provide independent verification of the evaporation sub-model used to interpret LII data, and suggests that the assumption of phase equilibrium is reasonable given the timescales important to nanoparticle laser-heating and evaporative cooling. For germanium, only the atomic line emission intensity in Figure 52 was analyzed, but simultaneously for the three detectable lines. Just as for silicon, the experimental and simulated data for germanium are in close agreement.

It was possible to retrieve a particle size for silicon as well as for germanium, with $d_{p,\text{Si}} = 22 \pm 16$ nm and $d_{p,\text{Ge}} = 32 \pm 30$ nm from the measurements of the prompt line-emission intensity. The difference in uncertainties is mainly related to the number of measured fluences, which covers 13 fluences (8–100 mJ/mm²) for silicon but only 6 fluences (4–14 mJ/mm²) for germanium, respectively.

7.5. Conclusions

This chapter presents measurements of atomic emissions from laser-heated silicon nanoparticles, which can be separated temporally into a prompt thermal part that coincides with laser-induced evaporation and lasts for approximately 50 ns, and a delayed non-thermal excitation part that occurs 100–300 ns later in the cooling process and lasts for hundreds of nanoseconds. A model for the prompt part is based on evaporation of the nanoparticle, the assumption that the evaporated atoms are in thermal equilibrium with those in the molten nanoparticle, and the assumption that the electronic excitation is in thermal equilibrium. The derived model includes a cascade process for a thermally-excited atom depopulating the higher energy levels to the ground state based on spontaneous relaxation. The simulated thermal emission matches the experimental observations, and provides an independent validation of the evaporation sub-model used to analyze time-resolved LII data.

A subsequent non-thermal excitation process evokes an atomic emission signal lasting up to 3 μ s, depending on the laser fluence. The measured atom temperature during this period has been much higher than in the prompt phase. It is assumed that evaporated silicon atoms are re-energized through a gas-phase collisional process, likely involving electron-impact ionization. Ongoing research is focused on developing a coupled transport/electromagnetic model to elucidate the unexplained phenomena.



8. Narrowing uncertainties by data synthesis

“Information is the oil of the 21st century, and analytics is the combustion engine.” - Peter Sondergaard

Both TiRe-LII and phase-selective LIBS can be used to measure fundamental materials properties, like the evaporation enthalpy, heat capacity, particle temperature, elemental composition, particle size, and others, but so far each type of measurement has been considered independently. The Bayesian approach can be used to combine the complementary information in each data class to find a single, robust estimate for the quantities of interest.

8.1. Revised inference focused on evaporation parameters

Chapter 6 and 7 focus on the inference of particle size d_p and accommodation coefficient α . All other parameters are integrated out during marginalization. In contrast, the evaporation parameters C_1 and C_2 from the Antoine equation, defined by Eq. (6.13), are the target parameters of this chapter. Therefore, the measurements for all three techniques shown in Chapter 6 and 7 are revised with a new focus on evaporation-relevant properties C_1 and C_2 , while the other parameters are marginalized out. In the following Sections 8.1.1 to 8.1.3 the inference process will be briefly discussed and subsequently in Sections 8.2 and 8.3 an illustrative approach is given to understand the synthesis of various probability densities. In Section 8.4 the data synthesis based on the combination of LII and LIBS measurements is carried out.

8.1.1. LII temperature decay

Time-resolved laser-induced incandescence is based on the heat-transfer model (Eq. (6.1)), which relates the time-resolved particle temperature to the particle diameter d_p , thermal accommodation coefficient α , and vapor pressure properties, here C_1 and C_2 from the Antoine equation, see Chapter 6. Through least-squares minimization the simulated temperature trace is fitted to the experimental data.

Figure 43 shows the minimization result of the heat-transfer model to the LII measurement of silicon and germanium nanoparticles together with posterior probability distribution with respect to the particle size and accommodation coefficient. Figure 53 illustrates the likelihood function and the 90% credible interval for C_1 and C_2 . The temporally-resolved fitting is the same as in Figure 43, and therefore is left out in this chapter. The posterior probability density, perceivable through the black ellipses, is aligned with its major axis on the diagonal from top right to bottom left.

The mean values of the inferred vapor pressure parameters (for both materials) are included in the 90% credible interval of the used literature values. According to the

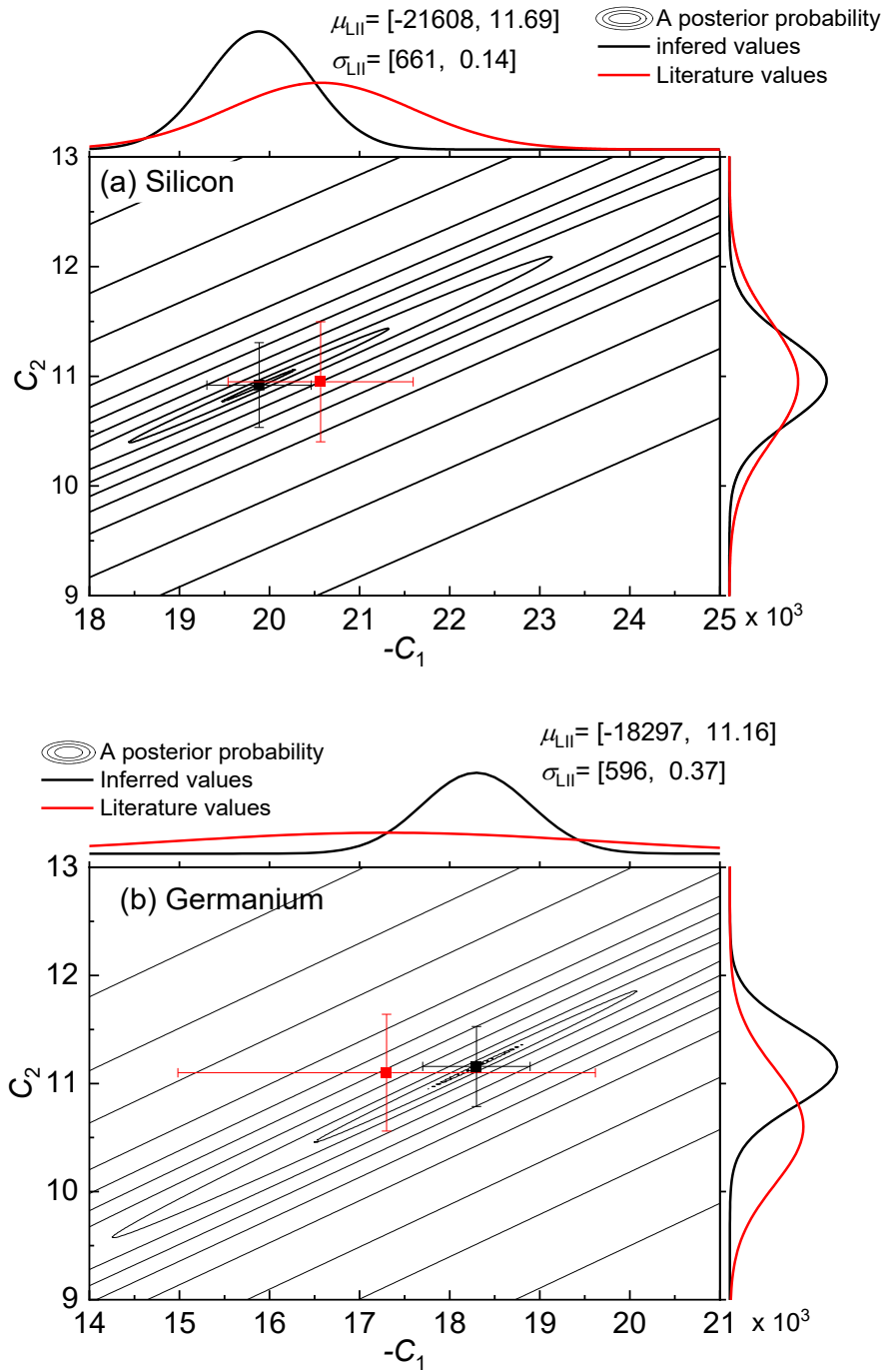


Figure 53: Marginalized posterior function of laser-induced incandescence fitting results. The surface of the likelihood function is plotted with black ellipses representing lines of constant probability. The literature values and \mathbf{x}_{MLE} are plotted as symbols with uncertainties plotted as error bars.

Student t -test [182] with a significance level of 0.05, the measurement supports the literature values.

The parameters of interest C_1 and C_2 were repeatedly inferred for laser fluences $F_0 = [2.5, 4.0, 6.0, 8.0]$ mJ/mm². The values of C_1 , C_2 , and d_p inferred from these measurements are consistent with each other, in Table 7.

Table 7: Resulting Antoine coefficients inferred for various laser fluences.

Fluence / mJ mm^{-2}	C_1	C_2	d_p / nm
2.5	-18297 ± 596	11.16 ± 0.37	35.6 ± 27
4.0	-18373 ± 562	11.13 ± 0.30	37.6 ± 25
6.0	-17220 ± 822	10.79 ± 0.26	43.9 ± 38
8.0	-17479 ± 866	10.81 ± 0.27	43.4 ± 38

The Antoine coefficients are consistent with the literature values and reflect a low scattering between the various measured fluences of approximately 5%. This emphasizes the high quality and reproducibility of the measurement.

Moreover, the uncertainties attached to the Antoine coefficients are much lower than those of the particle sizes, which yields measurement uncertainties of $\sim 70\%$ and differ by nearly 20% between the experiments with various laser fluences.

8.1.2. Peak temperature LII

The peak-temperature determination also applies the LII heat-transfer model, described in Eq. (6.1). In this special case, the laser absorption has been incorporated into the heat-transfer model to estimate the highest temperature reached during laser heating. While time-resolved LII utilizes just a single laser-fluence value together with a temporally-resolved particle-temperature trace for fitting the HMT to the measured data, peak-temperature LII uses only the peak temperature as a function of various laser fluences, shown in Figure 41.

The peak temperature reached shortly after the laser pulse can also be utilized to infer the Antoine coefficients, in Figure 54. The inferred values of C_1 and C_2 nearly perfectly match the literature values, *cf.* Chapter 6.1.3.

The fitting result to the peak temperatures, as well as the temperature values 50 and 100 ns after the peaks are shown in Figure 41. Already 50 ns after the temperature peak, the particle temperature drops below the boiling point, at which evaporation, which is the dominant cooling process, becomes negligible. Therefore, the peak temperature, and the temperatures measured shortly after the temperature peak, are perfectly suitable to determine evaporation properties of the laser-heated nanoparticles.

According to Planck's law, the peak temperature should lead to the highest incandescence intensity, and according to the Poisson-Gaussian noise distribution of the streak-camera measurements, this data should also have the best signal-to-noise ratio which results in the lowest uncertainty in temperature. It needs to be noted, however, that the peak incandescence/temperature is most affected by undesirable effects like Bremsstrahlung (Chapter 7) and fluorescence, and a rapid variation in particle properties. Additionally, the peak intensity and peak temperature can be

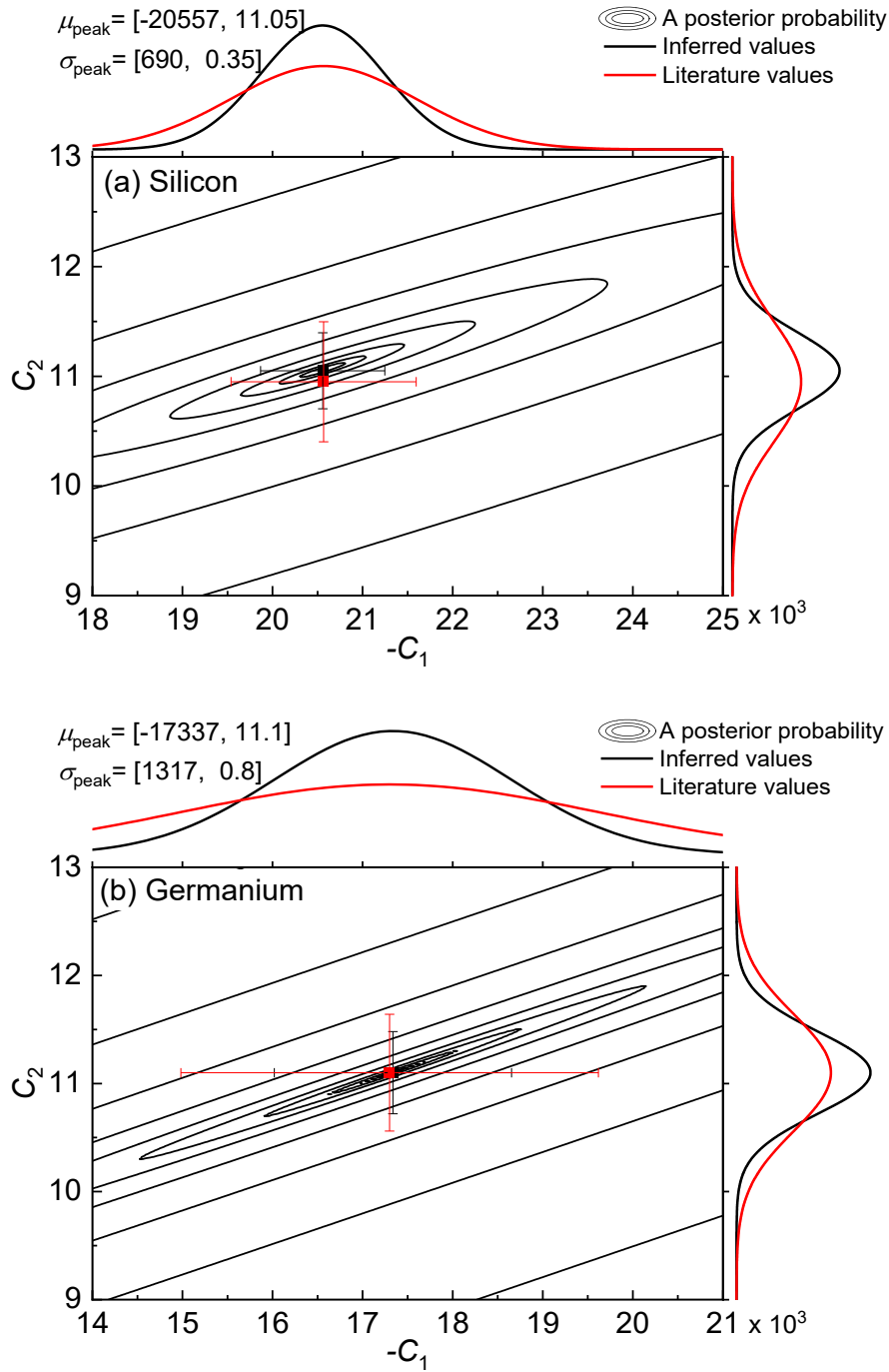


Figure 54: Marginalized posterior function of laser-induced incandescence peak-temperature fitting. The surface of the likelihood function is plotted with black ellipses representing lines of constant probability. The literature values and \mathbf{x}_{MLE} are plotted as symbols with uncertainties as error bars.

reduced due to temporal bleeding, described in Chapter 6.4, but is not further included in this part of the evaluation.

8.1.3. *LIBS atomic emission intensity*

Laser-induced atomic line emissions are presented in chapter 7. When nanoparticles evaporate, small amounts of the evaporated species are electronically excited, such that atomic line emissions become observable. These line emissions could be related to the heat-transfer model, and hence are suitable to infer vapor pressure properties.

Figure 55 shows once more the likelihood function and the 90% credible interval. The major axis is rotated against the C_1 -axis. The inferred vapor pressure values deviate from the provided literature values by 5% and 6% for C_1 and C_2 , for silicon, and by 8% and 4% in the case of germanium, respectively. Due to the narrower uncertainties of the silicon literature data, the 90% credible intervals of measurement and literature values do not overlap, which might seem alarming at first glance. But here again, the Student t -test supports (with a significance level of 0.05) the hypothesis that measurement values and literature values are equal. For germanium the mean values of the inferred vapor pressure parameters are included in the 90% credible interval of the used literature values.

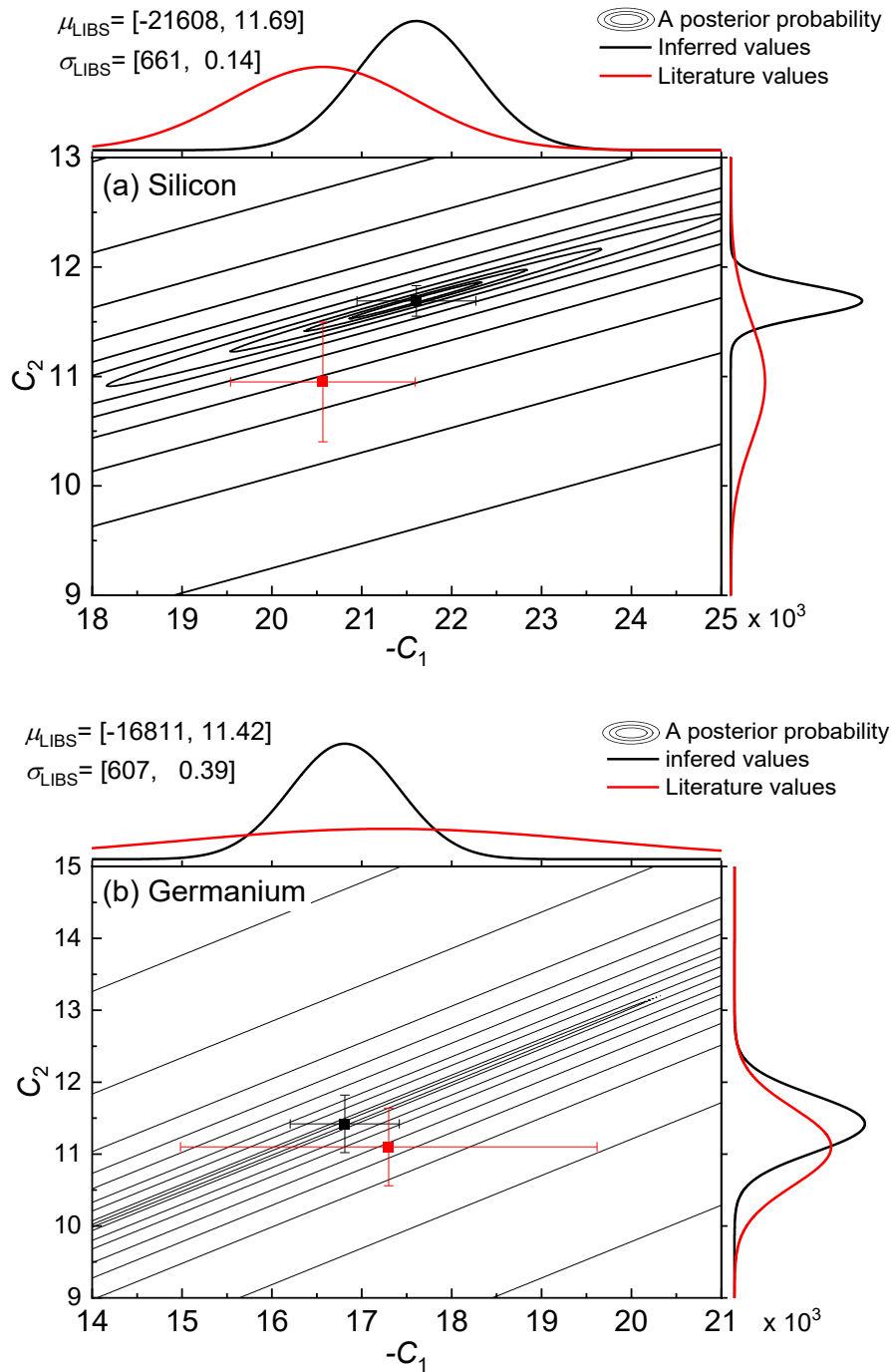


Figure 55: Marginalized posterior function of laser-induced breakdown line intensities fitting results. The surface of the likelihood function is plotted with black ellipses representing lines of constant probability. The literature values and \mathbf{x}_{MLE} are plotted as symbols with uncertainties as error bars.

8.2. Credibility regions

Least-squares minimization assumes a sufficiently linear behavior of the model at the maximum likelihood estimate (MLE), in the absence of prior information, or the maximum a posteriori (MAP) estimate, if informative priors are used. By this assumption, normally-distributed independent measurement and prior

uncertainties translate into normally distributed parameter uncertainties. In Figure 53 to Figure 55 the confidence ellipses are plotted, and show a slight rotation against each other. This rotation highlights that the measurement models contain independent information, and therefore data synthesis can narrow uncertainties more effectively compared to the central limit theorem. To assure the necessary linearity, the models were checked according to Appendix C.

Due to the assumptions during the inference, the resulting probability density contours surrounding the maximum likelihood estimate or maximum a posterior density are elliptical, representing multivariate normal distributions. The rotation of these confidence ellipses can be computed by singular value decomposition (SVD) of the Jacobian at the MAP estimate [183]. SVD is related to the eigenproblem of the covariance matrix, and traces back the rotation of the ellipses to an orthonormal basis by rotation, followed by elongation/contraction and rotation again. The transformation matrix is $\mathbf{M} = \mathbf{U}\mathbf{\Sigma}\mathbf{V}^T$, where \mathbf{M} is the resulting transformation matrix with $m \times n$ components \mathbf{U} and \mathbf{V}^T are the two corresponding rotation matrices and $\mathbf{\Sigma}$ is the elongation/contraction matrix, which carries the orthogonal inversed standard deviations. The main information needed is the orthogonal coordinate system, the so called principal axes and the inverse standard deviation.

Therefore, it is possible to calculate both the uncorrelated uncertainty values of the rotated orthonormal coordinate system and the rotation angle according to [183]

$$\boldsymbol{\sigma}_{\text{principal}} = \text{diag}(\mathbf{\Sigma}) \quad (8.1)$$

$$\beta = \tan^{-1}(V_{2,1}/V_{1,1}) \quad (8.2)$$

with $\boldsymbol{\sigma}_{\text{principal}}$ a vector containing the standard deviations for each parameter, β the rotation angle of the credible interval ellipse, and $V_{1,1}$ the first entry of the matrix composed of the eigenvectors.

According to the minimax theorem, the largest singular value of a Euclidian space is equal to the operator norm, and the following singular values are usually listed in decreasing order.

8.3. Synthesizing multivariate normal distributions

Consider the synthesis of two bivariate normally distributed variable vectors \mathbf{X}_1 and \mathbf{X}_2 in four different cases, shown in Figure 56 to Figure 59.

$$i) \quad \boldsymbol{\mu}_{1,2} = [0, 0], \boldsymbol{\sigma}_{1,2} = [1, 1], \rho_{1,2} = 0$$

The covariance matrix is consequentially

$$\mathbf{\Sigma} = \begin{bmatrix} 1 & 0 \\ 0 & 1 \end{bmatrix}. \quad (8.3)$$

For case *i*) the bivariate normal distribution is composed of two independent normal distributions, one for each coordinate axis, which is unique for all probability distributions. The marginal probability distributions of the originating distributions

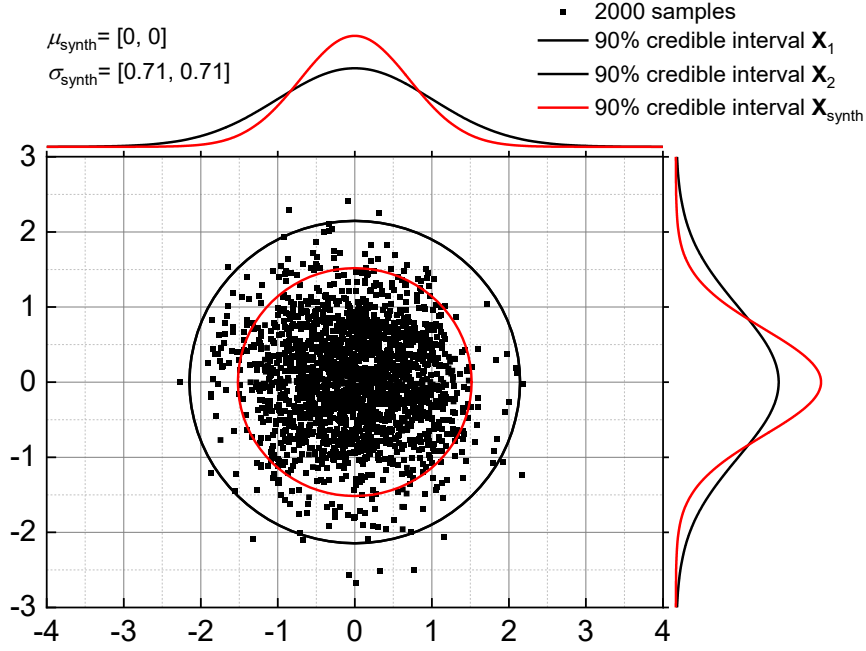


Figure 56: Two 2D probability densities and the resulting synthesized probability density. The black symbols are samples to illustrate the curvature of the resulting density. The marginal probability distribution is plotted at the edges of the 2D density to highlight the effect of data synthesis.

are $\sigma_{1,2} = [1, 1]$. When the mean of the originating distributions is $\mu_{1,2} = [0, 0]$ the synthesized mean is also $\mu_{\text{synth}} = [0, 0]$. The superposition of both distributions results in $\sigma_{\text{synth}} = [0.71, 0.71]$. Obviously, the synthesized standard deviation follows the central limit theorem with $1/\sigma \propto \sqrt{N}$, while the number of measurements are doubled the standard deviation yields $\sigma_{N=2} = \sigma_{N=1}/\sqrt{2} \approx 0.71$.

ii) $\mu_{1,2} = [0, 0]$, $\sigma_{1,2} = [1, 1]$, $\rho_{1,2} = 0.8$

The same as *i*) but with a correlation of $\rho = 0.8$. The covariance matrices are

$$\Sigma = \begin{bmatrix} 1 & 0.8 \\ 0.8 & 1 \end{bmatrix}. \quad (8.4)$$

When the normal distributed variables \mathbf{X}_1 and \mathbf{X}_2 are correlated in the same way (*cf.* case *ii*) the marginal distributions of both yields a slightly lower standard deviation with $\sigma_{1,2} = [1, 1]$ and the superposition yields $\sigma_{\text{synth}} \approx [0.71, 0.71]$ which also satisfies the central limit theorem.

Due to the fact, that the resulting probability density distribution is correlated, the principal axes are inferred by PCA to illustrate the effect of parameter correlation.

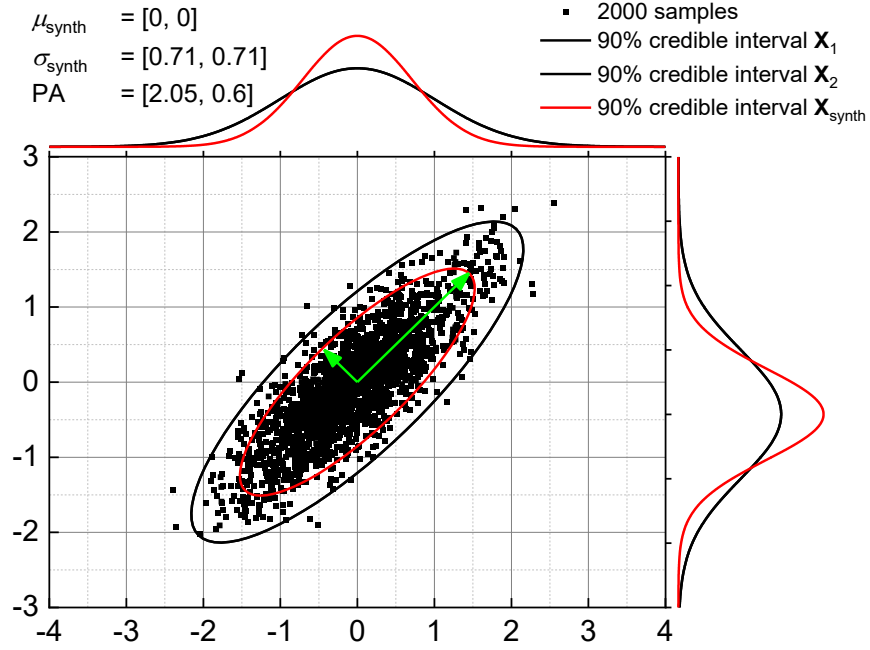


Figure 57: 2D probability densities for case ii). The resulting uncertainty ellipse is correlated as well. The principal axes (PA) are included by green arrows. The marginalized probability densities are the same as in example i).

iii) $\boldsymbol{\mu}_{1,2} = [0, 0]$, $\boldsymbol{\sigma}_{1,2} = [1, 1]$, $\rho_1 = 0.8$, $\rho_2 = -0.8$

The same as ii) but with different correlations of $\rho_1 = 0.8$ and $\rho_2 = -0.8$. The covariance matrices are

$$\boldsymbol{\Sigma}_{1/2} = \begin{bmatrix} 1 & +/ - 0.8 \\ +/ - 0.8 & 1 \end{bmatrix}. \quad (8.5)$$

As soon as the correlation coefficients $\rho_{1,2}$ differ, the improvement is better than the central limit theorem provides. Case iii) and Figure 58 describe such a condition, $\rho_1 = 0.8$ and $\rho_2 = -0.8$, which results in an orthogonal gradient of both probability densities.

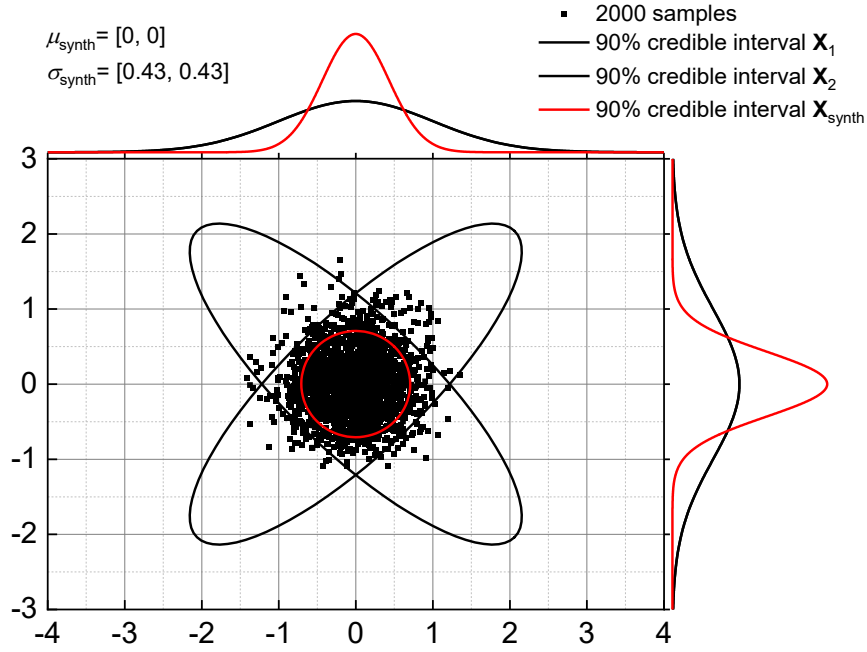


Figure 58: Within case iii), the correlation of originating probability density distributions yields crossed principal axes.

The resulting uncertainty is $\sigma_{\text{synth}} = [0.43, 0.43]$, which is more than $\sqrt{4}$ times better than a single result and $\sqrt{2}$ times better than example *i*). Through the correlation of the normal distributions the uncertainty in the synthesized probability distribution can be achieved.

iv) $\mu_1 = [-1, 0]$, $\mu_2 = [1, 0]$, $\sigma_{1,2} = [1, 1]$, $\rho_1 = 0.8$, $\rho_2 = -0.8$

The same as *iii*) but the first distribution is shifted by $\mu_1 = [-1, 0]$ and $\mu_2 = [1, 0]$. In case *iv*) the probability densities are shifted along the horizontal axis and separated by two units. The standard deviation remains like case *iii*) but the mean $\mu_{\text{synth}} = [0, 0.79]$ is now shifted along the y -axis.

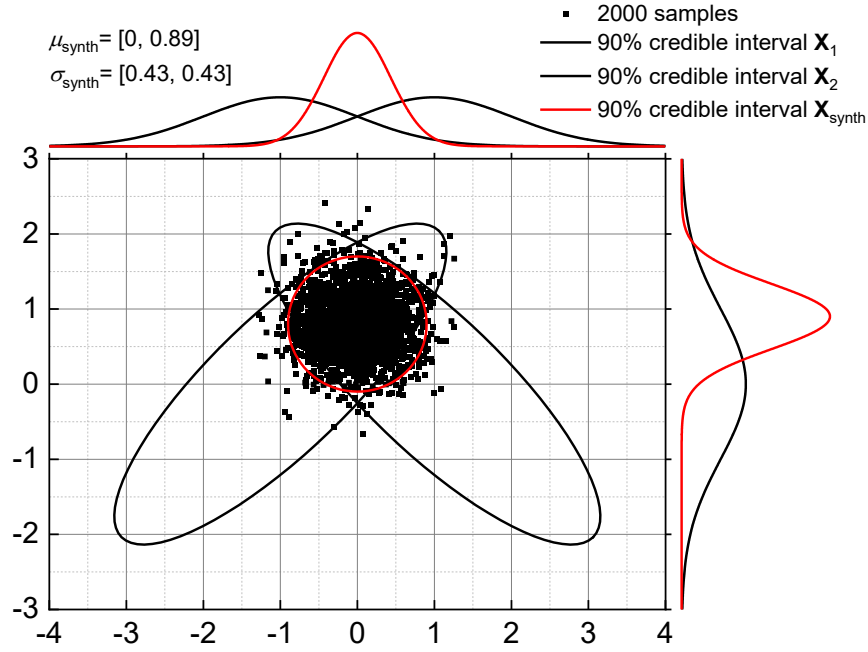


Figure 59: The mean value of both combined probability densities is additionally shifted along the horizontal axis.

Surprisingly, the mean value of the synthesized density shows a shift along the upright axis, which cannot be retrieved by the marginalized probabilities. Cases *i*) to *iii*) demonstrate ideal examples, which are uncommon with general inference problems.

8.4. Results and discussion

8.4.1. Silicon as a test case

The preceding sections (Chapter 8.2 and 8.3) generally highlight the application and advantages of data synthesis. The independent measurement likelihood functions in Figure 53 to Figure 55 show a strong correlation of both parameters of interest $\mathbf{m} = [C_1, C_2]$ and therefore enable the application of data synthesis.

Bayes' equation can be applied to invert more than one likelihood function with prior information to yield the posterior probability density.

$$\begin{aligned}
 & p_{\text{synth}}(\mathbf{x}, \boldsymbol{\theta} | \mathbf{m}_{\text{synth}}) \\
 & \propto p_{\text{LII}}(\mathbf{m}_{\text{LII}} | \mathbf{x}, \boldsymbol{\theta}) p_{\text{peak}}(\mathbf{m}_{\text{peak}} | \mathbf{x}, \boldsymbol{\theta}) p_{\text{LIBS}}(\mathbf{m}_{\text{LIBS}} | \mathbf{x}, \boldsymbol{\theta}) p_{\text{pr}}(\mathbf{m}) p_{\text{pr}}(\boldsymbol{\theta}),
 \end{aligned} \tag{8.6}$$

While Chapter 6.5 (*cf.* values of silicon) sketches the likelihood functions for d_p and α as parameters of interest, here these ones are treated as nuisance parameters and integrated out during marginalization. Now, the evaporation-relevant parameters $\mathbf{m} = [C_1, C_2]$ are the target parameters and the nuisance parameters are $\boldsymbol{\theta} = [d_p, \alpha, F_0, C_{\text{LIBS}}]$.

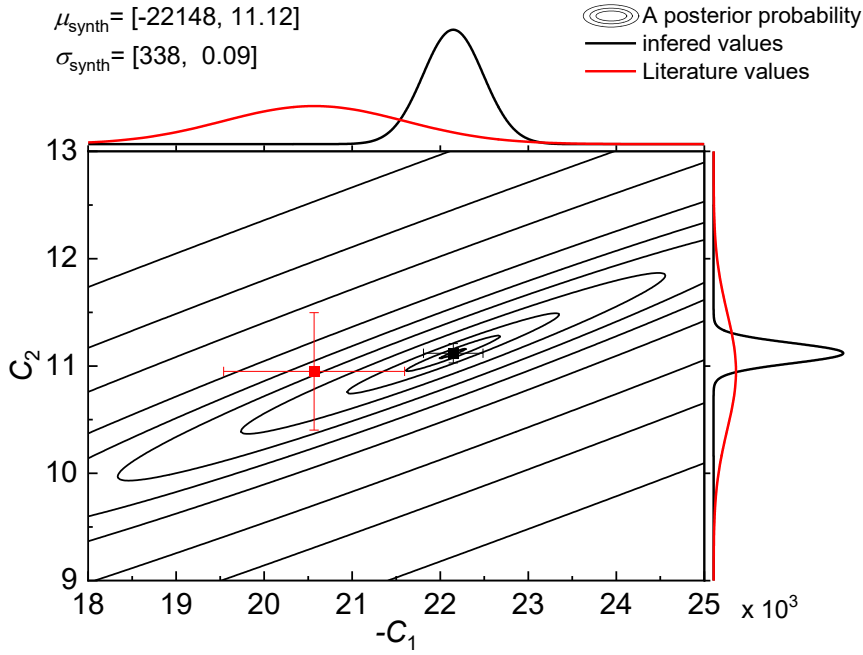


Figure 60: Inferred values of C_1 and C_2 . The log-likelihood is plotted with the black ellipses. The literature values (red dot) and \mathbf{x}_{MAP} (black dot) are illustrated with symbols and the uncertainties with error bars representing the 1σ interval. At the top and right of the graph the marginalized probability densities of the literature and a posterior data are shown.

The marginalized maximum *a posteriori* estimate only taking C_1 and C_2 into account together with the linearized probability density is shown in Figure 60.

Generally, the inferred likelihood function, uncertainties, and estimates are comparable to the ones calculated out of the single measurements. The maximum a posteriori estimate is $\mathbf{x}_{\text{synth}} = [-22148, 11.12]$ with a standard deviation of $\boldsymbol{\sigma}_{\text{synth}} = [338, 0.09]$.

The benefit of data synthesis can be assessed by comparing the posterior probability density to the ones obtained using each data set individually. As already mentioned the standard deviation is $\boldsymbol{\sigma}_{\text{synth}} = [338, 0.09]$, and 25% smaller than the standard deviation of convolution of the four independent marginal distributions: Literature values; LII; Peak temperature; and LIBS, with $\boldsymbol{\sigma}_{\text{marginal}} = [427, 0.13]$.

To get an impression of the results of data synthesis, Figure 61 shows the 90% credibility intervals and marginalized probability densities of the discussed techniques. Obviously, the synthesized value of C_1 is strongly influenced by the correlation of all the parameters of interest, as well as the nuisance parameters, resulting in a shift along the C_1 -axis. The example *iv*) in Chapter 8.3, Figure 59 shows such a case, where the correlation of two parameters forces the mean value μ_{synth} to leave the connection line between the mean values of the originating probability distributions. Here, the dimensionality of the problem is six, and therefore, the correlation between the four nuisance parameters is difficult to assess.

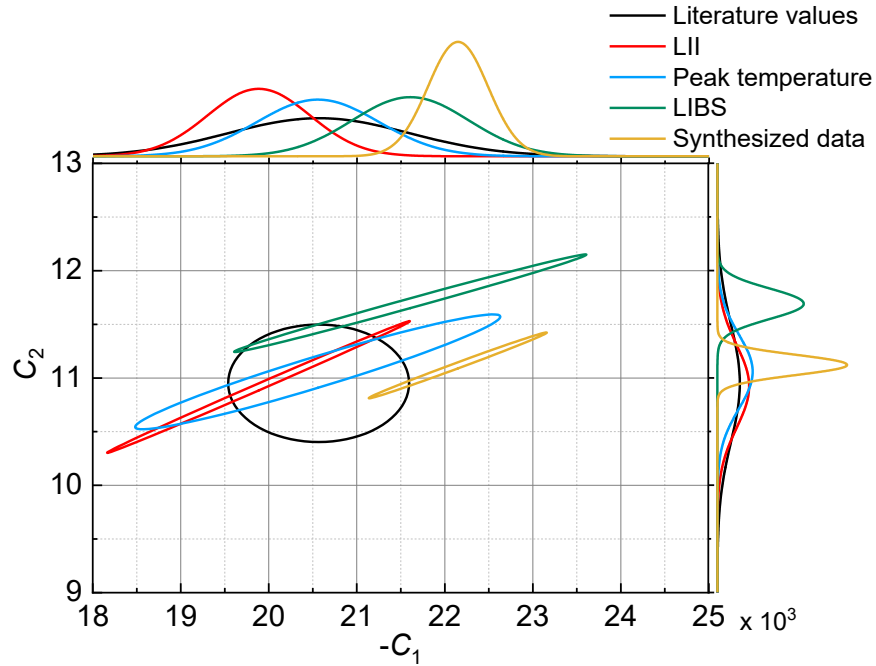


Figure 61: 90% credible intervals of previously described measurements and the literature values. At the edges of the graph, the marginalized probability densities of those measurements are plotted.

8.4.2. Refined vapor pressure properties of liquid germanium

Eight million tons of silicon were processed in 2015 [184], while the annual production of germanium was 165 tons in 2014 [185]. The much higher need for silicon, with a nearly five orders of magnitude higher production, correlates with the weaker data basis of germanium in the scientific literature.

The revised inference in Chapter 8.1 in general show a reduction of uncertainties in the Antoine coefficients of interest C_1 and C_2 , but a large scattering shown in Table 8. Firstly, *a posteriori* estimates of each individual measurement technique are contained in the 90% credible interval of the literature values. Secondly, the inferred uncertainties are smaller than the literature uncertainties. The biggest improvement was obtained by laser-induced incandescence temperature decay and laser-induced plasma emissions, because both “observe” the impact of evaporation for a longer time. The peak temperature of the laser-heated nanoparticles is reached within the laser pulse duration (approximately 10–15 ns), where evaporation is less significant.

Table 8: Inferred Antoine parameters through temperature decay, peak temperature, and LIBS line intensity measurements for germanium

Technique	C_1	C_2
Literature values	-17300 ± 1730	10.60 ± 0.51
LII – temperature decay, 5 mJ/mm ²	-18297 ± 596	11.16 ± 0.37
LII – peak temperatures, fluence study	-17337 ± 1317	11.10 ± 0.8
LIBS – line emissions, fluence study	-16811 ± 607	11.42 ± 0.39
Data synthesis	-18052 ± 109	11.10 ± 0.03

The data were evaluated analogously to chapter 8.4.1. Figure 62 shows the resulting posterior probability and the marginalized probability distribution of C_1 and C_2 of the synthesized and literature values. Obviously, with $\mathbf{x}_{\text{synth}} = [-18052, 11.10]$, the synthesized parameters of interest show a very good agreement with the provided literature values.

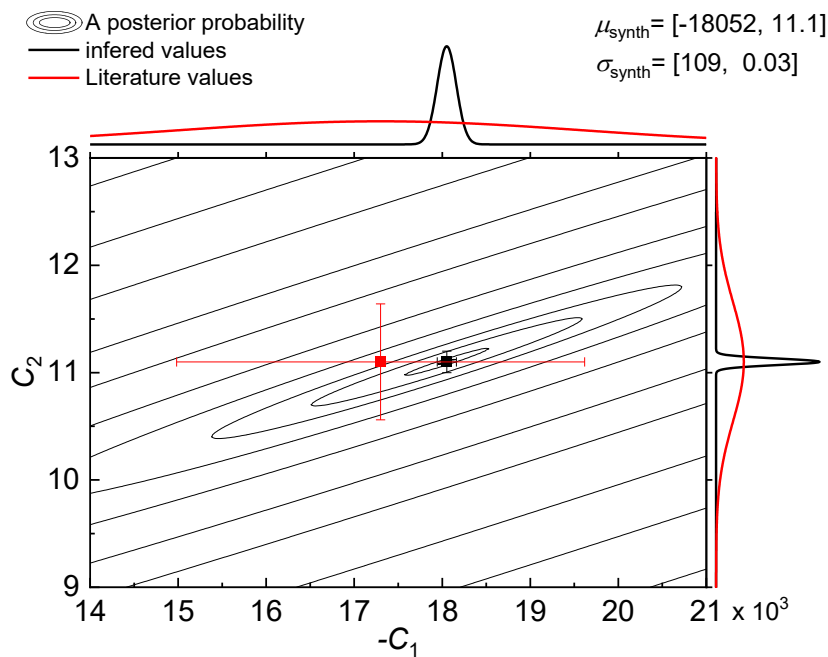


Figure 62: Inferred values of C_1 and C_2 . The log-posterior function is plotted with the black ellipses. The literature values (red dot) and \mathbf{x}_{MAP} (black dot) are illustrated with error bars representing the 1σ interval. At the top and right of the graph the marginalized probability densities of the literature and a posterior data are shown.

In Figure 63, the 90% credible intervals of all presented germanium measurements are assembled in a single graph. The literature values at $\mathbf{x}_{\text{lit}} = [-17300, 11.1]$ have an uncertainty of $\sigma_{\text{lit}} = [-1730, 0.51]$, which is the largest uncertainty in this graph. The other uncertainty ellipses of each applied technique are enveloped by the uncertainty ellipse of the literature values.

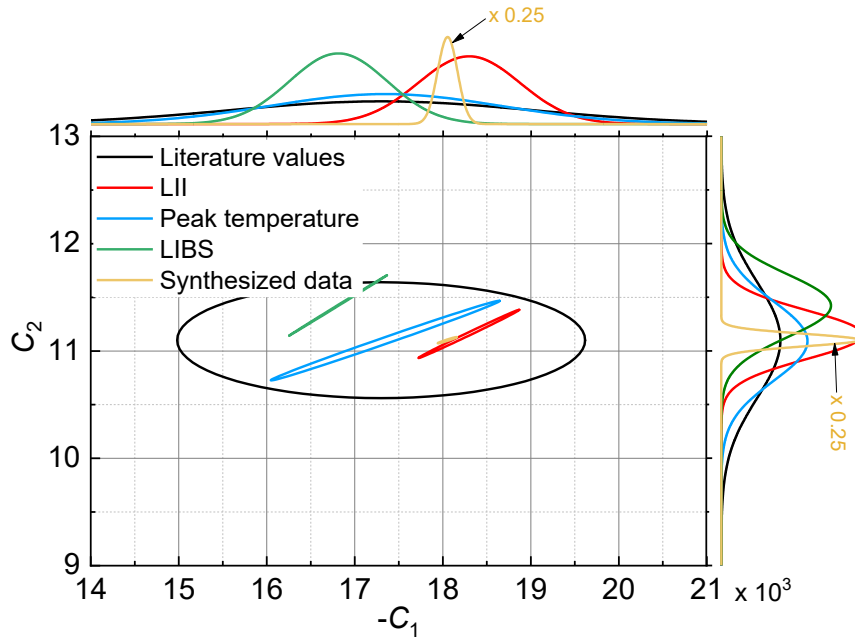


Figure 63: 90% credible intervals of the previously described germanium measurements and the literature values plotted analogously to Figure 61.

8.5. Conclusions

In this Chapter it has been shown that data synthesis can be used to shrink uncertainties when complementary measurements exist. The synthesis approach was shown for two different materials, silicon and germanium, while firstly demonstrating the vapor-pressure parameters for each single measurement technique and then advancing to the data synthesis technique.

With silicon and germanium, a very good agreement between the single measurements and the synthesized data was achieved, where the 90% credible intervals overlap within the literature values. This gives strong emphasis for a consistency in measurement and literature data.

The presented techniques tend to probe independent features of the vapor pressure curve. Especially the LIBS based measurements introduce a large uncertainty of the C_2 parameter for both materials. In contrast, the synthesized values show very good agreement to the literature values in the C_2 values but generally seem to overestimate C_1 .

Both parameters have a different effect on the behavior of the vapor pressure. According to Eq. (6.13) the vaporization enthalpy $\Delta H_v = -C_1 \ln(10)$ is connected to C_1 . As a result, C_1 influences the slope of the vapor pressure curve. C_2 is a scaling parameter, which adjusts the magnitude of evaporation. LII and peak temperature/fluence curve measurements incorporate the temperature. In contrast, the LIBS approach uses a relative intensity measurement and so is insensitive to evaporation parameters scaling the absolute amount of evaporated mass, here C_2 .



9. Outlook

The presented work shows the applicability of laser-based diagnostics on engineered nanoparticles (such as silicon and germanium) for measuring the mean particle size and evaporation parameters C_1 and C_2 . In principle, the measurement techniques are not only limited to these two material systems and can be extended to copper, molybdenum, iron, and many other elementary materials with high evaporation temperature, such that incandescence becomes measurable.

The largest interest for future research should be concentrated on the validating and expanding the spectroscopic model. The spectroscopic model consists two indispensable parts; one part is relevant for calculating the complex refractive index of the material and the second part describes the interaction of light with nanoparticles.

Both parts of the spectroscopic model are necessary to calculate the particle temperature that is the key property for laser-induced incandescence measurements and phase-selective laser-induced breakdown spectroscopy. The spectroscopic model behaves very non-linearly during maximum-likelihood estimation; therefore small uncertainties in the input parameters can introduce large uncertainties in the temperature determination. This uncertainty in the spectroscopic model is going to be transferred into the uncertainty in the quantities of interest: particle diameter, accommodation coefficient, and evaporation properties.

In this work, the calculation of the complex refractive index is governed by the Drude model for metals. Deviations from the simulation to the measurements below 400 nm point towards a more comprehensive theory that should be used to describe the complex band structure of the liquid material. Possible remaining partial covalent character of the atom–atom interaction in the liquid phase requires a model that accounts for additional intraband transitions and their corresponding transition energies.

The interaction of light with the nanoparticles is simulated based on Mie theory. Due to the infinite multipole development of the electromagnetic field, simplifications need to be done. While the parameters of the spectroscopic model can be inferred using the simplifications proposed by Bohren and Huffman [88], the evaluation of spectrally and temporally resolved laser-induced incandescence measurements becomes unfeasible because of the limited computational power. The optimum amount of simplification should be explored in future research.

In the context of particle-size and vapor-pressure-property determination, the application of phase-selective laser-induced breakdown spectroscopy is still young. The proposed mechanism that explains the observed atomic emissions fits very well. Nevertheless, independent validation experiments—probably through pump-probe experiments with an additional tunable dye-laser—are necessary to validate or falsify the presented model. Additionally, only the first, prompt atomic emission can be explained through this model. The longer lasting second peak cannot be

quantified, yet. Finding out the origin of the second peak will support the proposed model and adding it into the particle-property inference process will certainly improve the determination of the desired properties.

Data synthesis approaches can achieve great improvements in measurement uncertainties. In this work, it has been shown, that the uncertainties in vapor pressure properties can be reduced by an all-at-once minimization for various measurement techniques. Obviously, the optical parameters should be the next target parameter. To include the optical properties in a data synthesis approach, the current procedure in LII-signal analysis, going from $I(t, \lambda) \rightarrow T(t) \rightarrow d_p$ in separate steps, must be replaced to evaluate a full LII-signal image $I(t, \lambda) \rightarrow d_p$ directly. With this a direct, coupled inference of ω_p and τ would be possible. In addition, the measurement of the spectrally-resolved line-of-sight attenuation can be included, so that the data synthesis involves TiRe-LII, ps-LIBS, and spectrally-resolved LOSA. With this step, the significance of the individual measurements would be covered correctly.

10. Conclusions

The goal of this work was to explore the applicability of laser-based diagnostics on engineered metallic nanoparticles. The task was subdivided into four research questions that build on one another. In the following, the results related to these questions will be concluded.

1. *How can the temperature of silicon and germanium nanoparticles be determined?*

The essential prerequisite for the analysis of time-resolved laser-induced incandescence (TiRe-LII) measurements and phase-selective laser-induced breakdown spectroscopy (ps-LIBS) is the availability of a working spectroscopic model. The spectroscopic model relates the spectrally-resolved signal intensity to a nanoparticle temperature, which is the key parameter for modeling the heat transfer between nanoparticle and gas phase, and determines the saturation vapor pressure.

In this work, a spectroscopic model was selected that consist of the Drude model of a free electron gas for metals to calculate the complex refractive index and Mie theory to describe the interaction of light with the nanoparticle. The selected model was compared to spectrally-resolved extinction measurements and related to the results of a thorough literature survey. The model shows that the wavelength region that is usually used for TiRe-LII is not sensitive enough for recovering the Drude model parameters with high accuracy. On the one hand, this has a favorable effect, because simulated absorption spectra for a large range of Drude parameters are very similar and therefore, the resulting temperature will not be sensitive to those parameters. On the other hand, the current wavelength range is not suitable to infer the Drude parameters with high significance.

When the scattering particles approximately have the same size as the wavelength of the interacting light, the angular distribution of the scattering exhibits complex structures. In addition, the large imaginary part of the complex index of refraction of the nanomaterial intensifies this effect. Consequentially, the interaction of light with the nanoparticle has been described in this thesis by Mie's theory, which is capable of modeling the light scattering, absorption, and extinction of the materials investigated. A comparison of the simplified Rayleigh approximation with Mie's theory reveals a better consistency of the Mie theory with the performed absorption measurements. Thus, the application of the Rayleigh approximation in the context of TiRe-LII and ps-LIBS seems suitable.

2. *Does the cooling model established for soot-related LII also apply to engineered metallic nanoparticles?*

Time-resolved laser-induced incandescence is often used for characterizing soot aerosols. TiRe-LII applies a heat-and-mass-transfer model (HMT) that links the cooling of the nanoparticles to particle properties like particle diameter, thermal accommodation coefficient, and vapor pressure. The HMT combines evaporative,

conductive, and radiative heat-transport to simulate the nanoparticle cooling subsequent to the heating laser-pulse.

This work focusses on the adoption of the established model for soot to engineered nanoparticles consisting of silicon or germanium. It has been shown, that minimizing strategies of measured and simulated nanoparticle temperature decay yielded a very good agreement in nanoparticle size with the results of *ex situ* transmission electron microscopy.

The largest uncertainties in the HMT were induced by the evaporation part of the heat- and mass-transfer model. Literature values of the Antoine parameters for the saturation vapor pressure were included as normal priors into the inference process and through Bayes' equation translated into a statistically rigorous maximum *a posteriori* estimate. The resulting uncertainties are considerably larger compared to naïve least-squares fitting, but accurately reflect the current state of knowledge.

It has also been discovered that the clean conditions during silicon and germanium synthesis avoid major flaws of LII observed in soot related work that can be caused by changing “maturity” of the soot, contamination of the surface with hydrocarbons, and additional signal contribution from soot precursors and PAHs.

3. *Can the plasma emission be correlated to particle properties and fundamental characteristics such as the evaporation properties?*

At high laser fluences, additional emissions of highly excited species from the nanoparticle vapor were observed. In this work, a thermal-equilibrium approach of the emitted vapor is presented. The vapor “leaves” the nanoparticle surface at the current surface temperature with the corresponding Boltzmann energy-distribution. The evaporated atoms equilibrate with the surrounding gas-phase through a de-excitation cascade. The de-excitation cascade model developed here includes all documented transitions of either silicon or germanium listed in the NIST database. During the cascade, optically visible transitions can be recorded temporally.

The measured line emissions showed a sequence of two intensity peaks, a first, prompt peak at the time of the laser pulse, and a second, delayed peak. The lifetime of the first peak could be identified to be the fluorescence lifetime of the corresponding transition, the origin of the second peak has not yet been fully clarified.

The comparison of the de-excitation cascade with the atomic-line emission-intensity yielded excellent results, and could be used to infer the mean nanoparticle size and the evaporation properties of the aerosol.

4. *Can the large uncertainties of the evaporation properties of high-temperature nanomaterials currently reported in literature be reduced by combining LII and LIBS?*

The individual measurements LII and LIBS already highlight the benefits of laser diagnostics for aerosol diagnostics, but data synthesis techniques can be used to further reduce the remaining uncertainties. The main idea is an all-in-one minimization of all measurements. Due to highly correlated parameters, some of the measurement-specific uncertainties compensate each other. As a result, the measured uncertainties can be further reduced – much more than by simply repeating one of the individual measurements. Data synthesis is well known in control system development but not in laser diagnostics. In this thesis, a rigorous approach has been elucidated.

Due to the computational complexity, not every parameter afflicted with uncertainty can be included into the inference process. The parameters with the presumably largest impact on the overall uncertainty are the Antoine coefficients. These coefficients are in the first instance inferred by TiRe-LII and ps-LIBS individually. Then, data-synthesis combines the measurements of time-resolved laser-induced incandescence at various laser fluences and phase-selective laser-induced breakdown spectroscopy. The resulting standard deviation of the probability density distribution was narrowed by a factor of four and ten, for silicon and germanium, respectively, compared to the probability density distributions from the individual measurements. Even a combination of the individual marginal probability distributions could not improve the uncertainty more than $\sqrt{3}$ times in the presented case.

Another positive aspect of the presented approach is that it could explore temperature ranges that were not yet accessible. A well-established technique like the Knudsen effusion cell can be used to measure the saturation vapor pressure up to approximately 2,500 K. The approach presented here can be applied up to temperatures of 4,500 K, and therefore significantly extends the temperature range for vapor-pressure measurements exceeding the boiling temperature into superheating.

In conclusion, this work highlights the rigorous implementation of statistical approaches for optical aerosol diagnostics. The significance and interpretability of experimental results is greatly increased through a comprehensive discussion of uncertainties.

Publications

Articles in peer-reviewed journals

- C. Weise, J. Menser, S. Kaiser, A. Kempf, I. Wlokas, *Numerical investigation of the process steps in a spray flame reactor for nanoparticle synthesis*, Proceedings of the Combustion Institute 35.2, p. 2259–2266, 2015.
- J. Menser, et al. *Laser-induced incandescence from laser-heated silicon nanoparticles*, Applied Physics B 11.122 (2016) p.1-15.
- K. Daun, J. Menser, R. Mansmann, S. Moghaddam, T. Dreier, C. Schulz, *Spectroscopic models for laser-heated silicon and copper nanoparticles*, Journal of Quantitative Spectroscopy and Radiative Transfer 197, p. 3–11, 2016.
- J. Menser, et al. *Laser-induced atomic emission of silicon nanoparticles during laser-induced heating*, Applied Optics, 56.11, p. 50–57, 2017
- R. Mansmann, T. Terheiden, P. Schmidt, J. Menser, T. Dreier, C. Schulz, *LIISim: a modular signal processing toolbox for laser-induced incandescence measurements*, Applied Physics B 124.4, p. 69, 2018
- J. Menser, F. Schneider, T. Dreier, S. Kaiser, *Multi-pulse shadowgraphic RGB illumination and detection for flow tracking*, Experiments in Fluids 59.6, p. 60, 2018

Non peer-reviewed contributions

- J. Menser, et al., *Approach to standardize a spray-flame nanoparticle synthesis burner*, LII Workshop, 2014.
- J. Menser, et al., *Spectrally- and temporally-resolved laser-induced incandescence (LII) on gas-borne silicon nanoparticles*, LII Workshop, 2014.
- J. Menser, et al., *Multi-pulse RGB illumination and detection for particle tracking velocimetry*, Proceedings of the European Combustion Meeting, 2015.
- K. Daun, J. Menser, et al., *Laser-Induced Incandescence Measurements of Silicon and Copper Nanoparticles: Spectroscopic Model*, ICHMT digital library, 2016

Conference presentations

- J. Menser, et al., *Laser-induced atomic emission of silicon nanoparticles during synthesis in a microwave plasma reactor*, Laser Applications to Chemical, Security and Environmental Analysis, Heidelberg, Germany, 2016.
- J. Menser, et al., *Validation of the evaporation model for LII/LIBS characterization of silicon nanoparticles*, Workshop on laser-induced incandescence, Tahoe City, CA, USA, 2016

-
- J. Menser, et al., *Optical Properties of Gas-borne Silicon and Germanium Nanoparticles: Optical Extinction and Laser-induced Emission*, Gas-phase Synthesis of Functional Nanomaterials: Fundamental Understanding, Modeling and Simulation, Scale-up, Duisburg, Germany, 2017
 - J. Menser, et al., *Transition from laser-induced incandescence (LII) to laser-induced breakdown (LIBS)*, Workshop on laser-induced incandescence, Tutzing, Germany 2018
 - J. Menser, et al., *Instantaneous 3D imaging of turbulent stratified methane/air flames using computed tomography of chemiluminescence*, International Conference on Experimental Fluid Mechanics, Munich, Germany, 2018

References

1. Aster, R.C., B. Borchers, and C.H. Thurber, *Parameter estimation and inverse problems*. 2005, Elsevier Academic Press, Amsterdam, The Netherlands.
2. Leparoux, M., C. Schreuders, and P. Fauchais, *Improved plasma synthesis of Si-nanopowders by quenching*. *Adv. Eng. Mat.*, 2008. **10**(12): p. 1147-1150.
3. Hartner, S., et al., *Electrical Transport in Semiconductor Nanoparticle Arrays: Conductivity, Sensing and Modeling*, in *Nanoparticles from the Gasphase: Formation, Structure, Properties*, A. Lorke, et al., Editors. 2012, Springer Berlin Heidelberg: Berlin, Heidelberg. p. 231-271.
4. Mangolini, L., E. Thimsen, and U. Kortshagen, *High-yield plasma synthesis of luminescent silicon nanocrystals*. *Nano Lett.*, 2005. **5**(4): p. 655-659.
5. Schierning, G., et al., *Microcrystalline silicon formation by silicon nanoparticles*. *Journal of Applied Physics*, 2008. **103**(8): p. 084305-6.
6. Qualcomm. *Snapdragon 8cx Compute Platfor*. 2018 21.12.2018]; Available from: <https://www.qualcomm.com/products/snapdragon-8cx-compute-platform>.
7. Hülser, T., et al., *Gas-phase synthesis of nanoscale silicon as an economical route towards sustainable energy technology*. *KONA Powder and Particle Journal*, 2011. **29**(29): p. 191-207.
8. Hecht, C., et al., *Gas-temperature imaging in a microwave-plasma nanoparticle-synthesis reactor using multi-line NO-LIF thermometry*. *Z. Phys. Chem.*, 2011. **225**(11-12): p. 1225-1235.
9. Feroughi, O.M., et al., *Experimental and numerical study of a HMDSO-seeded premixed laminar low-pressure flame for SiO₂ nanoparticle synthesis*. *Proc. Combust. Inst.*, 2016. **36**: p. in press.
10. Zhang, Y., et al., *Novel low-intensity phase-selective laser-induced breakdown spectroscopy of TiO₂ nanoparticle aerosols during flame synthesis*. *Combustion and Flame*, 2013. **160**(3): p. 725-733.
11. O'Farrell, N., A. Houlton, and B.R. Horrocks, *Silicon nanoparticles: applications in cell biology and medicine*. *International Journal of Nanomedicine*, 2006. **1**(4): p. 451-472.
12. Zhou, X., et al., *Facile synthesis of silicon nanoparticles inserted into graphene sheets as improved anode materials for lithium-ion batteries*. *Chemical Communications*, 2012. **48**(16): p. 2198-2200.
13. Kuneš, J., *Dimensionless physical quantities in science and engineering*. 2012: Elsevier.
14. Mijatovic, D., J.C. Eijkel, and A. van den Berg, *Technologies for nanofluidic systems: top-down vs. bottom-up—a review*. *Lab on a Chip*, 2005. **5**(5): p. 492-500.
15. Wang, Y. and Y. Xia, *Bottom-up and top-down approaches to the synthesis of monodispersed spherical colloids of low melting-point metals*. *Nano letters*, 2004. **4**(10): p. 2047-2050.
16. Xia, D., et al., *Top-down approaches to the formation of silica nanoparticle patterns*. *Langmuir*, 2007. **23**(10): p. 5377-5385.

-
17. Stein, M., D. Kiesler, and F. Kruijs, *Effect of carrier gas composition on transferred arc metal nanoparticle synthesis*. Journal of Nanoparticle Research, 2013. **15**(1): p. 1-14.
 18. Tiwari, D.K., J. Behari, and P. Sen, *Time and dose-dependent antimicrobial potential of Ag nanoparticles synthesized by top-down approach*. Current Science, 2008: p. 647-655.
 19. Onischuk, A.A., et al., *Studying of silane thermal decomposition mechanism*. International Journal of Chemical Kinetics, 1998. **30**(2): p. 99-110.
 20. Dejoseph, C.A., P.D. Haaland, and A. Garscadden, *On the Decomposition of Silane in Plasma Deposition Reactors*. IEEE Transactions on Plasma Science, 1986. **14**(2): p. 165-172.
 21. Giesen, B., et al., *Formation of Si-nanoparticles in a microwave reactor: Comparison between experiments and modelling*. Journal of Nanoparticle Research, 2005. **7**(1): p. 29-41.
 22. Kammler, H.K., L. Mädler, and S.E. Pratsinis, *Flame Synthesis of Nanoparticles*. Chemical Engineering and Technology, 2001. **24**(6): p. 583-596.
 23. Pratsinis, S.E., *Flame aerosol synthesis of ceramic powders*. Progress in Energy and Combustion Science, 1998. **24**(3): p. 197-219.
 24. Mädler, L., et al., *Controlled synthesis of nanostructured particles by flame spray pyrolysis*. Journal of Aerosol Science, 2002. **33**(2): p. 369-389.
 25. Li, S., et al., *Flame aerosol synthesis of nanostructured materials and functional devices: Processing, modeling, and diagnostics*. Progress in Energy and Combustion Science, 2016. **55**: p. 1-59.
 26. Chrystie, R.S., et al., *SiO multi-line laser-induced fluorescence for quantitative temperature imaging in flame-synthesis of nanoparticles*. Applied Physics B, 2017. **123**(4): p. 104.
 27. Bessler, W.G. and C. Schulz, *Quantitative multi-line NO-LIF temperature imaging*. Applied Physics B, 2004. **78**(5): p. 519-533.
 28. Crosley, D.R. and G.P. Smith, *Rotational energy transfer and LIF temperature measurements*. Combustion and Flame, 1982. **44**(1): p. 27-34.
 29. Reschiglian, P., et al., *Chemiluminescence and bioluminescence: past, present and future*. 2010: Royal Society of Chemistry.
 30. Shanker, R., C. Linton, and R. Verma, *The chemiluminescent flame spectrum of SiO*. Journal of Molecular Spectroscopy, 1976. **60**(1-3): p. 197-209.
 31. Kluge, S., H. Wiggers, and C. Schulz, *Mass spectrometric analysis of clusters and nanoparticles during the gas-phase synthesis of tungsten oxide*. Proceedings of the Combustion Institute, 2017. **36**(1): p. 1037-1044.
 32. Schulz, C., et al., *Laser-induced incandescence: recent trends and current questions*. Applied Physics B, 2006. **83**(3): p. 333-354.
 33. Michelsen, H.A., et al., *Laser-induced incandescence: Particulate diagnostics for combustion, atmospheric, and industrial applications*. Progress in Energy and Combustion Science, 2015. **51**: p. 2-48.

-
34. Menser, J., et al., *Laser-induced incandescence from laser-heated silicon nanoparticles*. Applied Physics B, 2016. **122**(11): p. 277.
 35. Menser, J., et al., *Laser-induced atomic emission of silicon nanoparticles during laser-induced heating*. Applied Optics, 2017. **56**(11): p. E50-E57.
 36. Roth, P. and A.V. Filippov, *In situ ultrafine particle sizing by a combination of pulsed laser heatup and particle thermal emission*. Journal of Aerosol Science, 1996. **27**(1): p. 95-104.
 37. Vander Wal, R.L., T.M. Ticich, and A.B. Stephens, *Can soot primary particle size be determined using laser-induced incandescence?* Combustion and Flame, 1999. **116**(1): p. 291-296.
 38. Sipkens, T.A., et al., *In situ nanoparticle size measurements of gas-borne silicon nanoparticles by time-resolved laser-induced incandescence*. Applied Physics B-Lasers and Optics, 2014. **116**(3): p. 623-636.
 39. Mansmann, R., et al., *Sequential signal detection for high dynamic range time-resolved laser-induced incandescence*. Optics Express, 2017. **25**(3): p. 2413-2421.
 40. Goulay, F., et al., *A data set for validation of models of laser-induced incandescence from soot: temporal profiles of LII signal and particle temperature*. Applied Physics B, 2013. **112**(3): p. 287-306.
 41. Mansmann, R., T. Dreier, and C. Schulz, *Performance of photomultipliers in the context of laser-induced incandescence*. Applied Optics, 2017. **56**(28): p. 7849-7860.
 42. Singh, J., et al., *Laser-induced breakdown spectroscopy (LIBS)*. Analytical and Bioanalytical Chemistry, 2011. **400**(10): p. 3191-3192.
 43. Cremers, D.A. and L.J. Radziemski, *Quantitative LIBS Analysis*, in *Handbook of Laser-Induced Breakdown Spectroscopy*. 2013, John Wiley & Sons Ltd. p. 185-222.
 44. Wiens, R.C., S. Maurice, and F. Rull Perez, *The SuperCam remote sensing instrument suite for the Mars 2020 rover mission: A preview*. Spectroscopy, 2017. **32**(LA-UR-17-26876).
 45. Johannes, K., L. Zhongshan, and A. Marcus, *Laser-induced breakdown spectroscopy in a partially premixed turbulent jet flame*. Measurement Science and Technology, 2013. **24**(7): p. 075205.
 46. Hsu, P.S., et al., *Femtosecond-laser-induced plasma spectroscopy for high-pressure gas sensing: Enhanced stability of spectroscopic signal*. Applied Physics Letters, 2018. **113**(21): p. 214103.
 47. Milan, M. and J. Laserna, *Diagnostics of silicon plasmas produced by visible nanosecond laser ablation*. Spectrochimica Acta Part B: Atomic Spectroscopy, 2001. **56**(3): p. 275-288.
 48. Zhang, Y., et al., *A new diagnostic for volume fraction measurement of metal-oxide nanoparticles in flames using phase-selective laser-induced breakdown spectroscopy*. Proceedings of the Combustion Institute, 2015. **35**(3): p. 3681-3688.
 49. Wang, Y. and N. Herron, *Nanometer-sized semiconductor clusters: materials synthesis, quantum size effects, and photophysical properties*. The Journal of Physical Chemistry, 1991. **95**(2): p. 525-532.

-
50. Talebi Moghaddam, S. and K.J. Daun, *Plasma emission during time-resolved laser-induced incandescence measurements of aerosolized metal nanoparticles*. Applied Physics B, 2018. **124**(8): p. 159.
 51. Hoff, P.D., *A first course in Bayesian statistical methods*. 2009: Springer Science & Business Media.
 52. Lynch, S.M., *Introduction to applied Bayesian statistics and estimation for social scientists*. 2007: Springer Science & Business Media.
 53. Andrieu, C., et al., *An Introduction to MCMC for Machine Learning*. Machine Learning, 2003. **50**(1): p. 5-43.
 54. Tierney, L., *A Note on Metropolis-Hastings Kernels for General State Spaces*. The Annals of Applied Probability, 1998. **8**(1): p. 1-9.
 55. Smith, A.F.M. and G.O. Roberts, *Bayesian Computation Via the Gibbs Sampler and Related Markov Chain Monte Carlo Methods*. Journal of the Royal Statistical Society. Series B (Methodological), 1993. **55**(1): p. 3-23.
 56. Åkesson, E.O. and K.J. Daun, *Parameter selection methods for axisymmetric flame tomography through Tikhonov regularization*. Applied Optics, 2008. **47**(3): p. 407-416.
 57. Strong, D. and T. Chan, *Edge-preserving and scale-dependent properties of total variation regularization*. Inverse problems, 2003. **19**(6): p. S165.
 58. von Toussaint, U., *Bayesian inference in physics*. Reviews of Modern Physics, 2011. **83**(3): p. 943-999.
 59. Petermann, N., et al., *Plasma synthesis of nanostructures for improved thermoelectric properties*. Journal of Physics D: Applied Physics, 2011. **44**(17): p. 174034.
 60. Lorke, A., et al., *Nanoparticles from the Gasphase*. NanoScience and Technology. 2012.
 61. Schreiber, P.W., A.M.H. II, and K.R. Benedetto, *Argon and Nitrogen Plasma Viscosity Measurements*. The Physics of Fluids, 1971. **14**(12): p. 2696-2702.
 62. Eckbreth, A.C., *Laser diagnostics for combustion temperature and species*. Vol. 3. 1996: CRC Press.
 63. Knipping, J., et al., *Synthesis of High Purity Silicon Nanoparticles in a Low Pressure Microwave Reactor*. Journal of Nanoscience and Nanotechnology, 2004. **4**(8): p. 1039-1044.
 64. Viñes, F., J.R.B. Gomes, and F. Illas, *Understanding the reactivity of metallic nanoparticles: beyond the extended surface model for catalysis*. Chemical Society Reviews, 2014. **43**(14): p. 4922-4939.
 65. Wiggers, H., *Nanopartikel-Entstehungsvorgänge*. 2015.
 66. Massey, F.J., *The Kolmogorov-Smirnov Test for Goodness of Fit*. Journal of the American Statistical Association, 1951. **46**(253): p. 68-78.
 67. Migliorini, F., K.A. Thomson, and G.J. Smallwood, *Investigation of optical properties of aging soot*. Applied Physics B, 2011. **104**(2): p. 273-283.

-
68. Thomson, K.A., et al., *Diffuse-light two-dimensional line-of-sight attenuation for soot concentration measurements*. Applied Optics, 2008. **47**(5): p. 694-703.
 69. Choi, M.Y. and K.A. Jensen, *Calibration and correction of laser-induced incandescence for soot volume fraction measurements*. Combustion and flame, 1998. **112**(4): p. 485-491.
 70. Little, M.A. and N.S. Jones. *Sparse Bayesian step-filtering for high-throughput analysis of molecular machine dynamics*. in *Acoustics Speech and Signal Processing (ICASSP), 2010 IEEE International Conference on*. 2010. IEEE.
 71. Dasch, C.J., *One-dimensional tomography: a comparison of Abel, onion-peeling, and filtered backprojection methods*. Applied optics, 1992. **31**(8): p. 1146-1152.
 72. Maffi, S., et al., *Investigation on thermal accommodation coefficient and soot absorption function with two-color TIRE-LII technique in rich premixed flames*. Applied Physics B, 2011. **104**(2): p. 357-366.
 73. Snelling, D.R., et al., *Two-dimensional imaging of soot volume fraction in laminar diffusion flames*. Applied Optics, 1999. **38**(12): p. 2478-2485.
 74. Hindasageri, V., R. Vedula, and S. Prabhu, *Thermocouple error correction for measuring the flame temperature with determination of emissivity and heat transfer coefficient*. Review of Scientific Instruments, 2013. **84**(2): p. 024902.
 75. Hindasageri, V., R.P. Vedula, and S.V. Prabhu, *Thermocouple error correction for measuring the flame temperature with determination of emissivity and heat transfer coefficient*. Review of Scientific Instruments, 2013. **84**(2): p. 024902.
 76. Tsutomu, S., *Spectral Emissivity of Silicon*. Japanese Journal of Applied Physics, 1967. **6**(3): p. 339.
 77. Farrow, R.L., P.L. Mattern, and L.A. Rahn, *Comparison between CARS and corrected thermocouple temperature measurements in a diffusion flame*. Applied Optics, 1982. **21**(17): p. 3119-3125.
 78. Kim, C., S. Hong, and Y. Kim, *Radiation-corrective gas temperature measurement in a circular channel*. Advanced Computational Methods and Experiments in Heat Transfer XII, 2012. **75**: p. 157.
 79. Kim, C.S., et al., *Temperature Measurement With Radiation Correction for Very High Temperature Gas*. 2010(49392): p. 99-104.
 80. Bessler, W.G., et al., *A versatile modeling tool for nitric oxide LIF spectra*. Proceedings of the Third Joint Meeting of the U.S. Sections of The Combustion Institute, 2003(Chicago, March 16-19, 2003, paper PI05).
 81. Kronemayer, H., W.G. Bessler, and C. Schulz, *Gas-phase temperature imaging in spray systems using multi-line NO-LIF thermometry*. Applied Physics B, 2005. **81**(8): p. 1071-1074.
 82. Glumac, N.G., *Formation and consumption of SiO in powder synthesis flames*. Combustion and Flame, 2001. **124**(4): p. 702-711.
 83. Buffat, P. and J.P. Borel, *Size effect on the melting temperature of gold particles*. Physical Review A, 1976. **13**(6): p. 2287-2298.

-
84. Sharkov, E.A., *Passive microwave remote sensing of the Earth: physical foundations*. 2003: Springer Science & Business Media.
 85. Mie, G., *Beiträge zur Optik trüber Medien, speziell kolloidaler Metallösungen*. *Annalen der Physik*, 1908. **330**(3): p. 377-445.
 86. Ambrosio, L.A. *Approximations to the Mie scattering coefficients for plasmonic and negative-index Rayleigh scatterers*. in *Microwave and Optoelectronics Conference (IMOC), 2015 SBMO/IEEE MTT-S International*. 2015. IEEE.
 87. García-Cámara, B., et al., *Light scattering resonances in small particles with electric and magnetic properties*. *JOSA A*, 2008. **25**(2): p. 327-334.
 88. Bohren, C.F. and D.R. Huffman, *Absorption and Scattering of Light by Small Particles*. 1983, New York: John Wiley & Sons.
 89. Schebarchov, D., B. Auguie, and E.C. Le Ru, *Simple accurate approximations for the optical properties of metallic nanospheres and nanoshells*. *Physical Chemistry Chemical Physics*, 2013. **15**(12): p. 4233-4242.
 90. Mishchenko, M.I., L.D. Travis, and A.A. Lacis, *Scattering, absorption, and emission of light by small particles*. 2002: Cambridge university press.
 91. Santoro, R., H. Semerjian, and R. Dobbins, *Soot particle measurements in diffusion flames*. *Combustion and Flame*, 1983. **51**(2): p. 203-218.
 92. Dalzell, W. and A. Sarofim, *Optical constants of soot and their application to heat-flux calculations*. *Journal of Heat Transfer*, 1969. **91**(1): p. 100-104.
 93. López-Yglesias, X., P.E. Schrader, and H.A. Michelsen, *Soot maturity and absorption cross sections*. *Journal of Aerosol Science*, 2014. **75**: p. 43-64.
 94. Vander Wal, R.L., *Laser-induced incandescence: excitation and detection conditions, material transformations and calibration*. *Applied Physics B*, 2009. **96**(4): p. 601-611.
 95. Bond, T.C. and R.W. Bergstrom, *Light absorption by carbonaceous particles: An investigative review*. *Aerosol Sci. Tech.*, 2006. **40**(1): p. 27-67.
 96. Hadwin, P.J., et al., *Quantifying uncertainty in soot volume fraction estimates using Bayesian inference of auto-correlated laser-induced incandescence measurements*. *Applied Physics B*, 2016. **122**(1): p. 1-16.
 97. Kawamura, H., et al., *Normal spectral emissivity of undercooled liquid silicon*. *Measurement Science and Technology*, 2005. **16**(2): p. 386-393.
 98. Shvarev, K.M., B.A. Baun, and P.V. Gel'd, *Optical Properties of Liquid Silicon*. *Sov. Phys. Solid State*, 1975. **16**: p. 2111-2112.
 99. Li, K.D. and P.M. Fauchet, *Drude parameters of liquid silicon at the melting temperature*. *Applied physics letters*, 1987. **51**(21): p. 1747-1749.
 100. Kittel, C., *Einführung in die Festkörperphysik*. 2002.
 101. Alekseev, V.A.e., A.A. Andreev, and M. Sadovskii, *Semiconductor-metal transition in liquid semiconductors*. *Physics-Uspekhi*, 1980. **23**(9): p. 551-575.

-
102. Takasuka, E., et al., *Emissivity of liquid germanium in visible and near infrared region*. Journal of applied physics, 1997. **82**(5): p. 2590-2594.
 103. Hodgson, J., *The optical properties of liquid germanium, tin and lead*. Philosophical Magazine, 1961. **6**(64): p. 509-515.
 104. Gibbon, P., *Short Pulse Laser Interactions with Matter: An Introduction*. 2005: Imperial College Press.
 105. Bittencourt, J.A., *Fundamentals of plasma physics*. 2013: Springer Science & Business Media.
 106. Lide, D., *The 84th Edition of the CRC Handbook of Chemistry and Physics*. 2004, CRC Press.
 107. Rhim, W., et al., *Measurements of thermophysical properties of molten silicon by a high-temperature electrostatic levitator*. International Journal of Thermophysics, 1997. **18**(2): p. 459-469.
 108. Zhou, Z., S. Mukherjee, and W.-K. Rhim, *Measurement of thermophysical properties of molten silicon using an upgraded electrostatic levitator*. Journal of Crystal Growth, 2003. **257**(3): p. 350-358.
 109. Kimura, S. and K. Terashima, *A review of measurement of thermophysical properties of silicon melt*. Journal of Crystal Growth, 1997. **180**(3-4): p. 323-333.
 110. Rhim, W.-K. and T. Ishikawa, *Thermophysical properties of molten germanium measured by a high-temperature electrostatic levitator*. International Journal of Thermophysics, 2000. **21**(2): p. 429-443.
 111. Nakanishi, H., et al., *Temperature dependence of the density of molten germanium and silicon measured by a newly developed Archimedian technique*. Journal of Crystal Growth, 1999. **203**(1): p. 75-79.
 112. Sato, Y., et al., *Viscosity and density of molten germanium*. High Temperatures. High Pressures, 2000. **32**(3): p. 253-260.
 113. Martin-Garin, L., et al., *Masses volumiques de l'argent, du germanium et des alliages Ag-Ge à l'état liquide*. Journal of the Less Common Metals, 1975. **41**(1): p. 65-76.
 114. Cusack, N., *The electronic properties of liquid metals*. Reports on Progress in Physics, 1963. **26**(1): p. 361.
 115. Sasaki, H., et al., *Temperature dependence of the electrical resistivity of molten silicon*. Japanese journal of applied physics, 1995. **34**(7R): p. 3426.
 116. Schnyders, H. and J. Van Zytveld, *Electrical resistivity and thermopower of liquid Ge and Si*. Journal of Physics: Condensed Matter, 1996. **8**(50): p. 10875.
 117. Fuchs, M.S.K., *Optical properties of liquid silicon: the integral equation approach*. Journal of Physics: Condensed Matter, 2000. **12**(19): p. 4341.
 118. Takasuka, E., et al., *Emissivity of liquid silicon in visible and infrared regions*. Journal of applied physics, 1997. **81**(9): p. 6384-6389.
 119. Jellison, G.E. and D.H. Lowndes, *Measurements of the Optical Properties of Silicon and Germanium using Nanosecond Time-Resolved Ellipsometry*. App. Phys. Lett., 1987. **51**: p. 352-354.

-
120. Li, K.D. and P.M. Fauchet, *Picosecond determination of the dielectric function of liquid silicon at 1064 nm*. Solid State Communications, 1987. **61**(3): p. 207-209.
 121. Abraham, A., J. Tauc, and B. Velicky, *Optical Properties of Liquid Germanium*. Physica Status Solidi, 1963. **3**(4): p. 767-772.
 122. Jellison, G.E. and D.H. Lowndes, *Measurements of the optical properties of liquid silicon and germanium using nanosecond time-resolved ellipsometry*. Applied Physics Letters, 1987. **51**(5): p. 352-354.
 123. Werner, W.S.M., *Electron transport in solids for quantitative surface analysis*. Surface and Interface Analysis, 2001. **31**(3): p. 141-176.
 124. Seah, M.P. and W.A. Dench, *Quantitative electron spectroscopy of surfaces: A standard data base for electron inelastic mean free paths in solids*. Surface and Interface Analysis, 1979. **1**(1): p. 2-11.
 125. Ashcroft, N.W. and D.N. Mermin, *Festkörperphysik*. 3. verbesserte Auflage ed. 2007: Oldenbourg.
 126. Georgescu, D., et al., *Experimental assessment of the phonon confinement in TiO₂ anatase nanocrystallites by Raman spectroscopy*. Journal of Raman Spectroscopy, 2012. **43**(7): p. 876-883.
 127. Zhu, K.-R., et al., *Size and phonon-confinement effects on low-frequency Raman mode of anatase TiO₂ nanocrystal*. Physics Letters A, 2005. **340**(1-4): p. 220-227.
 128. Wedler, G., *Lehrbuch der Physikalischen Chemie*. 2005: Wiley.
 129. Michelsen, H., et al., *Modeling laser-induced incandescence of soot: a summary and comparison of LII models*. Applied Physics B, 2007. **87**(3): p. 503-521.
 130. Liu, F., et al., *Heat conduction from a spherical nano-particle: status of modeling heat conduction in laser-induced incandescence*. Applied physics B, 2006. **83**(3): p. 355-382.
 131. Liu, F., et al., *Effects of primary soot particle size distribution on the temperature of soot particles heated by a nanosecond pulsed laser in an atmospheric laminar diffusion flame*. International Journal of Heat and Mass Transfer, 2006. **49**(3-4): p. 777-788.
 132. Sutherland, W., *LII. The viscosity of gases and molecular force*. The London, Edinburgh, and Dublin Philosophical Magazine and Journal of Science, 1893. **36**(223): p. 507-531.
 133. Dawe, R.A. and E.B. Smith, *Viscosities of the Inert Gases at High Temperatures*. The Journal of Chemical Physics, 1970. **52**(2): p. 693-703.
 134. Loyalka, S.K., *Mechanics of aerosols in nuclear reactor safety: A review*. Progress in Nuclear Energy, 1983. **12**(1): p. 1-56.
 135. Vander Wal, R.L. and M.Y. Choi, *Pulsed laser heating of soot: morphological changes*. Carbon, 1999. **37**(2): p. 231-239.
 136. Sipkens, T., et al., *Examination of the thermal accommodation coefficient used in the sizing of iron nanoparticles by time-resolved laser-induced incandescence*. Applied Physics B, 2015. **119**(4): p. 561-575.
 137. Sipkens, T., et al. *Thermal Accommodation Coefficients for Time-Resolved Laser-Induced Incandescence Sizing of Metal Nanoparticles*

-
- in Monatomic Gases.* in *ASME 2012 International Mechanical Engineering Congress and Exposition*. 2012. American Society of Mechanical Engineers.
138. Rowley, R., et al., *DIPPR data compilation of pure chemical properties*. Design Institute for Physical Properties, 2006.
 139. Tomooka, T., Y. Shoji, and T. Matsui, *High Temperature Vapor Pressure of Si*. J Mass Spectrom Soc Jpn, 1999. **47**(1): p. 49-53.
 140. Lopatin, S.I., et al., *Determination of the saturation vapor pressure of silicon by Knudsen cell mass spectrometry*. Russian Journal of Inorganic Chemistry, 2012. **57**(2): p. 219-225.
 141. Sevast'yanov, V.G., et al., *Experimental and Theoretical Determination of the Saturation Vapor Pressure of Silicon in a Wide Range of Temperatures*. Russian Journal of Inorganic Chemistry, 2010. **55**(13): p. 2073-2088.
 142. Desai, P.D., *Thermodynamic Properties of Iron and Silicon*. Journal of Physical and Chemical Reference Data, 1986. **15**(3): p. 967-983.
 143. Sevast'yanov, V., et al., *Experimental and theoretical determination of the saturation vapor pressure of silicon in a wide range of temperatures*. Russian Journal of Inorganic Chemistry, 2010. **55**(13): p. 2073-2088.
 144. Stevanovic, M.M., *Evaluation of the Temperature-Dependence of Vapor-Pressure for Silicon and Germanium*. Thermochemica Acta, 1984. **77**(1-3): p. 167-176.
 145. Severin, V.I., et al., *Saturated Vapour Pressure and Enthalpy of Sublimation of Germanium*. Mendeleev Communications, 1991. **1**(2): p. 43-46.
 146. Lamoreaux, R., D. Hildenbrand, and L. Brewer, *High-Temperature Vaporization Behavior of Oxides II. Oxides of Be, Mg, Ca, Sr, Ba, B, Al, Ga, In, Tl, Si, Ge, Sn, Pb, Zn, Cd, and Hg*. Journal of physical and chemical reference data, 1987. **16**(3): p. 419-443.
 147. Searcy, A.W. and R.D. Freeman, *Measurement of the Molecular Weights of Vapors at High Temperature. II. The Vapor Pressure of Germanium and the Molecular Weight of Germanium Vapor*. The Journal of Chemical Physics, 1955. **23**(1): p. 88-90.
 148. Billings, B.H. and D.E. Gray, *American Institute of Physics handbook*. 3rd ed ed. 1972: McGraw-Hill, New York.
 149. Honig, R.E., *Vapor pressure data for the solid and liquid elements*. RCA review, 1969. **30**: p. 285-305.
 150. Nanda, K.K., et al., *Higher Surface Energy of Free Nanoparticles*. Physical Review Letters, 2003. **91**(10): p. 106102.
 151. Thomson, W., *4. On the equilibrium of vapour at a curved surface of liquid*. Proceedings of the Royal Society of Edinburgh, 1872. **7**: p. 63-68.
 152. Millot, F., et al., *The surface tension of liquid silicon at high temperature*. Materials Science and Engineering a-Structural Materials Properties Microstructure and Processing, 2008. **495**(1-2): p. 8-13.
 153. Aqra, F. and A. Ayyad, *Theoretical Study of a Thermophysical Property of Molten Semiconductors*. Journal of Metallurgy, 2011. **2011**.

-
154. Bladh, H., *On the Use of Laser-Induced Incandescence for Soot Diagnostics*, in *Combustion Physics, Department of Physics*. 2007, Lund University.
 155. Melton, L.A., *Soot diagnostics based on laser heating*. Applied Optics, 1984. **23**(13): p. 2201-2208.
 156. Sipkens, T.A. and K.J. Daun, *Defining regimes and analytical expressions for fluence curves in pulsed laser heating of aerosolized nanoparticles*. Opt Express, 2017. **25**(5): p. 5684-5696.
 157. Sipkens, T.A., *Advances in the Modeling of Time-Resolved Laser-Induced Incandescence*. 2018.
 158. Beyer, V. and D.A. Greenhalgh, *Laser induced incandescence under high vacuum conditions*. Applied Physics B, 2006. **83**(3): p. 455-467.
 159. Giulietti, D. and L.A. Gizzi, *X-ray emission from laser-produced plasmas*. La Rivista del Nuovo Cimento (1978-1999), 2008. **21**(10): p. 1-93.
 160. Sipkens, T.A., et al., *General error model for analysis of laser-induced incandescence signals*. Applied optics, 2017. **56**(30): p. 8436-8445.
 161. Ytrehus, T. and S. Østmo, *Kinetic theory approach to interphase processes*. International Journal of Multiphase Flow, 1996. **22**(1): p. 133-155.
 162. Koffman, L., M. Plesset, and L. Lees, *Theory of evaporation and condensation*. The Physics of fluids, 1984. **27**(4): p. 876-880.
 163. Rouse, A., et al., *Non-thermal melting in semiconductors measured at femtosecond resolution*. Nature, 2001. **410**: p. 65.
 164. Capitelli, M., et al., *Laser-induced plasma expansion: theoretical and experimental aspects*. Spectrochimica Acta Part B: Atomic Spectroscopy, 2004. **59**(3): p. 271-289.
 165. Hague, C.F., C. Senemaud, and H. Ostrowiecki, *Experimental density of states of liquid silicon*. Journal of Physics F: Metal Physics, 1980. **10**(10): p. L267.
 166. Aguilera, J.A. and C. Aragón, *Characterization of a laser-induced plasma by spatially resolved spectroscopy of neutral atom and ion emissions.: Comparison of local and spatially integrated measurements*. Spectrochimica Acta Part B: Atomic Spectroscopy, 2004. **59**(12): p. 1861-1876.
 167. Kung, R.T.V. and C.H. Chang, *Neutral Bremsstrahlung radiation of Ne, Ar and O*. Journal of Quantitative Spectroscopy and Radiative Transfer, 1976. **16**(7): p. 579-586.
 168. Liu, H., et al., *Early phase laser induced plasma diagnostics and mass removal during single-pulse laser ablation of silicon*. Spectrochimica Acta Part B: Atomic Spectroscopy, 1999. **54**(11): p. 1607-1624.
 169. Biberman, L. and G. Norman, *Emission of Recombination Radiation and Bremsstrahlung from a Plasma*. J. Quant. Spectry. Radiative Transfer, 1963. **3**(3): p. 221-245.
 170. Weber, J.K.R., et al., *Optical and thermodynamic property measurements of liquid metals and alloys*. Advances in Space Research, 1991. **11**(7): p. 43-52.

-
171. Daun, K., et al., *Spectroscopic models for laser-heated silicon and copper nanoparticles*. Journal of Quantitative Spectroscopy and Radiative Transfer, 2017. **197**: p. 3-11.
172. Dressler, M.J., *The Saha-Langmuir Equation and its Application*. Journal of Applied Physics, 1968. **39**: p. 338-339.
173. Van Vechten, J.A., *Pulsed Laser Annealing and Sputtering*, in *Semiconductions Probed by Ultrafast Laser Spectroscopy, Volume II*. 1984, Academic Press: New York. p. 95-169.
174. Hauge, C.F., C. Senemaud, and H. Ostrowiecki, *Experimental Density of States of Liquid Silicon*. Journal of Physics F: Metal Physics, 1980. **10**: p. L267-L270.
175. Landström, L. and P. Heszler, *Analysis of blackbody-like radiation from laser-heated gas-phase tungsten nanoparticles*. The Journal of Physical Chemistry B, 2004. **108**(20): p. 6216-6221.
176. Perdew, J.P., *Energetics of charged metallic particles: From atom to bulk solid*. Physical Review B, 1988. **37**(11): p. 6175-6180.
177. Leung, T.L.F. and H.M. van Driel, *Time-resolved thermionic and photoemission from nanosecond, pulsed laser excited germanium and silicon*. Applied Physics Letters, 1984. **45**(6): p. 683-685.
178. Liu, J.M., et al., *Phase transformation on and charged particle emission from a silicon crystal surface, induced by picosecond laser pulses*. Applied Physics Letters, 1981. **39**(9): p. 755-757.
179. Martin, W.C. and R. Zalubas, *Energy levels of silicon, Si I through Si XIV*. Journal of Physical and Chemical Reference Data, 1983. **12**(2): p. 323-380.
180. Kramida, A., et al. 2015, National Institute of Standards and Technology, Gaithersburg, MD.
181. Mitrani, J.M., et al., *Modeling thermionic emission from laser-heated nanoparticles*. Applied Physics Letters, 2016. **108**(5): p. 054101.
182. Student, *The Probable Error of a Mean*. Biometrika, 1908. **6**(1): p. 1-25.
183. Golub, G.H. and C. Reinsch, *Singular value decomposition and least squares solutions*. Numerische Mathematik, 1970. **14**(5): p. 403-420.
184. United States Geological Survey. *Mineral Commodity Summaries - Silicon*. 2012 [cited 2018 0.01.2018]; Available from: <https://minerals.usgs.gov/minerals/pubs/commodity/silicon/mcs-2012-simet.pdf>.
185. Weigel, A. *Jahresproduktion von Gallium und Germanium könnte viel höher sein*. 2016 [cited 2018 04.01.2018]; Available from: <https://www.hzdr.de/db/Cms?pOid=47950&pNid=3093>.
186. Viertl, R., *Probability and Bayesian statistics*. 2012: Springer Science & Business Media.
187. Miller, S. and D. Childers, *Probability and random processes: With applications to signal processing and communications*. 2012: Academic Press.
188. Robert, C., *The Bayesian choice: from decision-theoretic foundations to computational implementation*. 2007: Springer Science & Business Media.

-
189. Holland, P.W. and R.E. Welsch, *Robust regression using iteratively reweighted least-squares*. Communications in Statistics-theory and Methods, 1977. **6**(9): p. 813-827.
 190. Wang, Y., *Gauss-Newton method*. Wiley Interdisciplinary Reviews: Computational Statistics, 2012. **4**(4): p. 415-420.
 191. Moré, J.J., *The Levenberg-Marquardt algorithm: implementation and theory*, in *Numerical analysis*. 1978, Springer. p. 105-116.
 192. Marquardt, D.W., *An Algorithm for Least-Squares Estimation of Nonlinear Parameters*. Journal of the Society for Industrial and Applied Mathematics, 1963. **11**(2): p. 431-441.
 193. Conn, A.R., N.I. Gould, and P.L. Toint, *Trust region methods*. 2000: SIAM.
 194. Häggström, O., *Streifzüge durch die Wahrscheinlichkeitstheorie*. 2006: Springer-Verlag.
 195. Dormand, J.R. and P.J. Prince, *A family of embedded Runge-Kutta formulae*. Journal of computational and applied mathematics, 1980. **6**(1): p. 19-26.

Appendix A. Probability density distributions

The probability density distribution $f(\mathbf{x})$ yields a parameter-dependent value with which the parameter is probable [51, 186]. A probability distribution must fulfil:

- f is positive: $f(\mathbf{x}) \geq 0$ for all $\mathbf{x} \in \mathbb{R}$
- f is integrable
- f is normed: $\int_{\Omega} f(x)dx = 1$ or $\sum_{i=-\infty}^{\infty} f(x_i) = 1$

Additionally, the following probability distributions fulfil:

- f is bias-free: The estimated value $E[f(x)] = \int_{-\infty}^{\infty} xf(x)dx$ equals the location parameter μ . The distribution can be assumed for independent variables without inducing an offset to our measurement estimate. (A counterexample is the lognormal-distribution)

The nature of the uncertainty specifies the applicable probability distribution. Figure 64 (left) shows the three most applied continuous probability distributions: normal-distribution (Gaussian); the Lorentz distribution; and the Laplace-distribution. Figure 64 (right) shows the Poisson distribution for four different parameters λ , and for further simplifications a normal distribution. The multivariate case is shown for the normal distribution in Figure 65.

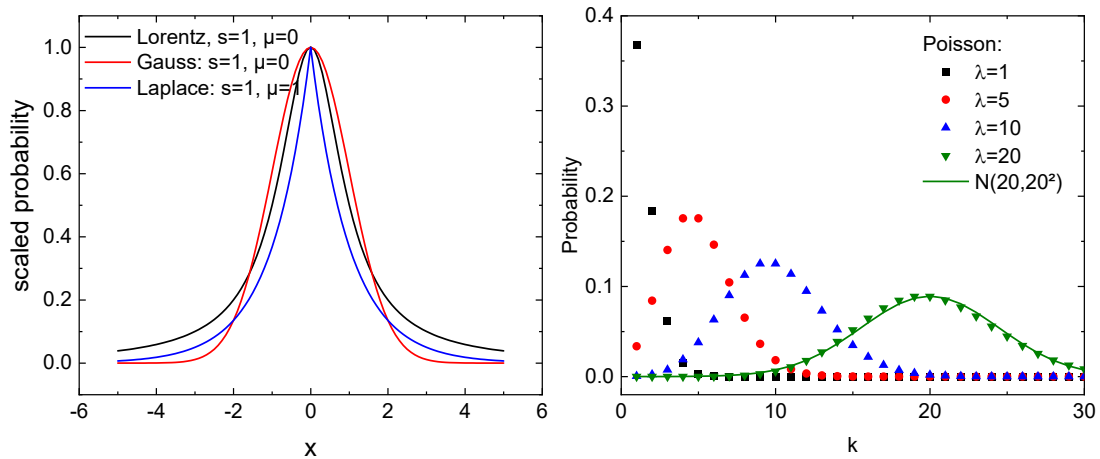


Figure 64: Left: Lorentz, normal, and Laplace distribution normalized to the peak value for comparison. The mean value is 0 and the width parameter set to 1. It shows that the normal distribution exhibits the broadest form in the center region, but then steeply drops to a value near zero. Right: Discrete Poisson distribution for several parameters. With values $\lambda > 30$, the Poisson distribution can be approximated by a normal distribution.

Normal distribution

Undoubtedly, the most prominent representative of probability distribution is the (Gauss)-normal distribution $f(x) = \mathcal{N}(\mu, \sigma^2)$. Governed by the central limit theorem

[187] it can be shown, that a superposition of many randomly influenced distributions will converge to a normal distribution.

$$\mathcal{N}(x|\mu, \sigma^2) = \frac{1}{\sqrt{2\pi\sigma^2}} \exp\left(-\frac{(x-\mu)^2}{2\sigma^2}\right), \quad (\text{A.1})$$

with the mean value μ , and the standard deviation σ .

The normal distribution has following properties:

- A superposition of two normally distributed number sequences $A \sim \mathcal{N}(\mu_A, \sigma_A^2)$ and $B \sim \mathcal{N}(\mu_B, \sigma_B^2)$ will also be a normal distribution with $A + B \sim \mathcal{N}(\mu_A + \mu_B, \sigma_A^2 + \sigma_B^2)$.
- More interestingly, the normal distribution is self-conjugated [188]. The combination of a normal distribution with $p(x|\theta) = \mathcal{N}(x, \sigma^2)$ under the constraints of another normal distribution $p(\theta) = \mathcal{N}(\mu, \tau^2)$, is also normally distributed with $p(\theta|x) = \mathcal{N}\left(\frac{\sigma^2\mu + \tau^2x}{\sigma^2 + \tau^2}, \frac{\sigma^2\tau^2}{\sigma^2 + \tau^2}\right)$. This fact must not hold for other distributions and enables a simplification during estimating model parameters.
- The entropy $H(x) = -\int f(x) \ln f(x) dx$ of the normal distribution is $\ln(\sigma\sqrt{2\pi e})$, which is the highest for all probability distributions. In consequence, the normal distribution can be used as *a priori* distribution for maximum entropy methods.

The normal distribution is suitable to describe electronic noise. The fluctuation of an electronic signal is induced by a random transmission of electrons moving thermally through a potential barrier. The amount of electronic noise scales with $T^{1/2}$. In consequence, a normally distributed noise floor will be present during every measurement. Depending on the signal-to-noise ratio, a proper treatment of this noise needs to be implemented.

Poisson distribution

Since light is quantized, photons are recorded with a continuous mean flux of the light intensity, but with discrete single events. The distribution of events can be explained by the Poisson distribution (Figure 64, right). The Poisson distribution is a discrete distribution

$$\mathcal{P}(k|\lambda) = \frac{\lambda^k}{k!} \exp(-\lambda), \quad (\text{A.2})$$

with the expected value and variance λ , and the control variable k . For low event numbers it shows a strong asymmetric shape but converges for larger event numbers (>30) to a normal distribution with $\mathcal{P}_\lambda \sim \mathcal{N}(\lambda, \lambda^2)$. The possibility to describe the Poisson distribution with the normal distribution is of interest for the proper weighting of the recorded signal intensities.

If two datasets are Poisson-distributed random numbers, the sum of both is also Poisson-distributed; with $A \sim \mathcal{P}(\lambda_1)$ and $B \sim \mathcal{P}(\lambda_2)$ is $A + B \sim \mathcal{P}(\lambda_1 + \lambda_2)$

Lorentz distribution

The Lorentz or Cauchy distribution is a broadly used function in spectroscopy. Light-emitting transitions within an atom or molecule can be modeled by a sinusoidal oscillation enveloped by an exponential intensity decay. The resulting line shape is a Lorentz-distribution.

$$f(x|s, t) = \frac{1}{\pi} \frac{s}{s^2 + (x - t)^2}. \quad (\text{A.3})$$

Also in statistics, the Lorentz distribution is widely used. It is a super-Gaussian function; which is—loosely interpreted—a Gaussian-like function with larger curvature, while distributions, like the Gaussian distribution, exhibit relatively small curvatures. The larger curvature, expressed by the fourth central moment, enables to capture values with more extreme but rare events.

The entropy of the Lorentz distribution is $\log(4\pi s)$.

Laplace distribution

The Laplace-distribution, sometimes called the double-exponential distribution, is composed by two exponential functions originating at the location parameter.

$$f(x|\mu, b) = \frac{1}{2b} \exp\left(-\frac{|x - \mu|}{b}\right). \quad (\text{A.4})$$

The properties of the Laplace distribution are:

- The entropy $H(x) = -\int f(x) \ln f(x) dx$ is $\ln(2be)$.
- The Laplace distribution is super-Gaussian, which means it has a steeper slope around the peak.

The Laplace distribution is, for example used in financial science to calculate currency exchange rates.

Multivariate normal distribution

As parameter estimation is not only applicable to one dimensional problems, but as well to multi-dimensional problems the multivariate normal distribution is shown in the following. The two-dimensional case can be written as

$$\mathcal{N}(\mathbf{x}|\boldsymbol{\mu}, \boldsymbol{\Sigma}^2) = \frac{1}{\sqrt{(2\pi)^p \det(\boldsymbol{\Sigma})}} \exp\left(-\frac{1}{2}(\mathbf{x} - \boldsymbol{\mu})^T \boldsymbol{\Sigma}^{-1}(\mathbf{x} - \boldsymbol{\mu})\right), \quad (\text{A.5})$$

with $\boldsymbol{\mu}$ the p -dimensional vector containing the corresponding mean value, and $\boldsymbol{\Sigma}$ the $p \times p$ Covariance matrix, discussed in the following.

The covariance matrix $\boldsymbol{\Sigma}$ serves for the same purpose for the multivariate normal distribution like the standard deviation σ for the 1D case. With uncorrelated samples, the covariance matrix is diagonal with elements of $1/\sigma^2$ for the associated samples (see Figure 65a). The two dimensions can be separated and treated independently.

$$(a) \rightarrow \boldsymbol{\Sigma}^{-1} = \begin{pmatrix} \sigma_1^{-2} & 0 \\ 0 & \sigma_2^{-2} \end{pmatrix} = \begin{pmatrix} 1 & 0 \\ 0 & 1 \end{pmatrix}. \quad (A.6)$$

The second case (Figure 65b) shows a correlated multivariate normal distribution. One can introduce a correlation coefficient ρ , which specifies the constriction of the normal distribution and scales it to match the required normalization to one and guarantees the preservation of the marginal distribution (the distribution where all but one parameter is deducted). Negative values of ρ result in a constriction along the upward diagonal, while positive values result in a constriction along the downward diagonal.

$$(b) \rightarrow \boldsymbol{\Sigma}^{-1} = \frac{1}{\sqrt{1-\rho^2}} \begin{pmatrix} \sigma_1^{-2} & \rho(\sigma_1\sigma_2)^{-1} \\ \rho(\sigma_1\sigma_2)^{-1} & \sigma_2^{-2} \end{pmatrix} = \begin{pmatrix} 1.66 & -1.33 \\ -1.33 & 1.66 \end{pmatrix} \quad (A.7)$$

For both examples in Figure 65a and b, the marginal distributions are indistinguishable and have the standard deviation $\sigma_1 = \sigma_2 = 1$. Usually, error bars or uncertainties of reported (physical) values only account for these marginal distributions, if at all, but do not quantify the correlation. It should be noted that by using the marginal distribution values during Bayesian inference, the uncertainties of the inferred values are overestimated, which leads to a conservative guess.

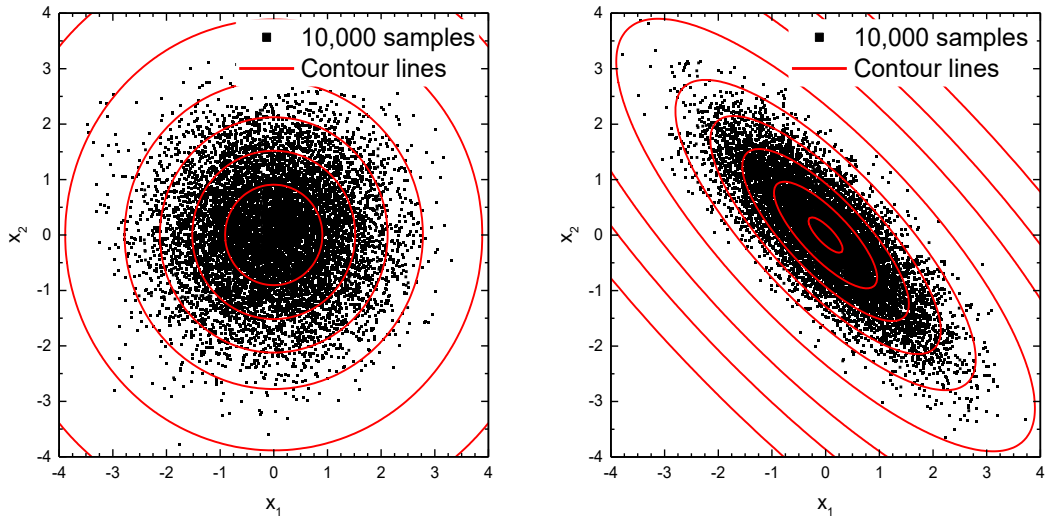


Figure 65: Two-dimensional normal distributions with the same standard variations $\sigma_1 = \sigma_2 = 1$ along the x_1 - and x_2 -axis, and mean value $\mu_1 = \mu_2 = 0$. The red lines show contour lines, and the black symbols 10,000 random samples to illustrate the probability densities. (a) No correlation of the two dimensions with $\rho=0$. This multivariate distribution is constructed from two separated, one dimensional normal distributions. (b) The covariance coefficient is set to $\rho = -0.8$.

Appendix B. Metrics

Mathematically, the length or size of a vector, matrix, or function is defined by a metric, a generalized distance [51]. The metric $\|\cdot\|$ maps a real or complex vector or function to a single positive, real value, which then can be interpreted as a length or distance. During minimization, the metric of the distance between measurement data and model data should be minimized.

Another nature of metrics, which should be considered, is that the metric induces a certain probability distribution, or vice versa, the probability distribution requires the treatment with a particular metric. E.g., the normal distribution will be approximated best with a $(L)2$ -metric, while the Laplace distribution is the counterpart for the $(L)1$ -metric. This does not mean, that a probability distribution presupposes the respective metric, but departing from this characteristic may induce bias errors or inferior convergence.

In the context of Bayes' equation, parameters are not single values, but probability distributions (PDF). These PDFs are used to describe the quantities of interest, such like the probability of a particle size, which is assumed to be normally distributed with the mean value and the corresponding standard deviation. The integration shown in Eq. (A.8) is applicable to all functions within this work. To enable for computer aided numerical minimization the functions are discretized. The continuous functions are sliced into discrete steps which then build vectors. Discrete, vector based values can be normalized by the p -metric.

$$\|f(x)\|_{Lp} = \left(\int_{\Omega} |f(x)|^p dx \right)^{1/p}, \quad \|\mathbf{x}\|_p = \left(\sum_{i=1}^n |x_i|^p \right)^{1/p}, \quad (\text{A.8})$$

where x is a variable, \mathbf{x} is a vector, x_i are the vector elements, and p is the factor of the norm.

For $1 \leq p \leq \infty$ the p - and Lp -metric is properly defined, but only metrics with $p = 1$, 2, and ∞ are commonly used. Figure 66 shows an illustrative example of the three metrics that are presented in the following.

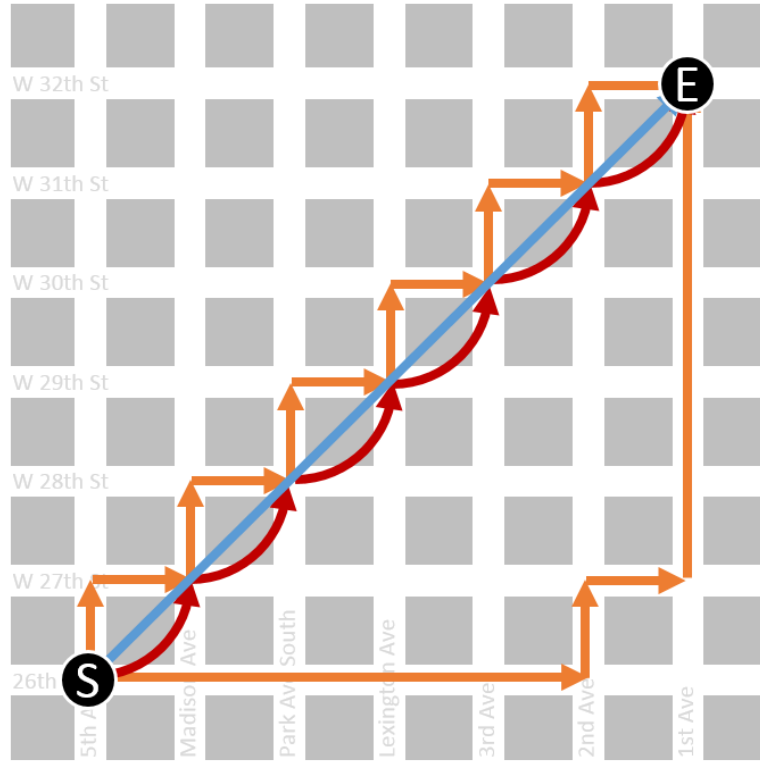


Figure 66: A schematic map of Manhattan as an illustrative example for the presented norms. The Manhattan metric is shown in orange. When each block has a side length of 1, the distance from the start (S) to the end (E) is, for both shown paths, 12. You must move six times east and six times north in random sequence to reach the end. The Euclidian metric (blue) uses the diagonal elements, as well. The length from start to the end is $6 \cdot \sqrt{2} \approx 8.5$. The maximum metric (red) uses the longest distance for scaling, so here the distance between S and E is 6. This image is based loosely on [1].

Euclidian metric, $p = 2$

The Euclidian metric—or the Euclidian distance—is the distance between two points on surfaces or volumes, which can be basically measured by a ruler. With the distance between measurement data and model solution, the principle is, per se the same, but a little more abstract.

The Euclidian metric is induced by the 2- or L_2 -norm, respectively, and during minimization used to define the least-squares solution:

$$\|x\|_2 = \sqrt{\sum_{i=1}^n |x_i|^2}, \quad \|f(x)\|_{L_2} = \sqrt{\int_{\Omega} |f(x)|^2 dx}, \quad (\text{A.9})$$

Manhattan metric, $p = 1$

The Manhattan metric or the 1- or L_1 -norm is calculated by either summing up the absolute values of a vector or by integration of the function over the domain of the function:

$$\|\mathbf{x}\|_1 = \sum_{i=1}^n |x_i|, \|f(x)\|_{L_1} = \int_{\Omega} |f(x)| dx. \quad (\text{A.10})$$

The convergence of the 1- or L_1 - norm is constant over the complete domain and with this, it yields a faster convergence and more often (when possible) finding the minimum to be 0. The (L)1-norm penalizes values, which are located far away from the model-function not that strong so that outliers within the measurement do not distort the minimization process (compared to the (L)2-norm).

The (L)1-norm has several disadvantages. On the one hand, it does not produce unique solutions. The orange line in Figure 66 reveals that both pathways from the start to the end have the same length of 12: the (L)1-norm enhances ambiguous results.

On the other hand, the (L)1-norm assumes Laplace-distributed measurement noise ϵ . Due to a discontinuity in the derivative of the Laplace-function, Eq. (A.4), an analytical solution of the minimization problem is not possible and has to be done iteratively. A common approach for (L)1-norm minimization is the iteratively reweighted least squared (IRLS) algorithm [189], which starts from the L_2 -norm minimum, and then iteratively converges to the (L)1-norm minimum. The derivation of the connection between (L)1-norm minimization and maximum likelihood estimation for Laplacian noise is similar to the (L)2-norm case.

Maximum metric, $p = \infty$

The maximum metric is not further of interest for this work, but is shown for the sake of completeness.

$$\|\mathbf{x}\|_{\infty} = \lim_{p \rightarrow \infty} \left(\sum_{i=1}^n |x_i|^p \right)^{\frac{1}{p}} \rightarrow \|\mathbf{x}\|_{\infty} = \max_i (|x_i|) \quad (\text{A.11})$$

In one dimension, all metrics will result in the same value, but, for a larger number of parameters differ with $\|\mathbf{x}\|_{\infty} \leq \|\mathbf{x}\|_2 \leq \|\mathbf{x}\|_1$.



Appendix C. Application of Bayes' equation

The following examples should help to get familiar with the “Bayesian” way of interpreting data in an ascending complexity. A detailed introduction into parameter estimation and Bayes' equation can be found in [1, 51, 52].

C1. Measurement, Model, Operator

Generally, the analysis of experimental data, which is used to generate further knowledge can be split up into four parts; the measured data $\mathbf{d} = [d_1, d_2, \dots, d_m]$ itself, a model dataset $\mathbf{m} = [m_1, m_2, \dots, m_n]$, a function G , which correlates the measurement with the model data and measurement noise $\boldsymbol{\varepsilon}$,

$$G(\mathbf{m}) = \mathbf{d} + \boldsymbol{\varepsilon}, \quad (\text{A.12})$$

The measured data can be a single value (e.g., a temperature value) a series of values (e.g., evolution of a pressure within a reaction chamber or an absorption spectrum) or even multidimensional data like images, time-series or superposition of different measurement techniques. The vector syntax does not limit the dimension to one. With a proper mapping, multidimensional data can be rewritten to a one dimensional series of values.

The model data is, counterintuitively, not the equation(system) that defines the model. It is the parametrization of the model function. For example, $f(x) = a x + b$ is the model function and $[a \ b]$ are the model data or model parameters. During a minimization $[a \ b]$ are the quantities-of-interest (QoI), while $f(x)$ is required to solve the problem, with $f(x) = a x + b \rightarrow f(x) = G([a \ b])$. For this example we can further simplify $f(x) = [x \ 1] [a \ b]^T$, where $\mathbf{G} = [x \ 1]$ and $\mathbf{m} = [a \ b]$.

The purpose of the model function or operator is, on the one hand, to convert the size of the model parameter vector to the size of the measurement data vector, and on the other hand, to calculate reasonable values to solve the minimization problem. Depending on the complexity of the model, it can be an invertible linear equation system (e.g., linear regression, see section C3), a non-invertible equation system, or even a set of differential and integral equations (our application).

This interpretation automatically induces the need of treatment for measurement errors or measurement noise $\boldsymbol{\varepsilon}$.

Since the model solution that minimizes the 2-norm is known, the propagation of the uncertainty becomes important. Depending on the model complexity, the further proceeding should be subdivided.

Linear model

When using a linear model, e.g., during linear regression, the uncertainty in model parameters can be inferred analytically. For illustration, the model and the

measurement data is weighted with the weighting matrix $\mathbf{W} = \text{diag}(1/\sigma_1, 1/\sigma_2, \dots, 1/\sigma_N)$, with the effect that the weighted data is $\mathbf{d}_w = \mathbf{W}\mathbf{d}$, and the weighted model is $\mathbf{G}_w = \mathbf{W}\mathbf{G}$.

Provided that the measurement data has a covariance $\text{Cov}(\mathbf{d}_w)$ we can then write the covariance of the model parameters $\text{Cov}(\mathbf{m})$

$$\text{Cov}(\mathbf{m}) = (\mathbf{G}_w^T \mathbf{G}_w)^{-1} \mathbf{G}_w^T \text{Cov}(\mathbf{d}_w) \mathbf{G}_w (\mathbf{G}_w^T \mathbf{G}_w)^{-1}, \quad (\text{A.13})$$

and, if the data error is uncorrelated—the off-diagonal elements of the covariance are (close to) zero—and Eq. (A.13) simplifies to

$$\text{Cov}(\mathbf{m}) = (\mathbf{G}_w^T \mathbf{G}_w)^{-1}. \quad (\text{A.14})$$

The uncertainties in the model parameters τ can be estimated by selecting the diagonal elements of the covariance $\text{diag}[\text{Cov}(\mathbf{m})] = (\tau_1^{-2}, \tau_2^{-2}, \dots, \tau_M^{-2})$.

Linearizing the model

Assuming normally distributed data errors, the likelihood follows Eq. (A.18). A closer look to the exponent $(\mathbf{d} - \mathbf{G}\mathbf{m})^T \boldsymbol{\Sigma}_d^{-1} (\mathbf{d} - \mathbf{G}\mathbf{m})$ reveals the possibility to linearize the model $\mathbf{G}\mathbf{m}$ by a Taylor series expansion around the maximum likelihood estimate \mathbf{x}_{MLE} . The linearized model can be converted to approximate the uncertainties of the model parameters,

$$\boldsymbol{\Sigma}_m = (\mathbf{J}^T)^{-1} \boldsymbol{\Sigma}_d (\mathbf{J})^{-1}, \quad (\text{A.15})$$

where $\boldsymbol{\Sigma}_m$ is the covariance matrix of the model parameters and \mathbf{J} is the Jacobian matrix of the model function—which is basically introduced during Taylor series expansion—with $\mathbf{J} = \delta \partial(\mathbf{G}\mathbf{m})/\partial\mathbf{m}$, where $\partial(\mathbf{G}\mathbf{m})/\partial\mathbf{m}$ is the derivative matrix and δ is a scalar infinitesimal change in the model parameters.

The Jacobian can be calculated analytically, but is here inferred by the difference quotient during the minimization process.

Uncertainties of the model parameters are $\text{diag}[\boldsymbol{\Sigma}_m] = [\tau_1^{-2}, \tau_2^{-2}, \dots, \tau_M^{-2}]$.

What is the likelihood function?

The model should be fitted to the measured data $\mathbf{G}\mathbf{m} - \mathbf{d} = \boldsymbol{\varepsilon}$, with $\boldsymbol{\varepsilon}$ normally distributed noise and $\mathbf{d} = [d_1, d_2, \dots, d_N]$ having N measurement points. The joint probability of all data points is the likelihood function, $f(d_1|\mathbf{m}) \cdot f(d_2|\mathbf{m}) \dots f(d_N|\mathbf{m}) = \mathcal{L}(\mathbf{m}|\mathbf{d})$ with

$$\mathcal{L}(\mathbf{m}|\mathbf{d}) = \prod_{i=1}^N \frac{1}{\sigma_i \sqrt{2\pi}} \exp \left\{ -\frac{1}{2} \left(\frac{d_i - (\mathbf{G}\mathbf{m})_i}{\sigma_i} \right)^2 \right\}, \quad (\text{A.16})$$

with σ_i the noise and $(\mathbf{G}\mathbf{m})_i$ the model solution associated to the data point d_i . We can further simplify Eq. (A.16) by involving the product into the exponential function

$$\mathcal{L}(\mathbf{m}|\mathbf{d}) = \frac{1}{(2\pi)^{n/2} \prod_{i=1}^N \sigma_i^2} \exp \left\{ -\frac{1}{2} \sum_{i=1}^N \left(\frac{d_i - (\mathbf{G}\mathbf{m})_i}{\sigma_i^2} \right)^2 \right\}, \quad (\text{A.17})$$

or by using the covariance matrix instead of the standard deviations

$$\mathcal{L}(\mathbf{m}|\mathbf{d}) = \frac{1}{(2\pi)^{\frac{n}{2}} \det(\boldsymbol{\Sigma})} \exp \left\{ -\frac{1}{2} (\mathbf{d} - \mathbf{G}\mathbf{m})^T \boldsymbol{\Sigma}^{-1} (\mathbf{d} - \mathbf{G}\mathbf{m}) \right\}. \quad (\text{A.18})$$

Maximum likelihood estimate

The maximum likelihood estimation is a method, which allows to estimate model parameters maximizing the probability of all possible model realizations compared to the measured data. The goal is to maximize the likelihood function, which, in the end, results in the best consistency between model and data, and is called the maximum likelihood estimate \mathbf{x}_{MLE}

$$\mathbf{x}_{\text{MLE}} = \max \mathcal{L}(\mathbf{m}|\mathbf{d}) = \max \frac{1}{2^{N/2} \prod_{n=1}^N \sigma_i} \exp \left\{ -\frac{1}{2} \sum_{n=1}^N \left(\frac{d_i - (\mathbf{G}\mathbf{m})_i}{\sigma_i^2} \right)^2 \right\}, \quad (\text{A.19})$$

In Appendix A, the multivariate normal distribution is discussed in detail. It is possible to rewrite the σ_i^{-2} term to fit to the covariance matrix, $\boldsymbol{\Sigma} = \text{diag}(\sigma_1^2, \sigma_2^2, \dots, \sigma_N^2)$, which results in a weighted data vector $d_{w,i} = d_i/\sigma_i^2$ and function $\mathbf{G}_{w,i} = \mathbf{G}_i/\sigma_i^2$ and

$$\mathbf{x}_{\text{MLE}} = \max \text{const} \cdot \exp \left\{ -\frac{1}{2} \|\mathbf{d}_w - \mathbf{G}_w \mathbf{m}\|_2^2 \right\}. \quad (\text{A.20})$$

The inverse of the exponential function (the natural logarithm) is monotonic; the constant factor does not affect the position of the maximum value of the likelihood function, as well as the $-1/2$ within the exponent.

$$\mathbf{x}_{\text{MLE}} = \min \|\mathbf{d}_w - \mathbf{G}_w \mathbf{m}\|_2^2, \quad (\text{A.21})$$

which can further be written as

$$\mathbf{x}_{\text{MLE}} = \min (\mathbf{d} - \mathbf{G}\mathbf{m})^T \boldsymbol{\Sigma}^{-1} (\mathbf{d} - \mathbf{G}\mathbf{m}). \quad (\text{A.22})$$

The maximum likelihood estimate \mathbf{x}_{MLE} is the $(L)2$ -norm minimization squared.

Common minimization techniques are the Gauss-Newton[190], Levenberg-Marquardt[191, 192] and the Trust-Region algorithm[193]. The latter two are based on the Gauß-Newton algorithm.

C2. Bayesian inversion

A pregnancy test states a positive result. What is the probability of being pregnant?
[194] We want to find the probability of a born child given a positive pregnancy test $p(\text{preg} | +)$?

Let us now summarize the information and collect the additional information to solve this problem:

- The test is positive
→ $p(+) = 1$
- Probability of getting pregnant is roughly: 7 days of fertility within 28 days of a cycle with a general probability of getting pregnant by a single encounter of 0.25
→ $p(\text{preg}) = 0.0625$
- Sensitivity of pregnancy tests
→ $p(+|\text{preg}) = 0.97$
- Specificity of pregnancy tests
→ $p(+|\text{not preg}) = 0.01$

$$p(\text{preg}|+) = \frac{p(+|\text{preg})p(\text{preg})}{p(+|\text{preg})p(\text{preg}) + p(+|\text{not preg})p(\text{not preg})} = 0.866$$

This means, even with such high sensitivity of 97% the probability of being pregnant is much lower with approx. 87%. Here, Bayes' equation propagates the sensitivity and specificity and inverts the conditional probability.

If the supposed to be pregnant woman wants to increase the significance of the test, she can repeat it, but now with "updated" probability of being pregnant

$$p(\text{preg}) = p(\text{preg} | +) p(+) \rightarrow p(\text{preg} | ++) = 0.998$$

C3. Linear Regression

Linear regression means least-squares fitting on a linear model. In principle, the parameter estimates can be found by inverting the model function \mathbf{G} .

$$\begin{aligned}\mathbf{G}\mathbf{m} &= \mathbf{d} \mid \cdot \mathbf{G}^T \\ \mathbf{G}^T\mathbf{G}\mathbf{m} &= \mathbf{G}^T\mathbf{d} \mid \cdot (\mathbf{G}^T\mathbf{G})^{-1} \\ \mathbf{m} &= (\mathbf{G}^T\mathbf{G})^{-1}\mathbf{G}^T\mathbf{d},\end{aligned}\tag{A.23}$$

with $\mathbf{d} = [d_1, d_2, d_3, \dots, d_m]^T$ a row vector containing the measurement data, $\mathbf{m} = [m_1, m_2, m_3, \dots, m_n]^T$ a column vector containing the model parameters and \mathbf{G} a $m \times n$ matrix, with the equation system of the linear model. We must include the step with the transposed matrix multiplication (row 1 → 2, Eq.(3.1)) because only a square matrix can be inverted.

Also, these steps show why it is called linear regression; the data and the model are combined linearly, but the model function itself can also be non-linear. The

demonstration of such a “simple” example allows the presentation of, firstly the analytic inversion of the model, secondly followed by sampling techniques.

A typical example for linear regression with a non-linear model function is the oblique throw:

$$h(t) = h_0 + v_0 t + \frac{1}{2} g t^2 \quad (\text{A.24})$$

This function can be transformed into the previously mentioned form by

$$h(t) = a + bt + \frac{1}{2} ct^2 = \underbrace{[1 \ t \ 0.5t^2]}_{\mathbf{g}} \underbrace{[a \ b \ c]^T}_{\mathbf{m}} \quad (\text{A.25})$$

Table 9: Data for the numerical experiment, with time vs. height

Time / s	Height / m
0.1	1.44
0.2	1.73
0.3	2.07
0.4	2.21
0.5	2.27
0.6	2.23
0.7	2.07
0.8	1.87
0.9	1.51
1.0	1.07
1.1	0.58

The values of Table 9 are shown in Figure 67 with red symbols.

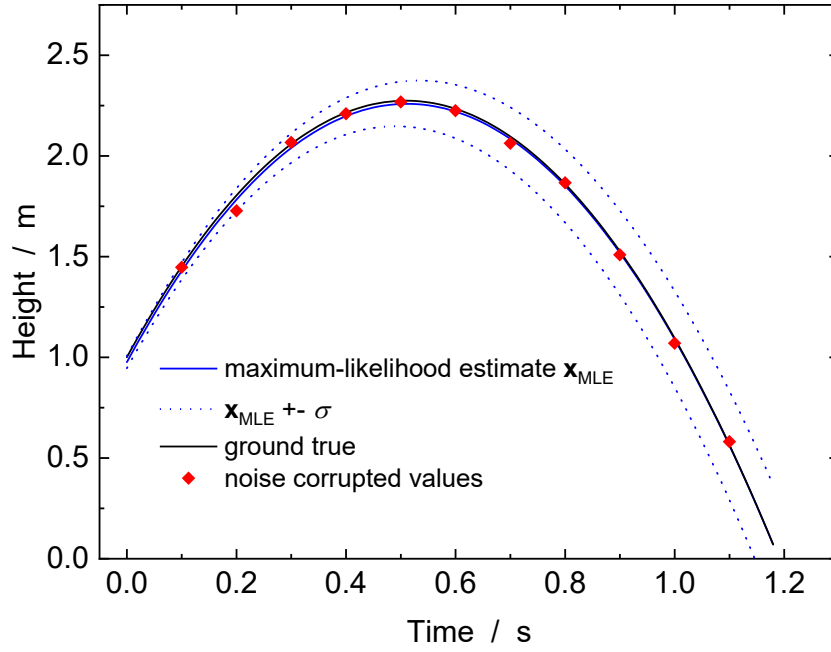


Figure 67: Numerical experiment of the oblique throw. The red symbols are the data of the numerical experiment of Table 9, the black line is the true profile without noise, the blue line is the result of the linear regression together with the blue dotted lines showing the result \pm the standard deviation, resulting in the largest error.

For the considered time steps in Table 9 and the model function (Eqs. (A.23) and (A.25)) it is possible to perform a linear regression:

1. Construction of \mathbf{G} with $G_i = [1 \ t \ 0.5t^2]$, where i indexes each time step

$$\mathbf{G} = \begin{pmatrix} 1 & 0.1 & -0.005 \\ 1 & 0.2 & -0.02 \\ 1 & 0.3 & -0.045 \\ \vdots & \vdots & \vdots \\ 1 & 1.1 & -0.605 \end{pmatrix}$$

2. Inverting \mathbf{G}

$$(\mathbf{G}^T \mathbf{G})^{-1} \mathbf{G}^T = \begin{pmatrix} 0.818 & 0.49 & 0.22 & \dots & 0.27 \\ -2.55 & -1.20 & -0.13 & \dots & -1.64 \\ -3.49 & -1.39 & 0.23 & \dots & -3.49 \end{pmatrix}$$

3. Calculating the model parameters \mathbf{m}^*

$$\mathbf{m}^* = (\mathbf{G}^T \mathbf{G})^{-1} \mathbf{G}^T \mathbf{d} \Leftrightarrow \mathbf{m}^* = \begin{pmatrix} h_0 \\ v_0 \\ g_0 \end{pmatrix} = \begin{pmatrix} 0.96 \\ 5.01 \\ 9.80 \end{pmatrix}$$

4. Demining the norm of the residual in order to attain the standard deviation

$$\|\mathbf{d} - \mathbf{G}\mathbf{m}^*\| = \left\{ \sum (\mathbf{d} - \mathbf{G}\mathbf{m}^*)^2 \right\}^{1/2} = 0.0775$$

5. Degrees of freedom (DOF) of the underlying model

$$\text{DOF} = \text{number of measurements} - \text{number of parameters} = 11 - 3 = 8$$

6. Then the standard deviations of the model parameters are

$$\boldsymbol{\sigma} = \sqrt{\text{diag}\left(\frac{\|\mathbf{d} - \mathbf{G}\mathbf{m}^*\|}{\text{DOF}}(\mathbf{G}^T\mathbf{G})^{-1}\right)} = \begin{pmatrix} 0.030 \\ 0.113 \\ 0.187 \end{pmatrix}$$

With this procedure it is possible to infer model parameters—or the best fit solution—and the uncertainties in these parameters, with $h_0 = 0.96 \pm 0.03$ m, $v_0 = 5.01 \pm 0.11$ m/s and $g_0 = 9.80 \pm 0.18$ m/s².

C4. Non-linear fitting through the example of thermal radiation

The particle temperature, measured by incandescence intensity measurements is a crucial part of this work. Generally, the incandescence of a hot body can be described by Planck's law (*cf.* Chapter 5.1.5),

$$I_b(\lambda, T) = C_k \frac{8\pi h}{\lambda^5} \frac{1}{\exp\{hc/\lambda k_B T\} - 1}, \quad (\text{A.26})$$

with a scaling factor C_k , which incorporates detector efficiency, collection angle and other constants, the wavelength λ , Planck's constant h , and Boltzmann's constant k_B . This function is obviously not linear and, hence cannot be used directly for a linear regression, contrary to example C3.

To explain the basic principle of temperature fitting through the measurement of incandescence spectra, an artificial incandescence spectrum with added noise is generated. The noise was modeled as Poisson/Gaussian with

$$\begin{aligned} \epsilon &= \mathcal{N}(0, 3^2) + 0.7 \mathcal{P}(I_b) \\ \epsilon &= \mathcal{N}(0, 3^2) + 0.7 \cdot \mathcal{N}(I_b, I_b) \end{aligned} \quad (\text{A.27})$$

It should be noted, that Eq. (A.27) incorporates a continuous and a discrete probability distribution. The continuous normal/Gaussian distribution represents the stochastic nature of the electronic circuitry, while the discrete Poisson distribution describes all kinds of quantized transitions, like photon noise and shot noise. The scaling factors are chosen arbitrarily as illustrative example.

Measuring the temperature with the help of incandescence spectra requires data with the incandescence intensity together with the associated wavelengths or wavelength bands. Within the given example the following information is generated.

Table 10: Data for the numerical experiment, with wavelength vs. intensity.

Wavelength / nm	Intensity / arb.u.
400	6.55
433	27.30
467	71.67
500	69.71
533	120.12
567	133.15
600	182.03
633	180.97
667	232.24
700	225.92

The likelihood is

$$\mathcal{L}(T, C) = p(\mathbf{I}|T, C) \propto \exp \left\{ - \sum_{j=1}^N \frac{[I_j - C \cdot I_B(\lambda_j, T_j)]^2}{2\sigma_{I,j}^2} \right\} \quad (\text{A.28})$$

The resulting numerical measurement was fitted by the non-linear least squares algorithm `lsqnonlin`, which is included in MATLAB. On the one hand, `lsqnonlin` applies different algorithms for solving the minimization problem, and on the other hand directly outputs the Jacobian matrix if required. The result of such a fitting is presented in Figure 68. The input values (red diamonds) carry the information of the “true” blackbody radiation curve (black line) with added noise according to Eq. (A.27). The maximum likelihood estimate (blue line) is the “fitting result”.

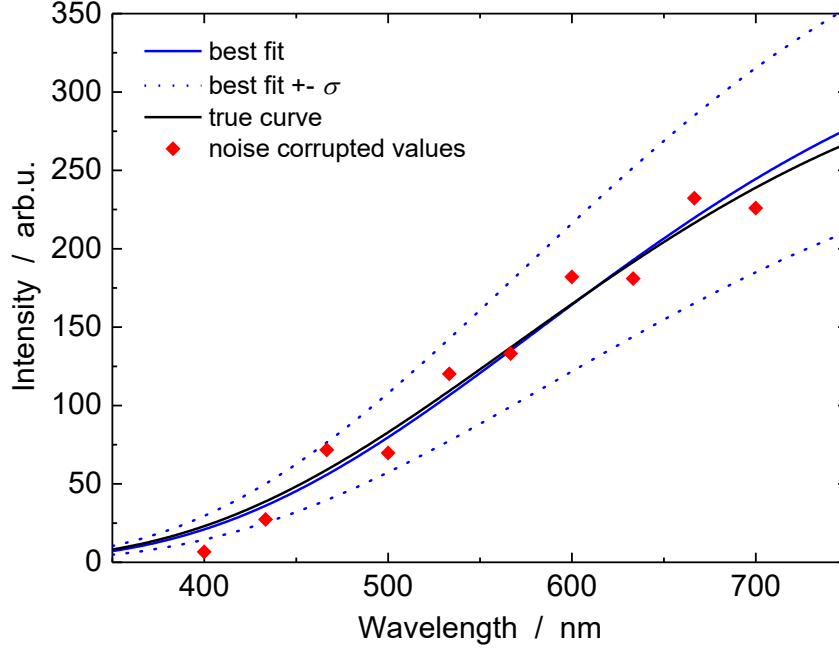


Figure 68: Example of a numerical experiment fitting Planck's law to a noise-corrupted artificial blackbody emission spectrum.

The blue dashed lines envelope the credible interval; which is, basically, nothing more than the 1σ (84%) credible interval.

Obviously, Planck's law is not linear, but when the model at \mathbf{x}_{MLE} is sufficiently linear, the Jacobian can be used to approximate the uncertainty in model parameters and the correlation of those. To test the linearity of the model in order to achieve an easier temperature fitting, the linear approximation of the likelihood is compared with the 'true' likelihood calculated by sampling the likelihood.

To sample the likelihood profile, the likelihood function can be computed when the parameters of interest T and C are varied in a sufficiently large parameter range around \mathbf{x}_{MLE} . To compute the 2D likelihood profile in Figure 69, the temperature is sampled from 2340 to 4980 K with an increment $\Delta T = 7.5$ K, while the scaling factor C is sampled from 0 to 2.4 with an increment of $\Delta C = 8.5 \times 10^{-3}$. The resulting likelihood map is a matrix with 315×281 cells.

The 1D marginal distribution is the integral over all parameters, without the marginal one

$$p(T|\mathbf{I}) = \int_0^{\infty} p(\mathbf{I}|T, C) dC, \quad p(C|\mathbf{I}) = \int_0^{\infty} p(\mathbf{I}|T, C) dT, \quad (\text{A.29})$$

where the integral turns into a sum over the dimension, which is integrated out,

$$p(T|\mathbf{I}) = \sum_{i=1}^{N_C} p(\mathbf{I}|T, C_i)\Delta C, \quad p(C|\mathbf{I}) = \sum_{j=1}^{N_T} p(\mathbf{I}|T_j, C)\Delta T_p. \quad (\text{A.30})$$

Sampling the likelihood is only feasible for strongly nonlinear models or for test cases, like this. The non-linear least-squares minimization `lsqnonlin` finds the solution in 25 steps or 75 function evaluations, respectively. Sampling with a sufficient resolution needs more than 100,000 function evaluations, which means approx. 2,000 times higher computational costs. Even more elaborate sampling techniques like MCMC or Gibbs sampling need approx. 5000 samples for such a simple problem.

In Figure 69, the sampled likelihood is shown in black deformed ellipses. The deformation is an indicator for the non-linear model. The important question is, if the linearization is a suitable approximation. Therefore, the linearized likelihood, in form of the 90% credible interval is overlaid. At first glance, the two parameters T and C are strongly correlated with $\rho(T, C) = 0.99$. Due to the correlation, one can metaphorically think about the likelihood function around \mathbf{x}_{MLE} as a “valley”. Within the linearized model this “valley” runs along the major axis of the ellipse, and thus is a straight line, while the valley of the sampled likelihood function is convex.

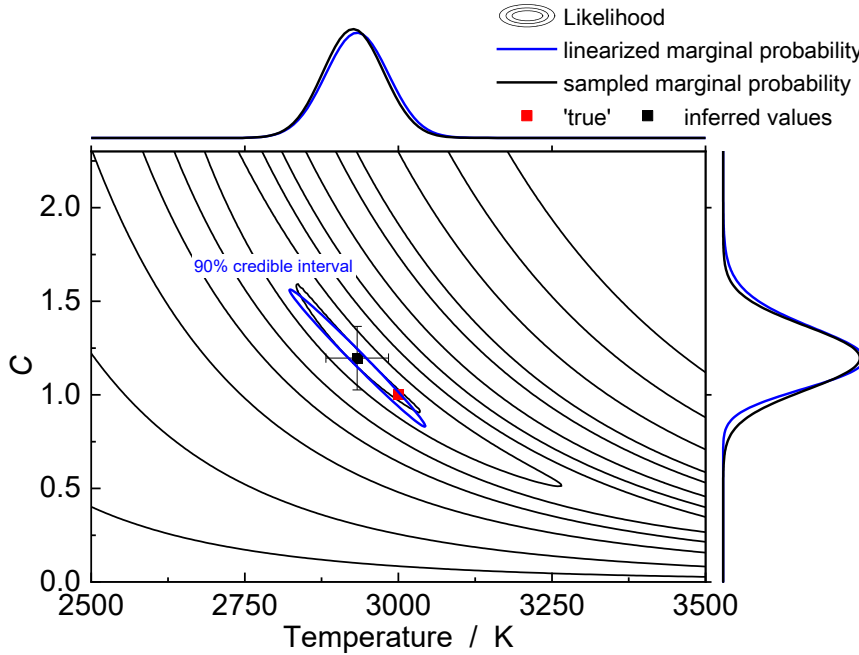


Figure 69: Comparison of the sampled and linearized likelihood function of a temperature fitting. The likelihood functions are drawn in black ellipses (sampled) or blue ellipses (linearized), respectively. The black symbol represents the maximum-likelihood estimate \mathbf{x}_{MLE} with error bars. The red symbol is the ‘true’ value of T and C . At the borders of the graph, the marginal probability densities are shown as black lines and the linearized integrated sampled marginal probability densities, according to the normal distributed model are shown as blue lines.

Even better representatives for the mismatch of linear to sampled model are the marginal probability distributions. There, the linear marginal probability distribution is a Gaussian normal distribution and the sampled marginal probability distribution is nearly Gaussian, but with a skewness $\neq 0$.

In the end, the difference in the resulting uncertainties is very small, with

$$T_{\text{sampled}} = 2933 \begin{Bmatrix} +40 \\ -58 \end{Bmatrix} \text{ K} \quad \leftrightarrow \quad T_{\text{linear}} = 2933 \pm 51 \text{ K, and}$$

$$C_{\text{sampled}} = 1.19 \begin{Bmatrix} +0.18 \\ -0.15 \end{Bmatrix} \quad \leftrightarrow \quad C_{\text{linear}} = 1.19 \pm 0.17,$$

therefore, the linear approximation for uncertainty determination in the temperature evaluation is sufficiently accurate.

C5. Bayes' statistics for laser-induced incandescence

In this work, the temporal variation of temperature and mass balance during the cooling phase of laser-heated nanoparticles is modeled by the differential equations introduced in Chapter 6.1. The solver used in MATLAB is the `ode45` solver, which is based on the Dormand-Prince method [195] using fourth and fifth order solutions for error estimation.

To achieve a more realistic numerical experiment, solely Poisson noise with $\epsilon = \mathcal{N}(0,0) + 1 \cdot \mathcal{N}(T_p, T_p)$ (similar to Eq. (A.27)) is added to the simulated temperature traces. Due to the—in this section neglected step—from intensity to temperature, the temperature error in a real experiment will be different. The resulting numerical experiment temperatures $T_{p,j}$ are shown in Figure 70.

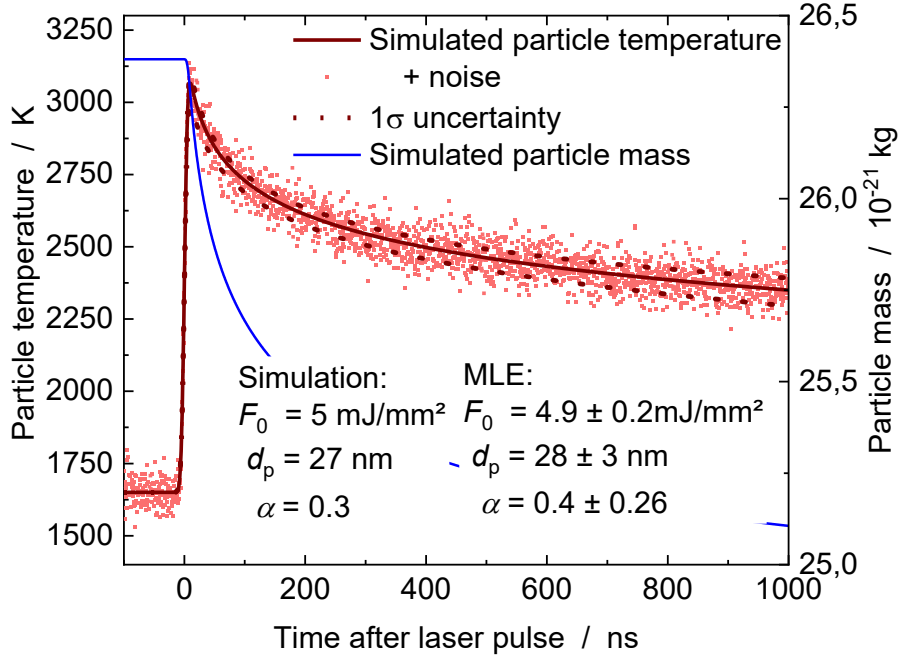


Figure 70 Numerical LII experiment: The dark red full line is the exact simulated temperature for the given conditions. The blue curve is the simulated mean particle mass. The light red symbols are the exact solution plus Poisson noise. The dark red symbols show the maximum likelihood estimate plus or minus the resulting parameter error.

According to Chapter C4, it can be tested, if a linear approximation of the least-squares model is feasible. Therefore, the likelihood distribution of the parameters of interest \mathbf{x} in this experiment is sampled over a sufficiently highly resolved section, here $d_{p,\text{sample}} = [20, 20.2, 20.4, \dots, 35]$ and $\alpha_{\text{sample}} = [0, 0.01, 0.02, \dots, 0.6]$ yielding a two dimensional 81×61 value space. By solving the integral, in Eq. (3.8), the marginal distribution of the likelihood function can be compared to the normal distributions of the Matlab `lsqnonlin` solution, which assumes a nearly linear behavior at \mathbf{x}_{MLE} .

In Figure 71, the logarithmic likelihood function and the corresponding marginal distributions $p(d_p|\mathbf{T})$ and $p(\alpha|\mathbf{T})$ for the normal and sampling approach are shown.

Firstly, the lines of constant uncertainty of the sampled likelihood are perfect ellipses. As already explained in Appendix A, ellipses represent the shape of correlated normal distributions. When the normally distributed measurement noise translates into a normally distributed parameter error, the model itself is “linear enough” to assume a linear behavior at \mathbf{x}_{MLE} .

Secondly, the marginal distributions are symmetrical Gaussian distributions, with nearly the same mean and standard deviation for both approaches, with

$$d_{\text{sampled}} = 27.2 \pm 1.7 \text{ nm} \quad \leftrightarrow \quad d_{\text{linear}} = 27.2 \pm 1.52 \text{ nm}, \text{ and}$$

$$\alpha_{\text{sampled}} = 0.33 \pm 0.15 \quad \leftrightarrow \quad \alpha_{\text{linear}} = 0.33 \pm 0.134,$$

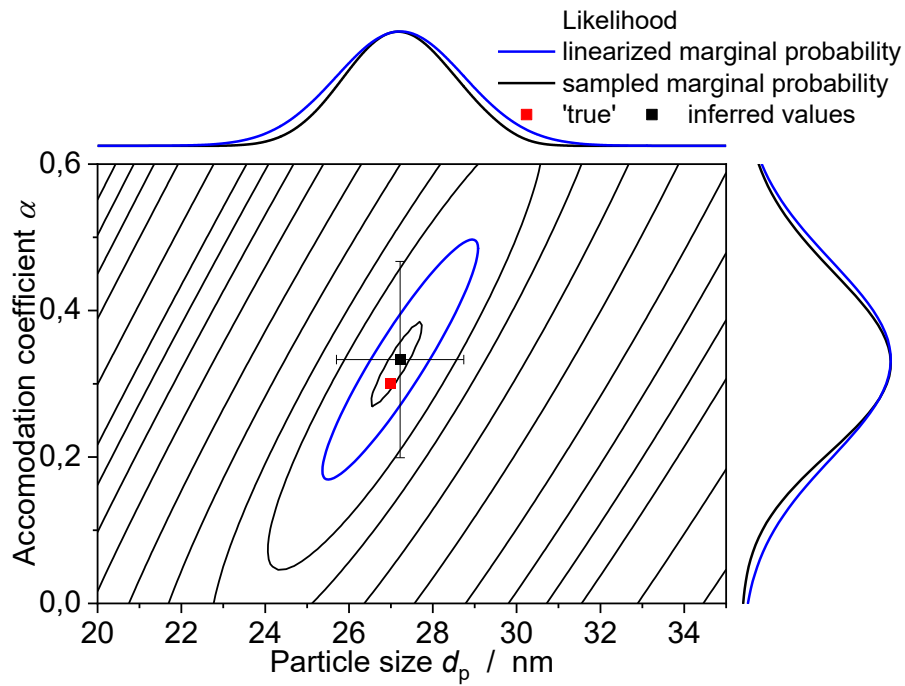


Figure 71: Log-likelihood function of a numerical LII experiment.

so that the linear approximation for uncertainty determination in the particle size fitting is very well suitable. The small underestimation of the uncertainty is owed to not perfect linearity. Certainly, \mathbf{x}_{MLE} will be correctly found, but the uncertainties can be slightly misestimated.



Acknowledgments

Firstly, I would like to express my sincere gratitude to my advisor Prof. Christof Schulz for the continuous support during my Ph.D study and related research; for his patience, motivation, and immense knowledge. His guidance helped me in all the time of research and writing of this thesis. I could not have imagined having a better advisor and mentor for my Ph.D study than you.

I would like to thank Prof. Kyle Daun, not only for his insightful comments and encouragement, but also for all the hard question which incited me to widen my research from various perspectives. Your enthusiasm and your unquenchable thirst for knowledge infected me. Thank you for this!

My sincere thanks also goes to Prof. Dreier, who provided me an opportunity to join his team. Without his precious support it would not be possible to conduct this research.

Thank you, my fellow labmates for the stimulating and fruitful discussions and for all the fun we have had in the last six years. In particular, I am grateful to Raphael Mansmann for the curiosity we share – and which guided us through science, research, Friday evening experiments and of course beer brewing.

Last but not the least, I would like to thank my family: mom and dad, my brother and my sister, my nieces and my nephews for supporting me spiritually throughout writing this thesis and my life in general.

DuEPublico

Duisburg-Essen Publications online

UNIVERSITÄT
DUISBURG
ESSEN

Offen im Denken

ub | universitäts
bibliothek

Diese Dissertation wird über DuEPublico, dem Dokumenten- und Publikationsserver der Universität Duisburg-Essen, zur Verfügung gestellt und liegt auch als Print-Version vor.

DOI: 10.17185/duepublico/70148

URN: urn:nbn:de:hbz:464-20190523-155347-1



Dieses Werk kann unter einer Creative Commons Namensnennung
- Weitergabe unter gleichen Bedingungen 4.0 Lizenz (CC BY-SA
4.0) genutzt werden.